Multiwavelength observations of cosmological transients

Adam Benjamin Higgins

Supervisors:

Rhaana Starling

Nial Tanvir

Thesis to be submitted for the degree of

Doctor of Philosophy

X-ray & Observational Astronomy Group

Department of Physics and Astronomy

University of Leicester

June 5, 2019

Multi-wavelength observations of cosmological transients

Adam Benjamin Higgins

Abstract

Astrophysical transients encompass some of the most powerful and violent explosions in the universe, providing a unique opportunity to observe extreme, physical environments across multiple wavelengths. These events are usually powered by a compact central engine, such as a black hole or neutron star, and involve the release of vast reservoirs of energies (typically $> 10^{50}$ ergs). One such class of transient, Gamma-ray Bursts (GRBs), temporarily reach luminosities that exceed the rest of the observable gamma-ray universe, allowing us to observe these events at cosmological distances.

In this thesis, I discuss multiwavelength observations of a number of astrophysical transients classes, with a particular focus on GRBs. Understanding the physical properties of such extreme events can aid with testing of our underlying, theoretical models, and the nature of the universe around us. In Chapter 2, I present the detailed multiwavelength analysis of an optically dark GRB 140713A and the origin of the missing optical flux. In Chapter 3, I discuss my investigation into the sub-threshold trigger population of the *INTEGRAL* satellite including a comparison of the *INTEGRAL* and *Swift* GRB samples. In Chapters 4 and 5, I introduce the SPLOT optical linear polarimetry, pilot survey, utilising polarimetry as an independent tool to highlight new transients of scientific interest and the role polarimetry may have in future transient surveys.

Declaration

I hereby declare that no part of this thesis has been submitted to this or any other University as part of the requirement for a higher degree. The work herein was conducted by the undersigned except for contributions as acknowledged in the text.

Adam Benjamin Higgins

June 5, 2019

Acknowledgements

The work I present in this thesis would not have been possible without the support of many fantastic people along the way.

I would like to start by saying a huge thank you to my supervisor Rhaana. I feel I have been very lucky to have benefited from her vast knowledge and guidance over the past three and a half years, which has not only made my PhD possible but a thoroughly enjoyable experience. I would also like to thank Nial for providing expert insight and support on my research and Klaas, for introducing me to the world of polarimetry. His brilliant insight and collaboration into such a challenging topic has provided me with the fantastic opportunity to further explore transient astronomy.

Thanks to all the members of the G24A office, past and present, with whom I have been lucky enough to share my working hours with. My time spent with them has led to some of the most insightful, bizarre and downright hilarious conversations anyone has ever been a part of in all of human history. Also, thanks to all of the other PhD students, including Jordan, Claudia, Roger, Sam and Amery, who all started this journey with me in October 2015. I have met so many fantastic friends and colleagues over the years in Leicester, too many to fit into this one page acknowledgement, and I would like to thank all of you for the years of great memories.

All of this work would not have been possible without the continuous support of my family. My mum, dad, sister and grandparents have always supported me in following my passion for physics and motivated me to continue following my dreams. Finally, I would also like to thank Ella, who is a continuous source of inspiration.

Overall, it has been an honour and a privilege to have been at the University of Leicester over the years and I will very much miss the people, department, and Wing Wednesdays at the Loaded Dog. Good luck to everyone for the future.

Publications

Published Papers:

Investigating the nature of the INTEGRAL gamma-ray bursts and sub-threshold triggers with Swift follow-up,
Higgins et al. 2017, MNRAS 470, 314

The unpolarized macronova associated with the gravitational wave event GW 170817,
Covino et al., 2017, Nature Astronomy 1, 791

Multi-messenger observations of a binary neutron star merger,
Abbott et al., 2017, ApJL, 848, L12

ALMA and GMRT constraints on the off-axis gamma-ray burst 170817A from the binary neutron star merger GW170817,
Kim et al., 2017, ApJ, 850, L21

Calibration of EFOSC2 broadband linear imaging polarimetry,
Wiersema et al., 2018, PASA, 35

Infrared molecular hydrogen lines in GRB host galaxies,
Wiersema et al., 2018, MNRAS, 481, 1126

SPLOT: a snapshot survey for polarized light in optical transients,
Higgins et al., 2019, MNRAS, 484, 5023

Detailed multiwavelength modelling of the dark GRB 140713A and its host galaxy,
Higgins et al., 2019, MNRAS, 484, 5245

Polarimetry of relativistic tidal disruption event Swift J2058+0516,
Wiersema et al., submitted.

Conference proceedings and articles:

Searching the INTEGRAL WEAK alert population for Gamma-ray Bursts and other high energy transients,
Higgins et al., 2017, 11th INTEGRAL Conference Gamma-Ray Astrophysics

Shedding Light on the Geometry of Kilonovae,
Bulla et al., 2018, The Messenger, 174, 34

GCNs and ATels:

GRB 180805B: ESO/NTT optical observations,
Higgins et al., 2018, GRB Coordinates Network, 23090

Optical Polarimetry of Blazar PKS1510-089,
Higgins et al., 2016, The Astronomers Telegram, 9179

Optical observations of XTE J1709-267,
Wiersema et al., 2016, The Astronomers Telegram, 9181

Contents

List of Figures

List of Tables

1

Introduction

1.1 Transient astronomy

The field of transient astronomy has grown significantly over the last several decades. At present, it encompasses a huge array of short-lived and variable astrophysical phenomena ranging from the violent death of massive stars to accretion onto black holes (BH). Transients represent some of the most violent and luminous explosions in the universe and many can be observed across the entire electromagnetic spectrum, allowing us to uncover the internal mechanisms of some of the most extreme physical conditions. Transients provide a unique opportunity to observe these extreme physical processes throughout the cosmos and addition-

ally, use these events to shine light on the most distant corners of the universe.

During my PhD I have observed a variety of transient phenomena. I have spent a significant part of my time, and several investigations, focusing on Gamma-ray bursts (GRBs), and in this introduction I discuss the history, significant milestones and theory of GRBs. The theory of other transients I have researched can be found in the respective research chapters. I will conclude the introduction by giving a brief outline of the scientific research I have conducted throughout my degree and the subsequent chapters of this thesis.

1.2 Gamma-ray bursts and their discovery

GRBs are short-lived flashes of high energy photons first observed in the late 1960s by the *Vela* satellites which were US military satellites purposely built to monitor potential nuclear tests carried out by the Soviet Union. The satellites recorded observations of a number of GRBs over several years and from the data, observers concluded that the source of the gamma-rays did not originate from the Earth but instead that the GRBs must have an extra-terrestrial origin (Klebesadel et al., 1973). Over the next two decades no general consensus could be found as to the origin of GRBs (Fishman & Meegan, 1995). A number of possible progenitors were suggested, such as massive star death (Colgate, 1968) or neutron stars (NS; Hartmann et al. 1990), and some suggested that GRBs were produced from within the Milky Way (Quashnock & Lamb, 1993; Lamb, 1995). Unfortunately none of the gamma-ray missions at that time were capable of accurately localising GRBs resulting in little option of follow-up to attempt to observe longer wavelength counterparts.

In 1991, the landscape began to change with the launch of NASA's Compton Gamma Ray Observatory (*Compton*; Gehrels et al. 1993) carrying on-board the Burst and Transient Source Experiment (*BATSE*; Fishman et al. 1985) instrument - specifically designed to detect and localise GRBs. Observations with *BATSE* highlighted that GRBs were isotropically distributed over the sky, adding doubt to the Galactic origin theories and suggesting that GRBs had a

cosmological origin (Meegan et al., 1992). This cosmological origin was not confirmed until the 1996 launch of Italian-Dutch X-ray mission *BeppoSAX* (Boella et al., 1997). On 1997 February 28, the Wide Field Camera (WFC) detected GRB 970228. The GRB naming convention follows the format GRB YYMMDD where YY is the year, MM is the month and DD is the day of the discovery. Prior to 2010, if multiple GRB were observed on the same day then the name would be followed by a letter (e.g. A for the first, B for the second). Since 2010 the first GRB on a given day, even if only one was observed, will always be assigned with the letter A. Simultaneously, a coincident X-ray source was detected (Costa et al., 1997) using *BeppoSAX*'s Narrow Field Instruments (NFI) and a optical source using both the Isaac Newton Telescope (INT) and William Herschel Telescope (WHT) located at La Palma observatory (van Paradijs et al., 1997), both of which were rapidly fading. These were the first confirmed observations of longer wavelength counterparts to a GRB, termed 'afterglows'. The observations also highlighted the short-duration phenomenology needed to fully analyse GRBs.

An accurate distance estimate was finally made following the *BeppoSAX* detection of GRB 970508, a few months later. Follow-up observations using the Very Large Array (VLA) detected a coincident radio counterpart to the GRB (Frail et al., 1997) and further observations using the Keck telescope were made to obtain an optical spectrum (Metzger et al., 1997). The spectrum revealed a number of absorption lines all at a common redshift, $z = 0.835$ corresponding to a distance from Earth of ~ 6 billion light-years and showed that the origin of GRBs was cosmological. This new evidence highlighted the unique potential of observing GRBs; we now know that they are some of the most distant (Tanvir et al., 2009; Cucchiara et al., 2011) and luminous objects in the universe (Abdo et al., 2009).

1.3   Gamma-ray burst classification and progenitors

Another significant discovery from the *BATSE* instrument was the observational evidence for the bimodal distribution of GRBs (Kouveliotou et al. 1993; Figure 1.1). GRBs were

categorised based on their observed T_{90} - the time elapsed to receive the cumulative prompt gamma-ray flux from 5% to 95% above the standard background level (i.e. 90% of the flux). This bimodality has been observed in a number of other instrument GRB samples (see Qin et al. 2013 for examples). In this categorisation, $T_{90} < 2\,\mathrm{s}$ corresponded to a short GRB and a $T_{90} > 2\,\mathrm{s}$ to a long GRB. Kouveliotou et al. (1993) also highlighted that the longer duration GRBs, on average, have lower peak energies and softer spectral shapes (higher ratio of lower energy gamma-ray photons to higher energy gamma-ray photons). This dichotomy between the spectral and temporal properties of the sub-groups suggests that the underlying progenitors are different.
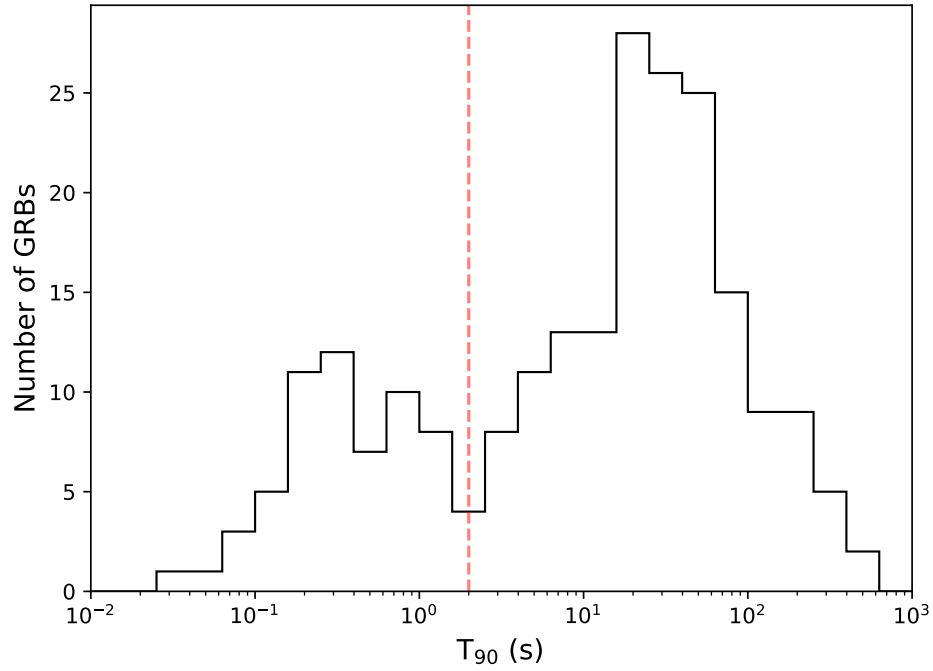
Figure 1.1: The bimodal distribution of GRBs within the first *BATSE* catalogue plotted by T_{90} duration. The dashed red line indicates the classical divide at $T_{90} = 2\,\mathrm{s}$.

1.3.1 Long gamma-ray bursts

Long GRBs (LGRBs) are thought to arise from a central engine, either a BH or NS, produced from the core-collapse of massive stars (Woosley, 1993; MacFadyen & Woosley, 1999;
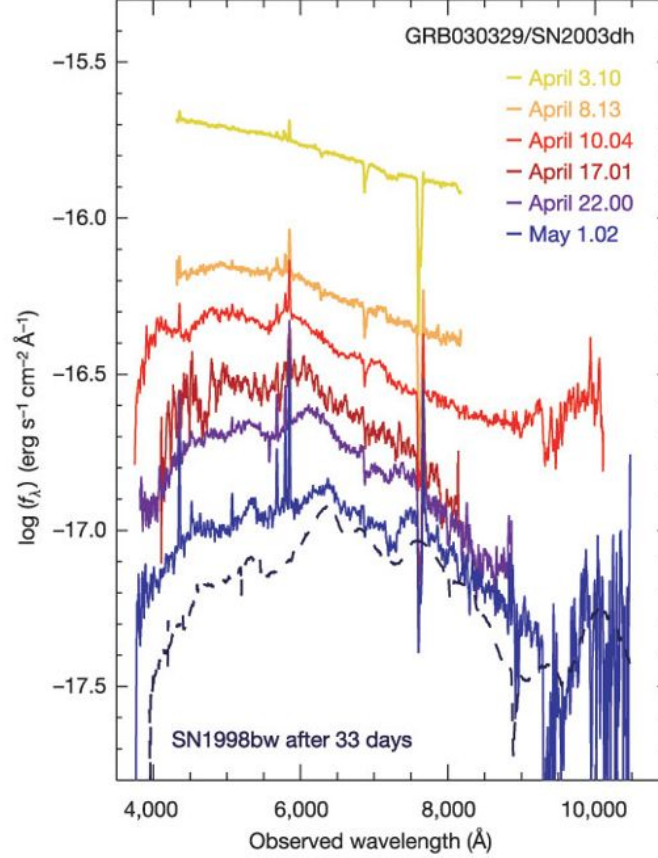
Figure 1.2: The temporal evolution of the optical spectra of GRB 030329/SN 2003dh (Hjorth et al., 2003). The power-law seen in the 2003 April 3 spectrum, days after the GRB detection, had significant evolved after two weeks. After a month the spectral properties are strikingly similar to that of SN 1998bw.

Hjorth & Bloom, 2012). This theory had been around since the 1960s (Colgate, 1968) but it was not until a GRB was discovered coincident with the location of a type Ic supernovae (SNe) at near-simultaneous times, GRB 980425 and SN 1998bw (Galama et al., 1998) that the connection between massive stars and GRBs could be investigated. This connection was verified after the discovery of GRB 030329 and the accompanying SN 2003dh (Hjorth et al., 2003). Once the bright afterglow of the GRB had faded in the optical, the supernova signature was detectable and became prominent over the next few weeks of observations. The evolution of the optical spectra provided further proof that the two events were connected (Figure 1.2). The early-time spectra could be modelled using a simple power-law - the expected shape for

a GRB afterglow but the late-time spectral shape had significantly altered and was strikingly similar to SN 1998bw (Galama et al., 1998; Hjorth et al., 2003). Further GRB-SNe joint observations have been observed cementing the fact that massive stars are the progenitors of LGRBs. LGRBs are also among the most distant events in the universe, with a mean redshift $<z> \sim 2.0$ (Berger, 2014) and have contributed two of the most distant events ever observed; GRB 090423 ($z \sim 8.2$; Salvaterra et al. 2009; Tanvir et al. 2009) and GRB 090429B ($z \sim 9.4$; Cucchiara et al. 2011).

LGRBs occur in galaxies or regions of galaxies where high levels of star formation are present (Bloom et al., 2002; Woosley & Heger, 2006). Their mean redshift also coincides with the peak cosmic star formation activity (Schady, 2017). Early observations of LGRBs suggested that they resided in low mass, low-luminosity, metal-poor, blue, dwarf galaxies (Le Floc'h et al., 2003; Savaglio et al., 2009). Further advances in optical follow-up have shown that LGRBs reside in a whole spectrum of hosts galaxies, including larger mass hosts of optically-dark (dust-obscured) GRBs (Perley et al., 2009, 2013) and metal-rich ($\sim$ solar metallicity) host galaxies (Krühler et al., 2012; Savaglio et al., 2012; Elliott et al., 2013; Schady et al., 2015).

Recent work has also suggested the possible existence of a third class of ultra-long GRBs, where several GRBs have been observed with $T_{90} \gtrsim 1000$ s; e.g. GRB 091024 (Gruber et al., 2011), GRB 101225A (Thöne et al., 2011; Campana et al., 2011), GRB 111209A (Gendre et al., 2013; Levan et al., 2014) and GRB 121027A (Levan et al., 2014). Possible progenitors of this sub-group include collapsing blue supergiants, such as Wolf-Rayet stars with radii far greater than the Sun or Tidal Disruption Events (TDEs) where a star is gravitationally disrupted by a nearby BH and is stripped of mass creating an accretion disc.

1.3.2 Short gamma-ray bursts

Short GRBs (SGRBs) have been localised in a wide variety of spatial positions. They have been discovered in host galaxies similar in morphology and levels of star formation to pre-

viously localised long GRBs (D'Avanzo et al., 2009) and, in some cases, have been found residing on the edges of their host or without a host at all (Berger, 2010). Moreover, a lack of association with SNe suggested that a massive star origin for SGRBs was incorrect (i.e. GRB 050509B, Bloom et al. 2006; GRB 050709, Fox et al. 2005; Hjorth et al. 2005; GRB 051221A, Soderberg et al. 2006). As SGRBs have very short durations, the progenitors of these events must have an equally short dynamical time scale, such as those theorised in NS-NS or NS-BH mergers (Eichler et al., 1989; Narayan et al., 1992). The compact binary progenitor could also explain the positions of SGRBs localised away from any potential host galaxies. Both compact objects would have to form from massive stars, post main-sequence and collapse. This results in a natal kick with high velocity, potentially propelling the binary system out of the host galaxy (Church et al., 2011; Eldridge & Stanway, 2016; Bray & Eldridge, 2016). Theoretical simulations of binary mergers agree with the observed properties of short GRBs discussed above (e.g. Belczynski et al. 2006). However, there had not been any direct observations of compact binary mergers as of 2014.

In 2015 the Advanced Laser Interferometer Gravitational-Wave Observatory (aLIGO; LIGO Scientific Collaboration et al. 2015) began searching for gravitational wave (GW) signals and on 2015 September 14, a BH-BH merger was detected for the first time (Abbott et al., 2016). The observation proved that compact binary mergers existed in nature but no electromagnetic radiation was observed alongside the event. The connection to SGRBs was confirmed on 2016 August 17 following the near-simultaneous aLIGO observations of the NS-NS GW source GW 170817 and GRB 170817A, detected by both the *Fermi* Gamma-Ray Burst Monitor (GBM; Meegan et al. 2009) and the INTErnational Gamma-ray Physics Laboratory (*INTEGRAL*; Winkler et al. 2003) space observatories (Figure 1.3; Abbott et al. 2017a). Numerous multi-wavelength afterglow observations were made over the subsequent weeks and months (see Abbott et al. 2017b and references there-in) to confirm the progenitor. Through the efforts of both GW and electromagnetic observations, has opened up the new era of multi-messenger astronomy. Unlike LGRBs, their shorter cousins, on average, exist at lower redshifts ($<z> \sim 0.5$) and typically have lower energy budgets (Berger, 2014).
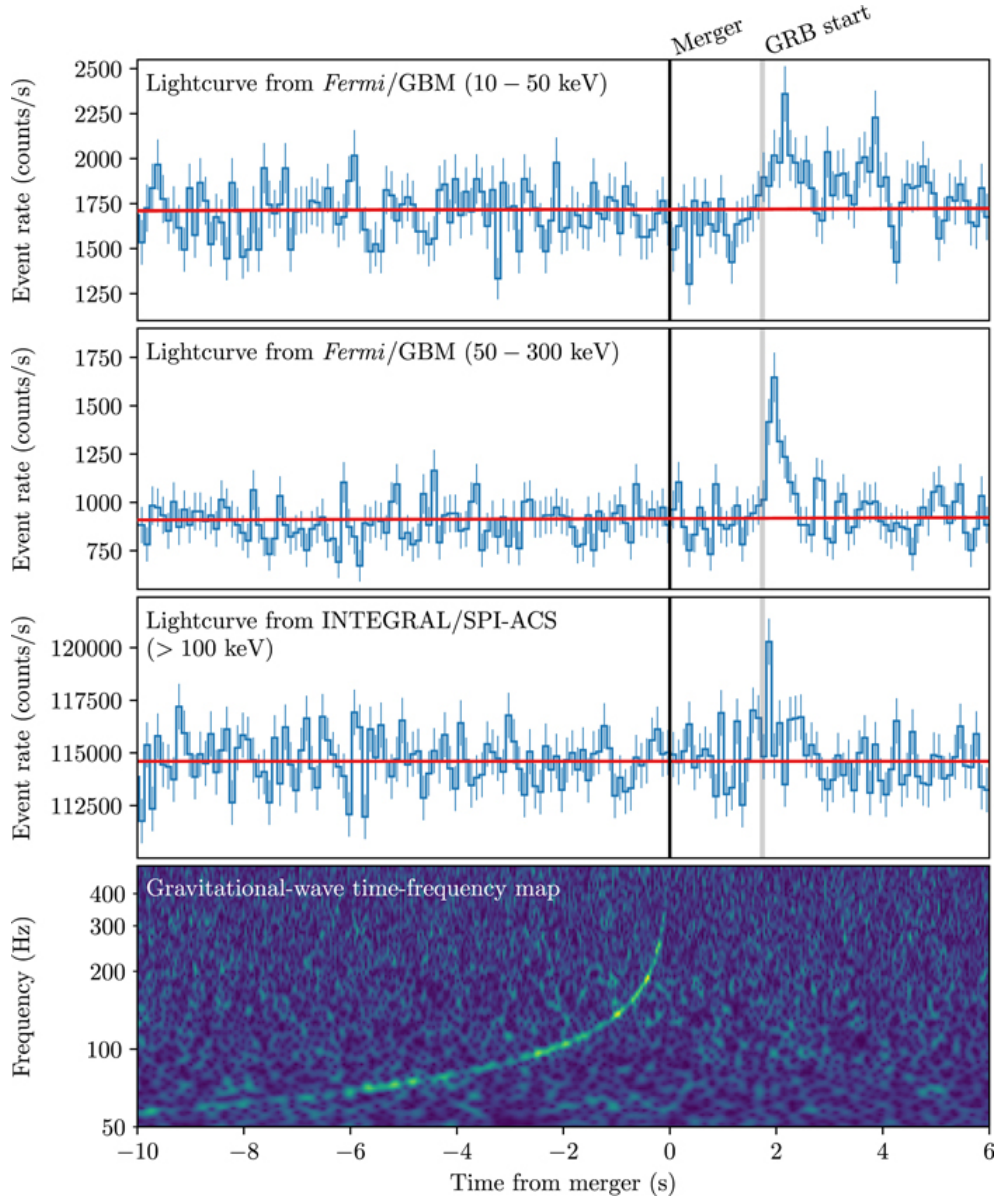
Figure 1.3: Timeline of detection of GW 170817 and GRB 170817A (Abbott et al., 2017a). The increase in frequency (fourth window) shows the final in-spiralling orbits by the BH and NS before the merger event (black line) observed by aLIGO followed by the GRB detection (grey line) ~ 2 s later observed by *Fermi* and *INTEGRAL* (top three windows).

1.4 Observing high energy emission

Many observatories past and present have dedicated their time to observing and understanding GRBs. The GRB research described in this thesis predominantly utilises data from two

currently operating missions, described in detail below.

1.4.1   The Neil Gehrels *Swift* observatory

The Neil Gehrels *Swift* Observatory (*Swift*; Gehrels et al. 2004) launched in 2004 is a multi-wavelength observatory with the primary mission to observe and study GRBs. *Swift* carries three instruments: the Burst Alert Telescope (BAT; Barthelmy et al. 2005), the X-ray Telescope (XRT; Burrows et al. 2005b) and the Ultraviolet/Optical Telescope (UVOT; Roming et al. 2005). *Swift* has revolutionised early-time multi-wavelength follow-up of GRBs. The satellite can autonomously and rapidly slew to a BAT detected GRB and provide simultaneous XRT and UVOT observations, with an accurate localisation, within $\sim 120\,\text{s}$ post-GRB. This also enables other satellites and ground-based facilities to initiate early-time follow-up observations.

BAT is a highly sensitive gamma-ray instrument. It is made of 32768 pieces of CdZnTe (CZT) creating an effective detector area of $1.2 \times 0.6\,\text{m}$ and has a D-shaped coded mask comprised of 54000 lead tiles that sits on a $5\,\text{cm}$ thick composite honeycomb panel. The area of the mask is $2.7\,\text{m}^2$ and has a half-coded field of view (FOV) of $23.6 \times 23.6\,\text{arcmin}$. It primarily works in the energy range of $15 - 150\,\text{keV}$ with an energy resolution of $\sim 7\,\text{keV}$ for imaging at Full-Width Half Maximum (FWHM), but has a non-coded response up to $500\,\text{keV}$. It has a sensitivity of $\sim 10^{-8}\,\text{erg cm}^{-2}$. BAT will trigger if an uncatalogued source was detected with a 6.5σ significance, disseminate the information via the Gamma-ray Coordinates Network (GCN[1]; Barthelmy et al. 1994, 2000) and localise a GRB position to within a few arcmin, often in $< 20\,\text{s}$. The main focus of BAT is to measure the high energy prompt emission of a GRB, but it can be further utilised to gather data in the hard X-ray range, either for surveys or single targets. BAT searches for sources using two different methods (Fenimore et al., 2003). The first method constantly monitors the gamma-ray count rate in the detector, and highlights any excess on short or long timescales, with short being defined as $\leq 64\,\text{ms}$. The second method involves BAT searching for uncatalogued sources in background images, taken every

---
[1]https://gcn.gsfc.nasa.gov/

8 s.

XRT is a focusing X-ray telescope, using a grazing incidence Wolter I to focus X-ray photons onto a Charge Coupled Device (CCD). XRT has an effective area of $0.11 \, \mathrm{m}^2$, a 23.6×23.6 arcmin FOV and a resolution of 18 arcsec (half-power diameter). It can measure the flux and spectra of a GRB among other properties and works in the energy range of $0.2 - 10 \, \mathrm{keV}$, with an energy resolution of $0.14 \, \mathrm{keV}$ at $5.9 \, \mathrm{keV}$ (FWHM). It has the capability to observe the X-ray afterglow emission of a burst for a period of weeks, and if needed months, reaching sensitivity levels of $\sim 10^{-14} \, \mathrm{erg} \, \mathrm{cm}^{-2} \, \mathrm{s}^{-1}$. XRT has four observing modes; Photon Diode (PD), Imaging (IM), Windowed-Timing (WT) and Photon Counting (PC) but only IM, WT and PC are currently operational. IM is used during the early-time slewing of the XRT and provides imaging of the target source, used to help provide the localisation. WT mode provides data on a target during slewing and periods of high flux (usually during the early afterglow phase) with $\sim 2 \, \mathrm{s}$ time resolution. CCD pixel columns are read off in place of single pixels so the brightest sources do not saturate the CCD. At lower fluxes, PC mode is used and can read the counts collected on a per pixel basis, however, it has a time resolution of $2.5 \, \mathrm{s}$. PC mode provides full spectroscopic resolution and can give the position of the source to within ~ 5 arcsec. The data obtained from the XRT is reduced and analysed automatically by the UK *Swift* Science Data Centre (UKSSDC; Evans et al. 2007, 2009)[2].

UVOT comprises of an optical assembly containing a 30 cm clear aperture Ritchey-Chértien telescope and has a total FOV of 17×17 arcmin. UVOT is co-aligned with XRT and possesses a range of filters, ranging from 170–600 nm, to allow spectra and broadband photometry to be carried out on GRBs. UVOT imaging can very accurately find the position of background stars within the FOV (< 1 arcsec) and when used in conjunction with XRT images of the target source can localise GRBs to within ~ 2 arcsec (Goad et al., 2007).

---

[2]http://www.swift.ac.uk/

1.4.2 INTErnational Gamma-Ray Astrophysics Laboratory

The INTErnational Gamma-Ray Astrophysics Laboratory (*INTEGRAL*; Winkler et al. 2003), launched in 2002 is a general purpose gamma-ray observatory but also observes GRBs. *INTEGRAL* carries two gamma-ray instruments; IBIS (Ubertini et al., 2003) and SPI (Vedrenne et al., 2003) complimented with the JEM-X (Lund et al., 2003) and OMC (Mas-Hesse et al., 2003) monitors. All four instruments are co-aligned.

IBIS is an imaging system comprising of two separate detector arrays; ISGRI and PICsIT. ISGRI is comprised of multilayer CdTe detectors with a detection area of $0.26\,\mathrm{m}^2$ and covers an energy range of $0.015 - 1\,\mathrm{MeV}$. PICsIT is comprised of CsI detectors and has a detection area of $0.29\,\mathrm{m}^2$ that covers an energy range of $0.175 - 10\,\mathrm{MeV}$. IBIS has a fully coded FOV of $9 \times 9\,\mathrm{deg}$ and a half-coded FOV of $19 \times 19\,\mathrm{deg}$, an angular resolution of $12\,\mathrm{arcmin}$ (FWHM) and a spectral resolution of $8\,\mathrm{keV}$ at $100\,\mathrm{keV}$.

SPI is a highly sensitive spectrometer comprised of $3\,\mathrm{cm}$ Tungsten blocks, creating a fully coded mask and 19 Germanium detectors arranged in an hexagonal shape with an effective area of $500\,\mathrm{cm}^2$. SPI works over an energy range of $0.02 - 8\,\mathrm{MeV}$ and has an energy resolution of $2.5\,\mathrm{keV}$ at $1.33\,\mathrm{MeV}$ with a fully coded FOV of $16\,\mathrm{deg}$ (corner to corner). The angular resolution of SPI is $2.5\,\mathrm{deg}$ but has the capability to localise objects to $\sim 10\,\mathrm{arcmin}$. To increase the sensitivity of SPI an Anti-Coincidence Shield (ACS) comprising of 91 BGO crystals was implemented with the purpose of reducing cosmic ray interactions with SPI components. Due to the large surface area of the ACS it is capable of detecting potential GRB events but it lacks the ability to localise the sources for follow-up observations (von Kienlin et al., 2003).

JEM-X is an X-ray monitor, working in the energy range of $4 - 35\,\mathrm{keV}$. It has a fully coded FOV with a diameter of $4.8\,\mathrm{deg}$ and an angular resolution of $3\,\mathrm{arcmin}$ (FWHM). OMC is the optical monitor working in a narrow wavelength range of $500 - 600\,\mathrm{nm}$. It possesses a fully coded FOV of $5 \times 5\,\mathrm{deg}$ and an angular resolution of $25\,\mathrm{arcsec}$.

1.4.3 The *INTEGRAL* Burst Alert System

INTEGRAL can trigger for GRB detections thanks to the *INTEGRAL* Burst Alert System (IBAS[3]; Mereghetti et al. 2003), software running at the INTEGRAL Science Data Centre (ISDC[4]; Courvoisier et al. 2003) since October 2002. No triggering system is located on-board *INTEGRAL*. Instead, data reaches the ISDC within $\sim 20\,$s of observation and are immediately fed into the IBAS pipeline which utilises a number of burst detection programs in parallel. When a GRB, or another transient event, is detected inside the IBIS FOV, it is localised to an uncertainty of $\sim 2\,$arcmin, and its coordinates are automatically distributed via the Internet as Alerts. IBAS also searches for GRBs detected using the ACS of the SPI instrument and attempts to triangulate the GRB position utilising the ACS gamma-ray lightcurves in conjunction with observations of other satellites within the InterPlanetary Network (IPN; Cline et al. 1999).

IBAS searches for GRBs in the IBIS data by utilising two different kinds of programs. The first, a rate monitor, looks for significant excesses of flux in the gamma-ray light curve. The second, an image monitor, searches for excesses in observed images by comparing them to reference, background images. Both monitors use data from ISGRI. Several instances of the rate and image monitors run in parallel, utilising a number of integration time scales and energy ranges. When one or more of these monitoring programs triggers for a gamma-ray excess, an imaging analysis is performed on the optimally selected time interval in order to confirm if a real source has been detected, and to derive the significance of the detection.

1.5 The relativistic fireball model

The most prominent theory to explain the GRB observed emission is the relativistic fireball model (Cavallo & Rees, 1978; Goodman, 1986; Paczynski, 1986). The fireball producing a

---

[3]http://ibas.iasf-milano.inaf.it/

[4]http://www.isdc.unige.ch/integral/

GRB is typically divided into two phases; the initial prompt gamma-ray emission, thought to arise from internal shocks within a relativistic jet, and the longer-lived, broadband afterglow emission, thought to arise when the jet shocks with the surrounding ambient medium and decelerates (Piran, 1999; Mészáros, 2006). This is illustrated in Figure 1.4 and discussed in detail below.
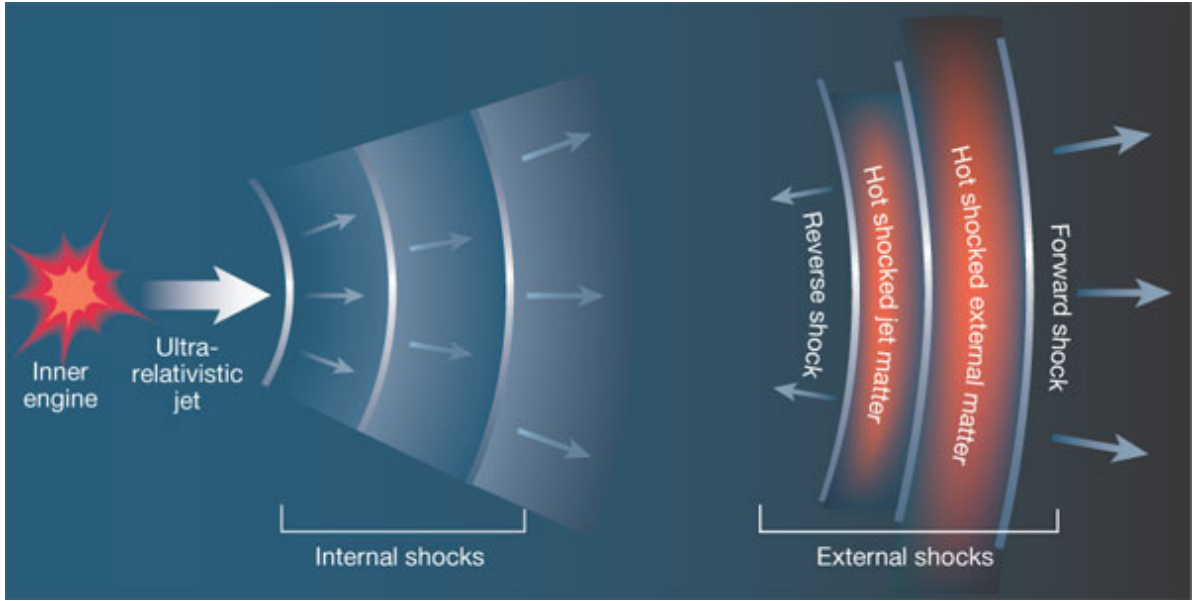
Figure 1.4: Schematic of the relativistic fireball model. The prompt gamma-ray emission is produced via internal shocks that arise within the fireball expanding outwards from the central engine. The later-time, broadband afterglow emission is produced when the jet shocks with the surrounding circumburst medium (Piran, 2003).

1.5.1 The compactness problem

At the range of cosmological distances we observe GRBs to exist, the central engine must produce a vast amount of isotropic energy, with average energy outputs of $<E_{\mathrm{iso}}> \sim 10^{52}$ ergs. Under these conditions, photons produced by the relativistic fireball model have sufficient energy to produce electrons and positrons via pair production (Ruderman, 1975; Schmidt, 1978). Observations of the prompt emission of a GRB also reveal that the flux varies on typical time-scales of milliseconds. You can estimate the size of the emitting region, r, from the

light travel time using the following relation

$$r_{\mathrm{obs}} \lesssim c\Delta t_{\mathrm{obs}} \qquad (1.1)$$

where Δt_{obs} is the variability time-scale and c is the speed of light. Taking $\Delta t_{\mathrm{obs}} \sim 10^{-3}\,\mathrm{s}$, you would require an emitting region of $\sim 300\,\mathrm{km}$. The high level of pair production that would occur in an emitting region as compact as this results in a region of high optical depth. Due to the high density, photons would be unable to escape from the region, resulting in thermal emission and an observable blackbody spectral shape. However the observed spectral shape is non-thermal with a high energy tail requiring the source to be optically thin (Piran, 1999), discussed further in section 1.5.3. This inconsistency between the size of the emitting region and the observed emission is known as the 'compactness' problem.

The compactness problem can be solved if the emitting region is travelling towards us at ultra-relativistic speeds. The mass, time and distance travelled for a relativistic particle are altered by the Lorentz factor, defined as

$$\gamma = \frac{1}{\sqrt{1 - \beta^2}} \qquad (1.2)$$

where $\beta = v/c$ and v is the speed of the particle. The diameter of the emitting region in its own rest frame would be much larger, and can be calculated using the following relation

$$r_{\mathrm{rest}} \lesssim c\Delta t_{\mathrm{rest}} = \frac{c\Delta t_{\mathrm{obs}}}{1 - \beta} \sim 2c\Delta t_{\mathrm{obs}}\gamma^2 \qquad (1.3)$$

where GRB outflows have high bulk Lorentz factors, $\Gamma \gtrsim 100$ (Piran, 1999; Lithwick & Sari, 2001; Panaitescu & Kumar, 2002; Zhang et al., 2003), resulting in rest frame emitting regions of $\sim 6 \times 10^6\,\mathrm{km}$, significantly reducing the effective density of the emitting region. Secondly, the wavelength of the observed emission, λ_{obs}, has been blue-shifted due to the relativistic doppler effect. The wavelength of the emitted region moving towards the observer is given by

$$\lambda_{\mathrm{emit}} = \frac{\lambda_{\mathrm{obs}}}{\gamma(1 - \beta)} \sim 2\gamma\lambda_{\mathrm{obs}} \qquad (1.4)$$

where a gamma-ray photon with $\lambda_{\mathrm{obs}} = 10^{-3}\,\mathrm{nm}$ and a Lorentz factor of $\gamma = 100$ would have an emitted wavelength of $\sim 0.2\,\mathrm{nm}$. The energy decrease from the observed to the rest frame is $\sim 1\,\mathrm{MeV}$ to $\sim 6\,\mathrm{keV}$, far below the required energy for pair production (1.02 MeV; Hubbell

14

2006). A significant fraction of observed high energy emission would therefore be emitted far below the pair production energy threshold, so no region of high optical depth arises and the photons are free to escape.

1.5.2 Relativistic jet emission

Several GRBs have been observed with extremely high isotropic energy outputs. GRB 080916C, detected in 2008 by *Fermi*, is the most energetic burst ever discovered and was estimated to have an energy output of $\sim (7-9) \times 10^{54}$ ergs (Abdo et al., 2009; Greiner et al., 2009), equivalent to four or five times Solar rest mass. Energy budgets this high are problematic for a stellar progenitor. In a similar fashion to the compactness problem, this is solved if the emission is relativistically accelerated in the form of jets with an opening angle, instead of isotropically.

How the central engine produces these relativistic jets remains to be fully understood. However, they are thought to arise from similar mechanisms observed in other astrophysical phenomena. There are two main theories of a BH producing jets. Jets can be formed via the Blandford - Znajek process (Blandford & Znajek, 1977), where energy is extracted from material accreting onto a rotating BH. They can also be formed via the Blandford - Payne process (Blandford & Payne, 1982), where energy is extracted through magnetic field lines from an accretion disk. Material within the jet that is accelerated to ultra-relativistic speeds is beamed in the direction of motion as $\theta \sim 1/\Gamma$ (Piran, 1999). For the prompt phase of the emission, Γ is approximately constant and the beaming angle remains constant. While this beaming angle is smaller than physical jet opening angle the observer sees all of the emission. Once the jet shocks with the surrounding medium, the fireball decelerates and Γ decreases (Sari & Piran, 1995; Piran, 1999). Once $1/\Gamma > \theta_{j/2}$, the beamed emission angle becomes larger than the jet cone, and jet material begins to spread out perpendicular to the direction of the observer. This effect, known as a jet break, manifests itself in a steepening in observed afterglow luminosity (see Figure 1.5; Sari et al. 1999).

Observations have provided evidence for this jet-like emission. Achromatic jet breaks have
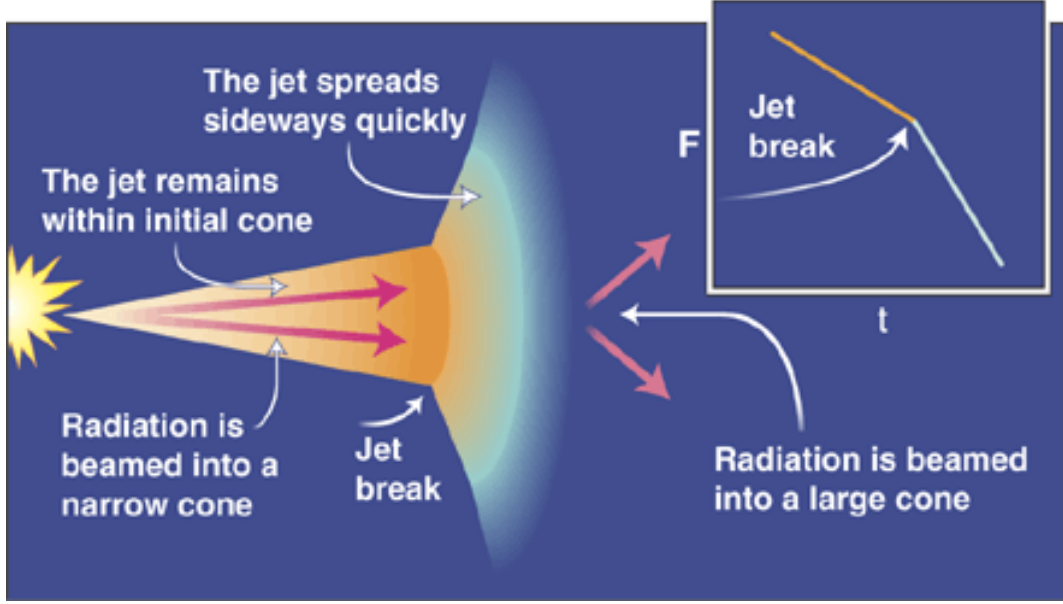
Figure 1.5: Illustration of the physical interpretation of a jet break. The break occurs when the jet material has decelerated sufficiently to the point where the beaming angle of the emission is greater than the jet half-opening angle and a significant fraction of ejecta spreads out perpendicular to the jet (Piran, 2002).

been seen in a number of GRB light curves at various wavelengths (e.g. GRB 990510; Harrison et al. 1999, GRB 060526; Dai et al. 2007, GRB 080319B; Tanvir et al. 2010). Frail et al. (2001) estimated the jet half-opening angles for a small number of *BATSE* GRBs. They highlighted that the half-opening angles covered a range of angles but a significant fraction possessed $\theta_{j/2} \lesssim 6\,\mathrm{deg}$, very narrow beaming cones. A more recent study on a sub-sample of *Swift* GRBs by Ryan et al. (2015) found similar results and also highlighted that the jet half-opening angles exhibited a large variance. More interestingly, it must be noted that other investigations found that the majority of the *Swift* GRB sample do not show evidence of a jet break (Mészáros, 2006; Willingale et al., 2007). One can estimate the energy budget corrected for relativistic beaming using the following relation

$$E_\gamma = (1 - \cos\theta_{j/2})E_{\mathrm{iso}} \tag{1.5}$$

where E_{iso} and E_γ are the equivalent isotropic and corrected gamma-ray energy outputs (Frail et al., 2001). Applying the jet scenario to the energetic GRB 080916C, discussed above, and utilising $E_{\mathrm{iso}} = 6.4 \times 10^{54}$ ergs and $\theta_{j/2} = 6\,\mathrm{deg}$ from Greiner et al. (2009), we find that

16

$E_\gamma \sim 4 \times 10^{52}$ ergs, equivalent to 0.02 Solar rest mass.

1.5.3   Prompt (internal shock) emission

The initial prompt gamma-ray emission seen in GRBs arises from the internal shocks of material present within an expanding fireball (e.g., Piran 1999; Zhang & Mészáros 2004; Kumar & Zhang 2015; van Eerten 2018). The collapse of a massive star or compact binary merger event produces a central engine, either a BH or NS. This releases a huge amount of gravitational energy in the form of a thermally driven fireball, expanding outwards from the central engine (Cavallo & Rees, 1978; Goodman, 1986; Paczynski, 1986). The emission is accelerated to ultra-relativistic speeds via high thermal or magnetic pressure present within the expanding fireball (Cavallo & Rees, 1978; Goodman, 1986; Paczynski, 1986, 1990; Shemi & Piran, 1990; Narayan et al., 1992). Electromagnetic energy is produced by internal shocks between shells of ejecta within the fireball that possess a distribution Lorentz factors (Mészáros & Rees, 1993; Rees & Meszaros, 1994; MacFadyen & Woosley, 1999).

The prompt emission has a distinct temporal and spectral shape. The temporal evolution of the emission (light curve) follows the profile of a number of successive Fast Rise Exponential Decay (FRED; Fishman & Meegan 1995; Norris et al. 1996) gamma-ray pulses that were first used to fit the temporal profiles of bright *BATSE* GRBs. The intensity of each pulse as a function of time was defined by Norris et al. (1996) as

$$
I(t) = \begin{cases} A\,e^{-\left(\frac{[t-t_{max}]}{\sigma_p}\right)^v}, & t < t_{\mathrm{max}} \\ A\,e^{-\left(\frac{[t-t_{max}]}{\sigma_d}\right)^v}, & t > t_{\mathrm{max}} \end{cases}
\tag{1.6}
$$

where A is the maximum intensity of the pulse, t_{max} is the time when the pulse is at maximum intensity, σ_p and σ_d are the rise and decay time constants, and v is a measure of the sharpness of the peak.

The spectral shape of the prompt emission is non-thermal and can be fit using the empirical

Band function (Band et al., 1993) following the form

$$F(E) = A \begin{cases} \left(\frac{E}{100\,\mathrm{keV}}\right)^{\alpha} e^{\left(-\frac{E}{E_0}\right)}, & E \leq (\alpha - \beta)E_0 \\ \left(\frac{E}{100\,\mathrm{keV}}\right)^{\beta} e^{(\beta - \alpha)}, \left(\frac{(\alpha - \beta)E_0}{100\,\mathrm{keV}}\right)^{(\alpha - \beta)}, & E > (\alpha - \beta)E_0 \end{cases} \quad (1.7)$$

where A is a normalisation constant at $100\,\mathrm{keV}$ measured in units of photons $\mathrm{s}^{-1}\,\mathrm{cm}^{-2}\,\mathrm{keV}^{-1}$, α and β are the spectral indices at low and high energies, and $E_{\mathrm{peak}} = (2 + \alpha)E_0$ is the peak energy measured in units keV as defined in Zhang et al. (2016a). This function describes a power law with an exponential cut-off at lower energies, and another, steeper power law at higher energies.

1.5.4 Afterglow (external shock) emission

The fireball expands away from the central engine and into the external circumburst medium (CBM), where it accumulates mass from its surroundings. Once the cumulative mass reaches the critical point at $m_C = M/\Gamma$, where M is the initial rest mass and Γ the bulk Lorentz factor of the fireball, it begins to decelerate (Sari & Piran, 1995) following a self-similar deceleration regime (Blandford & McKee, 1976). Two shocks form; a reverse shock, propagating back into the expanding relativistic shell, and a forward shock, propagating into the surrounding interstellar medium (ISM). The shocked shell and ISM material are separated by a contact discontinuity (Rees & Mészáros, 1992; Katz, 1994).

Synchrotron emission, which occurs when a relativistic charged particle is accelerated in the presence of a magnetic field, is thought to be the dominant mechanism in the afterglow process. A synchrotron spectrum can be defined by a set of four power law segments, split by three characteristic break frequencies; ν_{c} which represents the synchrotron cooling frequency, above which electrons lose energy via the synchrotron process efficiently, ν_{m} which represents the peak frequency and ν_a which represents the frequency at which self-absorption occurs, usually at radio frequencies (Sari et al., 1998; Granot & Sari, 2002; Zhang & Mészáros, 2004).

Two spectral regimes exist for synchrotron spectra. At early times, $\nu_m > \nu_c$ and the bulk of the electrons cool efficiently via synchrotron radiation. This regime if known as 'fast cooling' and the observed flux at a given frequency for this regime is

$$
F_\nu = F_{\max}
\begin{cases}
\left(\frac{\nu_a}{\nu_c}\right)^{\frac{1}{3}} \left(\frac{\nu}{\nu_a}\right)^2, & \nu_a > \nu \\[2mm]
\left(\frac{\nu}{\nu_c}\right)^{\frac{1}{3}}, & \nu_c > \nu > \nu_a \\[2mm]
\left(\frac{\nu}{\nu_c}\right)^{-\frac{1}{2}}, & \nu_m > \nu > \nu_c \\[2mm]
\left(\frac{\nu_m}{\nu_c}\right)^{-\frac{1}{2}} \left(\frac{\nu}{\nu_m}\right)^{-\frac{p}{2}}, & \nu > \nu_m
\end{cases}
\tag{1.8}
$$

where $F_{\max}$ is the peak synchrotron flux, occurring at frequency ν_m, and p is the slope of the electron energy distribution. Once $\nu_m \leq \nu_c$, the point at which the lifetime of the source and the cooling time are equal, only a small fraction of the electrons will cool efficiently via synchrotron radiation. This regime is known as 'slow cooling' and the observed flux at a given frequency in this regime is

$$
F_\nu = F_{\max}
\begin{cases}
\left(\frac{\nu_a}{\nu_m}\right)^{\frac{1}{3}} \left(\frac{\nu}{\nu_a}\right)^2, & \nu_a > \nu \\[2mm]
\left(\frac{\nu}{\nu_m}\right)^{\frac{1}{3}}, & \nu_m > \nu > \nu_a \\[2mm]
\left(\frac{\nu}{\nu_c}\right)^{-\frac{(p-1)}{2}}, & \nu_c > \nu > \nu_m \\[2mm]
\left(\frac{\nu_m}{\nu_c}\right)^{-\frac{(p-1)}{2}} \left(\frac{\nu}{\nu_m}\right)^{-\frac{p}{2}}, & \nu > \nu_c.
\end{cases}
\tag{1.9}
$$

The temporal evolution of the afterglow can be derived from the spectra and the evolution of the break frequencies. The shock front continues to expand outwards and both ν_m and ν_c decrease as a function of time; $\nu_m \propto t^{-\frac{3}{2}}$ and $\nu_c \propto t^{-\frac{1}{2}}$, respectively. The flux of the afterglow, at a given observed frequency, increases until the peak frequency is equal to the observed frequency. The flux of the afterglow then decreases as ν_m and ν_c continue to decrease. You can therefore deduce that the flux of X-ray afterglows peak earliest and radio afterglows peak later. Figure 1.6 describes the temporal evolution of the break frequencies, and illustrates the spectral shape of fast cooling and slow cooling.
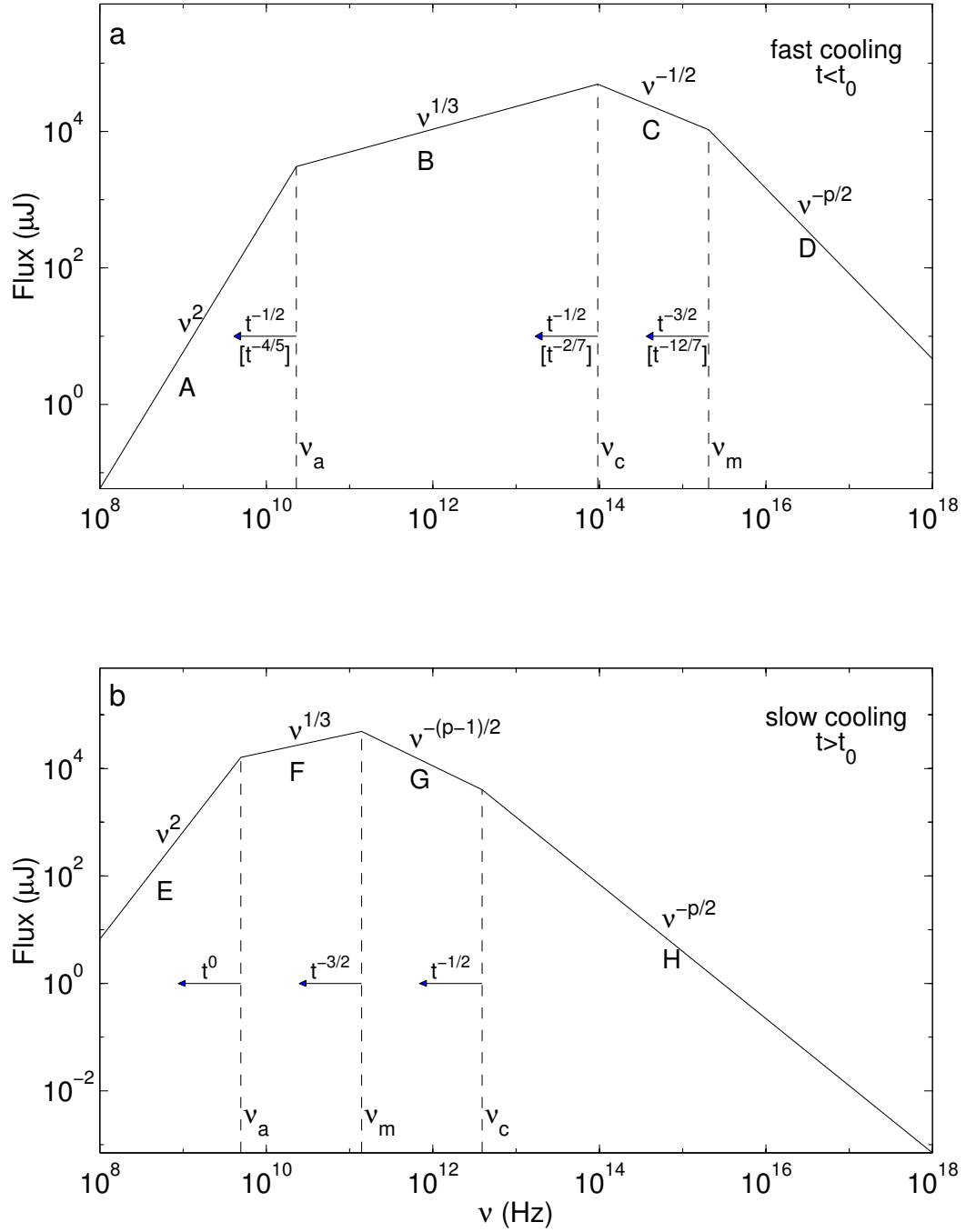
Figure 1.6: Illustration of the synchrotron spectra for the fast cooling (a) and slow cooling (b) regimes (Sari et al., 1998). The regime shifts from fast to slow at t_0; when the peak frequency, ν_m, falls below the cooling frequency, ν_c.

1.5.5 The canonical shape and morphology of afterglows

A synchrotron powered afterglow is emitted at all wavelengths from X-ray to radio (Piran, 1999) with the shortest wavelengths peaking earliest, and decaying away in the shortest time post-burst. The first confirmed observations of rapidly fading emission at X-ray and optical wavelengths were detected with GRB 970228 (Costa et al., 1997; van Paradijs et al., 1997) and the first radio observations with GRB 970508 (Frail et al., 1997). Observing each wavelength can give us important information about the GRB structure. X-ray afterglows are the most commonly observed afterglow emission. They are thought to accompany most if not all GRB: 1069 out of 1264 detected by *Swift* had X-ray afterglows detections. Optical afterglows are less common than their X-ray counterparts: 346 out of 1264 detected *Swift* GRBs also had detected optical afterglows (correct as of 2018 December 1)[5]. The cases of GRBs where no X-ray emission is detected may be a result (at least partially) of delayed follow-up XRT observations. By the time the observation started, the X-ray afterglow may have already been below detectable limits.

1.5.5.1 X-ray afterglow

The X-ray afterglow is the strongest of the multi-wavelength counterparts. Observations from *Swift* have shown that X-ray afterglows have similar shapes (Nousek et al., 2006; O'Brien et al., 2006; Racusin et al., 2009) with $\approx 40\%$ following a common canonical afterglow shape (Evans et al., 2009). The canonical light curve shape possesses five separate components. In reality, X-ray afterglows can contain any number or combination of the different components.

Most commonly, GRB afterglows exhibit a combination of the following three components:

- The early-time, steep power law (I) representing the tail end of the prompt emission (0) due to the curvature effect (Kumar & Panaitescu, 2000; Dermer, 2004; Dyks et al., 2005) where the travel time across the shock causes prompt emission to arrive at the

---

[5]https://swift.gsfc.nasa.gov/archive/grb_table/
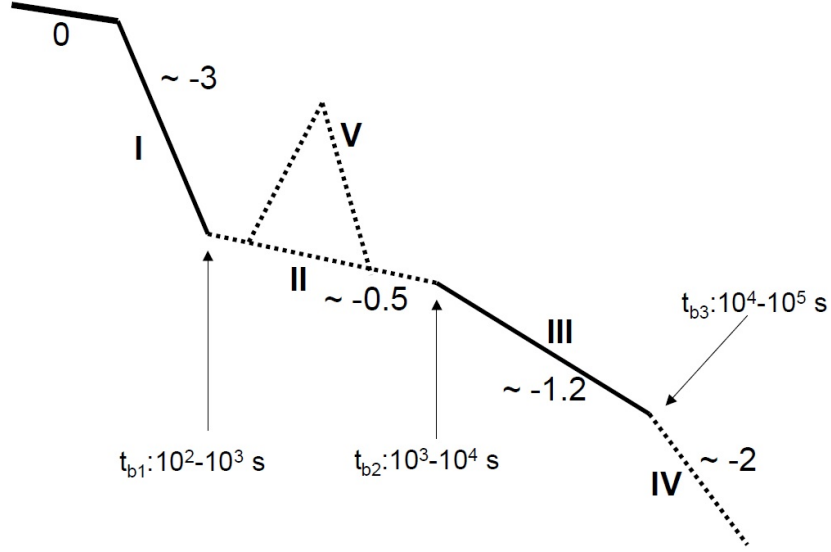
Figure 1.7: Illustration of the canonical shape of a GRB X-ray afterglow light curves (Zhang et al., 2006). The X-ray afterglow may be comprised of one or more components, depicted here with typical slopes and characteristic time-scales. The x-axis represents log(time) and the y-axis log(flux).

observer at different times.

- The normal decay phase (III), occurring as the shock front expands and decelerates (Sari & Piran, 1995).

- A jet break (IV), occurring once the shock front has decelerated enough and the beaming angle of the emitting material becomes wider than the jet opening angle (see section 1.5.2).

Some jets also exhibit the following afterglow components, though these are less common:

- The shallow decay phase (II), that may occur from a variety of mechanisms; energy injection from a long-term central engine (Zhang et al., 2006), delayed energy injection from ejecta with a wide range of Lorentz factors leading to late arrival shells of slower material (Rees & Mészáros, 1998) or an off-beam/multi-component jet model (Eichler & Granot, 2006; Zhang, 2007).

- X-ray flaring (V) during the afterglow phase that typically occurs several hundred seconds after the initial prompt emission. Extended activity or a restart of the central engine due to late time accretion may cause this flaring (O'Brien et al., 2006; Burrows et al., 2005a).

1.5.5.2 Radio afterglow

Observation of radio afterglows has provided further evidence for relativistic jets in GRBs. Early-time detections of radio counterparts have shown evidence for diffractive scintillation, where the radio flux varies significantly over short timescales. The scintillation is caused by electrons in the interstellar medium within our Galaxy. This only occurs when the observed emitting region is small at early times. Later-time radio observations do not show evidence of scintillations as the decelerating fireball becomes sub-relativistic and the effective size of the emitting region increases. Late-time radio observations can also be used to independently estimate the total energy budget of the GRB (Frail et al., 2000).

1.6 My contributions to the field

My work presented within this thesis covers a broad range of investigations, utilising a number of techniques and multi-wavelength observations to characterise the physics of non-thermal emission in energetic astrophysical transients.

Chapter 2 introduces GRB 140713A, a burst detected brightly at both X-ray and radio wavelengths, but was not detected in several optical bands despite searches to deep limits. The chapter aims to uncover the source of this optical darkness utilising full hydrodynamic jet simulations, numerical modelling of the GRB afterglow data, and host observations.

Chapter 3 describes a pilot investigation searching the sub-threshold trigger population of the *INTEGRAL* satellite for GRBs by utilising *Swift* follow-up observations. It also investigates

whether the *INTEGRAL* and *Swift* satellites observe the same underlying GRB populations.

Chapters 4 and 5 discuss the pilot SPLOT survey, whose aim was to test the feasibility of single epoch, optical polarimetry in both adding scientific value to transients or highlighting new sources of potential scientific interest. Chapter 5 also provides the details for the data calibration of SPLOT.

Chapter 6 summarises both the main conclusions of my work and the future of transient astronomy.

2

Detailed modelling of the optically dark GRB 140713A

2.1 Introduction

This chapter focuses on uncovering the cause of the optical darkness of GRB 140713A, utilising multi-wavelength observations in conjunction with numerical modelling of the GRB afterglow blastwave physics. The work was published in the Monthly Notices of the Royal Astronomical Society (MNRAS; Higgins et al. 2019a)

GRB 140713A was discovered by both *Swift* (Mangano et al., 2014) and *Fermi*/GBM (Zhang, 2014). It was a LGRB with a $T_{90} \sim 5\,\mathrm{s}$ ($15 - 350\,\mathrm{keV}$) and a fluence $F_\gamma = 3.7(\pm 0.3) \times 10^{-7}\,\mathrm{erg\,cm^{-2}}$ ($15 - 150\,\mathrm{keV}$; Stamatikos et al. 2014). A coincident X-ray source was reported by the *Swift*/XRT initially localising the source to an uncertainty of $2\,\mathrm{arcsec}$ (90% containment; Beardmore et al. 2014) though this was later improved to $1.4\,\mathrm{arcsec}$[6] (90% containment). A counterpart at radio wavelengths was also detected at $15.7\,\mathrm{GHz}$ with the Arcminute Microkelvin Imager (AMI) Large Array (Anderson et al., 2014) coincident with the *Swift*/XRT position. No optical source was detected for GRB 140713A, despite follow-up observations reaching deep sensitivity limits (Cano et al., 2014). A potential host galaxy was also found via observations from the $10.4\,\mathrm{m}$ Gran Telescopio Canarias (GTC; Castro-Tirado et al. 2014).

The lack of an optical detection from a GRB can have a variety of causes. At very high redshifts ($z \gtrsim 6$), the most likely cause for the absence of optical flux is Lyman-α absorption, occurring at $\lambda_\mathrm{obs} < 1216(1 + z)\,\text{Å}$ (Tanvir et al., 2009; Cucchiara et al., 2011), though GRBs at these redshifts are rare (Fynbo et al., 2009). If a GRB resides at lower redshifts, the observed optical darkness may result from a number of possibilities. Line-of-sight dust extinction originating in the GRB host, our Galaxy or the interstellar medium (ISM) can significantly suppress the rest frame optical flux of GRBs. A previous investigation by Perley et al. (2009) observing 29 host galaxies of optically dark GRBs concluded that $25 - 30\%$ of hosts (six out of 22 with estimated dust extinction) had a moderately high level of extinction ($A_\mathrm{V}^\mathrm{host} > 0.8\,\mathrm{mag}$). It is also possible that a GRB has either an intrinsically low luminosity or a synchrotron cooling break that lies below the optical band (see section 1.5.4). Either of these scenarios could plausibly produce an optical afterglow whose flux was either below the instrument sensitivity or later-time, optical follow-up simply was not deep enough. Coupled with a moderate extinction, an optically dark GRB may not have been detectable using optical follow-up at all.

Several methods have been proposed to classify a 'dark' GRB, comparing the X-ray properties to the optical/nIR upper limits. An investigation by Rol et al. (2005) estimated the minimum

---

[6]http://www.swift.ac.uk/xrt_positions/

optical flux expected for a 'regular' GRB by extrapolating back from the X-ray flux utilising both temporal and spectral afterglow information, assuming a synchrotron spectrum (see section 1.5.4). Further investigations by Jakobsson et al. (2004) and van der Horst et al. (2009) characterise 'thresholds' to classify a dark GRB using the optical-to-X-ray spectral index. The caveat to these thresholds is that comparisons can only be used provided the observations are made several hours after the GRB onset, ensuring the synchrotron cooling break is below optical wavelengths. Jakobsson et al. (2004) and van der Horst et al. (2009) both highlight that classifications using the spectral slopes alone may not be sufficient to fully determine whether a burst is truly dark. They suggest that these thresholds are only quick diagnostic tools and if multi-wavelength afterglow data are available (i.e. radio and X-ray) then broadband modelling can be used to estimate the expected optical fluxes to determine the host galaxy optical extinction (discussed in van der Horst et al. 2015).

A number of these dark GRBs have been investigated before, the earliest documented being GRB 970828 (Groot et al., 1998). Dark GRBs with well sampled data at both the X-ray and radio wavelengths that have been well studied in detail include GRB 020819 (Jakobsson et al., 2005), GRB 051022 (Castro-Tirado et al., 2007; Rol et al., 2007), GRB 110709B (Zauderer et al., 2013) and GRB 111215A (Zauderer et al., 2013; van der Horst et al., 2015) - a burst that appeared to reside in a host with very high extinction ($A_{\mathrm{V}}^{\mathrm{host}} > 7.5$ mag). However, this sample is still limited in size and highlights the importance to fully investigate new dark GRBs, the physical properties of the burst, the origin of the optical darkness and the use of dark GRBs as probes. As LGRBs trace cosmic star formation through their high energy emission (Perley et al., 2016), and a significant fraction of star formation is dust-obscured, dark GRBs may provide an independent way to investigate dust-obscured star formation (Blain & Natarajan, 2000; Ramirez-Ruiz et al., 2002).

In conjunction with the X-ray and radio observations of GRB 140713A, I performed detailed modelling on the data to estimate the expected optical flux. The modelling used the software package BOXFIT (van Eerten et al., 2012), which utilises full hydrodynamic simulations of relativistic jets. This was the first time hydrodynamic simulations had been used to investigate the afterglow physics of a dark GRB. I then compared this to host galaxy observations to

uncover the nature of the optical darkness of GRB 140713A.

2.2 Multi-wavelength observations of GRB 140713A

2.2.1 AMI and WSRT radio observations

GRB 140713A was observed from 2014 July 13 to October 2 with the Large Array of the AMI interferometer (Zwart et al., 2008) at a central frequency of $15.7\,$GHz (between $13.9 - 17.5\,$GHz), and with WSRT at 1.4 and $4.8\,$GHz. The AMI observations were taken as part of the AMI Large Array Rapid-Response Mode (ALARRM) program, which is designed to probe the early-time radio properties of transient events by automatically responding to transient alert notices (Staley et al., 2013; Staley & Fender, 2016; Anderson et al., 2018). AMI began observing GRB 140713A within $2\,$hrs of the *Swift*/BAT trigger. The $15.7\,$GHz data exhibits signs of scintillation, noticeable at time scales of up to two weeks post GRB. The AMI data reduction was performed by Gemma Anderson and the data were made available in Anderson et al. (2018) and Higgins et al. (2019a).

The WSRT observations were taken using the Multi Frequency Front Ends (Tan, 1991) in conjunction with the IVC+DZB back end in continuum mode. The bandwidth of the observations were $8 \times 20\,$MHz at all observing frequencies. The WSRT data were reduced by Alexander van der Horst and were made available in Higgins et al. (2019a). An observation at $1.4\,$GHz with the Giant Metrewave Radio Telescope (GMRT), 11 days after the burst, was also made (Chandra & Nayana, 2014). A table containing all radio data is available in Appendix A.

2.2.2 NOT optical observations

Observations of the field of GRB 140713A were conducted with the $2.5\,$m Nordic Optical Telescope (NOT) equipped with ALFOSC by Cano et al. (2014). They confirmed that no

source was detected within the XRT error circle. Their published 3σ upper limits for an isolated point source are given as $r > 24.30$, $i > 23.50$ and $z > 22.60$, at 0.1454, 0.1585 and 0.1738 days post-GRB, respectively in the AB magnitude system.

I converted the optical limits into flux by rearranging the following relation

$$M_{\mathrm{AB}} \sim -2.5\log_{10}(F_{\mathrm{Jy}}) + 8.90 \tag{2.1}$$

where M_{AB} is the source magnitude in the AB system and F_{Jy} is the flux density in Janskys. Equation 2.1 arises from modification to equation 3 in Frei & Gunn (1994) by transforming the cgs units to Janskys where $1\,\mathrm{Jy} = 10^{-23}\,\mathrm{erg\ s^{-1}\ cm^{-2}\ Hz^{-1}}$ and assumed a flat optical spectrum. I calculated flux densities of $r < 7.1 \times 10^{-7}\,\mathrm{Jy}$, $i < 1.5 \times 10^{-6}\,\mathrm{Jy}$ and $z < 3.4 \times 10^{-6}\,\mathrm{Jy}$.

2.2.3 Host galaxy observations and determination of redshift

While no optical afterglow detection was reported for this burst, a compact, steady source coincident with the XRT circle with $R \sim 24\,\mathrm{mag}$ was discovered by Castro-Tirado et al. (2014) and proposed as a potential host galaxy.

To calculate the likelihood of finding an unrelated galaxy within the XRT error circle of GRB 140713A, I used the following relation

$$P_{\mathrm{chance}} = 1 - e^{-\pi r^2 \sigma(\leq m_R)} \tag{2.2}$$

where r is the localisation error circle radius and $\sigma(\leq m_R)$ is the predicted number of galaxies per arcsec^2 brighter than the given R-band magnitude limit (Bloom et al., 2002). If $P_{\mathrm{chance}} < 0.1$, then one would assume that the observed galaxy is probably the host. Using the XRT error radius of 1.4 arcsec (90% confidence) and $m_R = 24\,\mathrm{mag}$ I found that $P_{\mathrm{chance}} = 0.028$. I therefore concluded that the observed galaxy was probably the host of GRB 140713A.

The potential host was observed with the Low Resolution Imaging Spectrometer (LRIS; Oke et al. 1995) on the Keck I 10m telescope on 2014 August 30 and 31. Both an optical spec-

Table 2.1: Host galaxy photometry for GRB 140713A using a number of filters and observatories. Values are not corrected for Galactic extinction; $E(B-V) = 0.05$ (Schlafly & Finkbeiner, 2011).

Filter	Magnitude (AB)	Instrument
u	24.30 ± 0.20	Keck/LRIS
g	24.22 ± 0.10	Keck/LRIS
R	24.00 ± 0.50	GTC/OSIRIS
i	23.11 ± 0.10	Keck/LRIS
z	22.49 ± 0.10	Keck/LRIS
$3.6\mu m$	21.45 ± 0.05	Spitzer/IRAC
$4.5\mu m$	21.82 ± 0.05	Spitzer/IRAC

trum and images of the potential host, taken in various filters, were obtained with LRIS. The LRIS data, and data reduction, were kindly provided by Daniel Perley. Complementary Spitzer/IRAC infrared photometry was also available. All host magnitudes can be seen in Table 2.1.

The reduced 1D, LRIS host spectrum highlighted two prominent emission features at wavelengths corresponding to a doublet [O II] at $3727\,\text{Å}$ and [O III] at $5007\,\text{Å}$, both at a common redshift of $z = 0.935$. The spectrum is shown in Figure 2.1.

Dan Perley also performed an SED fit to the above photometry. A host model with a total stellar mass of $2.2 \times 10^{10}\,M_\odot$ and a current star-formation rate of $1.2\,M_\odot\,\text{yr}^{-1}$ provided a very good fit to the photometry data (see Figure 2.2). These host parameters are typical of dark GRB hosts (Perley et al., 2013) and, more generally, of optically-selected galaxies (Contini et al., 2012) at similar redshifts.
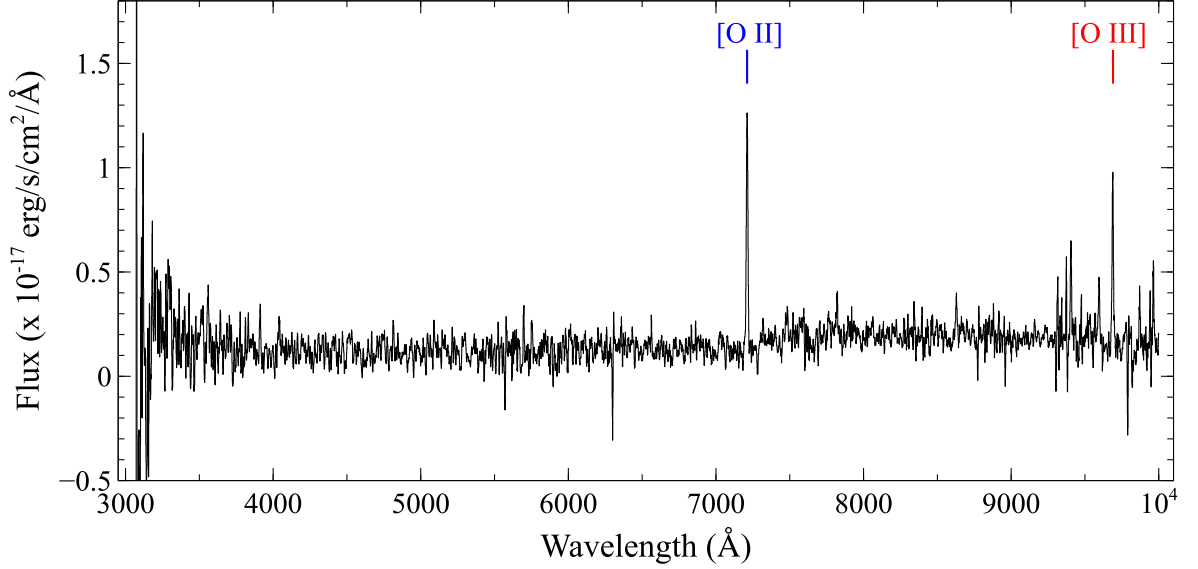
Figure 2.1: The reduced 1D, LRIS host galaxy spectrum. The two emission features; the [O II] doublet (blue) and the [O III] $5007\,\text{Å}$ (red) emission lines are clearly visible and both occur at $z = 0.935$. This figure is taken from Higgins et al. (2019a).

2.2.4 Swift XRT observations

The *Swift*/XRT began observing GRB 140713A ~ 80 s post-*Swift*/BAT trigger (Mangano et al., 2014). A coincident source was detected observations continued until $\sim 163\,\text{ks}$ post-*Swift*/BAT trigger for a total exposure time of $15.7\,\text{ks}$.

I obtained the $0.3 - 10\,\text{keV}$ flux and spectral data from the UKSSDC[2] (Evans et al., 2007, 2009). The X-ray light curve of GRB 140713A exhibited high levels of flaring over the period of $500-1500$ s post-*Swift*/BAT trigger. For this investigation I was only interested in analysing and modelling the afterglow emission of GRB 140713A, not the flares, which most likely arise from extended or secondary central engine activity. For this reason I removed the first 1500 s of afterglow data, focusing only on the late-time X-ray emission.

I performed spectral analysis of the late-time spectral data using XSPEC (v12.9; Arnaud 1996). I fit the X-ray data using an absorbed power law with a redshifted absorption component of

31
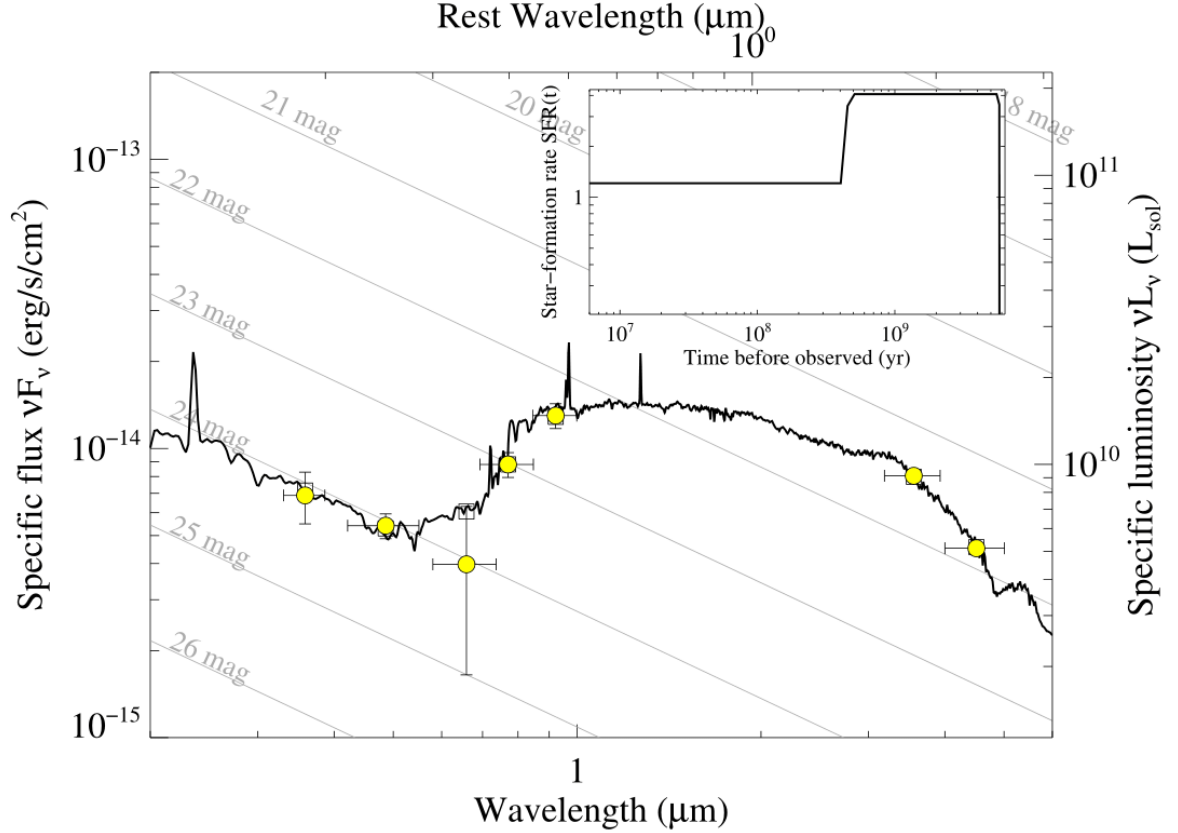
Figure 2.2: SED of the potential host galaxy of GRB 140713A. Overplotted are the photometry data (yellow) and the best-fitting model (black line). The inset shows the assumed star-formation history prior to the galaxy redshift. This figure is taken from Higgins et al. (2019a).

the following form

$$\text{TBABS}(z\text{TBABS}(\text{POWERLAW}))\tag{2.3}$$

where TBABS is set fixed at the Galactic column density, zTBABS is a free parameter, representing the host column density at a given redshift, and POWERLAW is the photon index. For GRB 140713A, the Galactic column density is $N_{\text{H,Gal}} = 4.97 \times 10^{20}\,\text{cm}^{-2}$, calculated using the method described in Willingale et al. (2013), and the redshift is $z = 0.935$ (determined in section 2.2.3). I set the element abundances and cross-section for X-ray absorption values to those given in Wilms et al. (2000) and Verner et al. (1996).

I modelled the spectrum using three different absorbers as GRB hosts typically have metallicities that are different from Solar metallicity (Schady et al., 2012). The three absorbers I used

were a Solar metallicity absorber ($Z_\odot$), a LMC-like metallicity absorber ($Z_\odot/3$) and a SMC-like metallicity absorber ($Z_\odot/8$), all at $z = 0.935$. Figure 2.3 shows the X-ray spectrum, best fit model using a Solar metallicity absorber and the residuals.
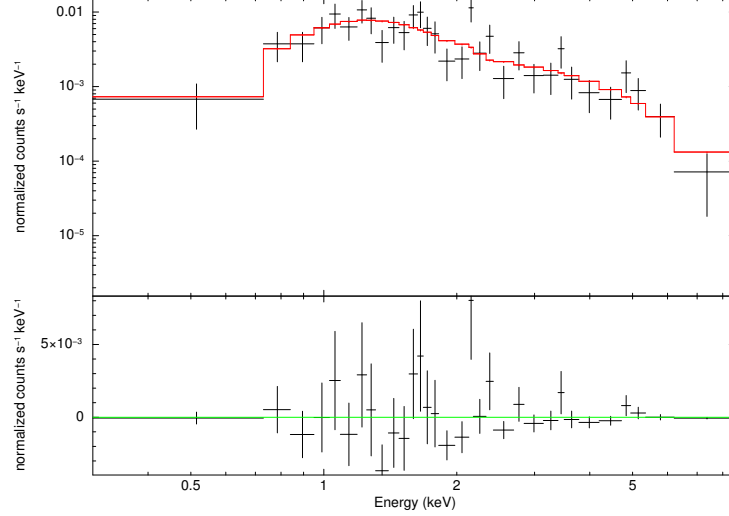
Figure 2.3: Observed X-ray spectrum of GRB 140713A from *Swift*/XRT excluding the early time flaring data (see section 2.2.4). The absorbed power law model (red) was created using a SMC metallicity absorber.

I found that the best-fit photon indices were $\Gamma_{\mathrm{Solar}} = 1.83^{+0.37}_{-0.33}$, $\Gamma_{\mathrm{LMC}} = 1.78^{+0.35}_{-0.32}$ and $\Gamma_{\mathrm{SMC}} = 1.74^{+0.34}_{-0.31}$, and best-fit excess intrinsic column densities were $N_{\mathrm{H,host,Solar}} = 2.56^{+1.48}_{-1.12} \times 10^{22}\,\mathrm{cm}^{-2}$, $N_{\mathrm{H,host,LMC}} = 5.10^{+3.07}_{-2.29} \times 10^{22}\,\mathrm{cm}^{-2}$ and $N_{\mathrm{H,host,SMC}} = 7.31^{+4.58}_{-3.36} \times 10^{22}\,\mathrm{cm}^{-2}$ for the Solar, LMC-like and SMC-like absorbers, respectively. All values above quoted at 90% confidence. All absorber best-fit models were similarly good statistically according to the C-statistic, where the three models all returned a C-stat = 114 for 155 degrees of freedom (equivalent to ~ 0.74), and produced consistent values of Γ and $N_{\mathrm{H,host}}$ within the confidence intervals.

The afterglow lightcurve fluxes were converted from unabsorbed flux into flux density at $2\,\mathrm{keV}$ via a PYTHON3[7] script using the following integral

$$F_{\mathrm{Tot}} = \int_{0.3\mathrm{keV}}^{10\mathrm{keV}} F_{2\mathrm{keV}} \left(\frac{E}{2\mathrm{keV}} \right)^{1-\Gamma} dE \tag{2.4}$$

where F_{Tot} is the flux observed by *Swift* at $0.3 - 10\,\mathrm{keV}$ and $F_{2\mathrm{keV}}$ is the flux density at $2\,\mathrm{keV}$.

---

[7]https://www.python.org/

$F_{2\text{keV}}$ was then calculated by integrating Equation 2.4 to find the following relation

$$F_{2\text{keV}} = \frac{2\,(\text{keV})^{1-\Gamma}(2-\Gamma)F_{\text{Tot}}}{10\,(\text{keV})^{2-\Gamma} - 0.3\,(\text{keV})^{2-\Gamma}} \times 4.15 \times 10^5 \qquad (2.5)$$

where 4.15×10^5 and represents the conversion from flux density (in ergs cm^{-2} s^{-1} keV^{-1}) to Janskys (Jy). This relation only holds where $\Gamma \neq 2$, which is true from the late time spectral fitting. As all three absorber models returned consistent parameter values, I used the the Solar metallicity absorber parameters to calculate the flux density. A table of the X-ray flux densities is available in Appendix A. The calculated flux densities at X-ray and radio wavelengths, and the optical 3σ upper limits, are displayed in Figure 2.4.
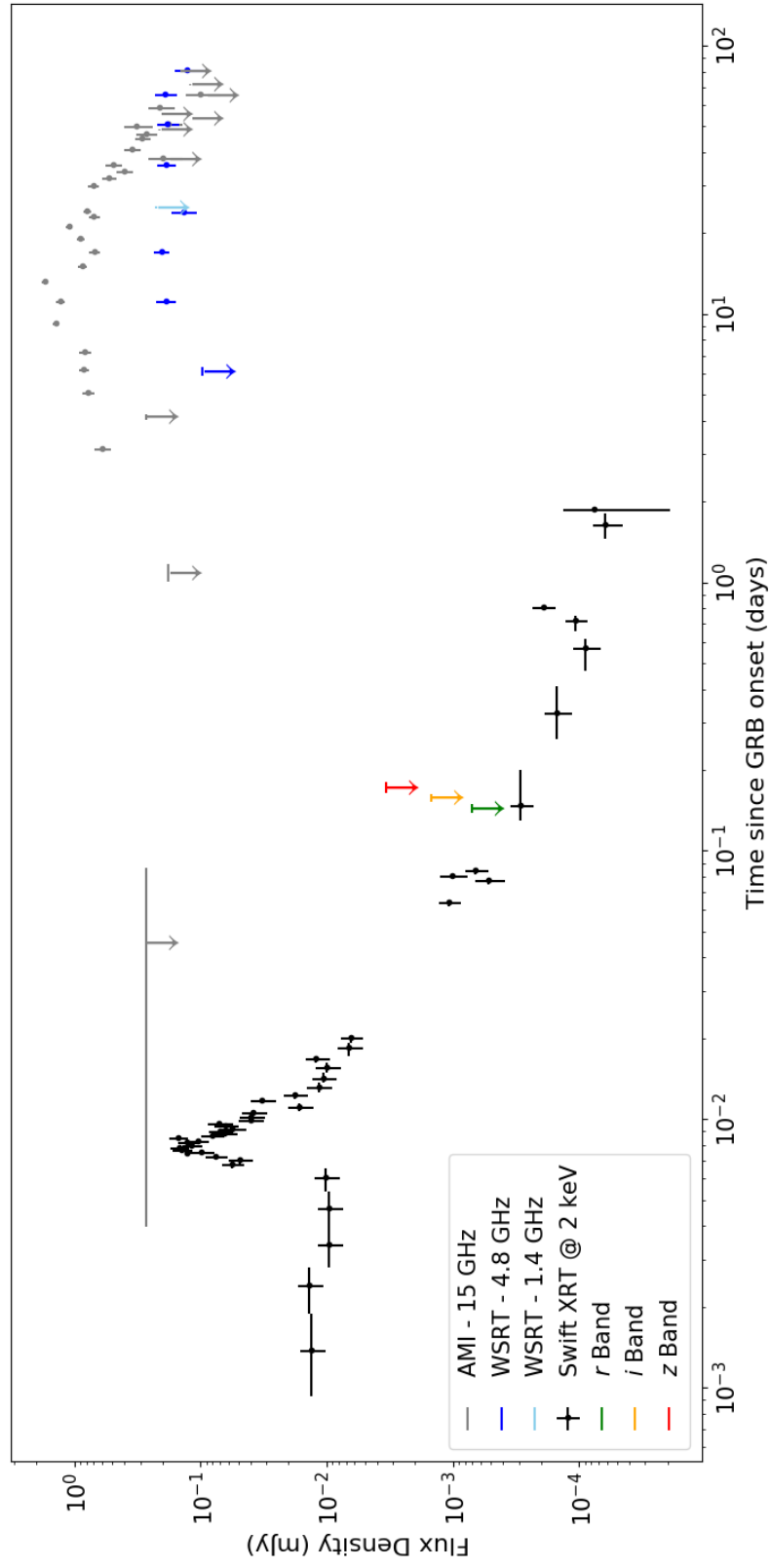
Figure 2.4: Multi-wavelength afterglow lightcurves and non-detections for GRB 140713A. The flux density detection errors are quoted at 1σ and the non-detections are given as 3σ upper limits.

2.3 Is GRB 140713A a traditionally dark GRB?

In section 2.1, I introduced two criteria that could aid the determination of determining whether a GRB was truly dark. Jakobsson et al. (2004) proposed that a GRB could be classified as dark if the optical-to-X-ray spectral index, $\beta_{OX} < 0.5$, 11 hours post-GRB, where the optical flux was measured in R-band and the X-ray flux at $2\,\mathrm{keV}$. At this time, a shallow spectral index would suggest that the optical flux was lower than expected for a relativistically expanding shell. van der Horst et al. (2009) further developed this criterion by including information on the X-ray spectral index. The dark GRB criterion was modified, now proposing that a GRB is dark if $\beta_{OX} - \beta_X < -0.5$ where β_X is the X-ray spectral index.

I tested the criterion on GRB 140713A. Firstly, I estimated β_{OX} using each of the optical upper limits and the X-ray flux at $2\,\mathrm{keV}$, calculated at 0.1454, 0.1585 and 0.1738 days post-GRB, to align with the optical times. I calculated β_X using the late-time *Swift* photon index from section 2.2.4 where $\beta_X = \Gamma_{\mathrm{Solar}} - 1 = 0.83^{+0.37}_{-0.33}$ (90% confidence). Table 2.2 highlights the results per optical band for each criterion. $\beta_{OX} < 0.5$ in all bands, indicating that the optical flux is well below the expected values for a 'standard' afterglow. The criterion in van der Horst et al. (2009) is not met in all bands. However, the 90% confidence intervals on the β_X are large. I used $\beta_X = 0.5$, the shallowest spectral index to produce the most constraining upper limits.

Table 2.2: Comparing the estimated optical-to-X-ray spectral indices of GRB 140713A to the two criteria described in section 2.3.

Filter	β_{OX}	$\beta_{\mathrm{OX}} - \beta_{\mathrm{X}}$
r	< 0.20	< -0.30
i	< 0.26	< -0.24
z	< 0.37	< -0.13

2.4 Broadband afterglow modelling with BOXFIT

2.4.1 Power law extrapolation

Modelling the afterglow of GRB 140713A was a crucial task to help uncover why an optical afterglow was not observed. Initially I conducted a very simple estimation for the expected optical flux of GRB 140713A, by extrapolating the shallowest X-ray spectral index ($\beta_X >$ 0.50) back to optical wavelengths using a simple power law. The expected optical flux could then be calculated by rearranging the following relation

$$\frac{\log(F_{op}) - \log(F_X)}{\log(\nu_{op}) - \log(\nu_X)} = \beta_X \tag{2.6}$$

where F_{op} and F_X are the optical and X-ray fluxes at the given frequencies ν_{op} and ν_X.

I took $F_X \sim 3 \times 10^{-7}$ Jy (from the observation time coincident with the optical upper limits) and $\nu_X = 4.84 \times 10^{17}$ Hz and $\nu_{op} = 4.81 \times 10^{14}$ Hz (r-band), 3.93×10^{14} Hz (i-band) and 3.28×10^{14} Hz (z-band). I estimated that the expected optical flux should have been $> 10^{-5}$ Jy, above the optical limits introduced in section 2.2.2. The expected optical flux was $\gtrsim 1$ order of magnitude brighter than the optical limits in all bands.

Interestingly, the X-ray afterglow lightcurve appeared to have a very shallow decline. This was highlighted in figure 2.4. A very shallow X-ray slope could indicate a low underlying electron energy distribution index, p. Assuming that the cooling break was below the X-ray band 1500 s post-GRB, which is likely in most cases (Curran et al., 2010; Ryan et al., 2015), I estimated p rearranging the closure relation (Granot & Sari, 2002; Zhang & Mészáros, 2004) below

$$F \propto t^{(2-3p)/4}. \tag{2.7}$$

I estimated from a simple power law that the X-ray afterglow slope was $-0.78(\pm0.09)$, with $1.6 < p < 1.8$. I conducted a similar test on the X-ray spectral data (Granot & Sari, 2002; Zhang & Mészáros, 2004) by rearranging the following closure relation

$$F \propto \nu^{-p/2}. \tag{2.8}$$

From earlier calculations of the spectral index (slope), where $\beta_X = 0.83^{+0.37}_{-0.33}$ (90% confidence), I estimated that $1.0 < p < 2.4$. These results suggested that the shocked electrons may have exhibited a hard energy distribution, where p could be low (< 2), and required attention.

2.4.2   Interpretation of the electron energy distribution

The post-shock number density of the accelerated electrons, n_e, at a given Lorentz factor, (γ_e), can be defined using a power law relation

$$n_e(\gamma_e) = n_0 \gamma_m^{p-1} \gamma_e^{-p}(p-1) \tag{2.9}$$

where γ_e^{-p} is the electron energy distribution between minimum and maximum Lorentz factors of γ_m and γ_M respectively, and n_0 is the electron number density behind the shock. I can then define the γ_m as a fraction of the blast wave energy available to the accelerated electrons using the following relation

$$\gamma_\mathrm{m} = \frac{\bar{\epsilon}_e E_0}{n_0 m_e c^2} \equiv \frac{(p-2)}{(p-1)} \frac{\epsilon_e E_0}{n_0 m_e c^2}. \tag{2.10}$$

where E_0 is the energy density if the post-shock fluid and and m_e is the mass of an individual electron (Granot & Sari, 2002). Following the prescription defined in Granot & Sari (2002), I replaced ϵ_e with $\bar{\epsilon}_e$. This benefit to this substitution is that Equation 2.10 is valid for scenarios where $p < 2$. The maximum Lorentz factor γ_M reflects the balance between shock-acceleration time and synchrotron loss time. Above this value, the flux emitted drops off exponentially. This typically occurs when $\gamma_M \gtrsim 10^7$, where the emitted radiation possesses a frequency orders of magnitude above the X-ray band. The highest frequency lightcurves I produced during this investigation were at X-ray frequencies ($2\,\mathrm{keV}$), and were therefore the lightcurve fluxes were not affected by this high energy 'cut off'.

E_e, the total energy density of the shocked electrons, can be calculated by integrating over the

electron energy distribution using the following relation

$$
\begin{aligned}
E_e &= \int_{\gamma_m}^{\gamma_M} \gamma_e m_e c^2 n_e(\gamma_e) d\gamma_e \\
&= (p-1) n_0 \gamma_m^{p-1} m_e c^2 \int_{\gamma_m}^{\gamma_M} \gamma_e^{1-p} d\gamma_e \\
&\approx
\begin{cases}
\gamma_m^2 n_e(\gamma_m) m_e c^2/(p-2), & p > 2, \\
\gamma_m^2 n_e(\gamma_m) m_e c^2 \ln\left[\frac{\gamma_M}{\gamma_m}\right], & p = 2 \\
\gamma_M^2 n_e(\gamma_M) m_e c^2/(2-p), & p < 2.
\end{cases}
\end{aligned}
\tag{2.11}
$$

where $\gamma_e m_e c^2$ is the rest mass energy of a relativistic electron and the integration limits are between γ_m and γ_M. For the $p > 2$ case, you can see that E_e does not depend on γ_M and in reality the upper limit on the integral for this case can $\rightarrow \infty$. For $p \leq 2$, you can clearly see that a high energy cut-off is required to calculate a realistic value for E_e. For $p > 2$, the energy available to the electrons is given by

$$
E_e = \epsilon_e E_0 = \bar{\epsilon}_e E_0 \frac{(p-1)}{(p-2)}
\tag{2.12}
$$

and γ_M can be ignored. To account for cases where $p < 2$, E_e, is given by the following relation

$$
E_e = \epsilon_e E_0 \left[1 - \left(\frac{\gamma_M}{\gamma_m}\right)^{2-p} \right] = \bar{\epsilon}_e \frac{(p-1)}{(p-2)} E_0 \left[1 - \left(\frac{\gamma_M}{\gamma_m}\right)^{2-p} \right]
\tag{2.13}
$$

where the energy is dependent on γ_M. I can find ϵ_e from the value of $\bar{\epsilon}_e$ and p derived from modelling the afterglow data.

2.4.3   BOXFIT settings and modelling

I utilised the software package BOXFIT[8] following the method described in van Eerten et al. (2012) to further investigate the afterglow of GRB 140713A. BOXFIT uses the results of radiative transfer, hydrodynamic simulations to calculate the physical parameters of a relativistically expanding GRB shock front and the circumburst medium. The modelling utilises the downhill simplex method (Nelder & Mead, 1965) with simulated annealing (Kirkpatrick et al.,

---

[8]https://cosmo.nyu.edu/afterglowlibrary/boxfit2011.html

1983). These methods are used to aid in finding the optimal set of GRB parameters, found by minimising the multi-dimensional χ^2 statistic. The χ^2 statistic is defined as

$$\chi^2 = \sum_{i=1}^{n} \frac{(y_i - m_i)^2}{\sigma_{y_i}^2} \tag{2.14}$$

where $(y_i - m_i)^2$ is the square of difference between the data, y_i, and the model, m_i, summed over n number of data points, and $\sigma_{y_i}^2$ is the variance of the data. The added benefit to using hydrodynamic jet simulations compared to the classical, analytical synchrotron models (i.e. Granot & Sari 2002) is that BOXFIT can fully compare the multi-wavelength data over the entire afterglow observations, where the physical conditions and regimes of the relativistic shock front can vary. The one limitation of BOXFIT is that the simulations are based on one single, initial injection of energy from the central engine. This is the reason I had to exclude the early X-ray flaring data (see section 2.2.4), as it is most probably caused by longer lasting or later-time, central engine emission.

The BOXFIT afterglow model used during this investigation had nine parameters. It is described by the following relation

$$\Phi = [E_{\mathrm{ISO}}, \; n, \; \theta_{\mathrm{j/2}}, \; \theta_{\mathrm{obs}}, \; p, \; \epsilon_e, \; \epsilon_B, \; \xi_N, \; z] \tag{2.15}$$

where E_{ISO} is the equivalent, isotropic energy output of the expanding blastwave, n is the circumburst particle number density at 10^{17} cm, $\theta_{\mathrm{j/2}}$ is the jet half-opening angle, θ_{obs} is the observer angle, ϵ_e and ϵ_B are the fractions of the internal energy deposited in the electrons and shock-generated magnetic field, ξ_N is the fraction of electrons that are accelerated, and z represents the redshift. BOXFIT requires the luminosity distance of a source. To calculate this, I assumed a standard ΛCDM universe cosmology and used the following values for the cosmological paramaters; $H_0 = 68\,\mathrm{km\,s^{-1}\,Mpc^{-1}}$ and $\Omega_{\mathrm{M}} = 0.31$, where H_0 and Ω_{M} are the Hubble constant and matter density (Planck Collaboration et al., 2016). I used the method described in Wright (2006) with $z = 0.935$ to calculate a luminosity distance, $d_{\mathrm{L}} = 1.92 \times 10^{28}$ cm.

Although the AMI 15.7 GHz lightcurve of GRB 140713A is very well sampled, the omission of the X-ray flaring period and upper limits resulted in a total data set of 44 data points. To

Table 2.3: The volume of afterglow model parameter space that is explored during the BOXFIT model fitting.

Parameter	Minimum	Initial	Maximum
$z^\dagger$	-	0.935	-
$d_\mathrm{L}^\dagger$ (cm)	-	1.92×10^{28}	-
E_ISO (ergs)	10^{47}	10^{53}	10^{56}
n (cm)$^{-3}$	10^{-5}	1.0	10^5
$\theta_\mathrm{j/2}$ (rad)	0.01	0.1	1.0
$\theta_\mathrm{obs}^\dagger$ (rad)	-	0	-
p	1.0	2.0	3.0
$\bar{\epsilon}_e$	10^{-5}	0.1	1.0
ϵ_B	10^{-10}	10^{-5}	1.0
$\xi_N^\dagger$	-	1.0	-

† represents the parameters whose values were fixed and therefore not estimated during the fitting.

counterbalance this, I fixed two of the nine model parameters from equation 2.15 - with a third already fixed by definition. The two parameters I fixed were θ_obs and ξ_N. I fixed $\theta_\mathrm{obs} = 0$ rad as a free observing angle parameter carries associated degeneracies, something that I cannot fully explore with the available amount of data. Fixing $\xi_N = 1$ also removes any associated degeneracies with this parameter that I also cannot fully explore. z and the associated D_L represent the distance to the GRB from Earth and are, by definition, fixed. The chosen limits for the six free parameters of my model, representing the total volume of parameter space, are shown in Table 2.3.

As I assumed that the GRB was on-axis, I set the resolution settings for both azimuthal and radial parameters to the BOXFIT guide recommended values of 1 and 1000, respectively. I also modified BOXFIT to allow fits where $p < 2$ by replacing ϵ_e with $\bar{\epsilon}_e$, where $\bar{\epsilon}_e = \epsilon_e(p-2)/(p-1)$. This is discussed above in detail. I set the initial annealing 'temperature' to 10^5 with 100 light-curve iterations per temperature. Once this was complete, BOXFIT saved the parameter

set of the lowest χ^2 fit, reduce the temperature to 98% of the previous value and perform the iterations again. Once the temperature reached 10^{-2} the modelling was complete and BOXFIT would calculate the global best fit (lowest χ^2 fit of all of the temperature iterations).

I ran BOXFIT modelling for two different circumburst density environments. The first was for a homogeneous medium, subsequently labelled as ISM/ISM-like, where the density profile was flat, and a stellar wind environment, labelled wind, where the density profile evolves as r^{-2}, with r the distance from the expanding shock-front to the central GRB engine. The ISM-like models were ran using the standard ISM parameter settings of BOXFIT whilst the stellar wind environment was run under the medium-boosted wind setting.

Once the global best fit for the data was found, I calculated the partial derivatives around the best-fit values by perturbing the data within their error bars. A bootstrap Monte Carlo (MC) method by perturbing the data set and calculating parameter set fits 10^4 times within the flux errors was then used to investigate the parameter distributions and confidence intervals. This method was utilised purely due to time constraints. The initial, global best fit modelling took ~ 3 days on 48 computer cores. Repeating that process 10^4 times was not feasible so the bootstrap method was introduced that took ~ 10 hours on only a couple of cores.

2.5 Results from the BOXFIT afterglow modelling

Figures 2.5 and 2.6 show the projected parameter distributions for the six free fitting parameters used in the BOXFIT afterglow modelling. Overall, the distributions are fairly well constrained and are all approximately log-normal or normal, so I quoted the most probable parameter values (medians) and 68% confidence intervals (equivalent to 1σ errors) as the 16th, 50th and 84th percentiles. The parameter values for both circumburst environments can be found in Table 2.4. The figures also highlights that some parameter pairs that are degenerate; correlation between p and $\log(n)$ and anti-correlation between $\log(E_{\text{iso}})$ and $\log(n)$, for example.
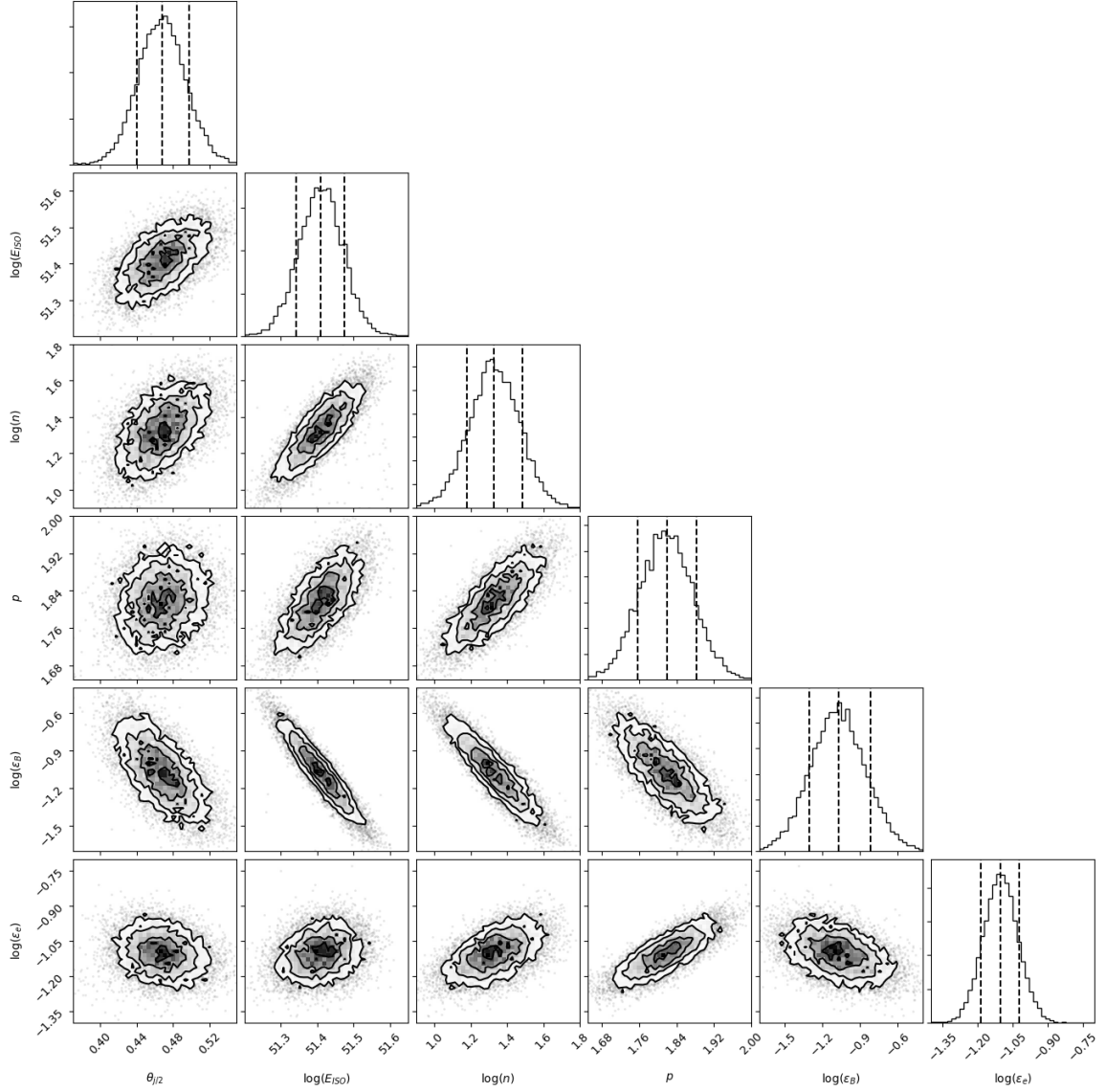
Figure 2.5: Projections of the afterglow model parameter distributions for a ISM-like environment, derived using the MC bootstrap method. The peak of the distributions (50th percentile) and 68% confidence (1σ) intervals (16th and 84th percentiles) are shown. The contours represent the the 1, 2, and 3σ confidence intervals in descending transparency. Figure taken from Higgins et al. (2019a).
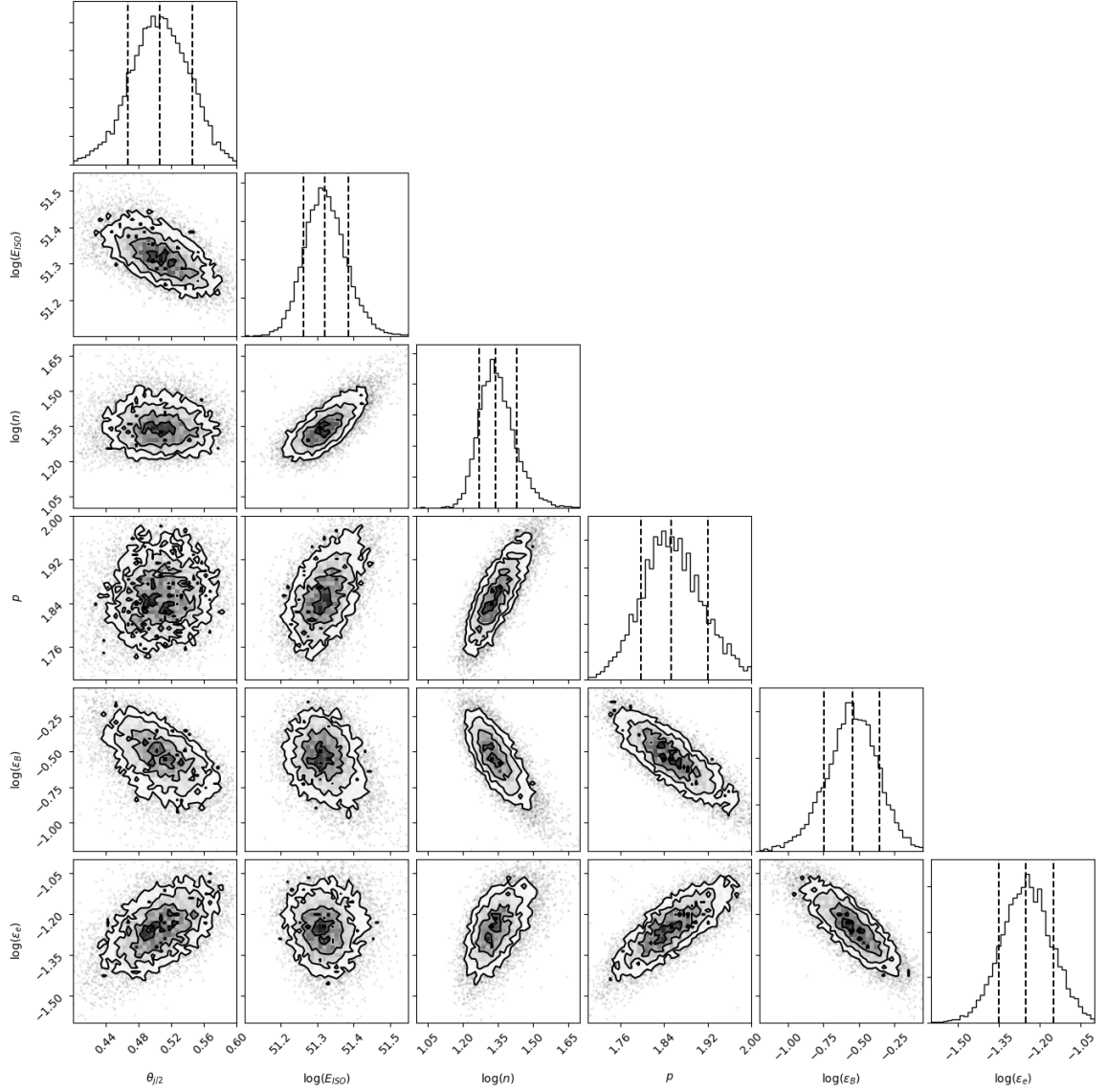
Figure 2.6: Projections of the afterglow model parameter distributions for a wind environment, derived using the MC bootstrap method. The peak of the distributions (50th percentile) and 68% confidence intervals (16th and 84th percentiles) are shown. The contours represent the the 1, 2, and 3σ confidence intervals in descending transparency.

Table 2.4: Parameter distributions for the two different circumburst density environments. The values quoted in the table are the peak (median) and 68% confidence intervals.

Environment	E_{ISO} (ergs)	n (cm^{-3})	$\theta_{\mathrm{j/2}}$ (rad)	$\theta_{\mathrm{obs}}^{\dagger}$ (rad)	p	$\bar{\epsilon}_e$	ϵ_B	$\xi_N^{\dagger}$	χ_r^2
ISM	$2.57^{+0.40}_{-0.33} \times 10^{51}$	$21.4^{+8.4}_{-5.8}$	$0.47(\pm0.03)$	0	$1.82(\pm0.06)$	$7.88^{+1.42}_{-1.28} \times 10^{-2}$	$8.30^{+5.60}_{-3.30} \times 10^{-2}$	1	4.21
Wind	$2.09^{+0.32}_{-0.25} \times 10^{51}$	$22.0^{+6.8}_{-3.1}$	$0.51^{+0.04}_{-0.03}$	0	$1.85^{+0.06}_{-0.05}$	$5.64^{+1.37}_{-1.06} \times 10^{-2}$	$2.80^{+1.36}_{-1.01} \times 10^{-1}$	1	4.70

The visible correlations between the afterglow model parameters means that a number of models comprised of different parameter sets provide similarly good fits to the data. These different parameters sets will give various estimates for the optical flux, dependent on the underlying spectral shape. This is overcome if both the self-absorption and peak synchrotron frequencies are well constrained. This can be clearly seen in Figure 2.7. I was therefore confident that the parameters were well constrained and that the derived optical flux was a good estimate of the true flux. The 68% confidence regions presented in Figure 2.7 were calculated by generating multi-wavelength light curves from a random sample of 500 parameter sets output from the MC bootstrap method. 500 sets is an adequate number to reproduce the full distribution of parameter sets derived from the bootstrap. I then plotted the 500 model flux values for each time bin into a histogram to determine the shape of the distributions. The flux distributions were approximately log-normal for each bin, so I took all flux values between the 16th and 84th percentiles to create the confidence intervals.

Table 2.4 and Figures 2.5 and 2.6 highlight how similar the best fit models were for the two different circumburst density environments. The global reduced χ^2 statistic, calculated by dividing the χ^2 value by the degrees of freedom (dof), for both fits were similar; $\chi^2_{r,\text{ISM}} = 4.21$ compared to $\chi^2_{r,\text{WIND}} = 4.70$. Both environments also exhibited similar parameter distributions. Five parameters were consistent within the 1σ confidence intervals; E_{ISO}, n, $\theta_{j/2}$, $\bar{\epsilon}_e$ and p, with ϵ_B consistent within 2σ. Both environments fail to reproduce several early time non-detections in the 4.8 and 15.7 GHz light curve. The flux at these times varies significantly, up to an order of magnitude, and on a short time scale. This is probably caused by scintillation, where the source emitting region is small at early times due to a highly relativistic outflow (the jet).

I further tested the feasibility of the derived afterglow parameters. Both environment models prefer a larger jet half-opening angle, where $\theta_{j/2,\text{ISM}} \sim 0.47\,\text{rad}$ and $\theta_{j/2,\text{wind}} \sim 0.51\,\text{rad}$. The estimated opening angles and afterglow parameters can be used to calculate the expected jet-break time using the following relation

$$t_{\text{jb}} = \left[\frac{1}{0.057} \theta_{j/2} \left(\frac{1+z}{2} \right)^{\frac{3}{8}} \left(\frac{E_{\text{ISO}}}{10^{53}} \right)^{\frac{1}{8}} \left(\frac{n}{0.1} \right)^{-\frac{1}{8}} \left(\frac{n_x}{0.2} \right)^{-\frac{1}{8}} \right]^{\frac{8}{3}} \tag{2.16}$$
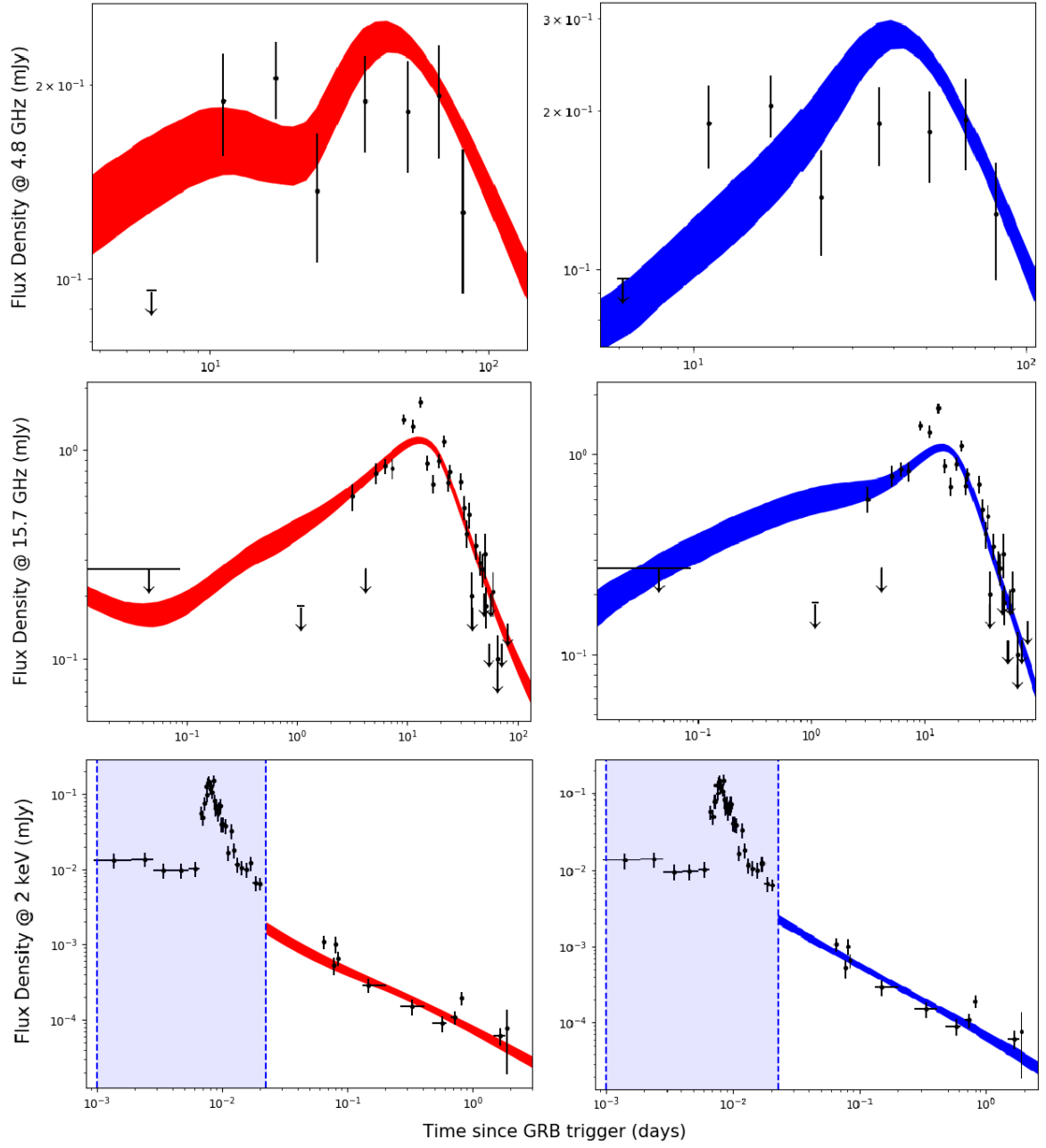
Figure 2.7: Multi-wavelength light curves of GRB 140713A for an ISM-like (red) and wind (blue) environment. The shaded regions represent the best fit 68% confidence region. The lightly shaded blue region in the 2 keV lightcurves represent the X-ray flare that was omitted from the modelling.

for an ISM-like environment (Frail et al., 2001; Starling et al., 2009) and the below relation

$$t_{\mathrm{jb}} = \left[\frac{1}{0.169} \theta_{\mathrm{j}/2} \left(\frac{1+z}{2} \right)^{\frac{1}{4}} \left(\frac{E_{\mathrm{ISO}}}{10^{52}} \right)^{\frac{1}{4}} A*^{-\frac{1}{4}} \right]^{4} \tag{2.17}$$

for a wind environment (Bloom et al., 2003), where t_{jb} is the time of the jet break in days, $A*$ is the density normalisation for a wind density profile, and n_x is an efficiency parameter taken to be 0.2 (e.g. Starling et al. 2009). I calculated that the jet-break should be seen at $t_{\mathrm{jb}} \sim 10 - 16\,\mathrm{days}$ in the ISM-like environment and $t_{\mathrm{jb}} < 1.5\,\mathrm{days}$ in the wind environment. This is illustrated in the 4.8 GHz ISM model lightcurve for the ISM environment (see Figure 2.7). GRBs exhibit a whole range of jet opening angles; some with very narrow beaming cones ($\theta_{\mathrm{j}/2} \lesssim 0.1\,\mathrm{rad}$; Frail et al. 2001; Ryan et al. 2015) and others with very wide angles (e.g., GRB 970508; Frail et al. 2000, GRB 000418; Panaitescu & Kumar 2002). The variance in jet half-opening angles is large and the derived values for GRB 140713A sit comfortably within the previously known distribution.

The models also preferred a low electron energy distribution slope, where $p \lesssim 1.90$ for both environments. Low p values are unusual for GRBs, but do occur and exist within the outer regions of the distribution (Curran et al., 2010; Ryan et al., 2015). As discussed in section 2.4.2, γ_M becomes important when $p < 2$ (see Equation 2.13). If I assume $\gamma_M \sim 10^7$ and $\gamma_m \sim 10^3$, and take p and $\bar{\epsilon}_e$ for both circumburst environments from Table 2.4, I calculate that for a given electron energy density, the equivalent value of ϵ_e is $\sim 15 - 20$ higher than the model estimated values for $\bar{\epsilon}_e$. In both circumburst environments you end up with $\epsilon_e \gtrsim 1$, which is not physical. This is solved when $\xi_{\mathrm{N}} < 1$. A linear decrease in ξ_{N} results in a linear increase in energy, E_{ISO} but simultaneous linear decreases in both ϵ_e and ϵ_B (Eichler & Waxman, 2005). Therefore, if I had chosen to model the afterglow data using $\xi_{\mathrm{N}} = 0.1$, the resulting energy would have been $E_{\mathrm{ISO}} \sim 10^{52}$ ergs and the efficiency parameters would be $\epsilon_B \sim 0.01$ and $\epsilon_e \sim 0.1$ for both circumburst environments in which case ϵ_e would be physical. This was not fully explored in the modelling as I did not have the available data to both effectively explore the full degeneracy of this parameter and confidently derive an optical flux.

2.6 The root of the optical darkness

The optical observations presented in this investigation were taken at sufficiently early times and to deep enough sensitivity limits that an optical afterglow should have been detected. Observations of an associated host galaxy in a number of optical and near-infrared bands were discussed in section 2.2.3, and the LRIS optical spectrum exhibited two strong emission regions; an [OII] doublet at a rest wavelength of $3727\,\text{Å}$ and an [OIII] line at $5007\,\text{Å}$, both occurring at the same redshift, $z = 0.935$. This evidence rules out both a low-luminosity afterglow and a high-redshift origin for the observed optical darkness of GRB 140713A.

To estimate the optical flux, I randomly sampled 500 parameter sets from the 10000 sets derived from the MC bootstrap and produced light curves in the r, i and z bands. I plotted the 16th, 50th and 84th percentiles of each time bin to illustrate the most-probable flux and 68% confidence intervals for both circumburst environments (see Figure 2.8). In similar fashion to the X-ray and radio lightcurve models, I found that the fluxes of the 500 light curve models, in each time bin, also followed log-normal distributions. Figure 2.9 illustrates this for both circumburst environments for the model time bins that represent the optical upper limit observations. Both environment models produce similar optical flux estimates, and both predict optical fluxes $\gtrsim 2$ orders of magnitude above the observed optical limits, suggesting that the observations were taken promptly enough, and more importantly, that an optical counterpart should have been detected. The ISM-like environment estimates are slightly fainter than the wind environment counterparts, so I used the ISM fluxes to calculate the lower limit on the magnitude discrepancy between the optical fluxes and upper limits. Using equation 2.1, I calculated that the discrepancy between the derived fluxes and upper limits were 5.7, 5.0 and 4.1 mag in the r, i and z bands, implying that the only plausible explanation for the optical darkness is line-of-sight optical extinction. The full results are presented in Table 2.5.

To derive the required rest-frame host extinction (A_V^{host}), I transformed the r, i and z wavelengths into the corresponding wavelengths in the rest frame of the host galaxy at $z = 0.935$ and used a number of extinction models; a Milky Way-like ($R_V = 3.1$; Cardelli et al. 1989),
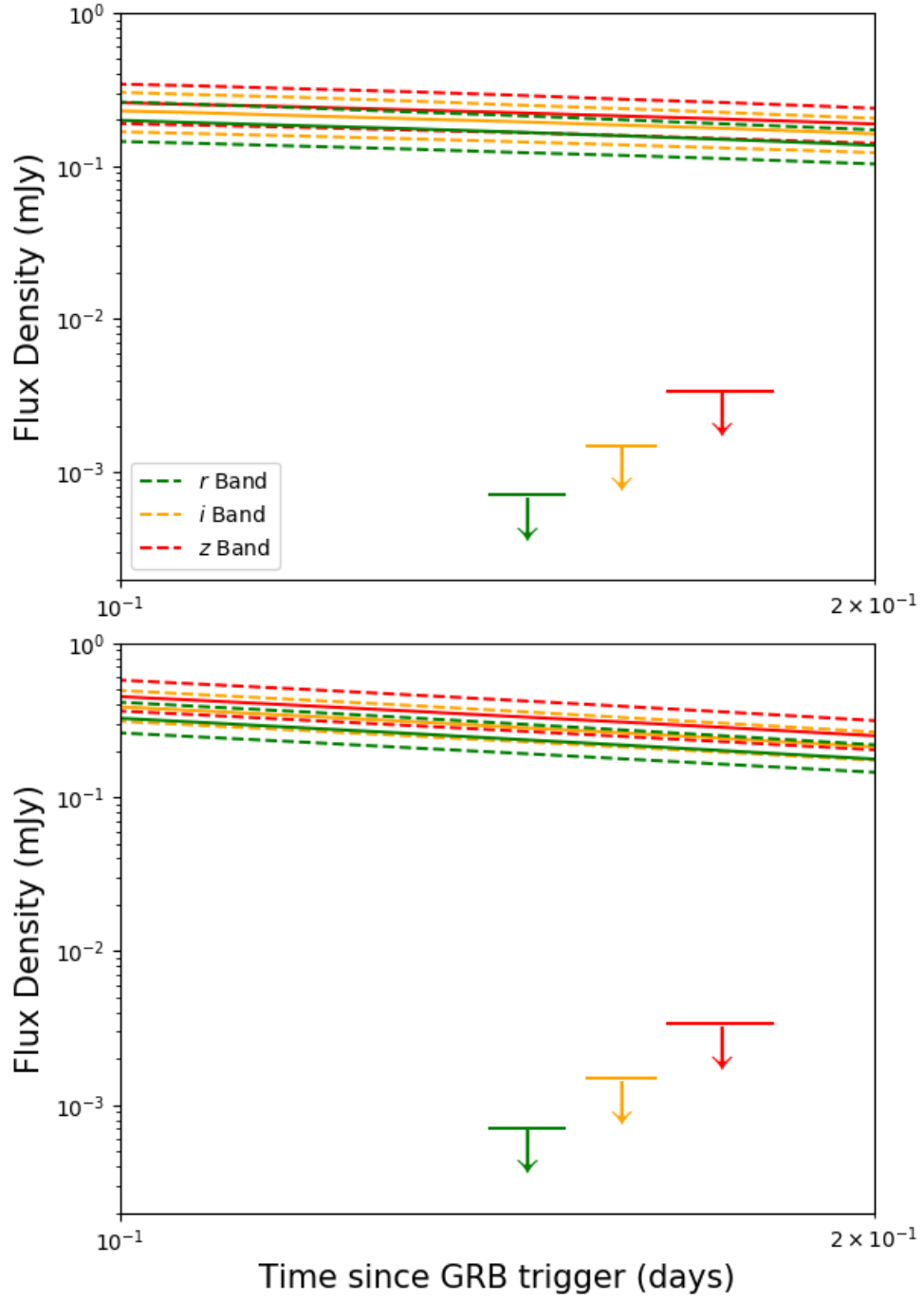
Figure 2.8: Optical light curves of the r (green), i (orange) and z (red) bands for an ISM-like environment (top) and a wind environment (bottom). The solid lines represent the most probable (median) values and the dashed lines represent the 68% confidence intervals.
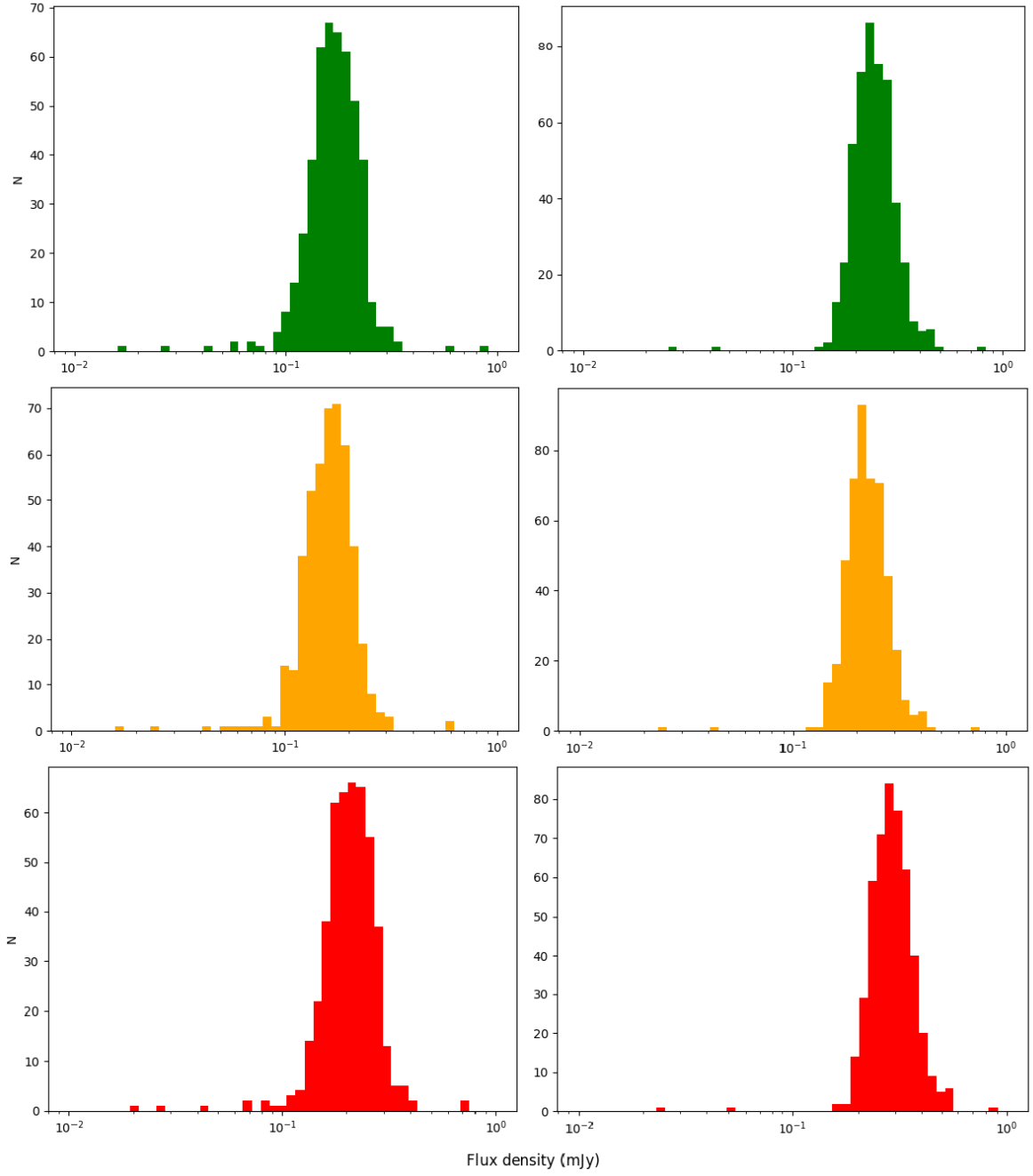
Figure 2.9: Optical flux distributions of the r (green), i (orange) and z (red) bands for the ISM-like (left panels) and wind (right panels) environments. The time bins represented in each window are 0.15 days for r band, 0.16 days for i band, and 0.17 days for z band, post-GRB. These distributions are made up of the 500 randomly sampled parameter-sets.

Table 2.5: Table containing the observed optical upper limits, BOXFIT derived fluxes, required level of extinction and derived host extinctions ($A_V^{\rm host}$) using Milky Way-like, LMC-like and SMC-like extinction models. The required level of extinction were calculated using the magnitude difference between the observational upper limit and the lower limit estimate from BOXFIT at the given wavelength (i.e. 18.6 mag for r band). the derived host extinction values have been corrected for Galactic extinction - $E(B-V) = 0.05$ mag; $A_V^{\rm host} = 0.16$ mag; (Schlafly & Finkbeiner, 2011). All errors are quoted at 68% confidence.

Filter	ΔT (Days)	Mag (AB)	Flux (mJy)	BOXFIT Flux (mJy)	BOXFIT Mag (mag)	Req Ext (mag)	Galactic $A_V^{\rm host}$ (mag)	LMC $A_V^{\rm host}$ (mag)	SMC $A_V^{\rm host}$ (mag)
r	0.15	> 24.3	$< 7.1 \times 10^{-4}$	$0.17^{+0.05}_{-0.04}$	$18.3(\pm 0.3)$	> 5.7	> 3.1	> 3.2	> 2.9
i	0.16	> 23.5	$< 1.5 \times 10^{-3}$	$0.19(\pm 0.05)$	$18.2(\pm 0.3)$	> 5.0	> 3.2	> 3.3	> 3.0
z	0.17	> 22.6	$< 3.4 \times 10^{-3}$	$0.20^{+0.06}_{-0.05}$	$18.1^{+0.4}_{-0.2}$	> 4.1	> 3.2	> 3.2	> 3.1

LMC-like ($R_V = 3.41$; Gordon et al. 2003) and SMC-like ($R_V = 2.74$; Gordon et al. 2003) model. I then subtracted the Galactic extinction contribution, calculated at $E(B - V)^{\text{Gal}} = 0.05$ mag (Schlafly & Finkbeiner, 2011). The three extinction models produced similar results; see Table 2.5, and the most constraining of the three limits was derived from the Milky Way-like extinction model where I found $A_V^{\text{host}} > 3.2$ mag, equivalent to $E(B - V)^{\text{host}} > 1.0$ mag.

As a secondary check to the above results, I independently estimated the host galaxy extinction level using the well known relationship between X-ray absorption and optical extinction (Gorenstein, 1975; Predehl & Schmitt, 1995). The most recent study to map this relationship (Güver & Özel, 2009) constrained this relationship to

$$N_{\text{H}}(\text{cm}^{-2}) = 2.21(\pm 0.09) \times 10^{21} A_V. \tag{2.18}$$

In section 2.2.4, I estimated the intrinsic hydrogen column density of GRB 140713A for a number of different metallicity absorbers. I found that $N_{\text{H,host}} = 2.6^{+1.48}_{-1.12} \times 10^{22}$ cm^{-2} (90% confidence, assuming Solar metallicity absorber) which results in a host extinction of $A_V^{\text{host}} = 11.6^{+7.5}_{-5.3}$ mag (90% confidence), equivalent to $E(B - V)^{\text{host}} = 3.7^{+2.4}_{-1.7}$ mag for the Milky Way-like extinction model using equation 2.18. Using the same method for the SMC-like and LMC-like absorber intrinsic column densities I also calculated in section 2.2.4 results in estimated host extinction values of $A_V = 23.1^{+13.9}_{-10.4}$ mag and $A_V = 33.1^{+20.7}_{-15.2}$ mag, respectively. All three of these estimates are in good agreement with the extinction limits calculated from the BOXFIT generated light curves. I therefore conclude that the source of the optical darkness in GRB 140713A is dust within the host galaxy.

2.6.1 Comparing the extinction of dark GRBs

As discussed in section 2.1, only a small sample of optically dark GRBs with accompanying radio data have been observed. The afterglow and environment parameter properties of these GRBs were compared in Zauderer et al. (2013). Below, I have tabulated the estimated host extinction requirements for the entire sample to date (Table 2.6). I have added the estimated host extinction for GRB 140713A, calculated during this investigation for completeness.

Table 2.6: Estimated host extinction for the sample of dark GRBs with complementary radio data. All extinctions are quoted directly from their respective sources unless otherwise stated, and are given in the rest frame of the host galaxy.

GRB Name	A_V^{host} (mag)	Investigation
970828	> 3.8	Djorgovski et al. 2001
000210	$0.9 - 3.2$	Piro et al. 2002
020809	$0.6 - 1.5$	Jakobsson et al. 2005
051022	$> 8.2^a$	Rol et al. 2007
110709B	> 5.3	Zauderer et al. 2013
111215A	> 7.5	Zauderer et al. 2013; van der Horst et al. 2015
140713A	> 3.2	This investigation

^{a}: This value represents the most constraining limit. I derived this from the quoted J band extinction in the host rest frame ($A_J^{\mathrm{host}} > 2.3\,\mathrm{mag}$) and transformed this into V-band extinction assuming a Milky Way-like extinction model.

Table 2.6 illustrates the variance in the required host extinctions, even within a small sample. The required extinction values range from the modest ($A_V^{\mathrm{host}} \lesssim 1.5\,\mathrm{mag}$) to very high ($A_V^{\mathrm{host}} > 8.2\,\mathrm{mag}$) and GRB 140713A is not atypical compared to the other dark GRBs. At least five of the seven GRBs required extinctions of $> 3\,\mathrm{mag}$. These levels of host extinction are in good agreement with larger sample studies of optically dark GRB host galaxies (Perley et al., 2009, 2013). The results may suggest that the underlying cause of optical extinction in a significant number of dark GRBs is, at least partially, due to line-of-sight dust extinction in the host galaxy. The dust may reside in the immediate local environment of the GRB progenitor or throughout the host galaxy.

2.7 Conclusions

The afterglow of GRB 140713A was detected in both the X-ray and radio bands but was not detected in the optical and near-infrared bands despite prompt observations to deep sensitivity limits. Observations of a likely host galaxy were made at a redshift of $z = 0.935$. This evidence immediately ruled out a high-redshift origin to the optical darkness. I investigated the origin of optical darkness using the afterglow modelling software BOXFIT, which utilised hydrodynamical jet simulations. I produced a number of models in both an ISM-like and wind circumburst environment, based on the BOXFIT derived best fit, to estimate the expected level of afterglow optical flux. The afterglow models provided good fits to the observed data, with the fits preferring a wide jet half-opening angle ($\theta_{j/2} \sim 0.5$ rad) and a shallow electron energy distribution slope where $p \sim 1.85$. Most importantly, the models of both the ISM-like and wind environments predicted that the observed optical flux should have been $\gtrsim 2$ orders of magnitude brighter than the observed upper limits, strongly implying that we should have easily detected the afterglow. This evidence ruled out that GRB 140713A had an intrinsically under-luminous optical afterglow. From the flux discrepancy between the BOXFIT derived optical flux values and the optical upper limits, I estimated that the required host extinction was $A_V^{\mathrm{host}} > 3.2$ mag in the rest frame of the host. I independently estimated the host galaxy extinction from the X-ray column density and found that this was consistent with the host requirements.

The above evidence allowed me to conclude that the origin of the optical darkness of GRB 140713A is most probably caused by a high level of line-of-sight dust extinction. The dust either resides in the local environment of the GRB progenitor or more widely throughout the host galaxy.

3

Investigating the nature of *INTEGRAL* GRBs and the sub-threshold trigger population

3.1   Introduction

This chapter focuses on the investigation into the *INTEGRAL* sub-threshold trigger population. I look for real transient events within the trigger population, with a focus on GRBs. I also investigate the properties of the *INTEGRAL* IBAS GRB sample and compare this to the

larger *Swift* sample. This investigation was published in MNRAS (Higgins et al., 2017).

There have been a number of investigations into GRB luminosity functions and formation rates. These investigations, and additionally a number of observations of nearby GRBs (Sazonov et al., 2004; Soderberg et al., 2004), have suggested that there could be a high number of low-luminosity GRBs in existence than current observations suggest (Daigne & Mochkovitch, 2007; Liang et al., 2007; Pescalli et al., 2016). Further investigations have implied that these apparent local GRBs may exist as a completely separate population (Norris, 2002; Norris et al., 2005; Chapman et al., 2007; Liang et al., 2007).

INTEGRAL is a general, all-purpose, gamma-ray observatory, as discussed in section 1.4.2. It can detect and distribute alerts for GRBs and other transient events thanks to IBAS[3], discussed in section 1.4.3. Since its launch in 2002, *INTEGRAL* has detected > 900 soft gamma-ray sources[4] and has detected and localised 114 GRBs using IBAS, correct as of 2016 July 1 when I concluded my investigation. As of 2018 December 1, the number of detected gamma-ray sources and GRBs increased to > 1100 and 127, respectively. This number does not include GRBs detected by SPI.

The IBIS instrument on-board *INTEGRAL* is more sensitive in the fully-coded FOV than *Swift*/BAT. This is because the diffuse cosmic background emission at X-ray energies of $15 - 200 \, \text{keV}$ is proportional to the FOV, so the smaller area of IBIS, discussed in section 1.4, results in a lower background. Figure 3.1 illustrates the sensitivity limits of current and past gamma-ray missions. *INTEGRAL* should, in theory, be able detect lower peak flux limits than the other currently operational observatories, especially for GRBs with hard spectra with peak energies $> 50 \, \text{keV}$ (Bošnjak et al., 2014).

If *INTEGRAL* is more sensitive to lower peak fluxes, it may be capable of detecting this theorised low luminosity local population of GRBs, according to previous investigations (Foley et al., 2008). It must be noted that *INTEGRAL* spends a significant amount of time observing areas of the sky, close to the centre of our Galaxy. The additional X-ray emission from the bright sources in the Galactic plane means that IBIS does not often reach the lowest sensitivity
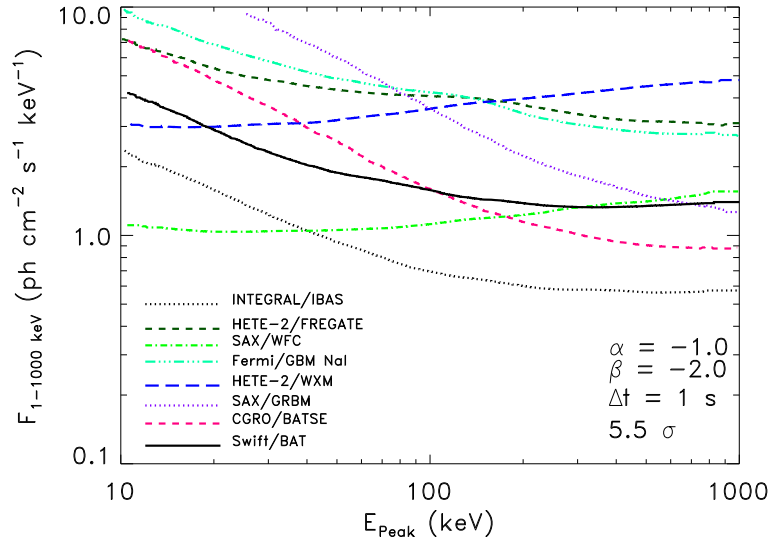
Figure 3.1: Peak flux sensitivity limits of past and current gamma-ray observatories (Bošnjak et al., 2014).

levels.

Section 1.4.3 describes the IBAS triggering programs in detail. IBAS implements two significance thresholds, aptly named as STRONG and WEAK. If a new source triggers IBAS with a high enough significance (typically $\gtrsim 8\sigma$ for STRONG alerts, though this has been shown to not be a definitive value), the information is distributed to the public in real time. Historically, sources with a lower significance (typically between $5.5 < \sigma < 8\sigma$ for the WEAK alerts) were not distributed publicly. It is difficult to establish whether low significance events are real sources from the IBIS data alone, so members of the IBAS team could manually investigate and analyse WEAK alerts to determine if a real source was detected, and then release the relevant information to the wider public. Since 2011 January 26, the IBAS WEAK alerts have been available to the public in real time, in conjunction with the STRONG alerts. Among the 114 GRBs detected and localised by IBAS as of 2016 July 1, 17 were detected from WEAK alerts, and 54 of the 114 GRBs were observed with *Swift*. The *Swift* observations of the 54 GRBs were conducted independently via an autonomous BAT trigger, or via a Target of Opportunity (ToO) request for follow-up, and have available XRT data.

3.2 *INTEGRAL* WEAK alert population

3.2.1 Chosen WEAK alerts for further investigation

Since early 2011, up to 2016 July 1, there had been 402 *INTEGRAL* WEAK alerts distributed publically. Six of these alerts were later promoted to STRONG triggers after further analysis, and were also confirmed as GRBs. For this pilot investigation, 15 WEAK alert triggers out of the remaining 396 were analysed. The 15 triggers investigated comprised of the following:

- 11 triggers that were not autonomously detected by *Swift*/BAT and whose follow-up was triggered from a requested ToO observation. The naming convention for these triggers was IGRWYYMMDD prior to any follow-up analysis. The convention roughly follows the format for GRBs and the IGRW is an acronym for '*INTEGRAL* WEAK'. These chosen triggers are henceforth referred to as 'chosen ToOs' for the rest of the investigation. For reference, 10 of these triggers were originally chosen by Rhaana Starling who requested the follow-up *Swift* ToO observations. The other one was chosen by me and I requested the ToO observation.

- Two other WEAK alerts, not part of the above 11, with *Swift* ToO observations requested elsewhere and had available *Swift*/XRT data. These two triggers are henceforth referred to as 'candidate GRBs'.

- Two further WEAK alerts whose events also simultaneously triggered *Swift*/BAT. These events also had follow-up *Swift*/XRT data. These two triggers are also henceforth referred to as candidate GRBs.

There were a number of criteria set for the 11 chosen ToOs selected by our team. The criteria were:

- WEAK alerts were chosen to be close to the $\sim 8\sigma$ STRONG threshold to increase the

chances of the trigger being caused by a real astrophysical event, as oppose to a false positive. The lowest trigger significance out of the 11 chosen ToOs was 6.7σ.

- The WEAK alert coordinates were cross-referenced with catalogues of previously known X-ray sources. This was to ensure that the triggers were not caused by known X-ray sources.

- The positions were cross-referenced against areas of high Galactic dust extinction, and not chosen if the Galactic column density was too high.

- ToOs were only requested for WEAK alerts if the trigger time coincided with the working hours of the on-call member of the *Swift* team.

This investigation was a pilot campaign investigating whether real transient events exist among the WEAK trigger population. I analysed $\sim 4\%$ of the entire WEAK alert population and do not claim to be able to deduce conclusions about the population as a whole. I highlight that the three criteria described above were not stringently adhered to for the 11 chosen ToOs and therefore I also do not claim that these triggers form a uniform or unbiased sub-sample of the WEAK alert population. The properties of each alert can be found in Table 3.1.

3.3 *Swift* follow-up analysis of WEAK alerts

The XRT and UVOT data for the chosen 15 WEAK triggers were analysed to determine the nature of the WEAK trigger events. The data were made available at the UKSSDC (Evans et al., 2007, 2009).

3.3.1 *Swift*/XRT

I produced cleaned event files for the 11 chosen ToOs the *Swift*/XRT pipeline tool (v0.13.2). The four candidate GRBs had existing XRT products made available by the UKSSDC, so I

Table 3.1: The properties of the chosen 15 WEAK alerts. The 11 chosen ToOs are displayed at the top and the four candidate GRBs are displayed separately at the foot of the table. The IBAS trigger no., detection significance, coordinates and localisation error (90% containment) were all taken from the IBAS database.

ToO name	*INTEGRAL* trigger no.	IBAS detection significance (σ)	RA (Deg; J2000)	Dec (Deg; J2000)	Localisation error (arcmin)
IGRW 160610[†]	7488/0	6.7	359.90	61.57	3.8
IGRW 151019	7277/0	7.0	292.82	31.14	3.5
IGRW 150903	7231/0	6.7	239.17	-33.81	3.6
IGRW 150610	7005/0	7.1	178.32	16.03	4.8
IGRW 150305	6905/0	7.6	269.79	-42.62	3.4
IGRW 140219	6467/0	6.7	204.10	-45.06	3.6
IGRW 130904	6931/0	6.7	256.88	-32.01	3.6
IGRW 110718	6323/0	6.8	256.78	40.05	3.6
IGRW 110608	6297/0	6.8	315.28	32.041	3.6
IGRW 110428	6169/0	7.2	320.27	-33.96	3.5
IGRW 110112	6127/0	7.4	10.56	64.41	2.6
IGRW 150831	7228/0	7.3	220.98	-25.65	3.4
IGRW 121212	6720/0	7.9	177.90	78.00	3.3
IGRW 100909	6060/0	7.7	73.95	54.65	2.0
IGRW 091111	-	7.2	137.81	-45.91	2.9

[†] represents the trigger that I personally requested *Swift* ToOs for.

used the existing cleaned event files. I searched for possible sources within the IBAS locali-sation region, given in 3.1, using the sky image files. If the probability of a suspected source arising from random statistical fluctuations was $< 0.3\%$ (equivalent to a 3σ detection), I con-cluded that the source was real. I calculated the number of counts for a detection using a 30 arcsec radius region centered on the detected source coordinates. If no source was detected in the IBAS localisation region, I calculated upper limits using a C++ script using the Bayesian analysis described in Kraft et al. (1991) with a background annulus with as large a radius as possible.

If a source was detected with *Swift*/XRT in the images of the initial ToO request, a further ToO observation was requested to determine the nature of the source. For a GRB, this second ToO would show a fading source or a source that is no longer detected (Costa et al., 1997; O'Brien et al., 2006). If the source was detected in the second ToO images, and confirmed to be fading, a third ToO observation was requested at a later date to confirm if the source had faded even further, and thus, confidently conclude if the source was in fact a GRB. All source detection coordinates were cross-referenced with the astrophysics catalogue database Vizier[9] (Ochsenbein et al., 2000) to determine if any existing sources could have produced the observed X-ray emission. An illustration of the above analysis is available in Figure 3.2.

From the 15 WEAK alerts that I analysed using the above method, six alerts, two of the chosen ToOs and the four candidate GRBs, produced a positive XRT detection. Observations requested using further ToOs found that five of these six sources were fading. The sixth detected source, associated with IGRW 151019, did not fade after a month confirming that this source was not a GRB. This source is discussed in detail in Section 3.3.4. I cross-referenced the coordinates of the six detected sources. No known, catalogued X-ray sources were found within ~ 2 arcmin of the XRT position at the time that the ToO observations were taken. The *Swift*/XRT properties of all 15 WEAK alerts can be found in Table 3.2. The detected sources and non-detection upper limits can also be seen in Figures 3.3 and 3.4.

Figure 3.3 highlights that two of the WEAK alerts, GRBs 121212A and 150831A, were rela-

---

[9] http://vizier.u-strasbg.fr/viz-bin/VizieR

Table 3.2: Properties for the six WEAK alerts with sources detected with *Swift*/XRT. The localisation error (90% containment), RA and Dec were taken from UKSSDC. T_{START} and T_{STOP} refer to the times elapsed between the GRB/trigger occurring and the time when the *Swift*/XRT observations began and finished. T_{EXP} is the total exposure time from the XRT observations.

ToO Name	*Swift* observation ID	Localisation Error (arcsec)	RA (Deg; J2000)	Dec (Deg; J2000)	T_{START} (s)	T_{STOP} (s)	T_{EXP} (s)
IGRW 151019	20558	2.5	292.7836	31.1319	9600	2810017	14938
GRB 150831A	653838	1.6	221.0243	-25.6351	82	38575	11828
IGRW 150305A	33663	3.5	269.7606	-42.6638	17838	735268	908
GRB 121212A	541371	1.4	177.7923	78.0371	60	145420	22940
GRB 100909A	20147	3.3	73.9488	54.6579	11693	25787	7720
GRB 091111	20120	7.7	137.8233	-45.9253	100360	197466	10386
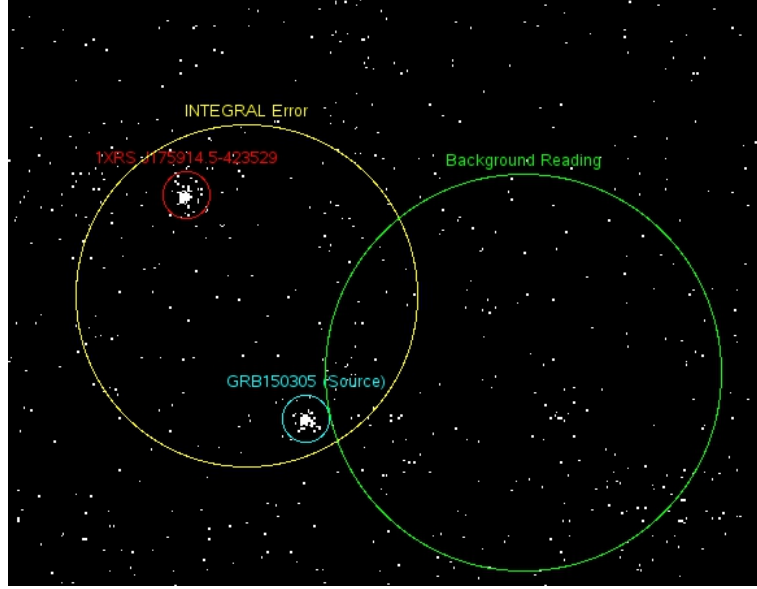
Figure 3.2: *Swift*/XRT image of IGRW/GRB 150305A. A new source (blue) can be clearly seen within the *INTEGRAL* error region (yellow). In this case, a previously catalogued X-ray source, 1XRS J175914.5-423529 (red) was also detected within the *INTEGRAL* error region. I have added an example background region (green) to the image.

tively well sampled by *Swift*/XRT, where relatively well means > 10 data bins, compared to the other alerts with detected sources. This occured as both events also triggered *Swift*/BAT. I further analysed the X-ray data of these alerts to obtain both a spectral fit and afterglow decay slope.

I fit the X-ray data of both GRB with the same absorbed power law as described by equation 2.3, however I set $z = 0$ for both GRBs, as the redshifts are unknown. The element abundances and cross-section for X-ray absorption were set at the values given in Wilms et al. (2000) and Verner et al. (1996), respectively. Galactic absorption was calculated using the method described in Willingale et al. (2013) and the effective host galaxy absorption was left as a free parameter. GRB 150813A had good data coverage in both the WT and PC XRT modes (described in Section 1.4.1), so the data from both modes were fit. GRB 121212A had poor WT coverage and so I only fit the PC data. I fit simple power laws to the lightcurves to estimate the decay slopes. The best-fit parameter for the slope was then found by minimising the χ^2 statistic. The spectral fit and afterglow decay slope parameters for both GRBs are
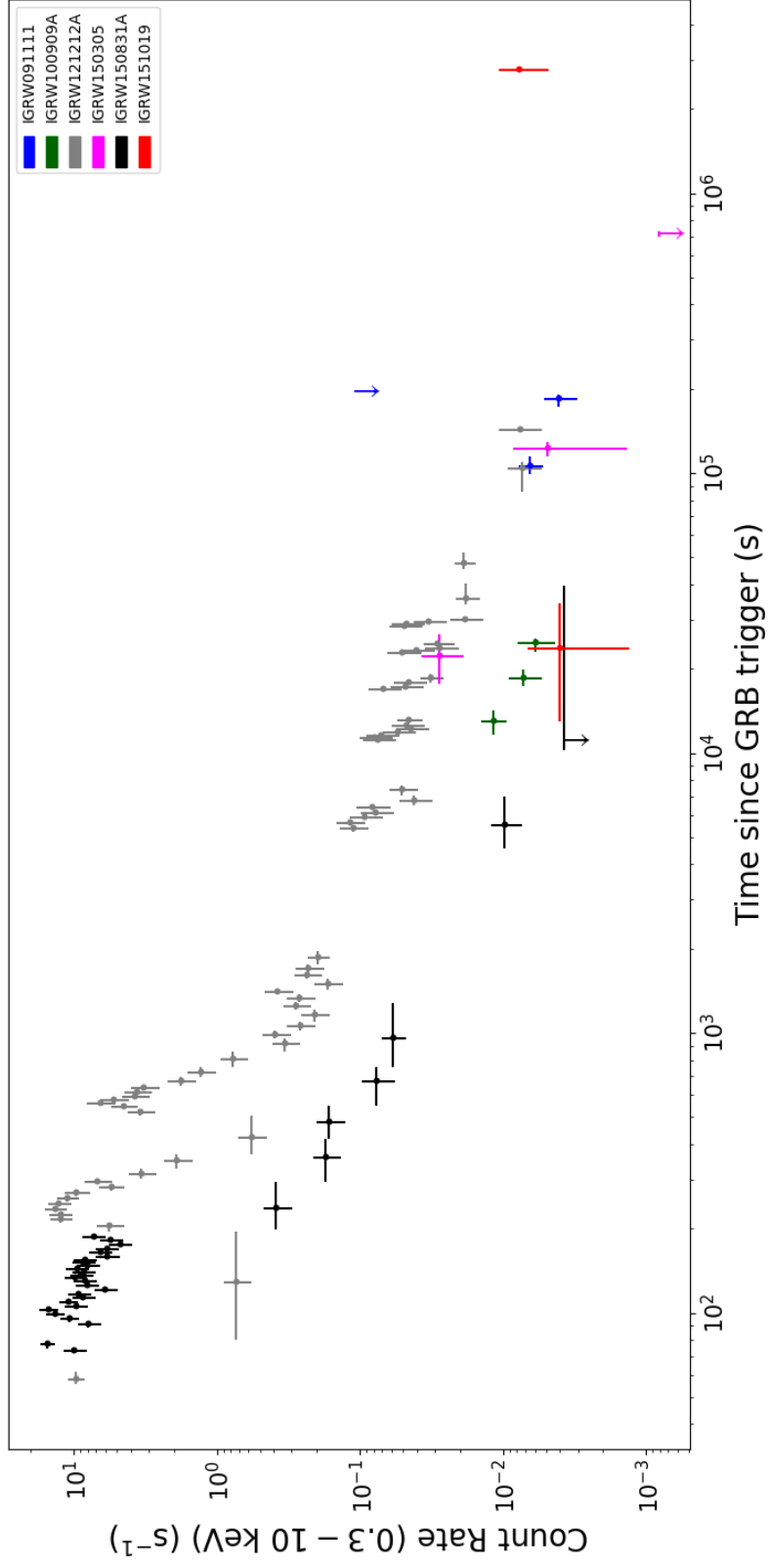
Figure 3.3: X-ray lightcurves of the six WEAK alerts with sources detected by *Swift*/XRT.
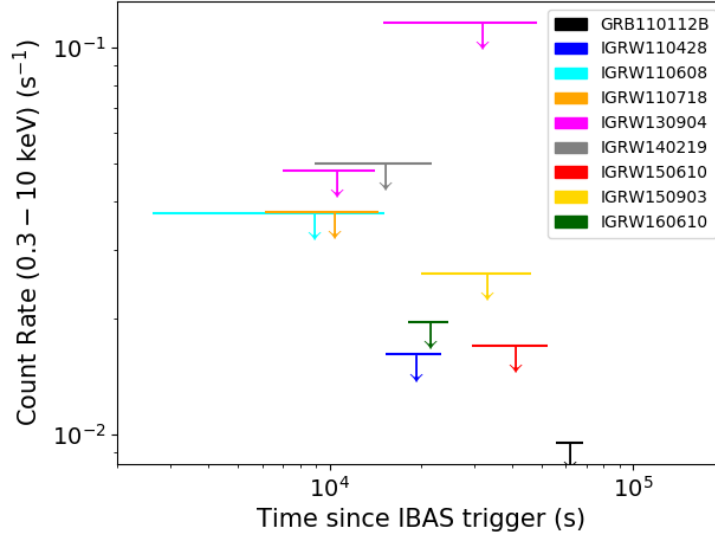
Figure 3.4: 3σ upper limits of the nine WEAK alerts with no source detected by *Swift*/XRT.

available in Table 3.3. The spectral fits for both GRB spectra are illustrated in Figure 3.5.

Table 3.3: X-ray spectral properties and afterglow lightcurve decay slope for GRB 121212A and GRB 150831A. The spectral analysis was performed using XSPEC. All quoted errors are for 90% confidence intervals except for the X-ray decay slopes which are quoted at 68%.

ToO Name	$N_{\mathrm{H,Gal}}$	$N_{\mathrm{H,Host}}$	Γ	C-Stat	α
	$(10^{20}\,\mathrm{cm}^{-2})$	$(10^{20}\,\mathrm{cm}^{-2})$		(dof)	
GRB 121212A	4.48	$21^{+0.5}_{-0.4}$	$2.24^{+0.14}_{-0.13}$	341 (369)	$-0.71^{+0.03}_{-0.03}$
GRB 150831A (WT)	11.4	$0^{+80.0}_{-0}$	$1.15^{+0.18}_{-0.18}$	322 (404)	$-2.67^{+0.22}_{-0.22}$
GRB 150831A (PC)	11.4	$0^{+18.0}_{-0}$	$1.53^{+0.28}_{-0.29}$	99 (93)	$-2.67^{+0.22}_{-0.22}$

One of the ToOs, IGRW 110112, was an XRT non-detection at $6.2(\pm0.6) \times 10^4$ s after the IBAS trigger. However, as it simultaneously triggered *Fermi*/GBM (Connaughton, 2011), it was classified as a GRB. IGRW 110608, one of the other XRT non-detections, had a very unusual X-ray background compared to the other ToOs. Upon further inspection, it was very high in places and had an irregular shape. This background probably effected any chance of detecting a statistically significant source in the image files.
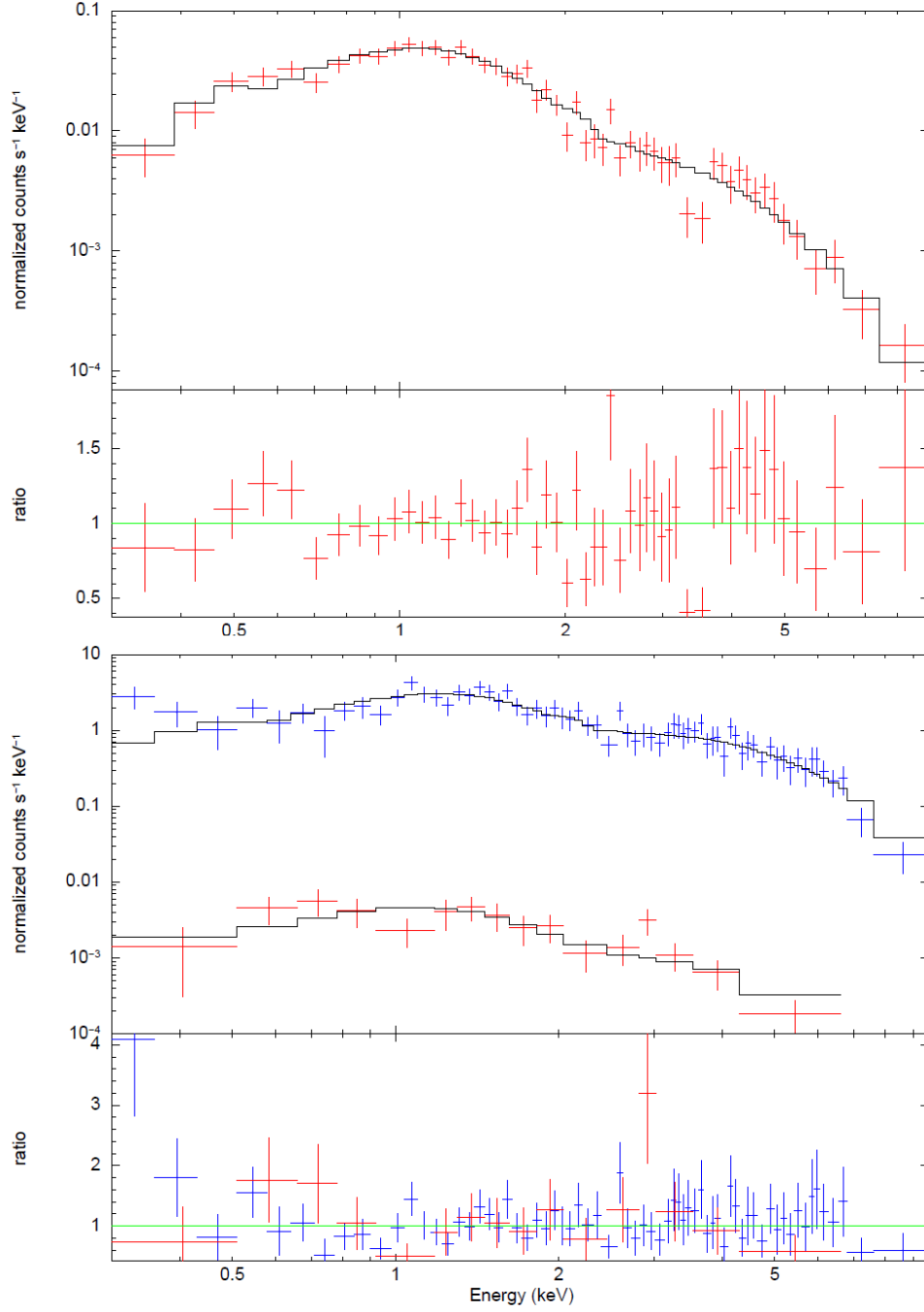
Figure 3.5: *Swift*/XRT spectra of GRB 121212A (top) and GRB 150831A (bottom). The WT (blue) and PC (red) mode data are overplotted with the best-fit absorbed power law model (black) produced using XSPEC (red). The best-fit parameters are presented in Table 3.3. Ratios are plotted over residuals due to the normalisation differences between the WT and PC mode data of GRB 150831A.

The ToO requests for these events were not high priority targets for *Swift*. This resulted in ToO observations starting at various times post-trigger (see Table 3.1 for examples). Additionally, there was a huge variance in Galactic column density depending on the position of the GRB. Due to a lack of redshift information and X-ray coverage for some triggers, I could not accurately estimate the host absorption. I plotted the time elapsed from trigger to the XRT observation, T_{START}, against the weighted mean Galactic column density, $N_{\text{H,Gal}}$ for all triggers, and split them by detection and non-detection (see Figure 3.6). This was to investigate if there was any correlation between detecting an X-ray source and both how quickly a ToO started, and $N_{\text{H,Gal}}$. One could assume that a quick response ToO observation and low $N_{\text{H,Gal}}$ would increase the chance of detecting a source.
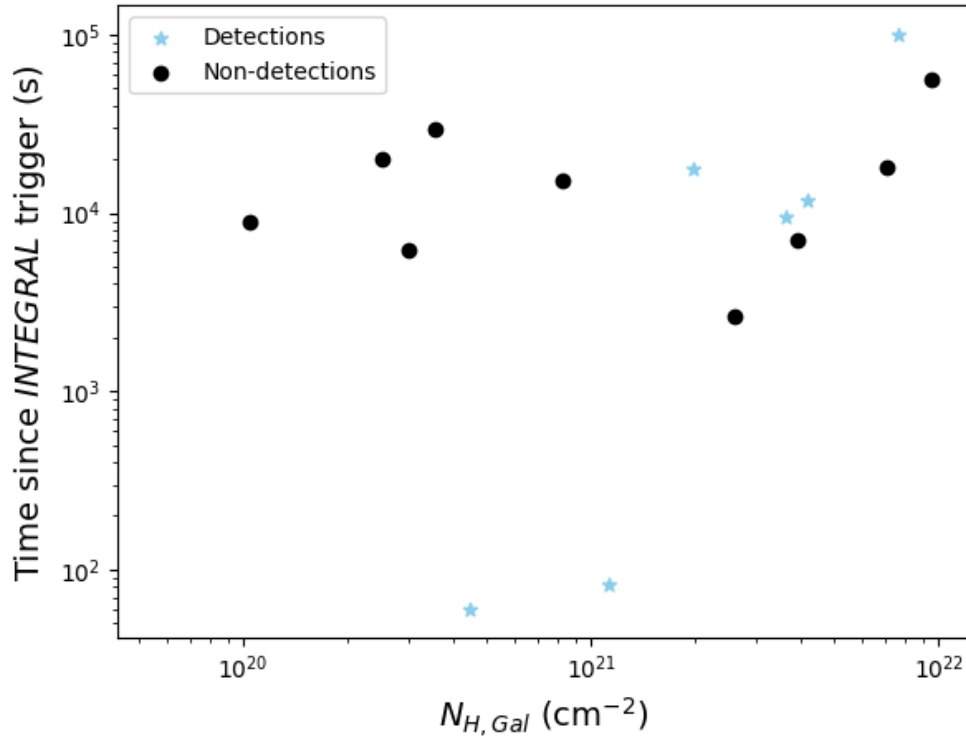
Figure 3.6: $N_{\text{H,Gal}}$ vs T_{START} for the 15 WEAK triggers. The *Swift*/XRT detections are in blue and the non-detections are in black.

Two sources were detected with ToO observations commencing $< 100\,\text{s}$ post-trigger. The 13 other WEAK alerts were all observed at $10^3 < T_{\text{START}} < 10^5\,\text{s}$ post-trigger. There was no obvious correlations between the detections and non-detections for these alerts. There were

also no obvious differences between the detections and non-detections for $N_{\rm H,Gal}$. Additionally, as only 15 alerts were followed up, I conclude that no differences were noted between the detections and non-detections with respect to these two variables.

3.3.2 *Swift*/UVOT

I analysed the *Swift*/UVOT data of the six WEAK alerts with detected X-ray sources to determine if any UV/optical counterparts were observed. The data comprised one or more UVOT filters each with multiple separate images. Multiple images were WCS coordinate aligned and summed together to produce one image. I produced a summed image for each exposure per filter. Images taken by UVOT were binned in two modes; 1×1 or 2×2 binning (see the *Swift*/UVOT Online Manual). I only analysed images that were taken in 1×1 binning mode. If there were multiple exposures in the same filter per ToO observation, I produced a summed image. The number of filters used during each ToO observations was dependent upon the designated filters used by *Swift* on the date of the observation. I derived the brightness of any possible sources, or upper limits for any non-detections, using the the *Swift* tool UVOTSOURCE. A source was detected if the significance was $> 3\sigma$ (Breeveld et al., 2010). I classed a source as marginally detected if $> 3\sigma$ and strongly detected if $> 5\sigma$.

An optical source was marginally detected with the UVOT white filter coincident with the XRT position of GRB 121212A. A Vizier catalogue search of the UVOT source position revealed no previously reported optical source. The UVOT position of the source was RA, Dec (J2000) 177.79341, 78.03780 deg with a 1σ positional error of 0.48 arcsec. A marginal detection was also registered in the v, b and u bands for GRB 091111. However, upon further analysis of the UVOT images, I found that the source was $\lesssim 30$ arcsec from a very saturated source. The photons from this source may have spilled over into the surrounding pixels, potentially affecting the validity of source detection and the background. A UV source detected with the $m2$ filter was present very close to the XRT position IGRW 151019. This source is discussed further in Section 3.3.4. Full results on the UVOT analysis are displayed in Table 3.4.

Table 3.4: *Swift*/UVOT observations of the six WEAK alerts with XRT detections. Magnitudes given in AB system. Galactic redenning values taken from the Infrared Science Archive (IRSA) using the method described in Schlafly & Finkbeiner (2011).

Name	white	v	b	u	$w1$	$m2$	$w2$	Source detected?	A_V (mag)
IGRW 151019	-	-	-	-	> 21.75	22.16($\pm$0.15)	-	Yes	0.75
GRB 150831A	> 21.54	> 19.82	> 19.90	> 21.34	> 21.85	> 22.39	> 23.10	No	0.30
GRB 150305A	-	-	-	-	> 22.68	> 22.74	-	No	0.45
GRB 121212A	23.89($\pm$0.38)	> 20.22	> 20.75	> 22.07	> 23.00	> 22.73	> 22.95	No	0.18
GRB 100909A	> 22.52	> 20.07	> 21.26	> 21.78	> 21.73	> 22.19	> 21.99	No	1.37
GRB 091111	-	19.48($\pm$0.24)*	18.92($\pm$0.28)*	21.76($\pm$0.23)*	> 21.94	> 22.35	> 22.32	No	4.79

* XRT position was $\lesssim$ 30 arcsec from the centre of a saturated source. Further analysis of the images suggest that the detections in the v, b and u filters may not be real.
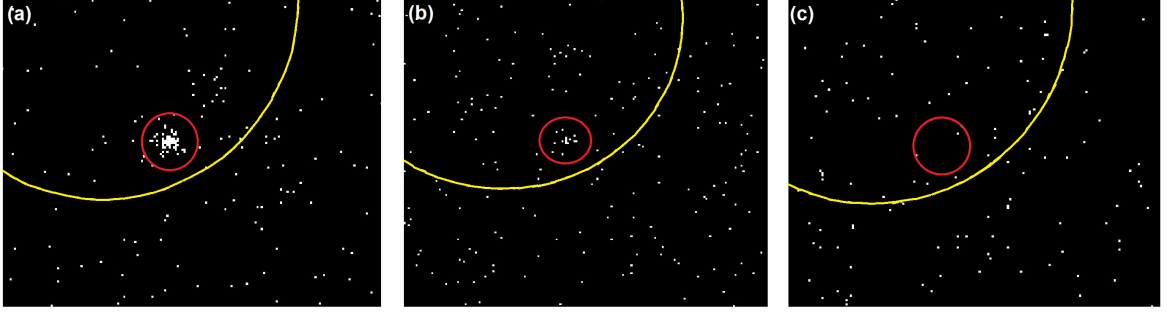
Figure 3.7: *Swift*/XRT images of the three ToO observations of IGRW/GRB 150305A. The detected source (red) within the *INTEGRAL* error circle (yellow) can clearly be seen fading over the observations. The images correspond to observation times of $(1.7 - 2.7) \times 10^4$ s (a), $(1.2 - 1.3) \times 10^5$ s (b) and $(7.0 - 7.4) \times 10^5$ s (c) post-trigger. The XRT exposure times are 3.0 ks (a), 3.7 ks (b) and 2.4 ks (c) for each observation, respectively.

3.3.3 IGRW/GRB 150305A

IGRW 150305 was confirmed as a GRB after the X-ray source continued to fade over the course of $\approx 8 - 9$ days and three ToO observations. Figure 3.7 illustrates the fading X-ray source. A marginal detection was made in the white UVOT filter. A Vizier search of the GRB position revealed no optical or X-ray catalogue matches for the XRT and UVOT positions.

The requested ToOs were the only X-ray observations of GRB 150305A. This resulted in a very poorly sampled lightcurve (three data bins), with a very approximate decay slope, $\alpha \approx 1$. Obtaining a spectrum is also not possible due to the very low number of counts detected: 102 in 6620 s. The crucial result was that this detection of a new GRB would not have been possible without the *Swift* follow-up of a *INTEGRAL* WEAK trigger. This source did not trigger and was not identified by any other space or ground based observatory (Starling, 2015).

3.3.4 IGRW 151019 - active galactic nucleus candidate

IGRW 151019 had showed no signs of fading after 4 weeks, illustrated in Figure 3.8. The count rate between the two ToOs had not decreased; the initial ToO XRT count rate was
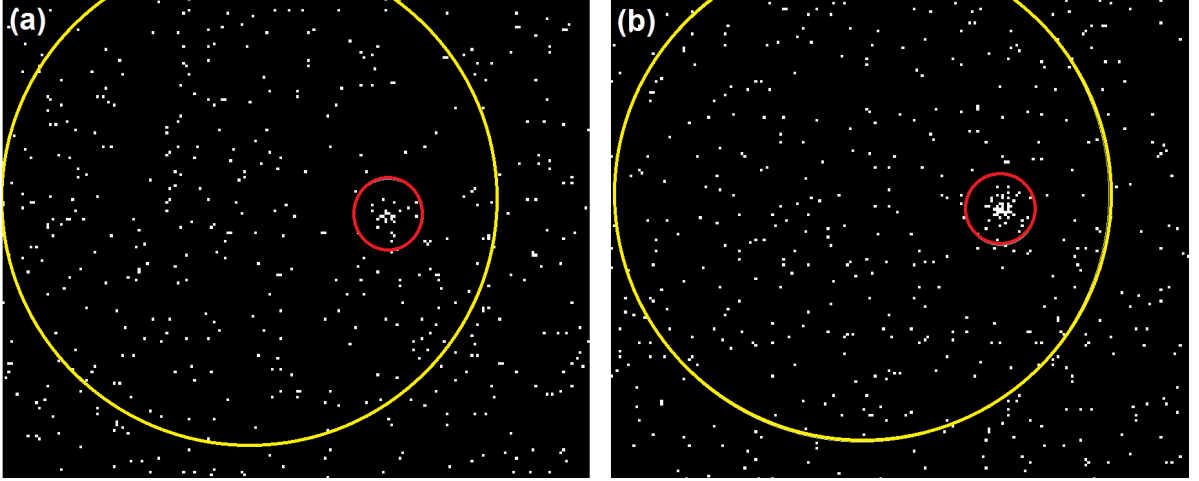
Figure 3.8: *Swift*/XRT images of the two ToO observations of IGRW 151019. The detected source (red) within the *INTEGRAL* error circle (yellow) clearly does not fade between the observations. The images correspond to observation times of $(9.6 - 28.7) \times 10^4$ s (a) and $(2.7 - 2.8) \times 10^6$ s (b) post-trigger. The XRT exposure times are 5.9 ks (a), 8.7 ks (b) for each observation, respectively.

$4.0(\pm 2.7) \times 10^{-3}$ s^{-1} and this increased by a factor of $\approx 1 - 8$ during the second ToO observation. A third ToO of this source was not required as the detected source clearly did not fade. IGRW 151019 was therefore confirmed as a steady source; a GRB would have significantly faded by the time the second ToO observation had occurred.

The X-ray spectral data for both observations were fit with an absorbed power law (equation 2.3; $z = 0$) with fixed $N_{\text{H,Gal}} = 3.63 \times 10^{21}$ cm^{-2}. The number of counts observed were fairly low and so the errors on the fits were large. The best-fit models are illustrated in Figure 3.9 and the parameters are displayed in Table 3.5. The spectral values for IGRW 151019 are fairly typical for Active Galactic Nuclei (AGN; Nandra & Pounds 1994; Tozzi et al. 2006; Brightman & Nandra 2011).

The AllWISE source J193108.05+310756.4 is coincident with the XRT position (90% containment error) of IGRW 151019 (Cutri, 2014) and lies ~ 1.8 arcsec from the centre of the XRT position. The UVOT source detected in the $m2$ filter (Table 3.4) had a position of RA, Dec (J2000) 292.78334, 31.13252 deg with a 1σ positional error of ~ 0.5 arcsec and a coincident Gaia source was found with their central positions also ~ 0.5 arcsec apart. However, both
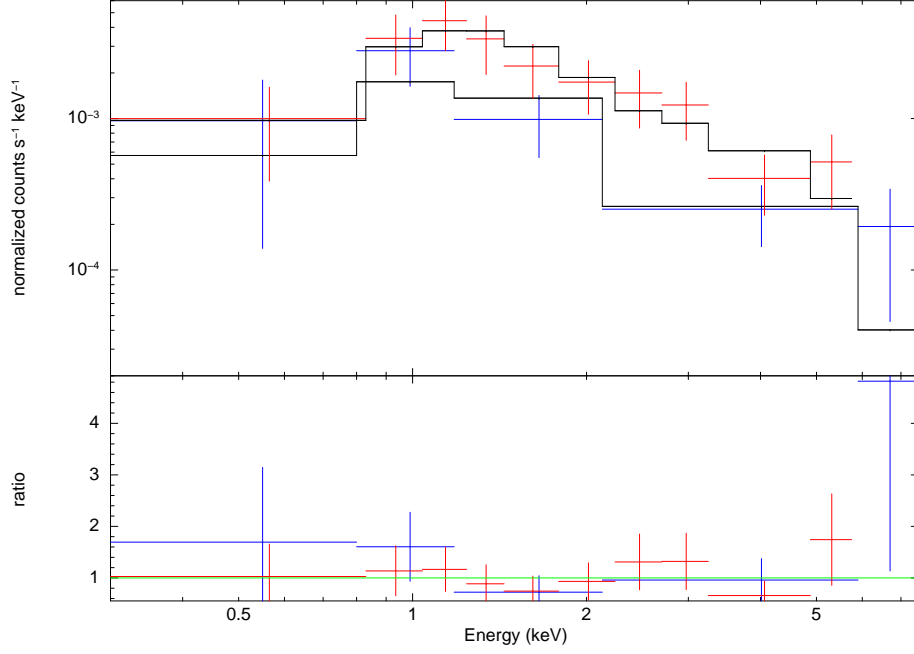
Figure 3.9: *Swift*/XRT spectrum for the first (blue) and second (red) ToO observations of IGRW 151019. The best-fit models (black) are overplotted.

Table 3.5: X-ray spectral properties for IGRW151019. The spectral analysis was performed using XSPEC. All quoted errors are for 90% confidence intervals.

IGRW151019 observation	$N_{\mathrm{H,Host}}$ $(10^{20}\,\mathrm{cm}^{-2})$	Γ	C-Stat (dof)
One	$0^{+32.6}_{-0}$	$2.13^{+0.94}_{-0.79}$	24 (23)
Two	$3.4^{+50.3}_{-3.3}$	$1.69^{+0.75}_{-0.40}$	50 (55)

the UVOT and Gaia sources lie just outside the 90% XRT containment region and therefore, I cannot confidently confirm that these two optical sources are associated with the detected XRT source.

Upon further investigation, the AllWISE source had WISE colours, $\mathrm{W1} - \mathrm{W2} = 0.8$ and

$W2 - W3 = 2.4$. The colours of the AllWISE source were found to be consistent with that of an AGN (Mingo et al., 2016). From the above evidence, I concluded that IGRW 151019 is a steady source, and probably an AGN. I note that it is also possible that a very short lived transient event may have triggered *INTEGRAL* before rapidly fading at X-ray wavelengths, but this cannot be verified.

3.4 Comparison of the *INTEGRAL* IBAS and *Swift*/BAT GRB samples

I reviewed previous *INTEGRAL* GRB work in Section 3.1, and highlighted that *INTEGRAL* could, in theory, detect lower peak flux limits and may be able to observe a low luminosity, local GRB population, if it exists. To probe these claims, I analysed the whole IBAS GRB population and compared it's properties to the *Swift*/BAT GRB sample. IBAS has detected and localised 114 GRBs (including both STRONG and WEAK alerts) including 54 with XRT detections. *Swift*/BAT has detected and localised 1060 GRBs with XRT detections for 846 GRBs (correct as of 2016 July 1). All subsequent values of T_{90}, peak flux, fluence, fluence errors and X-ray fluxes used below for the BAT sample were taken from the *Swift* GRB table[5].

I plotted the T_{90} and peak flux distributions of both GRB samples (see Figure 3.10). Analysis shows that the IBAS sample has a lower mean T_{90} (47 s compared to 70 s) and lower mean peak flux (2.0 ph cm^{-2} s^{-1} compared to 3.6 ph cm^{-2} s^{-1}). Interestingly though, BAT detects a higher fraction of SGRBs; $95/992$ (9.6%) for BAT GRBs compared to $6/114$ (5.3%) for IBAS GRBs. These results suggest that IBAS detects GRBs with lower T_{90}s and peak fluxes, on average. One could then imply that *INTEGRAL* may therefore, on average, detect fainter GRBs than *Swift* and with the addition of the lower IBIS sensitivity (discussed in section 3.1), *INTEGRAL* may be better suited to probing the low luminosity, local GRB population.

I analysed the BAT and IBAS GRB fluence distributions to test if *INTEGRAL* was detecting fainter GRBs in practice. A number of IBAS fluence values were taken from Vianello et al.
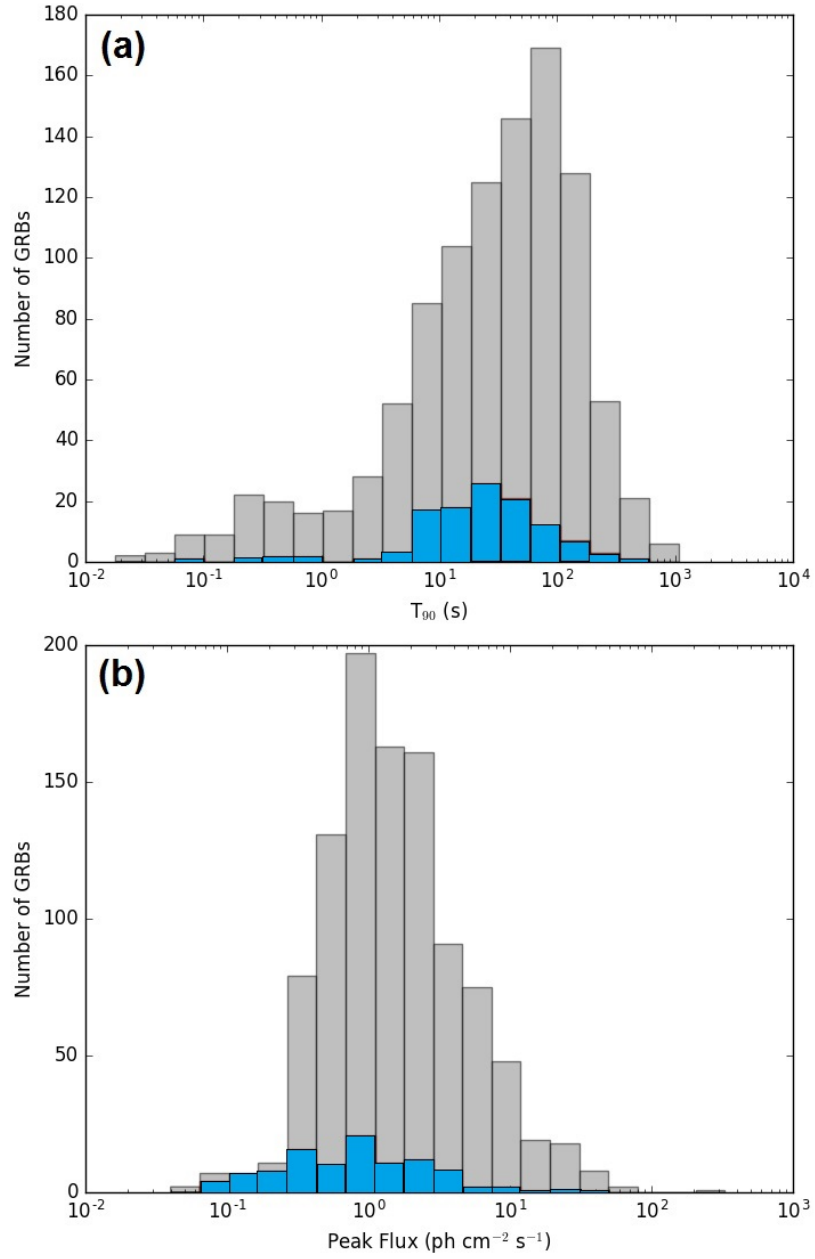
Figure 3.10: T$_{90}$ (a) and peak flux (b) distributions of the *Swift*/BAT (light grey) and IBAS (blue) GRB samples. The peak fluxes are measured in the $15-150$ keV energy range for *Swift* and the $20-200$ keV energy range for IBAS.

(2009) and Bošnjak et al. (2014). To calculate the fluences for the rest of the IBAS GRB sample, the IBAS GRB T_{90} values were multiplied by the average fluxes. The average fluxes that were not obtained in Vianello et al. (2009) and Bošnjak et al. (2014) were supplied by Rhaana Starling and Diego Götz. The T_{90} values taken from IBAS did not have any associated error limits. In total, I analysed 92 IBAS GRBs with calculated fluences. The properties of the entire IBAS GRB sample with published and estimated measurements can be found in Appendix B. The BAT and IBAS GRB fluence distributions are shown in Figure 3.11. The energy ranges for the fluence values are different for the two satellites; BAT values are measured in the $15 - 150$ keV energy range whereas the IBAS GRB fluences are measured in the $20 - 200$ keV energy range. The ratio of the fluxes between these two energy bands was $\frac{f_{20-200}}{f_{15-150}} \approx 1.22$ when derived using spectral fits for several GRBs in the IBAS sample. I assumed that this ratio held true with the fluence ratios between these two bands as well, though this ratio is approximate and may not be true for a large number of GRBs as every GRB has a unique spectral shape and hardness. I also assumed that the T_{90} values were constant between the two energy bands when calculating the above ratio, but this is not necessarily true. The IBAS fluence values converted into the BAT energy band are also shown in Figure 3.11.

For the IBAS GRBs also detected by the XRT, I used a single power law/several power law segments to estimate the X-ray flux at 11 hours post-trigger from the X-ray afterglow data. X-ray flux values at 11 hours (henceforth just 'X-ray flux') estimated at $< 10^{-14}$ erg cm^{-2} s^{-1} were omitted, as they were deemed too faint for *Swift* to detect in practice. In total, I obtained X-ray fluxes for 824 BAT and 33 IBAS GRBs.

3.4.1 Statistical analysis of the GRB samples

I performed a two sample Kolmogorov-Smirnov (K-S) test on the BAT and IBAS ($20 - 200$ keV) fluence and X-ray flux values. The test can indicate if the two GRB populations arise from the same underlying distribution. The K-S statistic is defined by the following
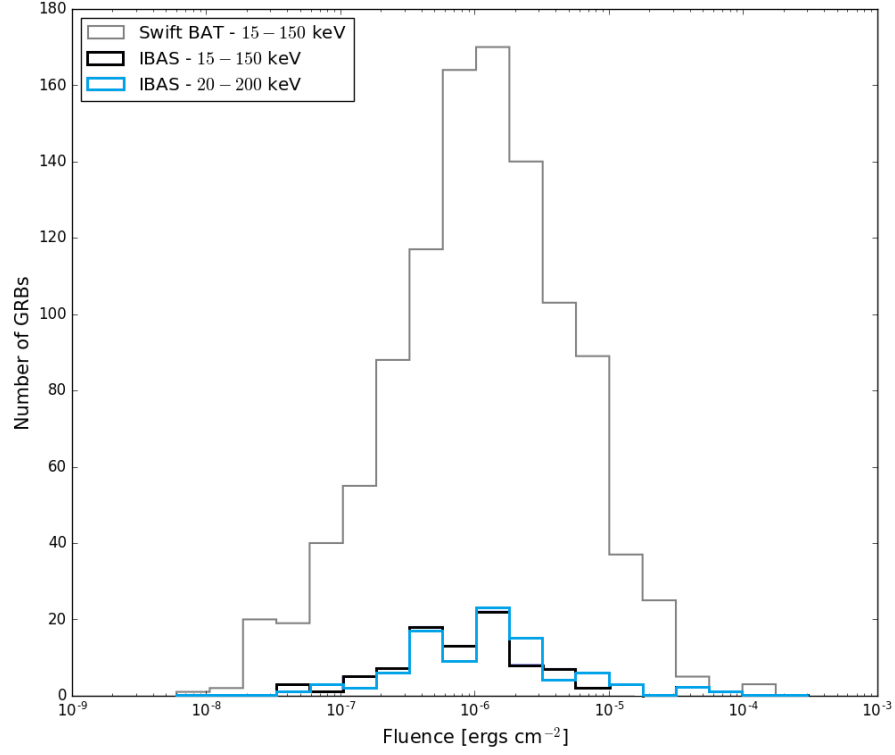
Figure 3.11: Fluence distributions of the *Swift*/BAT and IBAS GRB samples.

relation

$$D_{n,m} = \max |F_m(x) - F_n(x)| \tag{3.1}$$

where $D_{n,m}$ is the two sample K-S statistic, and $\max$ is the maximum separation of sets of differences between two empirical distribution functions, $F_n(x)$ and $F_m(x)$, which in my case represent the BAT and IBAS GRB samples. The BAT and IBAS GRB sample empirical distributions can be defined as

$$F_n(x) = \frac{1}{n} \sum_{i=1}^{n} I(x_i \le x) \tag{3.2}$$

where $F_n(x)$ is the empirical distribution function of a sample with n independent and ordered data points (GRBs), and $I(x_i \le x)$ is the indicator function. The probability of the two GRB populations arising from the same underlying population can be derived at various confidence levels using the following relation

$$D_{n,m} > C\sqrt{\frac{1}{n} + \frac{1}{m}} \tag{3.3}$$

77

where if the above inequality is satisfied, then the null hypothesis is rejected and the two distributions are not drawn from the same underlying distribution at the given confidence level. $C(\alpha)$ is a numerical representation of the confidence interval one would test. For the following tests, I chose to reject the null hypothesis at a 95% confidence level ($p = 0.05$) so $C = 0.136$.

I produced a PYTHON3 script to perform the K-S test on the IBAS and BAT fluence distributions, utilising the SCIPY (Jones et al., 2001) package[10]. The returned K-S statistic did not fulfill the inequality in equation 3.3, and was equivalent to $p = 0.37$. I could not reject the null hypothesis and I concluded that the IBAS and BAT GRB samples belong to the same underlying distribution. Moreover, the mean fluence values of the distributions are very similar in value; 3.66×10^{-6} erg cm^{-2} and 3.94×10^{-6} erg cm^{-2} for the BAT and IBAS GRB samples. Converting the IBAS fluence values into the $15 - 150$ keV energy range using the flux ratio of 1.22, I calculated a mean of 3.23×10^{-6} erg cm^{-2}. The K-S statistic between the BAT fluence distribution also did not satisfy the inequality and was equivalent to $p = 0.06$ resulting in the same conclusion.

I additionally tested for correlations between GRB fluence, T$_{90}$ and X-ray flux at 11 hours for both GRB samples using the Spearman rank test. The Spearman rank coefficient is defined as

$$r_{sp} = \sum_{i=1}^{n} \frac{\mathrm{cov}(rg_x, rg_y)}{\sigma_{rg_x} \sigma_{rg_y}} \qquad (3.4)$$

where $\mathrm{cov}(r_x, r_y)$ represents the covariance between GRB properties x and y in a sample $g(x, y)$, that has been order ranked by property x and is of size n, and σ_{rg_x} and σ_{rg_y} represent the standard deviation on the ranked properties r_x and r_y. The standard error on r_{sp} is given by

$$\sigma_{r_{sp}} = \frac{0.6325}{\sqrt{n-1}}. \qquad (3.5)$$

I tested for two correlations at the 3σ ($p = 0.0027$) level; fluence vs T$_{90}$ and fluence vs X-ray flux. For fluence vs T$_{90}$, I calculated r_s to be $0.52(\pm 0.07)$ and $0.66(\pm 0.02)$ for the IBAS and BAT GRB samples with associated p-values of 5.7×10^{-8} and 3.8×10^{-130}. These

---

[10]https://www.scipy.org/

results suggest that the correlations are both real and significant. For fluence vs X-ray flux, I calculated r_s to be $0.65(\pm0.11)$ and $0.61(\pm0.02)$ for the IBAS and BAT GRB samples with associated p-values of 2.4×10^{-5} and 3.96×10^{-90}. Again the test results suggest that the correlations between parameters are both real and significant. Earlier investigations have found similar correlations (Gehrels et al., 2008; Evans et al., 2009; Margutti et al., 2013; Grupe et al., 2013). I acknowledge that I see a fairly large variance in the data. A number of reasons could have contributed to this; lack of confidence intervals on IBAS T_{90} values and extrapolated values of X-ray flux, for example. Even with such areas of uncertainty, I conclude that the correlations are real and agree with previously reported results.

Figure 3.12 illustrates that all XRT X-ray afterglows of the BAT GRB sample, overplotted with all XRT observed IBAS afterglows. The entire IBAS sample sits comfortably within the BAT distribution. The mean X-ray flux at $11\,\text{hours}$ is $2.85 \times 10^{-12}\,\text{erg}\ \text{cm}^{-2}\ \text{s}^{-1}$ and $1.48 \times 10^{-12}\,\text{erg}\ \text{cm}^{-2}\ \text{s}^{-1}$ for the IBAS and BAT samples, respectively. The X-ray flux of the BAT sample is, on average, lower, but I also highlight that only 54 GRBs in the IBAS sample have available XRT data. Further to this, only 33 GRBs has sufficient XRT data to derive an X-ray flux at 11 hours.

I conclude that *Swift* and *INTEGRAL* regularly detect similar fluence GRBs. *Swift*/BAT detects a higher portion of SGRBs which are, on average, less luminous than LGRBs. This could in part be due to the differences in detection algorithms running for BAT and IBAS. The BAT GRB sample is $\sim 10\times$ larger than the IBAS sample, which may partly explain the short BAT GRB tail and the low number of SGRBs in the IBAS sample. I concluded from the above analysis that the BAT and IBAS GRB distributions are similar but are not identical.

3.5   Conclusions

15 *INTEGRAL* WEAK, sub-threshold alerts were analysed and followed up using *Swift* XRT and UVOT ToO observations. Of the 15 alerts, seven astrophysical events were discovered,
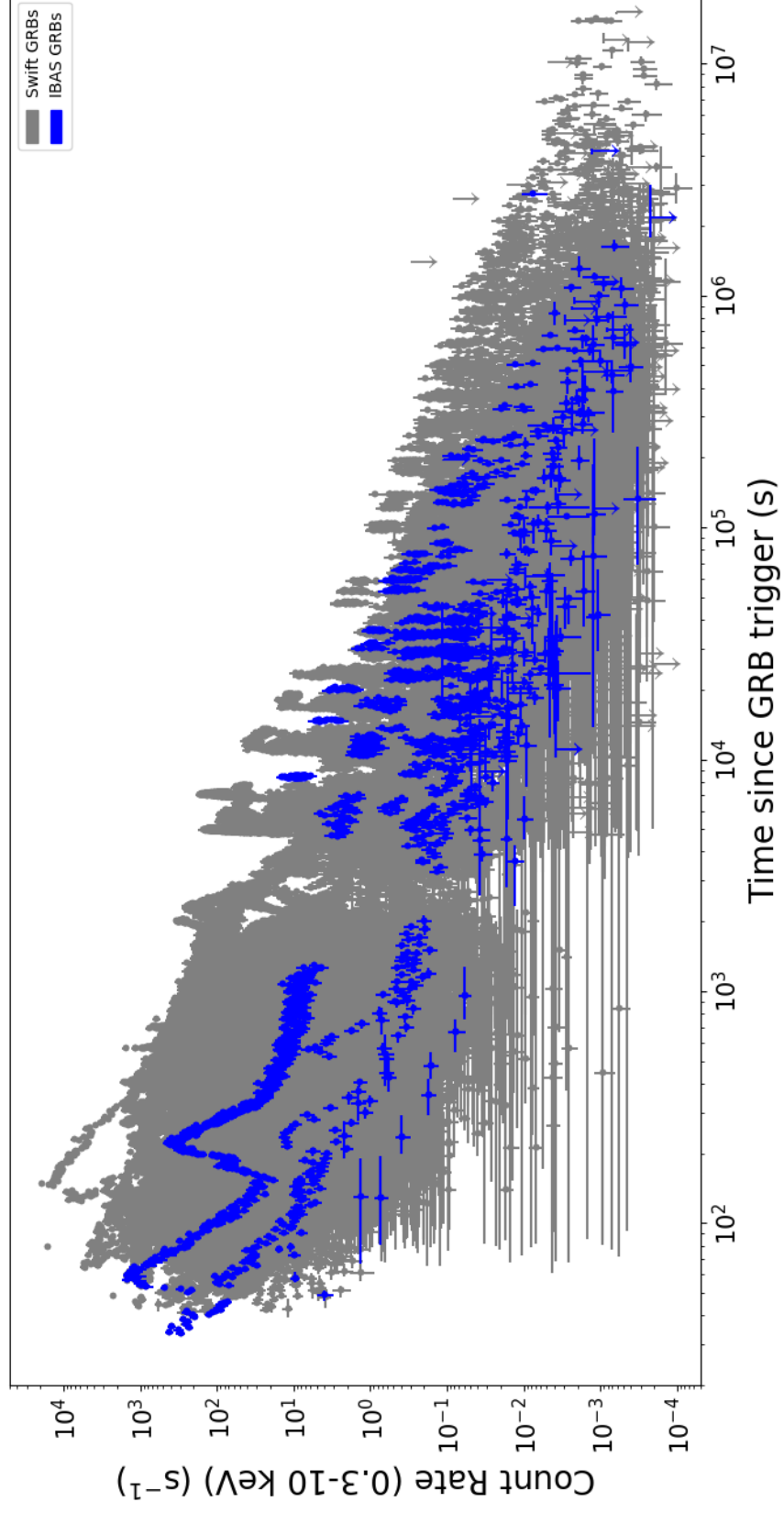
Figure 3.12: All XRT afterglows of the BAT (grey) and IBAS (blue) GRB samples.

six GRBs (one of which was short) and one candidate AGN. One of the GRBs discovered, IGRW/GRB 150305A, was confirmed directly from the XRT ToO observations, and was not observed with any other space or ground based observatory.

I also investigated whether *INTEGRAL* could detect a local population of low luminosity GRBs. I compared the fluence distributions of the IBAS and *Swift*/BAT GRB samples and concluded that the GRB fluence distributions were similar but not identical. I also tested for correlations between GRB properties. I found real and significant correlations between the gamma-ray and X-ray properties of both the IBAS and BAT samples, which were in agreement with similar correlations presented in previous investigations. The IBAS GRBs with XRT detected afterglows comfortably sat within the XRT distribution of the BAT GRB sample. In conclusion, *Swift* and *INTEGRAL* appear to detect and observe GRBs at similar fluence levels, with BAT appearing to be more sensitive to the detection of SGRBs.

This investigation has shown that real astrophysical events exist within the *INTEGRAL* WEAK alert population. Future investigations into follow-up of sub-threshold triggers may provide the evidence of a local, low-luminosity GRB population.

4

The SPLOT survey

4.1 Introduction

This chapter focuses on a Snapshot survey for Polarised Light in Optical Transients (SPLOT). This pilot survey utilised linear optical polarimetry to follow-up transients and determine whether polarimetry, as an independent tool, can add scientific value, or pick out sources of scientific interest from public transient alert streams. The survey was published in MNRAS (Higgins et al., 2019b).

Cosmological transients are observed at all wavelengths, ranging from low frequency radio to high energy gamma-rays emission, and with various lifetimes and variability timescales.

The number of transients discovered in the last decade has increased significantly thanks to a number of facilities whose primary aims are to observe the sky at optical wavelengths and detect new transient phenomena. Currently active missions include, but are not limited to

- the Mobile Astronomical System of Telescope-Robots (MASTER; Lipunov et al. 2004),

- the All Sky Automated Survey for SuperNovae (ASAS-SN; Shappee et al. 2014),

- the *Gaia* satellite (Gaia Collaboration et al., 2016),

- the Panoramic Survey Telescope and Rapid Response System (Chambers et al. 2016d; Pan-STARRS),

- the Optical Gravitational Lensing Experiment IV Transient Detection System (OGLE-IV; Wyrzykowski et al. 2014),

- the Zwicky Transient Facility (ZTF; Kulkarni 2016),

- the Gravitational-Wave Optical Transient Observer (GOTO)[11].

GRBs exhibit optical counterparts in $\sim 30\%$ of cases (see Section 1.5.5). These are often quickly-fading and require rapid follow-up. GOTO is specifically designed to provide swift optical follow-up to GW detections or GRB triggers, potentially observing GRB optical emission. However, the rate of observable GRBs (with optical afterglows) as a percentage of the total optical transient detections per night is low. Therefore, the SPLOT survey was not focused on GRB follow-up, but covered a whole host of transient phenomena.

Prior to ZTF coming online, $\sim 1 - 10$ new optical transients were detected per night. Since ZTF began observing (after the SPLOT survey observations finished), the rate of detected transient candidates has dramatically increased[12]. The number of transient detections will further increase when the optical Large Synoptic Survey Telescope (LSST; Ivezic et al. 2008) begins observations in 2020.

---

[11]https://goto-observatory.org/

[12]The LASIR broker provides an alert list: https://lasair.roe.ac.uk

Most surveys provide discovery alerts with accompanying photometry data. Photometry alone does not provide enough information to enable the filtration of potentially important or interesting new target sources. Some additional follow-up data is usually required to enable this. The most common follow-up tool is spectroscopy, providing flux information over a range of wavelengths, but obtaining good quality spectra often takes a significant amount of observing time and cannot be used on all new transients when the number of newly discovered sources per night increases.

Therefore, the ability to quickly filter and highlight the most scientifically interesting transient sources from survey alert streams, in (relatively) near real-time, is crucial. This has been attempted using spectroscopy for large programmes (i.e. the PESSTO survey at La Silla, Chile; Smartt et al. 2015). However, in addition to the huge time commitment to these spectroscopic surveys, there are a significant number of interesting transient phenomena that may not be easily distinguishable from astrometry, or low resolution spectroscopic features alone. The use of linear polarimetry may be able to independently assist with highlighting these sources of potential interest.

Below, I cover the use of linear polarisation in observing astrophysical sources, the survey outline and target selection for SPLOT and observations followed by the analysis and results of the SPLOT survey.

4.2   Linear polarimetry

Polarisation is a fundamental property of EM radiation (Rybicki & Lightman, 1979). A plane EM wave is linearly polarised, defined by the direction of oscillation of the electric field vector. If a photon is propagating towards the observer in the direction, z, and the time dependent electric field components in the x and y directions, $E_x(t)$ and $E_y(t)$ are defined as

$$E_x(t) = E_x(0)\cos(\omega t)$$
$$E_y(t) = E_y(0)\sin(\omega t)$$

(4.1)
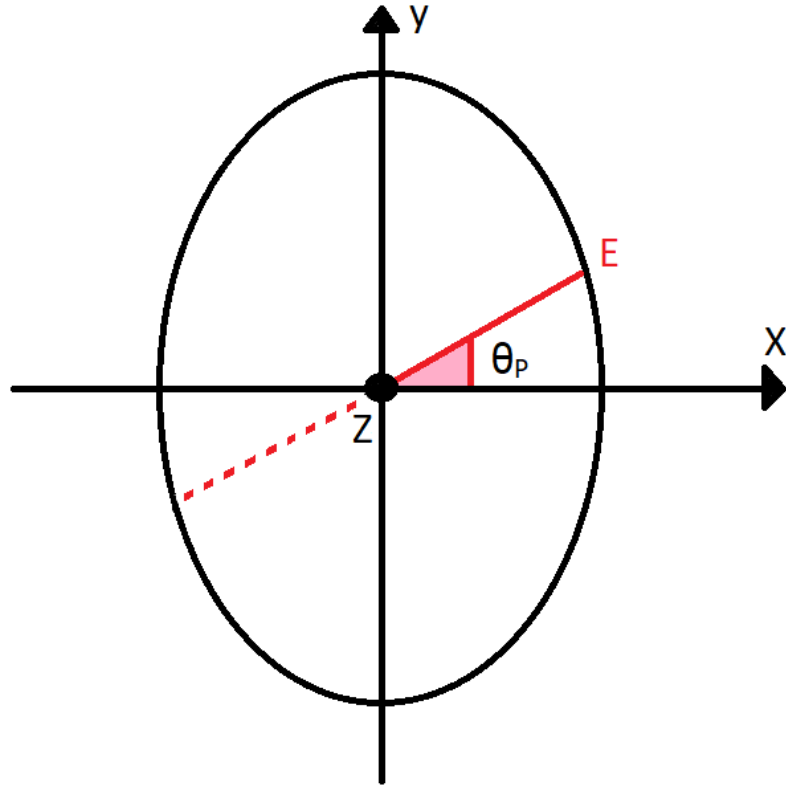
Figure 4.1: Illustration of the orientation of linear polarisation in plane EM waves. The propagation of the wave is coming out of the figure towards the reader.

where ω represents the angular frequency (Trippe, 2014), then the orientation of the linear polarisation, defined by the polarisation angle is given by

$$\theta_P = \arctan\left[\frac{E_y(t)}{E_x(t)}\right].$$ (4.2)

Figure 4.1 illustrates the linear polarisation of a plane wave. If a source is unpolarised, the orientation of the light received from the source will not favour a particular orientation of the electric field, on average. Linear polarisation of a source exists when the received light does prefer a particular orientation.

4.2.1 Linear polarimetry in transients

The physical environments of astrophysical transients are both extreme and complex. Intrinsic linear polarisation from observations can help decipher the complex geometry and magnetic field configuration of regions with optical emission (Trippe, 2014).

The emission of many transients is powered by non-thermal mechanisms, such as synchrotron emission from relativistic electrons. Synchrotron emission is intrinsically polarised. The polarisation for synchrotron particles can be characterised by the radiation power per unit frequency, both in the directions parallel and perpendicular to the direction of the magnetic field. Over the entire synchrotron spectrum, the (max) degree of linear polarisation for uniform field lines can be calculated using the following relation

$$P \sim \frac{p+1}{p+\frac{7}{3}} \qquad (4.3)$$

where p is the electron energy distribution spectral index (Rybicki & Lightman, 1979). In reality, the degree of linear polarisation from synchrotron is lower.

GRBs, some of the most explosive and luminous events in the universe, are powered by non-thermal emission (see section 1.3 for a full discussion). Synchrotron emission is the main mechanism powering GRB afterglow emission, ranging in wavelengths from the very low energy (radio) to the high energy (X-ray), and potentially the prompt emission. Therefore, they should exhibit polarisation. Previous investigations have shown that both GRB jet and afterglow emission is both linearly and circularly polarised (Wiersema et al., 2012a, 2014; Covino & Gotz, 2016). Similarly, relativistic jet emission in phenomena such as X-ray binaries (XRBs) should also exhibit linear polarisation (Russell & Fender, 2008)

AGN, galaxies with a very luminous central nucleus, are thought to be powered by accretion onto a supermassive BH (Hoyle & Fowler, 1963; Salpeter, 1964; Zel'dovich, 1964; Lynden-Bell, 1969). Observations confirming the existence of supermassive BHs at the centre of a number of galaxies provided evidence for this (see Kormendy & Ho 2013 and references within). The accretion mechanism accelerates particles to relativistic speeds. This results

in synchrotron emission which powers the lower energy (radio, microwave, infrared and optical) emission in AGN/Blazars. As discussed above, synchrotron emission exhibits linear polarisation and so AGN emission can be linearly polarised (Trippe, 2014).

SN are short-lived, powerful thermal explosions related to the death of stars. SN primarily arise from two progenitors. The first occurs when the core of massive stars ($\gtrsim 8\,\mathrm{M_\odot}$) collapses as radiation pressure cannot counterbalance the gravitational force (Woosley & Weaver, 1986; Bethe, 1990) and the star contracts. Type Ia SN are produced when a white dwarf star exceeds the Chandrasekhar limit via mass transfer from a donor star (Hillebrandt & Niemeyer, 2000). Electron degeneracy pressure cannot counterbalance gravitational collapse and the star contracts. In both cases, the gravitational collapse results in an increase in internal pressure and temperature, leading to a runaway thermonuclear reaction, the expulsion of the outer layers, and the release of a huge amount of energy. SN are classified via the presence (or absence) of elements in their spectra. For example, type I SN spectra exhibit no hydrogen lines whilst type II SN spectra do (Turatto, 2003).

Core-Collapse SN can exhibit significant levels of intrinsic linear polarisation if the explosion expels the ejecta asymmetrically (Shapiro & Sutherland, 1982; Wang et al., 1997; Wang & Wheeler, 2008). The polarisation arises due to Thompson scattering. On the other hand, multiple observations of the the continuum light of type Ia SN have shown that they exhibit little to no ($\lesssim 0.3\%$) linear polarisation (Wang et al., 1996; Wang et al., 1997; Wang & Wheeler, 2008). However, multiple measurements of significant levels of linear polarisation from type Ia SN in optical bands have been detected (e.g. SN2014J; Kawabata et al. 2014), probably caused by line-of-sight dust scattering the photons emitted by the SN. The dust induced polarisation arises as a result of linear dichroism in non-spherical dust grains, which are somewhat aligned with by large-scale magnetic fields. The extinction values differ depending on the cross-sectional area of the dust axes and this difference induces the linear polarisation. This dust contribution could be localised to the vicinity of the SN host. Therefore, type Ia supernova measurements of linear polarisation could be utilised to probe the local environment of SN progenitors. Linear optical polarimetry has been used to successfully follow-up numerous SN in the past (Wang & Wheeler, 2008) and a several investigations have shown that spec-

tropolarimetry can provide information on the geometry of SN (i.e. Maund et al. 2009; Reilly et al. 2017; Stevance et al. 2017).

If a stars orbit comes into close proximity to a BH, the tidal forces disrupt the star and some stellar material is accreted onto the BH, resulting in a TDE (Lacy et al., 1982; Rees, 1988). In recent time, numerous TDE candidates have been observed with thermal spectra (Komossa, 2015). However, three TDEs; *Swift* J1112.2−8238 (Brown et al., 2015), *Swift* J1644+57 (Bloom et al., 2011; Burrows et al., 2011) and *Swift* J2058+0516 (Cenko et al., 2012; Pasham et al., 2015) have been observed with accompanying relativistic jets, exhibiting non-thermal emission. Only one previous measurement of linear polarimetry for a TDE has been made. The source observed was *Swift* J1644+57, with $P = 7.1(\pm3.5)\%$ in the near-infrared, Ks filter and radio 3σ upper limits as constraining as $P < 2.1\%$ at $4.8\,$GHz (Wiersema et al., 2012b).

4.3 The SPLOT survey

The SPLOT survey was undertaken to investigate the feasibility of linear polarimetry as a independent tool to add scientific value and filter out transients of scientific interest from survey streams of optical transient, in near real-time. The astrophysical sources discussed in section 4.2.1 can all exhibit a range of observed linear polarisation behaviour, dependent on both the physics of the target and the environment or line-of-sight dust. Transient sources exist in a large volume of observable parameter space. Figure 4.2 illustrates the scale of absolute magnitudes and typical intrinsic linear polarisation values transients can exhibit over their physical time scales.

If you include additional observational parameters such as multi-wavelength follow-up, source colours, host galaxy information and more, the volume of this multi-dimensional observable parameter space becomes vast. Spectroscopy, arguably the most crucial analytical tool for understanding the nature of transients, may not highlight all sources of interest within this large
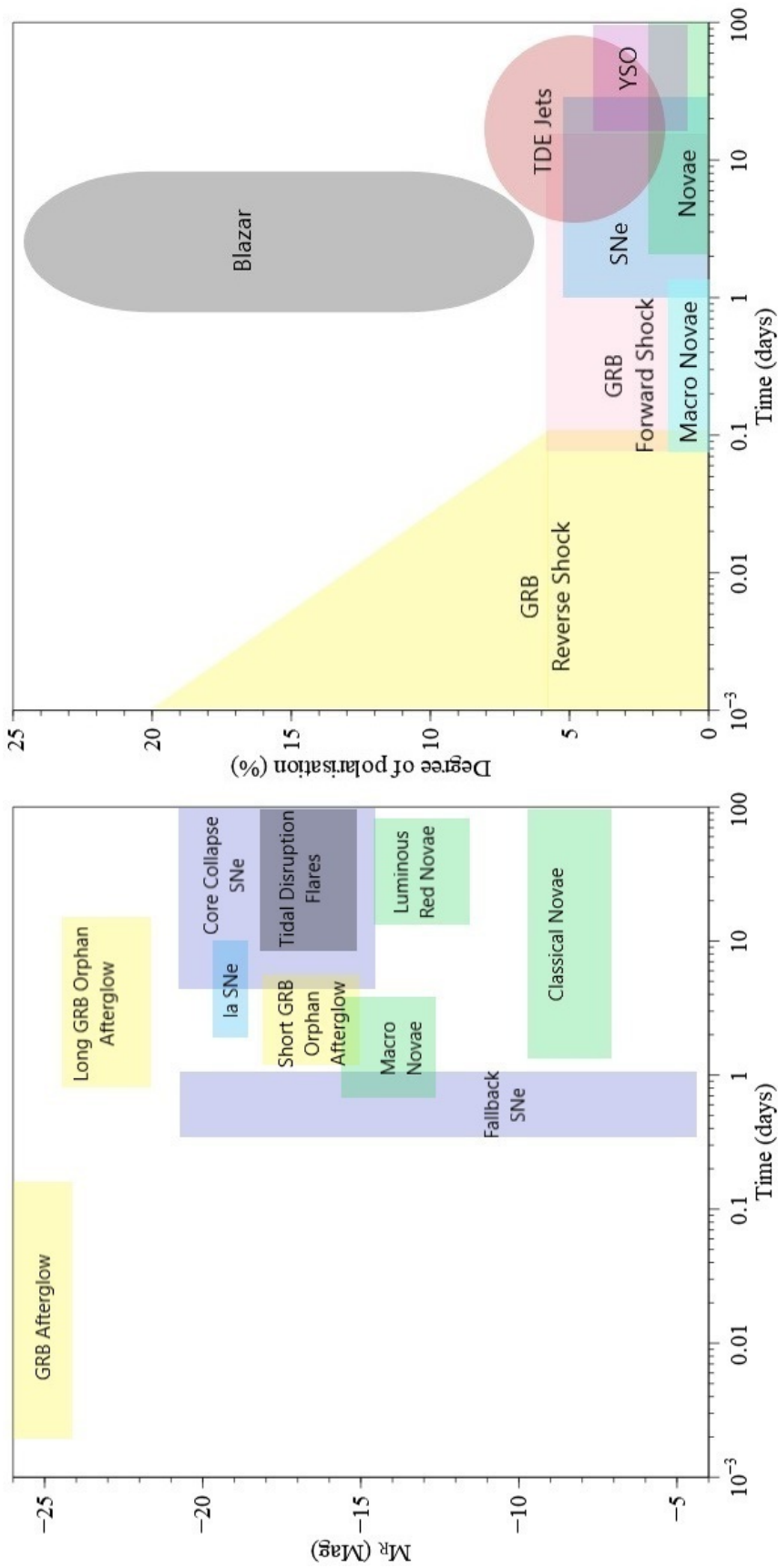
Figure 4.2: Illustration of the parameter space of optical transient absolute magnitudes (left) and previously observed linear polarisation detections (right), both plotted with the typical physical time scales. This represents the projected volume of parameter space that SPLOT will cover. The current statistics on some transient phenomena are very limited to a couple of measurements (e.g. TDEs discussed in Section 4.2.1). This figure taken from Higgins et al. (2019b).

volume of properties. This is where a pilot survey like SPLOT can test the feasibility of linear polarimetry to independently access areas of this observable space and aid in highlighting potential sources of astrophysical interest.

As discussed in section 4.2.1, SN have been followed up using polarimetry for many years. However, for other classes of transients, only a very limited number of polarimetric measurements exist (e.g. relativistic TDE; Wiersema et al. 2012b, Macronova; Covino et al. 2017). To address this, some fraction of the SPLOT survey was made available to follow-up any potentially rare transient sources, to improve the currently very limited sample sizes. Below, I have highlighted the main aims of the SPLOT survey:

- Observe a range of transient classes from a host of transient survey streams. This would enable the coverage of a large surface area of the absolute magnitude and linear polarimetric parameter space.

- Investigate the feasibilility of a SPLOT-like survey, and the effects of practical constraints such as weather, instrument calibration on the overall success of the survey.

- Provide polarimetric measurements to a sufficiently high precision ($\sigma_P \sim 0.2\%$). This would ensure that each source could be discussed individually and, as a number of transient classes have intrinsic polarisation signals $< 1\%$, a high level of precision is required to recover the polarisation signal.

- If possible, investigate and/or quantify the level of Galactic dust induced polarisation.

4.4 Observations

This section covers the observations of the SPLOT survey, including telescope choice, instruments, filters and source selection.

4.4.1 Choice of telescope, instrument and filters

The following points describe a set of target criteria. These were set to help guide the choice of telescope and instrument needed to fulfil the goals set out for the SPLOT survey. The criteria were:

- Reach sensitivity levels ~ 20 mag. It is typically at these brightnesses where you begin to sample the less common transients, especially if they reside outside of the Milky Way (Rau et al., 2009).

- Obtain polarimetric measurements with sufficient accuracy for the brightest sources ($\sigma_P \sim 0.2\%$) although for the faintest sources the uncertainties may increase to $\sigma_P \sim 0.5\%$.

- Observe ~ 50 transients.

- Ensure that we can execute each observation in < 1 hour, with the majority of observations much shorter than this.

The telescope chosen for the SPLOT survey was the European Southern Observatory (ESO) 3.6 m New Technology Telescope (NTT) at La Silla, Chile. The primary two instruments, mounted on separate Nasmyth mounts, on-board the NTT are the ESO Faint Object Spectrograph and Camera v2 (EFOSC2; Buzzoni et al. 1984) and the Son Of ISAAC (SofI; Moorwood et al. 1998) both of which have favourable field of views for transient astronomy and can perform both imaging and polarimetric observations in short intervals (see ESO 2016a and ESO 2016b for full design information on EFOSC2 and SofI, respectively). Campaigns such as the SN survey ePESSTO[13] (Smartt et al. 2015) have shown that using the NTT for large scale, follow-up, transient astronomy surveys can be very successful by utilising "visitor mode" at the NTT; where astronomers travel to the telescope and undertake observations in-situ. The size of the primary mirror, 3.6 m, is sufficient to observe transients as faint as 20 mag in the required execution times. To observe a sufficiently large number of sources,

---

[13]http://www.pessto.org

the majority of observations would be single epoch (subsequently referred to as "snapshot") observations, meaning that most sources would only be observed once.

The SPLOT survey was split up into the following observing runs:

R1: Five observing nights were allocated for SPLOT, running over the period of 2016 June $19 - 20$ and June $22 - 24$. The visiting observers were myself and Klaas Wiersema. Due to poor weather conditions, only data on June 19, 20 and 22 were obtained. EFOSC2 was used for the observations.

R2: Three observing nights were allocated for SPLOT, running over the period of 2017 August $7 - 9$. Klaas Wiersema was the sole observer for this run. The rotator encoder for the Nasmyth platform on which EFOSC2 instrument is mounted failed before the second observing run started. Consequently, Klaas had to use SofI for the observations. Due to poor weather conditions on the third night, only data on August 7 and 8 were obtained.

R3: Three further nights were allocated to SPLOT, running over the period of 2018 August $5 - 7$. I was the sole observer for this run. EFOSC2 was used for this run and data were obtained on all three nights. The polarimetric data for this third observing run have not been fully analysed yet and were not included in the first SPLOT paper (Higgins et al., 2019b). Therefore, I will not discuss the sources observed from this run in this chapter.

For the primary snapshot observations undertaken during SPLOT, the *V* (ESO #641) filter ($\lambda_{peak} \sim 550\,\text{nm}$) was chosen for the EFOSC2 observations. The justification for this filter was that it is similar to the primary bands of ASAS-SN, *Gaia* and MASTER. making the job of estimating source magnitudes at observing times less complex. It also coincided with the (near) peak, CCD response efficiency of the EFOSC2 instrument. Polarisation measurements taken during SPLOT comprise of three individual components. The first component represented the intrinsic polarisation level of the target, which arises from the internal physics and geometry of the source. The second and third contributions represented the polarisation signal arising from dust scattering in the Milky Way and within the environment of the

source, respectively. As the V filter is close to peak wavelength for the polarisation signal from Galactic dust scattering (Serkowski et al., 1975), it would be difficult to confidently quantify the three contributions individually without using more than one filter. To partially account for this, some targets were also observed in the B (ESO #639) and R (ESO #642) filters. Some sources that appeared interesting were also observed more than once in the V filter to determine any time-dependent polarisation behaviour. For R2, where SofI was used instead of EFOSC2, target sources were observed in the Z filter ($\lambda_{peak} \sim 900\,\mathrm{nm}$), the shortest wavelength infrared filter mounted on SofI .

Several SPLOT transients were observed at much later times, sometimes > 50 days, using the University of Leicester 0.5 m telescope (UL50)[14]. The telescope is a Planewave CDK20 [15], a 0.5 m telescope of corrected Dall-Kirkham design. Observations were taken with broadband Johnson-Cousins B and V filters. The UL50 cannot perform polarimetric observations so the telescope was used to obtain additional photometry. Observations with this telescope were taken by Klaas Wiersema.

4.4.2 The SPLOT sample

Target sources that were observed as part of the SPLOT survey were taken from, but not limited to, the following near real-time public alert systems:

- The Transient Name Server (TNS)[16]

- The *Gaia* alerts system[17]

- Astronomers Telegrams (ATels)[18]

---

[14]Located in Oadby village, Leicester, UK

[15]planewave.com

[16]https://wis-tns.weizmann.ac.il

[17]http://gsaweb.ast.cam.ac.uk/alerts/home

[18]http://www.astronomerstelegram.org

- GCN Circulars[19]

The nature of SPLOT was to use polarimetry as an independent tool to highlight sources of interest, source selection was conducted without a confirmation of transient class via spectroscopic follow-up for an object to enter our list of possible targets. Transients here not only refer to the new, short lived events, but also previously observed variables that may have produced alerts from new outbursts. This was to ensure that the the alert selection was non-restrictive. The main physical constraints on choosing a transient to observe were assuming it could also be observed in La Silla, was that the source could be observed for $\gtrsim 30$ minutes at airmass < 2, that the initial alert for the source had been released within the last six months and that the estimated brightness at the time of observing was $> 20 - 21$ mag. To build up a list of targets to observe I constantly reviewed the above transient alert systems for newly released transient detections. The coordinates and discovery magnitudes were checked for each source to ensure it fit the observing criteria. The targets were then fed into software application *iObserve*[20] (either the iOS application or website version) which provides information on the source such as altitude, Moon distance and parallactic angle (PA) to aid in construction of a nightly observing timetable. During R1 the *Gaia* alerts system was not available. This resulted in a number of older transients being observed over the three nights, where older refers to alerts or detections at an earlier date.

ESO Observing Blocks (OBs) were created using the software P2PP[21]. An OB was created for every new alert that fit the observing criteria, often on the fly and during the observing night. A set of reserve targets, typically older targets, were prepared during the previous day in case too few appropriate targets were detected in real-time. As the observing runs occurred during the Chilean winter, often patches of adverse weather conditions were present during the nights. Poor seeing, high winds and thicker cloud coverage meant that the faintest sources would require much longer execution times or were hit with larger measurement systematics. Strong winds from North of La Silla placed restrictions on the pointing direction of the NTT, typically

---

[19]https://gcn.gsfc.nasa.gov/gcn3_archive.html

[20]onekilopars.ec/iobserve/

[21]https://www.eso.org/sci/observing/phase2/P2PPTool.html

with restricted declinations of $\lesssim -30°$. Northern based surveys such as PanSTARRS seldom detected sources at such low declinations, so additional reserve OBs using targets from other transient streams with lower declinations were also created.

Over the first two runs, 48 optical transients and 8 standard stars, 3 polarised and 5 unpolarised, were observed. Images of all transients observed during SPLOT are illustrated in Figure 4.3. The standard stars were used for the EFOSC2 and SofI data calibration, which is discussed in detail in Chapter 5.
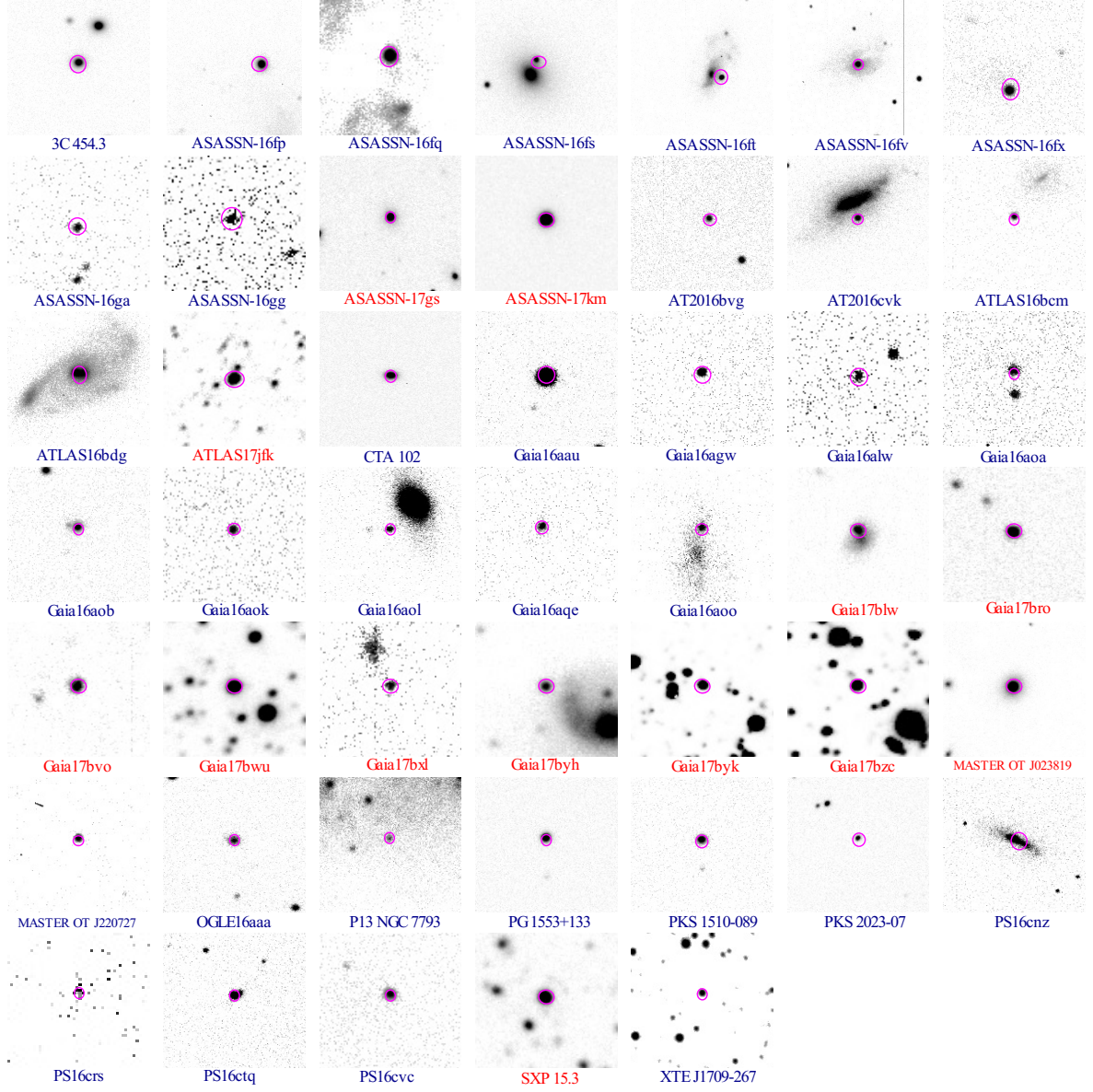
Figure 4.3: Images of the SPLOT sample sources. The image for GX 304-1 was saturated and not included in this mosaic. The images are purely to illustrate each source within their local environments and are not to be analysed. Images for EFOSC2 targets were taken in *V* band (blue) and in *Z* band (red) for SofI targets.

4.5 Polarimetry Measurements

In this section I cover the full polarisation data reduction and analysis of the EFOSC2 and SofI data (from the first two observing runs). The polarimetric data reduction, photometry and analysis described below was performed using PYTHON3 scripts I developed. EFOSC2 sample scripts for each of the above are available on my GitHub page[22]. A SofI data analysis script is available from me by request.

4.5.1 Polarimetric setup

The EFOSC2 polarimetric observations were conducted using a Wollaston prism, with a separation of 20 arcsec ("Woll_Prism20"), in conjunction with a half-wave plate. As light from a source enters the instrument, it passes through the half-wave plate, filtering the light. The filtered light then passed through the prism and is split into two beams, the ordinary o and extraordinary e, which are orthogonally polarised, and then reaches the CCD. A thin mask ("WollMask=") was placed between the two beams to ensure the two images (one produced per beam) did not overlap and complicate the analysis. The Wollaston prism and mask were mounted parallel to the CCD x-axis. An example image produced using the above setup is illustrated in Figure 4.4. The half-wave plate was rotated through four angles for each observation; 0 deg, 22.5 deg, 45 deg and 67.5 deg. Utilising four half-wave plate angles, instead of two, results in better polarimetric accuracy (Patat & Romaniello, 2006). Myself and Klaas decided arbitrarily to follow the convention of having the o beam as the top image and e beam as the lower image for EFOSC2 (see Figure 4.4). Using the opposing convention has no effect on the analysis and provides identical polarisation measurements. This is discussed in detail below.

SofI is constructed in a different way to EFOSC2. Although SofI similarly uses a Wollaston prism to split the incoming light, it does not have a half-wave plate. Instead, the angles

---

[22]https://github.com/abh13/EFOSC2_Scripts
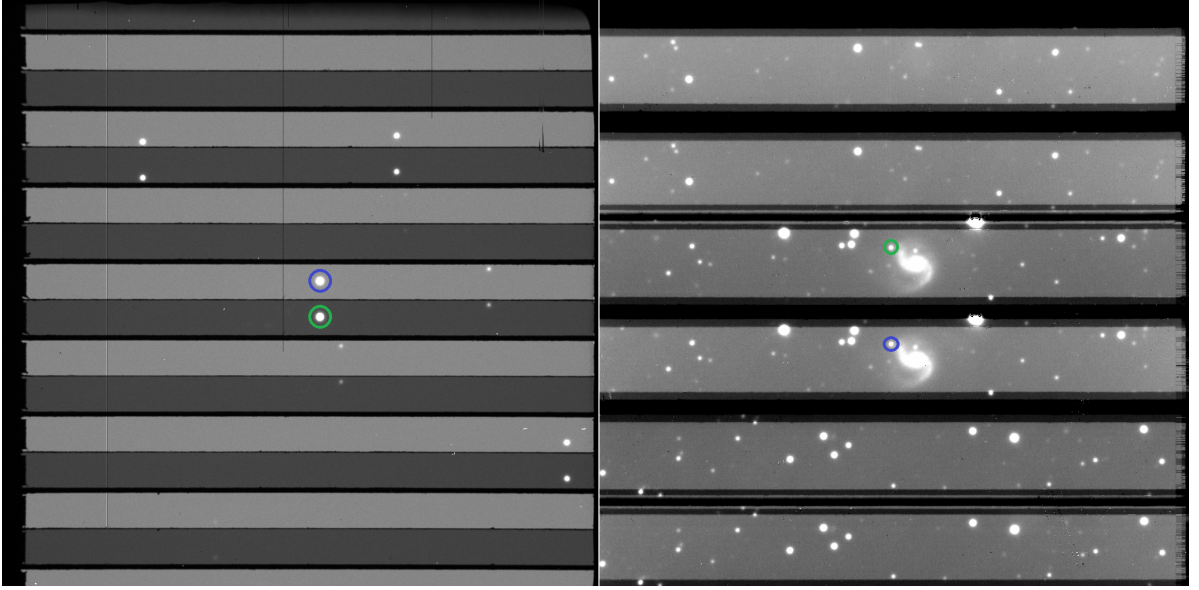
Figure 4.4: Polarimetric image of sources 3C454.3, taken with EFOSC2 (left), and Gaia17byh, taken with SofI (right), as part of the SPLOT survey. The images were taken with the half-wave plate (and instrument for SofI) at 0 deg. The two images represent the o beam (blue) and the orthogonally polarised e beam (green). The thin mask can be seen separating the two image strips. The target source was also placed at the centre of the optical axis. The larger mask sizes seen with Gaia17byh is caused by the dithering between image integrations for SofI exposures (see Section 4.5). In both images, the background in the o and e beams exhibit differences in brightness due to the polarisation of the night sky from scattered moonlight.

were simulated by rotating the instrument by 0 deg, 45 deg, 90 deg and 135 deg. This was equivalent to the half-wave plate angles at 0 deg, 22.5 deg, 45 deg and 67.5 deg. SofI science images at each half-wave plate angle were not composed of a single integration like EFOSC2 images, but were produced from the average of five integrations, where the target source was dithered by a small amount for each integration (typically $\sim$ few arcsec). The incoming light is also not detected by an optical CCD but an infrared array. For SofI, the o and e beam image convention was flipped for SofI; e beam as the top image and o beam as the bottom image. The justification for this is discussed in Chapter 5 as part of the data calibration. As with EFOSC2, the beam convention has no effect on the polarimetric measurements.

I obtained a number of bias frames and polarimetric flat fields at the beginning of each ob-

serving night with EFOSC2. The polarimetric flats were created with the instrument pointed at the closed dome with the half-wave plate continuously rotating, ensuring that any polarisation signal from the instrument or dome light was scrambled. Custom OBs were generated to achieve this. The CCD readout was set to 'normal' mode in all of the observations and 2×2 binning was used for superior SNR. The CCD image scale in this binning mode was ~ 0.24 arcsecond per pixel. The gain and read noise of the CCD was calculated using the method described in Janesick (2001); 1.18 electrons per ADU and 11 electrons for the EFOSC2 CCD.

As Klaas was the sole observer for the second observing run, he obtained the SofI dark frames and polarimetric flat fields, using the 'Special Flat' dome algorithm which is described in ESO (2016b).

As EFOSC2 and SofI are mounted on Nasmyth platforms, observations are experience significant levels of instrumental polarisation dependent on the telescope pointing direction (Giro et al., 2003). This is accounted for by creating a physical model of the NTT configuration and using the observations of the previously discussed standard stars to produce a calibration pipeline. I discuss this in full detail in Chapter 5. Both instruments also exhibit non-zero polarisation when a source is observed away from the optical axis (Patat & Romaniello, 2006). Therefore, the target source was always placed on the same pixel for each observation. For EFOSC2, the pixel position was $x, y \sim 1100, 1016$ (1×1 binning) and $\sim 550, 508$ (2×2 binning), at the centre of the optical axis. This simple adjustment is required to minimise this effect. For SofI, small dithers (changes in position) were applied to each observation and so the position of the target sources were not fixed, but kept fairly close to the optical axis, and within the centre of a mask. The positions of the sources can be seen in Figure 4.4.

4.5.2   Raw data reduction

The raw data files were made available at the ESO Science Archive Facility[23].

---

[23]http://archive.eso.org/cms.html

Master bias frames: To create a master bias frame for EFOSC2 observations, I stacked together all of the raw individual bias frame fits files, downloaded from the ESO archive. I then calculated the mean and standard deviation of the counts per pixel through the stacked frames, and produced the final bias frame from this. Master bias frames were produced for each observing night.

Klaas reduced the master dark frames for the SofI observations.

Master flat frames: To create the master flat frame for EFOSC2 observations, I stacked together all of the raw individual polarimetric dome flat frame fits files, downloaded from the ESO archive. I then removed the master bias frame from each individual flat frame. I calculated the mean and standard deviation of the counts per pixel through the stacked frames (in a similar fashion to the master bias frame) to create a single stacked frame. I calculated the median of the stacked frame over the entire CCD and divided the stacked frame through by the median to create the master flat frame, to account for the variance in pixel sensitivity over the CCD. Master flat frames were also produced for each observing night.

Klaas reduced the master flat frames for the SofI observations.

Polarimetric science images: To create the reduced science images for the polarimetric EFOSC2 observations, I downloaded the target source raw fits file from the ESO archive, subtracted the master bias frame from the raw image and then divided through by the master flat frame.

Klaas reduced the raw science images for the SofI observations.

4.5.3 Polarimetric image photometry

For a given SPLOT target observed with EFOSC2, I created four reduced science image files, for each angle of the half-wave plate. In each reduced science file, I performed the photometry on the o and e beam images by utilising the PHOTUTILS package (Bradley et al., 2019). Firstly, I calculated the FWHM of the target source by fitting a Gaussian in the x and y dimensions and calculating the average number of pixels. A circular aperture was placed over the target source, typically $1.5\times$FWHM and a larger, rectangular annulus was placed in the local vicinity of the source to calculate a local background rate (see Figure 4.5).
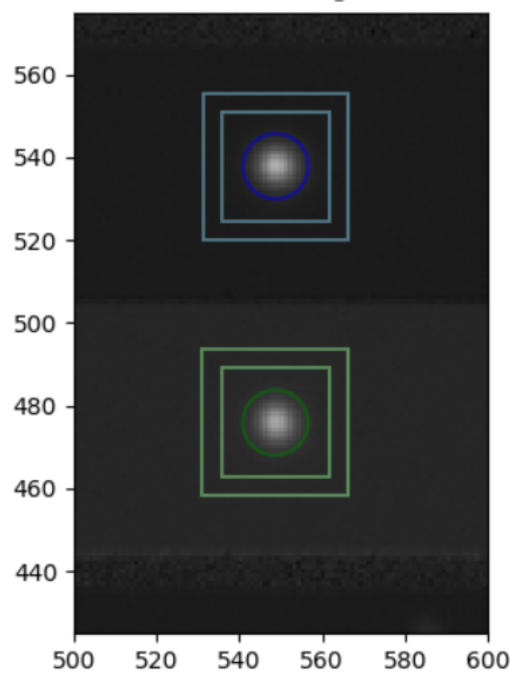
Figure 4.5: Zoom in of the reduced polarimetric image of 3C454.3, observed using EFOSC2 with the half-wave plate at $0\,$deg. The source aperture and background annuli can be seen for the o beam (blue) and e beam (green). The x and y axes show the pixel coordinates.

The number of counts (henceforth referred to as flux) for the source in the aperture area (background-subtracted), the background flux in the aperture area, the standard deviation of the background flux, and the area of both the source aperture and the background annulus for the ordinary and extraordinary beams, for each of the four half-wave plate angles, were

calculated and output to a text file.

The SofI photometry was obtained in a similar fashion to EFOSC2. The SofI background was more problematic than that for EFOSC2 images so the background subtraction was done locally, where possible, or estimated globally if this was too difficult. The data output to text files was equivalent to the EFOSC2 output outlined above but was performed using IRAF.

4.5.4 Data analysis

Once the photometry had been completed, I performed the polarimetric data analysis for both EFOSC2 and SofI observations. I calculated the standard error on the flux of each beam image using the following relation

$$\sigma_f = \sqrt{\frac{f}{\eta G N_{\text{depth}}} + A_{\text{ap}}\sigma_{\text{back}}^2 + \frac{\kappa(A_{\text{ap}}\sigma_{\text{back}})^2}{A_{\text{back}}}} \qquad (4.4)$$

where f is the background-subtracted flux of the source, G is the detector gain in electrons per ADU (1.1 for EFOSC2), $N_{\text{depth}} = 1$ is the depth of coverage A_{ap} is the area of the source aperture measured in pixels^2, σ_{back} is the uncertainty on the background flux per pixel, A_{back} is the area of the background region (annulus) measured in pixels^2 and $\kappa = 1$ represents the background-estimation method (Laher et al., 2012).

I then calculated the normalised flux difference, derived from the following relation

$$F_i = \frac{f_{o,i} - f_{e,i}}{f_{o,i} + f_{e,i}} \qquad (4.5)$$

where $f_{o,i}$ and $f_{e,i}$ is the flux of the o and e beams, at a given half-wave plate angle i (Patat & Romaniello, 2006). The error on the normalised flux difference was calculated as

$$\sigma_{F_i} = F_i\sqrt{\left(\frac{(\sigma_{f_{o,i}}^2 + \sigma_{f_{e,i}}^2)^{\frac{1}{2}}}{f_{o,i} - f_{e,i}}\right)^2 + \left(\frac{(\sigma_{f_{o,i}}^2 + \sigma_{f_{e,i}}^2)^{\frac{1}{2}}}{f_{o,i} + f_{e,i}}\right)^2}. \qquad (4.6)$$

To quantify the observed linear polarisation from the EFOSC2 observation, the polarisation could be derived using the Stokes vector notation, described by the following

$$[S] = [I, Q, U, V] \qquad (4.7)$$

where I represents the intensity of the source, Q and U represent the linear polarisation signal and V represents the circular polarisation signal (Chandrasekhar, 1960). Circular polarisation is not investigated with the SPLOT survey, and so it is subsequently ignored. For the rest of this investigation I will quote the normalised stokes parameters, defined as $q = Q/I$ and $u = U/I$.

The o and e beam fluxes are related to the Stokes Q and U parameters by

$$f_{o,i} = \frac{1}{2} [I + Q\cos(4\theta_i) + U\sin(4\theta_i)]$$
$$f_{e,i} = \frac{1}{2} [I - Q\cos(4\theta_i) - U\sin(4\theta_i)]$$

(4.8)

where θ_i is the half-wave plate angle. The normalised flux difference can then be rewritten as

$$F_i = q\cos(4\theta_i) + u\sin(4\theta_i).$$

(4.9)

Using half-wave plate angles of $\Delta\theta = \pi/8$, as described in section 4.5.1, I can derive the following expressions for q and u using the normalised flux differences above

$$q = \frac{2}{N} \sum_{i=0}^{N-1} F_i \cos\left(\frac{i\pi}{2}\right)$$
$$u = \frac{2}{N} \sum_{i=0}^{N-1} F_i \sin\left(\frac{i\pi}{2}\right)$$

(4.10)

where N is the number of half-wave plate angles (Patat & Romaniello, 2006). The uncertainties on q and u were calculated using the following expressions

$$\sigma_q = \frac{2}{N} \sqrt{\sum_{i=0}^{N-1} \sigma_{F_i}^2 \cos^2\left(\frac{i\pi}{2}\right)}$$
$$\sigma_u = \frac{2}{N} \sqrt{\sum_{i=0}^{N-1} \sigma_{F_i}^2 \sin^2\left(\frac{i\pi}{2}\right)}$$

(4.11)

derived from the summation of the individual half-wave plate angle errors in quadrature. The degree of linear polarisation could then be derived using the following formula

$$P = \sqrt{q^2 + u^2}$$

(4.12)

and the standard error on P via

$$\sigma_P = \sqrt{\frac{u^2\sigma_u^2 + q^2\sigma_q^2}{q^2 + u^2}} \tag{4.13}$$

assuming that q and u are independent variables. The angle of polarisation was calculated using the following relation

$$\theta_P = \frac{1}{2}\arctan\left(\frac{u}{q}\right) + \begin{cases} 0°, & \text{if } q > 0 \text{ and } \mathrm{u} \geq 0 \\ 180°, & \text{if } q > 0 \text{ and } \mathrm{u} < 0 \\ 90°, & \text{if } q < 0 \end{cases} \tag{4.14}$$

the additional offset is dependent on the signs of both q and u and aligns the polarisation angle with the standard definition of θ_P which begins at North and moves counterclockwise (see Figure 4.6). I calculated the error on θ_P via

$$\sigma_{\theta_P} = \frac{\sigma_P}{2P} \tag{4.15}$$

where σ_{θ_P} is dependent on the magnitude of linear polarisation (Patat & Romaniello, 2006).
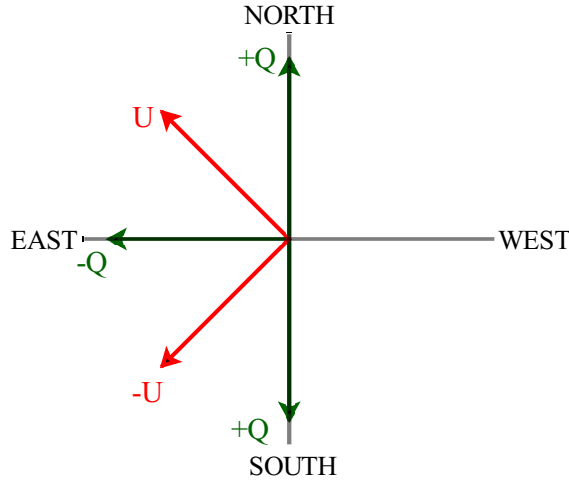
Figure 4.6: Illustration of the coordinate definition for Q and U (and therefore q and u) of the polarisation angle. Figure taken from Wiersema et al. (2012a).

As P is derived from the summation of q and u in quadrature, the observed polarisation has to be corrected for polarisation bias to uncover the true polarisation of the target source

(Serkowski, 1958). There are numerous estimators that can correct for polarisation bias in the literature, such as Maximum Likelihood (ML; Simmons & Stewart 1985) or Wardle-Kronberg (WK; Wardle & Kronberg 1974) estimators. For the SPLOT survey targets, I corrected for bias using the Modified ASymptotic (MAS) estimator Plaszczynski et al. (2014). Unlike the ML and WK estimators, the MAS estimator provides a non-zero polarisation signal at very low SNR. The MAS estimator is defined as

$$P_{\mathrm{MAS}} = P - \sigma_P^2 \left(\frac{1 - e^{\frac{-P^2}{\sigma_P^2}}}{2P} \right) \tag{4.16}$$

where P_{MAS} is the MAS estimation of the true, unbiased source polarisation P_0.

If the SNR of polarimetric measurements are sufficiently high ($P_0/\sigma_P \gtrsim 3$) that the distribution of P roughly follows a Gaussian distribution. As the SNR of a source decreases, the distribution of P_{MAS} no longer resembles a Gaussian but increasingly begins to follow a Rice distribution (Rice, 1944). This is especially significant for measurements where $P_{\mathrm{MAS}}/\sigma_P \lesssim 2$ (see Figure 4.7). The consequence of this transformation is the shift in confidence intervals; from symmetric to non-symmetric. For the majority of our observations where $P_{\mathrm{MAS}}/\sigma_P \gtrsim 3$, I simply quote $P_{\mathrm{MAS}} \pm \sigma_P$ for the mean and 68% confidence intervals. This is sufficiently accurate for these cases (Simmons & Stewart, 1985; Sajina et al., 2011). For cases where the SNR is lower than this threshold, the source detection is below 3σ and I quote a 95% confidence (2σ) upper limit on the polarisation measurement. Upper limits for the MAS estimator are calculated using the following expression

$$P_{\mathrm{Upper}}^{\alpha} = P_{\mathrm{MAS}} + P_{\alpha}(1 - \beta e^{-\gamma P_{\mathrm{MAS}}}) \tag{4.17}$$

where $\alpha = 0.95$, $P_{\alpha} = 1.95\sigma_P$, $\beta = 0.22$ and $\gamma = 2.54$ for a 2σ upper limit (Plaszczynski et al., 2014).
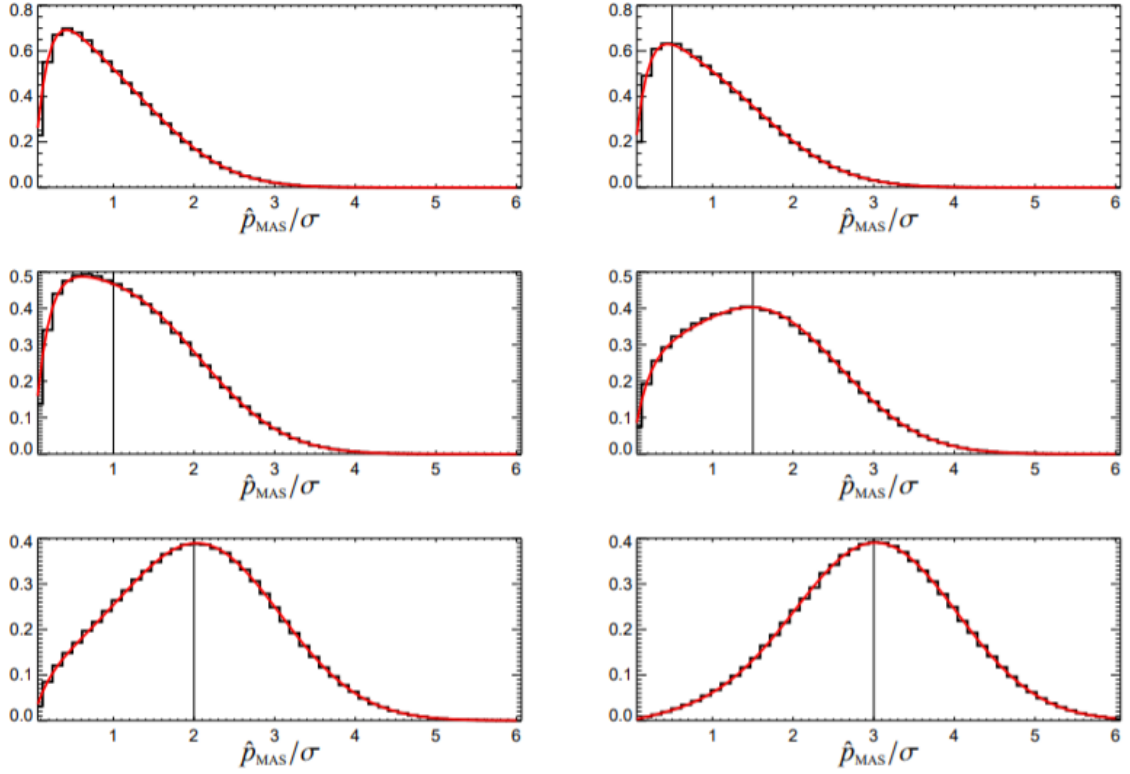
Figure 4.7: The distribution of P_{MAS} (red) for given SNR of the unbiased polarisation signal P_0/σ_P (black lines) taken from MC simulations performed by Plaszczynski et al. (2014). You can clearly see the transformation from a Rice to a Gaussian distribution by the time $P_0/\sigma_P \sim 3$, and that the peak of the P_{MAS} distribution traces P_0 well when $P_0/\sigma > 1$. Figure taken from Plaszczynski et al. (2014).

4.5.5 Results

I produced a number of figures to highlight the breadth of polarimetric parameter space covered by SPLOT. Figure 4.8 illustrates the q and u distribution of the SPLOT survey targets, split by filter. Figure 4.9 illustrates the q and u distributions of the SPLOT sample targets, split by source classification and SN type. Finally, Figure 4.10 quantifies the polarimetric parameter space as a function of the time elapsed between the distribution of the public alerts and the time of observation. This information is quantified in Table 4.1, which contains all of the polarimetric results for the SPLOT survey.
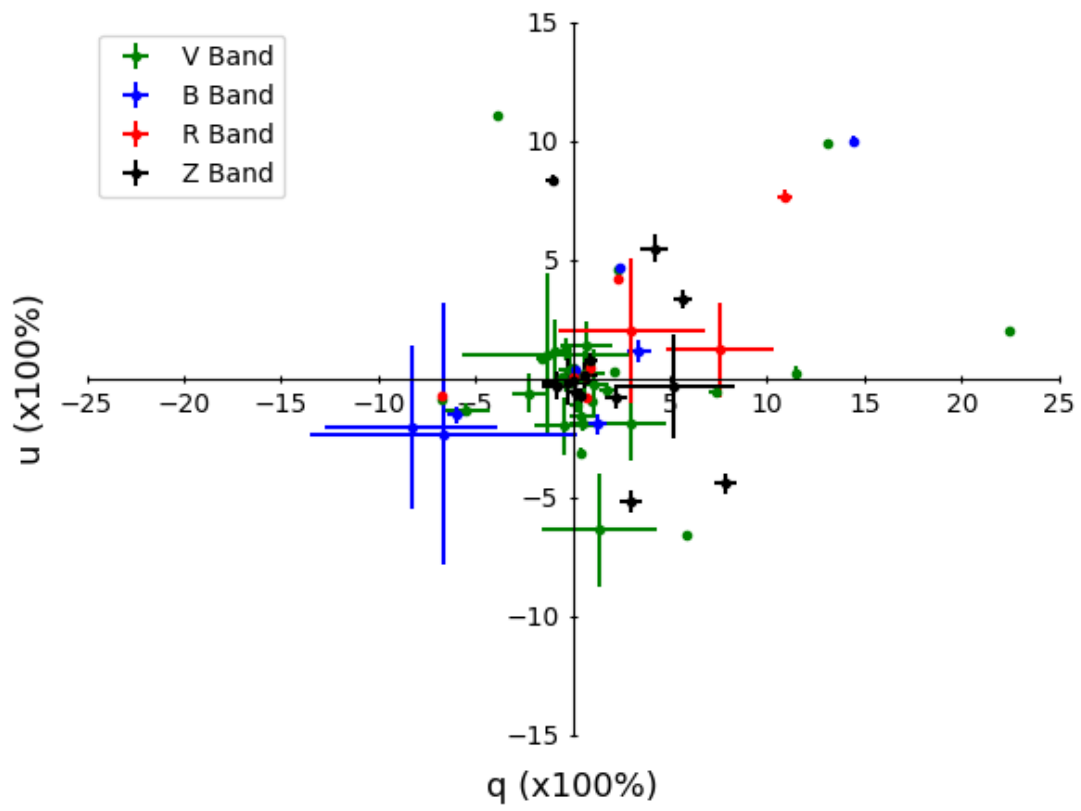
Figure 4.8: The q and u distribution of SPLOT survey targets, organised by filter.
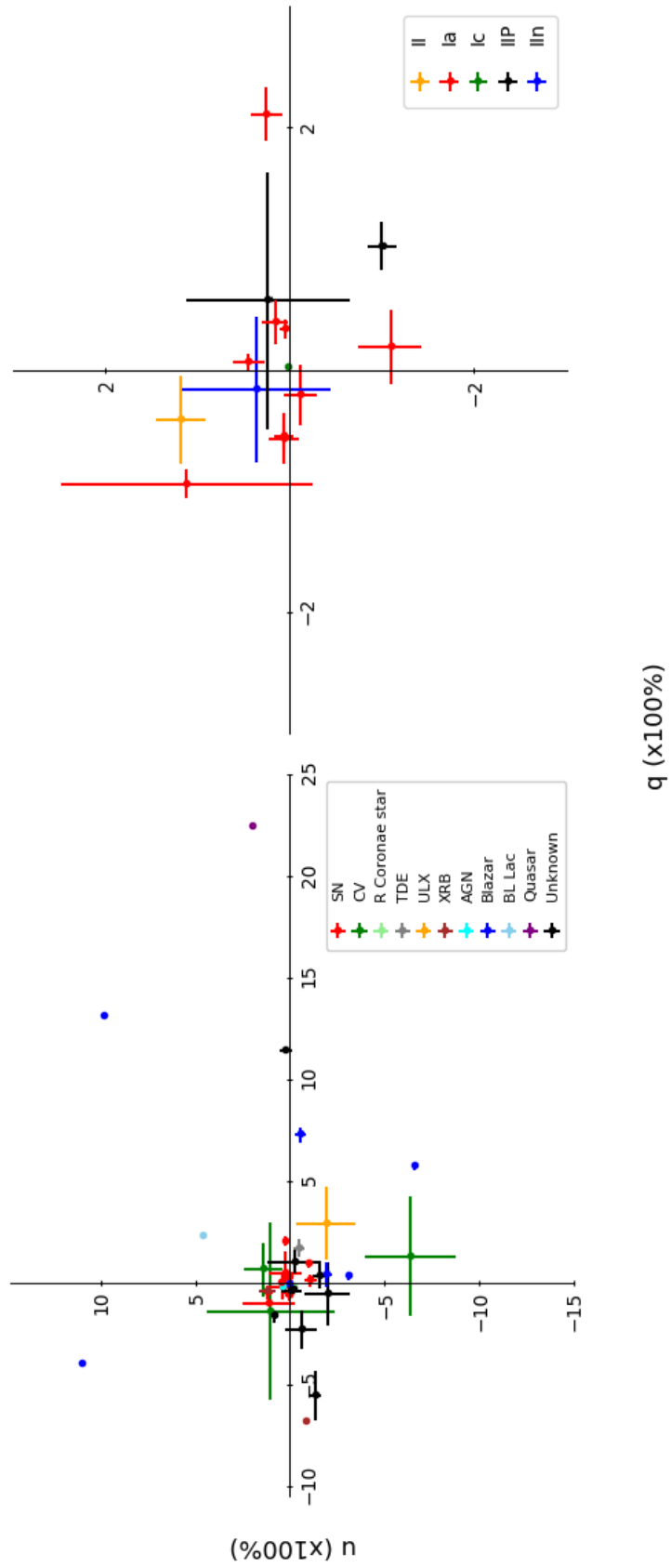
Figure 4.9: The *V* filter *q* and *u* distribution of the entire SPLOT survey targets, filtered by source classification (left) and the observed SN, filtered by individual type (right).
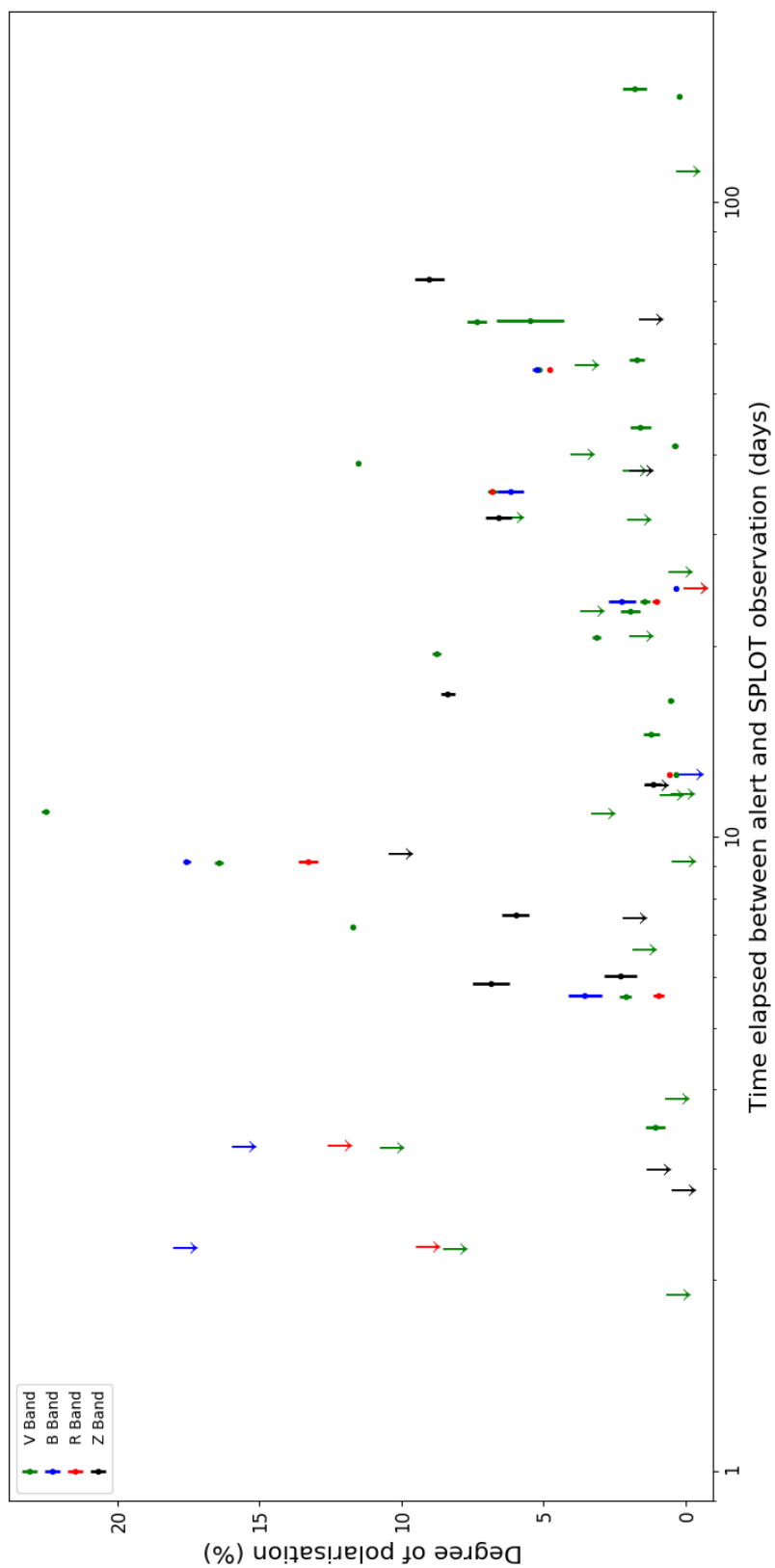
Figure 4.10: SPLOT survey polarisation distribution against time elapsed between the distributed alert and time of observations (see Table 4.1 for details). This figure mirrors the right panel of Figure 4.2.

Table 4.1: Polarimetric properties of the SPLOT survey. The time of observation and parallactic angle recorded are taken from the start of the half wave-plate exposure at 45 deg, approximately midway through the observation. All errors on detections are quoted to 68% confidence. Upper limits are quoted at 95% confidence (2σ).

Source name	Filter	Obs. date (mid, MJD)	Exposure time (s)[a]	Parallactic angle (mid, deg)	q (×100%)	u (×100%)	P (×100%)	θ (deg)	Time elapsed[b]	Source class[c]
3C 454.3	V	57560.4243	60	169.9	-3.88(±0.06)	11.03(±0.05)	11.70(±0.05)	54.7(±0.12)	7.21	Blazar
	V	57562.3199	2 x 60	-149.7	13.15(±0.14)	9.85(±0.15)	16.43(±0.14)	18.43(±0.24)	9.11	
	B	57562.3289	2 x 60	-152.7	14.45(±0.05)	9.98(±0.22)	17.56(±0.14)	17.32(±0.21)	9.12	
	R	57562.3380	2 x 60	-156.0	10.87(±0.38)	7.66(±0.26)	13.29(±0.34)	17.59(±0.74)	9.13	
ASASSN-16fp	V	57560.2842	1 x 15 + 2 x 30	-149.4	0.03(±0.02)	0.02(±0.03)	≤ 0.08	-	24.63	SN Ib
	B	57560.2920	2 x 30	-152.0	0.12(±0.14)	0.32(±0.01)	0.34(±0.05)	35.17(±4.21)	24.64	
	R	57560.2986	2 x 30	-154.2	0.07(±0.03)	0.05(±0.03)	≤ 0.10	-	24.65	
ASASSN-16fq	V	57559.9968	180	148.3	1.03(±0.20)	-1.01(±0.15)	1.44(±0.18)	157.89(±3.54)	23.44	SN IIP
	B	57560.0069	180	145.0	1.24(±0.54)	-1.92(±0.42)	2.24(±0.46)	151.45(±5.77)	23.45	
	R	57560.0170	180	142.0	0.67(±0.14)	-0.82(±0.11)	1.05(±0.12)	154.77(±3.29)	23.46	
ASASSN-16fs	V	57560.0830	2 x 180	170.9	-0.54(±0.10)	0.06(±0.11)	0.53(±0.10)	86.75(±5.28)	16.40	SN Ia
ASASSN-16ft	V	57559.3699	300	-139.8	-0.40(±0.36)	1.17(±0.27)	1.21(±0.28)	54.43(±6.42)	14.50	SN II
ASASSN-16fv	V	57559.1257	180	-42.8	0.35(±0.08)	0.05(±0.06)	0.35(±0.08)	3.86(±6.41)	12.52	SN Ia
	B	57559.1344	120	-39.1	0.01(±0.12)	0.06(±0.09)	≤ 0.22	-	12.53	
	R	57559.1418	120	-35.9	0.57(±0.09)	0.15(±0.07)	0.58(±0.09)	7.28(±4.16)	12.54	
ASASSN-16fx	V	57559.4174	180	-77.3	-0.20(±0.25)	-0.12(±0.18)	≤ 0.56	-	11.71	SN Ia
ASASSN-16ga	V	57559.2052	240	86.6	0.72(±1.32)	1.40(±1.02)	≤ 3.35	-	10.90	CV†
ASASSN-16gg	V	57559.2325	90	95.0	-1.31(±4.33)	1.01(±3.41)	≤ 8.55	-	2.24	CV†
	B	57559.2384	90	96.4	-6.68(±6.86)	-2.36(±5.52)	≤ 18.04	-	2.25	

Table 4.1: continued ...

Source name	Filter	Obs. date (mid, MJD)	Exposure time (s) [a]	Parallactic angle (mid, deg)	q (×100%)	u (×100%)	P (×100%)	θ (deg)	Time elapsed [b]	Source class [c]
	R	57559.2437	60	97.6	3.04(±3.80)	2.00(±3.05)	≤ 9.50	-	2.26	
	V	57560.2215	240	93.0	1.38(±2.95)	-6.37(±2.38)	≤ 10.77	-	3.24	
	B	57560.2408	240	97.6	-8.30(±4.42)	-2.05(±3.46)	≤ 15.98	-	3.25	
	R	57560.2537	240	100.5	7.58(±2.80)	1.19(±2.00)	≤ 12.60	-	3.26	
ASASSN-17gs	Z	57974.0350	5 x 3 x 60	138.5	7.87(±0.54)	-4.44(±0.43)	9.03(±0.52)	165.28(±1.63)	75.64	BL Lac
ASASSN-17km	Z	57973.1994	5 x 3 x 15	-96.8	0.07(±0.31)	-0.14(±0.25)	≤ 0.51	-	2.77	CV†
	Z	57973.4205	5 x 3 x 30	84.6	0.12(±0.35)	-0.57(±0.55)	≤ 1.39	-	2.99	
AT2016bvg	V	57559.1846	240	121.9	-2.21(±0.93)	-0.62(±0.83)	≤ 3.91	-	55.40	Unknown
	V	57560.1359	2 x 240	133.8	-1.57(±0.31)	0.80(±0.17)	1.73(±0.28)	76.58(±4.60)	56.35	
AT2016cvk	V	57559.2812	2 x 240	-80.0	-0.15(±0.60)	0.36(±0.80)	≤ 1.90	-	6.65	SN IIn
ATLAS16bcm	V	57560.1118	240	165.0	-0.56(±0.21)	0.06(±0.16)	≤ 0.91	-	11.64	SN Ia
ATLAS16bdg	V	57559.0906	180	122.8	2.12(±0.22)	0.25(±0.17)	2.12(±0.22)	3.33(±2.96)	5.60	SN Ia
	B	57559.1007	180	121.4	3.42(±0.60)	1.12(±0.48)	3.55(±0.59)	9.06(±4.72)	5.61	
	R	57559.1108	180	120.2	0.88(±0.20)	0.43(±0.15)	0.97(±0.19)	12.96(±5.49)	5.62	
ATLAS17jfk	Z	57974.2359	5 x 3 x 60	119.9	2.21(±0.58)	-0.85(±0.46)	2.30(±0.57)	169.47(±6.88)	6.04	Novae
CTA102	V	57559.4053	60	172.3	22.46(±0.14)	1.98(±0.11)	22.53(±0.14)	2.48(±0.17)	10.97	Quasar
	Z	57973.3216	5 x 3 x 60	151.4	5.70(±0.47)	3.32(±0.40)	6.58(±0.45)	15.13(±1.97)	31.81	
Gaia16aau	V	57559.3508	240	-60.0	-0.14(±0.06)	-0.17(±0.05)	0.22(±0.05)	115.70(±7.03)	146.58	RCB Star
Gaia16agw	V	57559.1566	240	101.6	-0.01(±0.31)	0.05(±0.20)	≤ 0.36	-	111.86	Blazar†
Gaia16alw	V	57562.2083	3 x 300	148.7	-5.45(±1.23)	-1.33(±0.29)	5.48(±1.20)	96.84(±6.13)	64.98	Unknown
Gaia16aoa	V	57562.0209	3 x 240	111.0	0.43(±0.61)	-1.58(±0.36)	1.59(±0.38)	142.59(±6.65)	44.27	Unknown

111

Table 4.1: continued . . .

Source name	Filter	Obs. date (mid, MJD)	Exposure time (s) [a]	Parallactic angle (mid, deg)	q (×100%)	u (×100%)	P (×100%)	θ (deg)	Time elapsed [b]	Source class [c]
Gaia16aob	V	57560.0454	240	99.0	-0.10(±0.17)	0.38(±0.13)	0.37(±0.12)	52.10(±9.53)	41.30	AGN†
Gaia16aok	V	57559.0372	2 x 300	92.8	11.51(±0.07)	0.22(±0.31)	11.51(±0.07)	0.56(±0.18)	38.79	Unknown
Gaia16aol	V	57560.0651	120	120.7	-0.45(±1.54)	-1.99(±1.21)	≤ 4.08	-	40.05	SN†
Gaia16aoo	V	57559.0088	240	137.1	0.58(±1.06)	0.23(±0.89)	≤ 2.21	-	37.74	SN IIP
Gaia16aqe	V	57562.4013	3 x 180	-123.5	1.12(±0.59)	-0.23(±1.41)	≤ 2.07	-	31.68	SN Ia
Gaia17blw	Z	57974.3484	5 x 3 x 60	-70.2	0.57(±0.72)	0.14(±0.55)	≤ 1.65	-	65.32	SN IIn
Gaia17bro	Z	57974.3966	5 x 3 x 60	-73.8	-0.81(±0.74)	-0.33(±0.57)	≤ 1.99	-	37.85	SN IIn
Gaia17bvo	Z	57974.0793	5 x 2 x 60	64.1	-1.03(±0.32)	8.32(±0.25)	8.37(±0.25)	48.53(±0.86)	16.76	YSO†
Gaia17bwu	Z	57973.1470	5 x 3 x 60	84.1	0.92(±0.33)	0.76(±0.27)	1.16(±0.30)	19.81(±7.25)	12.08	Red Star
Gaia17bxl	Z	57973.2327	5 x 3 x 60	-82.3	5.22(±3.13)	-0.34(±2.20)	≤ 10.45	-	9.39	SN
Gaia17byh	Z	57973.0822	5 x 3 x 60	-21.5	-0.29(±1.29)	-0.16(±0.97)	≤ 2.22	-	7.45	SN Ic
Gaia17byk	Z	57974.1218	5 x 3 x 60	90.7	2.98(±0.59)	-5.21(±0.46)	5.99(±0.49)	149.88(±2.35)	7.54	Unknown
Gaia17bzc	Z	57974.1937	5 x 2 x 60	98.0	4.20(±0.74)	5.46(±0.57)	6.86(±0.64)	26.21(±2.65)	5.86	Unknown
GX 304-1	V	57562.0537	5	37.9	-6.75(±0.16)	-0.86(±0.12)	6.80(±0.16)	93.58(±0.67)	35.01	HMXB
	B	57562.0557	5	37.9	-5.98(±0.45)	-1.55(±0.35)	6.17(±0.45)	97.29(±2.07)	35.01	
	R	57562.0578	5	37.9	-6.77(0.08)	-0.75(±0.06)	6.80(±0.08)	93.08(±0.34)	35.01	
MASTER J023819	Z	57974.2921	5 x 2 x 60	-75.4	0.20(±0.25)	-0.66(±0.20)	0.66(±0.20)	143.25(±8.36)	0.34	AGN†
MASTER J220727	V	57559.3162	2 x 240	-143.9	0.20(±0.31)	-1.09(±0.34)	1.06(±0.34)	140.24(±8.76)	3.48	SN Ia
OGLE16aaa	V	57560.3271	3 x 240	-76.6	1.79(±0.43)	-0.49(±0.31)	1.81(±0.42)	172.33(±6.44)	150.82	TDE
P13 NGC 7793	V	57560.3716	3 x 240	-88.8	3.01(±1.80)	-2.06(±1.62)	≤ 6.54	-	31.92	ULX
PG 1553+113	V	57560.2030	30	142.7	2.34(±0.10)	4.59(±0.08)	5.15(±0.09)	31.50(±0.49)	54.42	BL Lac

Table 4.1: continued . . .

Source name	Filter	Obs. date (mid, MJD)	Exposure time (s)[a]	Parallactic angle (mid, deg)	q (×100%)	u (×100%)	P (×100%)	θ (deg)	Time elapsed[b]	Source class[c]
	B	57560.2062	30	141.8	2.38(±0.16)	4.69(±0.13)	5.26(±0.13)	31.55(±0.73)	54.42	
	R	57560.2094	30	140.8	2.30(±0.08)	4.19(±0.07)	4.78(±0.07)	30.62(±0.43)	54.43	Blazar
PKS 1510-089	V	57558.9952	45	-128.1	5.81(±0.18)	-6.56(±0.15)	8.76(±0.16)	155.77(±0.54)	19.45	
	V	57560.1548	45	132.8	0.39(±0.21)	-3.12(±0.16)	3.14(±0.16)	138.55(±1.49)	20.61	
	V	57562.1839	60	124.4	0.48(±0.60)	-1.92(±0.33)	1.94(±0.35)	142.03(±5.08)	22.64	Blazar
PKS 2023-07	V	57559.2568	240	-147.2	7.35(±0.36)	-0.55(±0.28)	7.36(±0.35)	177.84(±1.38)	64.83	Unknown
PS16cnz	V	57559.0751	240	160.3	-0.29(±0.18)	-0.19(±0.13)	≤ 0.60	-	26.16	SN Ia
PS16crs	V	57562.1494	2 x 300	158.6	-0.99(±0.13)	1.11(±1.36)	≤ 3.72	-	22.68	Unknown
PS16ctq	V	57560.1844	2 x 240	102.4	-0.20(±0.23)	-0.04(±0.44)	≤ 0.50	-	9.16	SN Ia
PS16cvc	V	57560.4040	240	150.0	0.40(±0.18)	0.15(±0.14)	≤ 0.71	-	1.90	
	V	57562.3638	3 x 180	163.7	0.03(±0.07)	0.39(±0.18)	≤ 0.74	-	3.86	XRB
SXP 15.3	Z	57973.2826	5 x 3 x 30	-31.2	0.43(±0.42)	-0.72(±0.33)	≤ 1.45	-	12.07	
XTE J1709-267	V	57562.0869	3 x 240	-102.6	-0.34(±0.11)	1.21(±0.44)	≤ 2.00	-	20.71	LMXB

[a] Exposure times are given per half-wave plate angle.

[b] Time elapsed refers to the time between the distribution of the alert to the public and the observation date.

[c] For additional information about the classification of SPLOT targets, see Appendix C.

[†] Classification of the target was not spectroscopically confirmed.

4.6 Photometry Measurements

Every target in the SPLOT survey was imaged in either the V filter, for EFOSC2 images, or the Z filter for SofI observations. The images were taken directly after the four half-wave plate (or instrument rotation) angle polarimetric images. In the first observing run, a small number of SPLOT targets were additionally followed up using the UL50 in the V and/or B filters.

4.6.1 Image calibration

All images obtained during both observing runs, and at Oadby, occurred under weather conditions that meant that the observing nights were not photometric. To calibrate the images and obtain an estimated magnitude of the target sources, the image fits file coordinates were aligned to the World Coordinate System (WCS) using an online tool[24]. Once aligned, I used field stars within the image FOV and cross-matched the star positions to star catalogues. The four catalogues I used for calibration were the Sloan Digital Sky Survey - DR13 (SDSS)[25], the Pan-STARRs DR1 (Chambers et al., 2016d), the AAVSO Photometric All-Sky Survey - DR10 (APASS)[26], and the Skymapper Southern Sky Survey (Keller et al., 2007) catalogues.

For the EFOSC2 and UL50 image calibration, the APASS catalogue has observed stars directly in the V and B filters, but SDSS, Pan-STARRS and Skymapper have not. Both instruments have observations in r and g filters and were converted into the Johnson V and B magnitudes using the following analytical expressions

$$\mathrm{M}_V = \mathrm{M}_g - 0.5784(\mathrm{M}_g - \mathrm{M}_r) - 0.0038$$
$$\mathrm{M}_B = \mathrm{M}_g + 0.3130(\mathrm{M}_g - \mathrm{M}_r) + 0.2271$$

(4.18)

where M_g, M_r represent the catalogue field star magnitudes in the SDSS r and g bands. The standard error on the derived V and B filter magnitudes are estimated using the following

---

[24]http://nova.astrometry.net/upload

[25]https://www.sdss.org/

[26]https://www.aavso.org/apass

114

relations

$$\sigma_{M_V} = \sqrt{(0.4216\sigma_{M_g})^2 + (0.5784\sigma_{M_r})^2}$$
$$\sigma_{M_B} = \sqrt{(1.3130\sigma_{M_g})^2 + (0.3130\sigma_{M_r})^2}$$
(4.19)

where σ_{M_g} and σ_{M_r} represent the standard error for the SDSS r and g filters (expressions taken from Lupton 2005[27]).

I used the PYTHON3 package SEP (Barbary et al., 2016), based on Source Extractor (SExtractor; Bertin & Arnouts 1996), to detect sources within the image and perform aperture photometry to estimate the initial magnitudes of all sources. The detected source magnitudes and positions are then cross-matched with the catalogues listed above. If any SDSS object position was ≤ 1 arcsec away from a detected source, the estimated and catalogue magnitudes were recorded, and the star could not be re-matched with another catalogue. Any sources that were not matched with an SDSS catalogue object, were then cross-referenced with Pan-STARRS, APASS and Skymapper, in that order. Objects that I suspected were not stars were filtered out. The relation between the SEP estimated and catalogue magnitudes was fit with a first degree polynomial to calculate the offset. Data points that were $> 3\sigma$ away from the best-fit line were clipped away during the fitting process, with the remaining data refit. The best-fit model was produced using the CURVE_FIT function within the SCIPY package. The offset was then added to the estimated magnitude of the target source to calculate the actual magnitude. This method is illustrated in Figure 4.11.

I must highlight two caveats using the above expressions. Firstly, whilst the SDSS, Pan-STARRs and Skymapper r and g filters are very similar, they are not identical. This means that when I used the transformations above, there is a non-zero difference on the derived magnitudes, but these changes are expected to be very small. Secondly, The analytical expressions displayed in Equation 4.18 were based on measurements from a large sample of stars and have a small, additional uncertainty associated with the derivations of the expressions (typically ~ 0.01 mag). In light of these issues, the errors on our calculated magnitudes may be underestimated by up to ~ 0.1 mag.

---

[27] http://www.sdss3.org/dr8/algorithms/sdssUBVRITransform.php
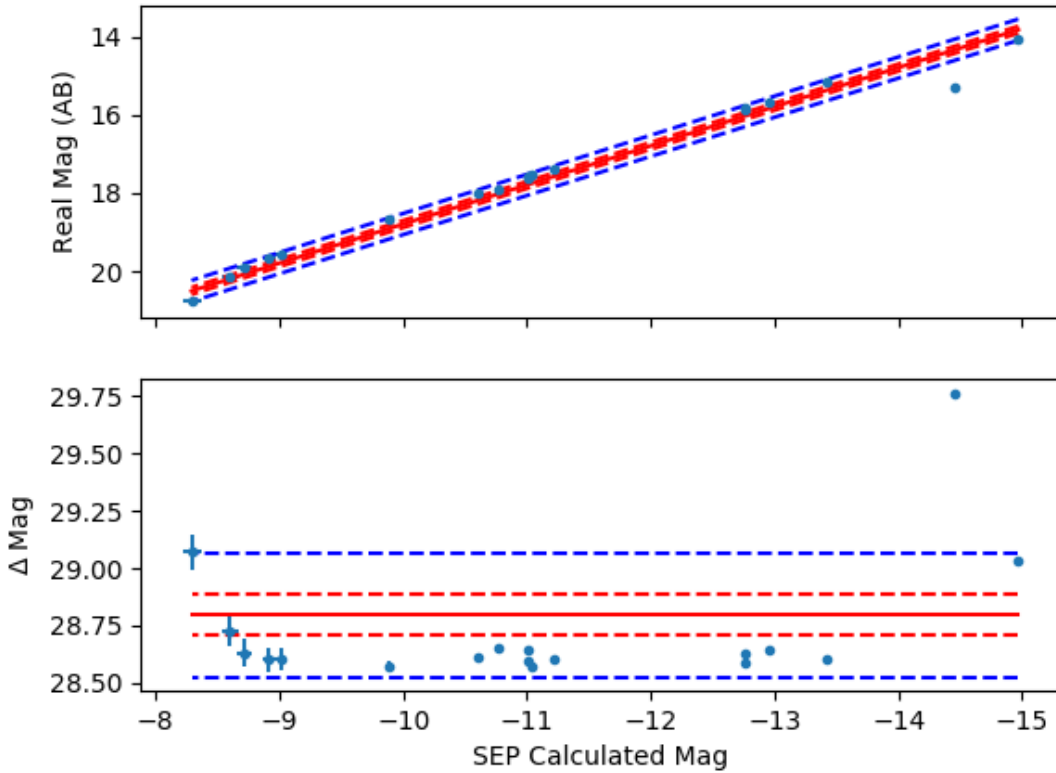
Figure 4.11: Magnitude calibration process for SPLOT target source photometry using field stars. The x axis represents the estimated magnitude purely derived from the SEP photometry. The y axis represents the catalogued magntiude of a star coincident with a SEP detected source. Overplotted are the best-fit and 1σ confidence intervals (red) and the 3σ confidence intervals (blue). The data outside of the 3σ intervals (in this case, the one datapoint) are clipped and the model is refit to recalculate the best-fit and 1σ confidence intervals.

For the SofI images, I used the same method above to calibrate the magnitudes of SPLOT targets. However, during the second run, a significant number of sources were at $< -30\,\mathrm{deg}$ due to adverse weather conditions (high winds). Most target FOVs subsequently only appeared in the Skymapper catalogue. The SofI Z filter is not equivalent to either the SDSS, Pan-STARRS or Skymapper z filters, with some filters possessing significantly different properties. The transformations between these filters is not known, so I only provide approximate magnitudes for SofI targets. Some SPLOT target fields had very few field stars that could be used. The FOVs for EFOSC2 and SofI are quite small; 4.1×4.1 and $4.9 \times 4.9\,\mathrm{arcmin}$, respectively. In

116

these cases, I could not calibrate a magnitude for these sources.

4.6.2 Results

The photometry results were used in conjunction with the polarimetric results to produce Figure 4.12, illustrating the polarimetic and brightness parameter space covered by the survey (in V-band). Table 4.2 contains the photometric properties for all SPLOT sources I could obtain a magnitude for.
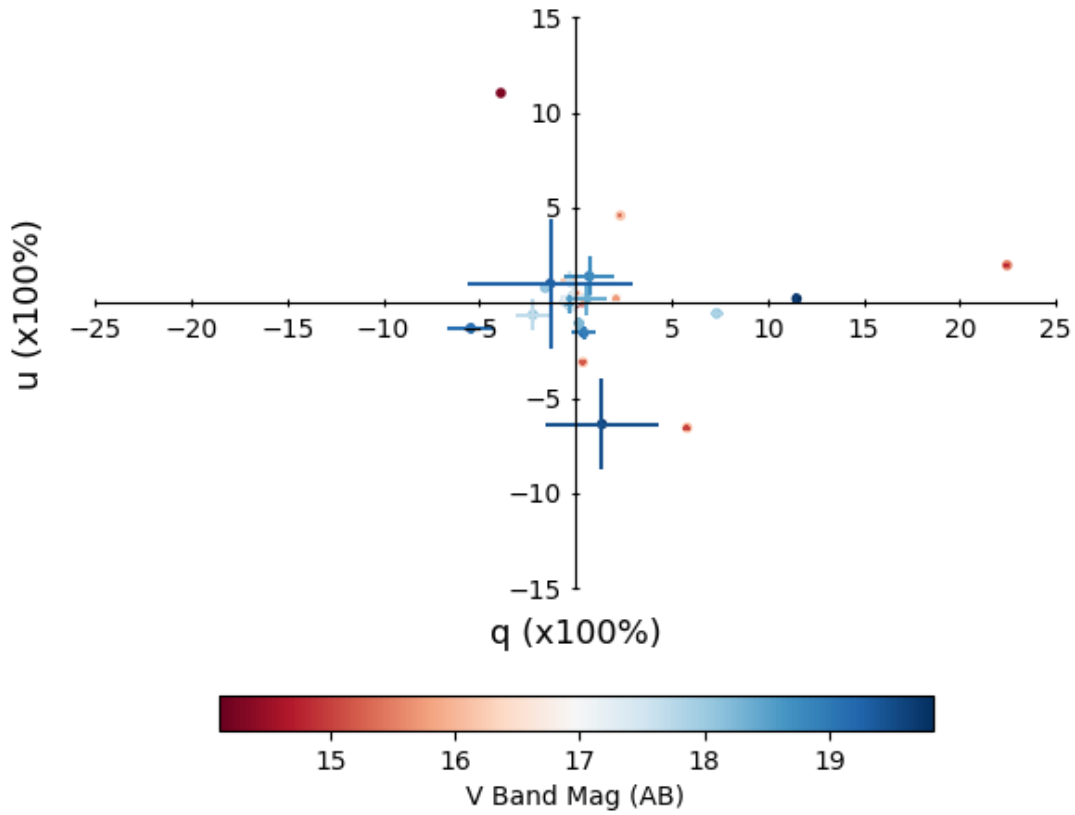
Figure 4.12: The q and u distributions of the SPLOT survey targets, overlaid with the magnitude of the source in V-band. This represents the breadth and depth of the SPLOT sample within the polarimetric and brightness parameter space.

Table 4.2: Table containing the calculated brightness of each source and the observation date for images where a magnitude could be obtained. All errors on the magnitudes are quoted to 1σ. Approximate magnitudes are given for SofI photometry.

Source name	Filter	Exposure time (s)	Obs. date (mid, MJD)	Magnitude (AB)
3C 454.3	V	30	57560.4269	14.26($\pm$0.02)
	V	30	57605.0446	15.11($\pm$0.01)
	V	30	57645.0503	15.99($\pm$0.03)
	B	30	57663.9217	16.50($\pm$0.04)
	B	30	57696.8793	16.04($\pm$0.01)
	B	30	57710.8737	16.55($\pm$0.02)
	V	30	57721.8178	15.82($\pm$0.10)
ASASSN-16fp	V	20	57560.3017	14.10($\pm$0.02)
	V	30	57605.0196	15.85($\pm$0.02)
ASASSN-16fs	V	30	57560.0934	17.21($\pm$0.04)
ASASSN-16ft	V	60	57559.3780	17.15($\pm$0.02)
ASASSN-16fv	V	30	57559.1458	15.04($\pm$0.01)
ASASSN-16fx	V	30	57559.4228	17.06($\pm$0.03)
ASASSN-16ga	V	30	57559.2120	19.04($\pm$0.04)
ASASSN-16gg	V	30	57559.2463	19.44($\pm$0.08)
	V	60	57560.2604	19.78($\pm$0.09)
ASASSN-17gs	Z	60	57974.0054	~ 16.5
ASASSN-17km	Z	5	57973.1920	~ 13.7
	Z	5	57973.4067	~ 13.7
AT2016bvg	V	30	57559.1913	18.10($\pm$0.07)
	V	60	57560.1491	18.26($\pm$0.02)
AT2016cvk	V	60	57559.2907	17.77($\pm$0.05)
ATLAS16bcm	V	60	57560.1186	17.61($\pm$0.02)
ATLAS16bdg	V	30	57559.1162	16.70($\pm$0.02)

Table 4.2: continued . . .

Source name	Filter	Exposure time (s)	Obs. date (mid, MJD)	Magnitude (AB)
ATLAS17jfk	Z	60	57974.2101	~ 18.6
CTA 102	V	20	57559.4079	$15.48(\pm 0.02)$
	V	30	57605.0320	$16.58(\pm 0.02)$
	B	30	57663.9612	$16.48(\pm 0.02)$
	B	30	57696.8702	$15.05(\pm 0.01)$
	B	30	57710.8650	$14.65(\pm 0.02)$
	V	30	57721.8110	$13.12(\pm 0.01)$
	B	30	57721.8600	$13.89(\pm 0.02)$
	V	30	57721.8647	$13.19(\pm 0.01)$
	Z	60	57973.2963	~ 15.7
	B	30	58062.8560	$17.04(\pm 0.03)$
Gaia16aau	V	60	57559.3576	$14.74(\pm 0.18)$
Gaia16agw	V	30	57559.1634	$17.58(\pm 0.01)$
Gaia16alw	V	60	57562.2399	$19.26(\pm 0.06)$
Gaia16aoa	V	60	57562.0405	$19.16(\pm 0.03)$
Gaia16aob	V	60	57560.0522	$17.27(\pm 0.01)$
Gaia16aok	V	60	57559.0532	$19.83(\pm 0.11)$
Gaia16aoo	V	30	57559.0156	$18.37(\pm 0.04)$
Gaia17blw	Z	60	57974.3190	~ 17.6
Gaia17bro	Z	60	57974.3714	~ 16.8
Gaia17bxl	Z	60	57973.2071	~ 19.4
Gaia17byh	Z	60	57973.0562	~ 17.3
MASTER OT J023819	Z	60	57974.2733	~ 14.8
MASTER OT J220727	V	60	57559.3293	$18.29(\pm 0.02)$
PG 1553+113	V	30	57508.0162	$16.18(\pm 0.02)$
PKS 1510-089	V	20	57558.9975	$16.02(\pm 0.01)$

Table 4.2: continued . . .

Source name	Filter	Exposure time (s)	Obs. date (mid, MJD)	Magnitude (AB)
	V	20	57560.1571	16.12($\pm$0.02)
PKS 2023-07	V	90	57559.2635	18.13($\pm$0.01)
PS16cnz	V	60	57559.0819	17.28($\pm$0.02)
PS16ctq	V	60	57560.1976	18.64($\pm$0.02)
PS16cvc	V	30	57560.4108	16.74($\pm$0.01)
	V	30	57605.0560	16.55($\pm$0.02)
SXP 15.3	Z	10	57973.2692	~ 15.0
XTE J1709-267	V	90	57562.1066	17.87($\pm$0.01)

4.7 Discussion

4.7.1 Sample sources and explored parameter space

In section 4.4 I described the observational criteria for the survey. To maximise the number of targets both myself and Klaas could observe, short exposure times were utilised. The short exposure times also minimised the change in parallactic angle over the four half-wave plate observations and enabled us to calibrate the data using the midpoint angle (see Chapter 5). In practice, the longest execution times for an OB was one hour, whilst the quickest execution times only took ~ 15 mins. The OBs could not get much shorter than this as time consuming overheads, such as source acquisition, half-wave plate rotations, and read-out times were ever present.

SPLOT was also designed to observe targets over a range of brightnesses, with limits of ~ 21 mag for the faintest sources. This limit was consistent to the limiting magnitudes of most transient survey alerts at the time. We both encountered variable, and at times adverse, weather conditions throughout the observing runs. We lost over two and a half nights out of the scheduled eight ($> 30\%$) to very poor weather. Additionally, the poor weather made it very challenging to observe the faintest targets whilst also keeping our execution times below an hour. The SPLOT survey observed 48 individual optical transients (not including calibration sources) and utilised numerous transient survey stream alerts. Filtering this list into source classification, SPLOT observed:

- 19 SN + candidates

- 8 sources with no follow-up classification observations

- 9 AGN (including BL Lacs, Blazars, strong candidate variables, etc)

- 3 XRBs

- 3 Cataclysmic variable (CV) candidates

- 1 ULX

- 1 TDE

- 1 Extragalactic Novae

- 1 R Coronae Borealis star

- 1 Young stellar object

- 1 Brightening red star

In terms of source selection, the target of ~ 50 sources was achieved and a host of transient phenomena were observed, with alerts picked up from various transient surveys alert streams. Eight observed targets had no prior classification information to test whether polarimetry alone could highlight sources of interest for further follow-up. Our polarimetry parameter space was also well sampled (see Figure 4.10). The weather restricted the range of source brightnesses that were covered during the survey; targets were still observed from $\sim 14 - 20$ mag (see Table 4.2 and Figure 4.12).

Overall, the sources observed during SPLOT fairly successfully covered a diverse range of transient classes and both polarimetric and brightness parameter space.

4.7.2   Science results precision

Myself and Klaas had aimed to achieve polarimetric results with uncertainties of $\sigma_P \sim 0.2\%$ for bright sources and $\sigma_P \sim 0.5\%$ for the faintest sources to ensure we could recover intrinsic polarisation signals for sources with $P < 1\%$. These uncertainties had two components; the errors on observed flux measurements and the error on our calibration method, discussed in Chapter 5. The measured flux uncertainties were dependent on the weather conditions at the time of the observations. During periods of adverse weather, which sporadically appeared throughout the observing runs, the polarimetric precision did not always reach what was initially aimed for. The full survey results and errors on measurements are presented in Table

4.1. The calibration method I produced for both EFOSC2 and SofI successfully removed the instrumental calibration to a precision of $P \sim 0.1\%$ and $P \sim 0.2\%$, respectively.

4.7.3   The effect of practical constraints on SPLOT

4.7.3.1   Weather conditions

The mixed, and sometimes adverse, weather conditions encountered during the SPLOT observing campaign, had a significant impact on the survey. As I discussed above $> 30\%$ of allocated observing time was lost to bad weather, which restricted the number of target sources observed for the survey. In periods of poor weather conditions, faint sources became very difficult to observe, both with an execution time within an hour and to achieve sufficient polarimetric accuracy, so brighter sources were observed to mitigate this. The consequence of this was that the brightness parameter space did not reach the very faint objects at ~ 21 mag.

Both observing runs were scheduled for times that coincided with a near-full Moon, meaning that the background light was higher than usual. Moonlight is also highly polarised and contributed to the measured q and u values of a source depending on the proximity of the source position to the moon. The moon could also produced additional, uneven background regions when thin cloud was present. The manifestation of the bright Moonlight on our results is a probable increase in the uncertainties associated with a small number of sources whose position was in close proximity of the Moon. With the full eight nights of observations allocated to SPLOT and favourable weather conditions, the sample size of the survey may have reached 100 sources and would have covered more fainter sources, expanding the volume of parameter space that SPLOT would have explored.

4.7.3.2 Estimating the brightness of targets

To estimate the magnitude of the target source at the time of observation, myself or Klaas had to extrapolate the discovery magnitude given by the transient survey alerts to the epoch of SPLOT observation. This was often difficult for two reasons; some sources had no follow-up classification measurements and the time elapsed between the alert and observation for some sources was large, especially during the first observing run.

Transients with very short lifetimes, such as some of the observed CV candidates and un-classified sources were sometimes fainter than our predictions, resulting in an underestimated exposure time per half-wave plate angle, a lower number of counts, and therefore higher polarimetric uncertainties. With the addition of variable weather conditions, the exposure times for some sources were significantly modified or the whole polarimetric sequence was restarted. For fainter sources, if the weather conditions changed dramatically over the length of an observation, the observation was aborted as the results would be contaminated with high levels of uncertainties.

4.7.4 Galactic dust polarisation measurements

The significance of dust induced polarisation in some SPLOT targets can be seen in the presented results. For example, several type Ia SN exhibited significant polarisation measurements (see figure 4.9), even though the intrinsic signal from these sources should be $\lesssim 0.3\%$. These detections suggested that the majority of the detected signal came from dust. Several sources were additionally observed in the B and R bands. 3C454.3 was one source that I observed in multiple bands. These observations highlighted the significant wavelength variations in the degree of polarisation detected. I observed a change of $\sim 4\%$ in polarisation between the B and R filters. This filter dependent variance in the degree of polarisation was also seen for ASASSN-16fq, ATLAS16bdg and GX 304-1, although the magnitude of the variation was not as significant as 3C454.3 (see Table 4.1). To fully characterise the wavelength dependent polarisation behaviour of SPLOT sources, multi-band snapshots of each target source would

have been required.

A future survey has the potential to characterise the Galactic dust contribution to polarisation measurements in a number of ways. The first method could use field stars measurements in the FOV of the target source to calculate the average field star polarisation value, under the assumption that all of the field stars are unpolarised. The FOV of EFOSC2 and SofI is too small to feasibly attempt this with the NTT. However, on another instrument this could be used as a rough estimate for the Galactic polarisation contribution at those coordinates, though the position of the stars will not cover the entire Galactic dust column density. The *Gaia* DR2 data provides accurate astrometry and distances to an unprecedented number of Galactic sources (Lindegren et al., 2018). Over time, and with more observations, this could be a crude way to produce a map of Galactic dust contribution to polarisation. A second method would be to utilise polarimetric sky surveys (e.g. SOUTH POL; Magalhães et al. 2012). Recent investigations have also found Galactic filamentary structures from polarimetric observations at low frequency radio wavelengths, some of which were also highlighted in Planck dust polarisation maps (e.g. Zaroubi et al. 2015). Bright, unpolarised transients observed using multi-band snapshots could also aid in mapping this structure.

4.7.5 Was the SPLOT survey a success?

4.7.5.1 SPLOT results

The SPLOT polarisation results, shown in Table 4.1, highlight the mixed success rate for the survey. For the periods of clear weather and thin-to-no cloud coverage, the set out precision was achieved within the required execution times. This was particularly successful using EFOSC2 in the first observing run. For periods where the weather was not so favourable, the uncertainties were larger and did not meet the aims. The execution times utilised during the runs and the 48 sources observed during SPLOT highlight that a SPLOT-like survey, utilising imaging polarimetry to investigate transients, is as efficient as a typical, spectroscopic transient classification program, for the snapshot single-band strategy targets.

4.7.5.2 Single or multi-band measurements

A number of sources in the SPLOT survey were observed in multiple filters to compare with the snapshot single filter measurements. The additional measurements were done with the EFOSC2 B and R filters. No multi-band comparisons were made in the second run using SofI. The chosen sources to observe in multiple filters were usually bright, to keep execution times to a minimum, but were not otherwise pre-selected via classification or position. I discussed above that measurements across multiple filters highlighted variations in the detected polarisation signal (e.g. 3C454.3), which implied that a contribution from line-of-sight dust scattering was present. The dust contribution can be further analysed using further measurements but this was not one of the primary aims of the SPLOT survey. Additionally, more multi-band observations would also have reduced the number of individual sources observed using snapshot observations.

4.7.5.3 Snapshot or multi-epoch measurements

In a similar vein to the above paragraph, we observed a small number of sources multiple times during the first observing run. This was conducted to determine the scientific value of using multi-epoch observations to highlight potential, short-time polarimetric variability. In the case of PKS 1510-089, the level of polarisation in V-band significantly decreased over a period of ~ 4 days, highlighting the rapid changes of internal structure of the source. The disadvantage to utilising multi-epoch observations is similar to multi-band observations; the number of individual sources you can observe is limited. For SPLOT, many multi-epoch measurements would have reduced the explored area of polarimetric parameter space, going against the primary aims.

4.7.5.4 Highlighting sources of astrophysical interest

Some of the sources observed during SPLOT belong to rare subclasses, some with very few polarimetric observations at all. As a result, the single measurement of polarisation taken as part of the survey is, by definition, of astrophysical interest. Below, I have highlighted four sources that are of scientific interest. It was not feasible to discuss all individual source measurments within this section, so for details on all 48 individual sources see Appendix C.

Gaia16aok: this source, arising form an outburst of a previously quiescent radio source, exhibited high levels of V-band polarisation; $P = 11.51(\pm 0.07)\%$. Although we do not know the dust contribution directly from the SPLOT observation, a source with no follow-up classification in conjunction with a high polarisation detection should warrant further follow-up observations. This was highlighted from a single snapshot observation.

Gaia17bvo: this galactic variable, with no follow-up classification information, was found to be highly polarised in Z-band; $P = 8.37(\pm 0.37)\%$. In similar fashion to Gaia16aok, this source would also warrant further follow-up observations.

OGLE16aaa: this TDE had a measured polarisation of $P = 1.81(\pm 0.42)\%$ in V-band, which is lower than previous measurements of relativistic TDEs and, more importantly, one of only a handful of TDE polarimetric observations (Wiersema et al. 2012a; Wiersema et al., in prep).

P13 NGC 7793: this pulsating ULX with a period of ~ 0.42 s, comprising of a black hole and a donor star, was found to have a polarisation of $P < 6.54\%$ in V band. In ideal observing conditions, this upper limit would be better constrained but this observation has provided the first polarimetric measurement of a ULX.

4.7.6 Looking to the future

The true test of the success of a SPLOT-like survey in highlighting sources of scientific interest from real-time transient stream alerts, is its use in the near future. With ZTF now distributing alerts to the public and LSST just around the corner, the number of transient detections is going to significantly increase. An imaging polarimetry survey could be adapted to use an algorithmic target selection process to filter transients alerts in real-time from one of these transient streams. This could increase the efficiency of transient selection and science return by maximising the survey size. Parameter limits such as alert age or discovery magnitudes could be implemented to customise the volume of parameter set explored. A remote, service mode operated programme or automated robotic telescope could maximise the number of transients observed, and make it easier to adapt to varying weather conditions. SPLOT has shown, along with ePESSTO, that visitor mode is feasible for transient surveys. To allow other observers to rapidly follow-up any highlighted targets of interest, the results could be made public through ATels or a broker like ANTARES[28] (Saha et al., 2016), which also publicises additional multi-wavelength information.

I discussed that I had completed a third observing run for SPLOT in August 2018. The source data have not been fully analysed, which is why it has been omitted from this chapter. The sources observed during this run often came from alerts that had been publicly distributed < 72 hours before the observation with several chosen on the afternoon before the observation. These targets should cover the part of multi-dimensional parameter space for very short timescales. I am currently working on this data with Klaas Wiersema, with the aim to present and submit this data in a second SPLOT-like paper.

---

[28]https://www.noao.edu/ANTARES

4.8   Conclusions

The SPLOT pilot survey was undertaken to investigate the feasibility of a linear optical polarimetry survey in adding scientific value to real-time transient alert streams, or highlighting unclassified sources of scientific interest. In total, 48 individual sources were observed as part of SPLOT. This included a number of unclassified sources with no previous follow-up, and a couple of sources, whose type had little-to-no previous polarimetric follow-up, including OGLE16aaa, a TDE and P13 NGC 7793, a pulsating ULX. With new, larger transient detection missions coming online, there will be a significant increase in the number of transients detected per night, and a way to filter interesting transients out from the continuous streams will be even more important. This investigation has highlighted the feasibility of a SPLOT-like survey in utilising polarimetry to independently highlight sources of scientific interest for further follow-up. Snapshot linear polarimetry can be utilised as an independent aid in the selection of transients for studying non-thermal emission processes and increase the exploration of the observational, multi-dimensional, parameter space in which astrophysical phenomena exists.

5

Calibration of SPLOT survey data

5.1 Introduction

This chapter focuses on the calibration of polarimetric observations for both EFOSC2 and SofI. A full calibration method was required for the SPLOT survey due to the telescopic configuration of the NTT. The calibration method was published in the Publications of the Astronomical Society of Australia (PASA; Wiersema et al. 2018). Sample PYTHON3 scripts for the EFOSC2 calibration are again available on my GitHub page[22]. SofI scripts are available at request.

The NTT hosts EFOSC2 and SofI on two separate Nasmyth platforms (see Figure 5.2). A
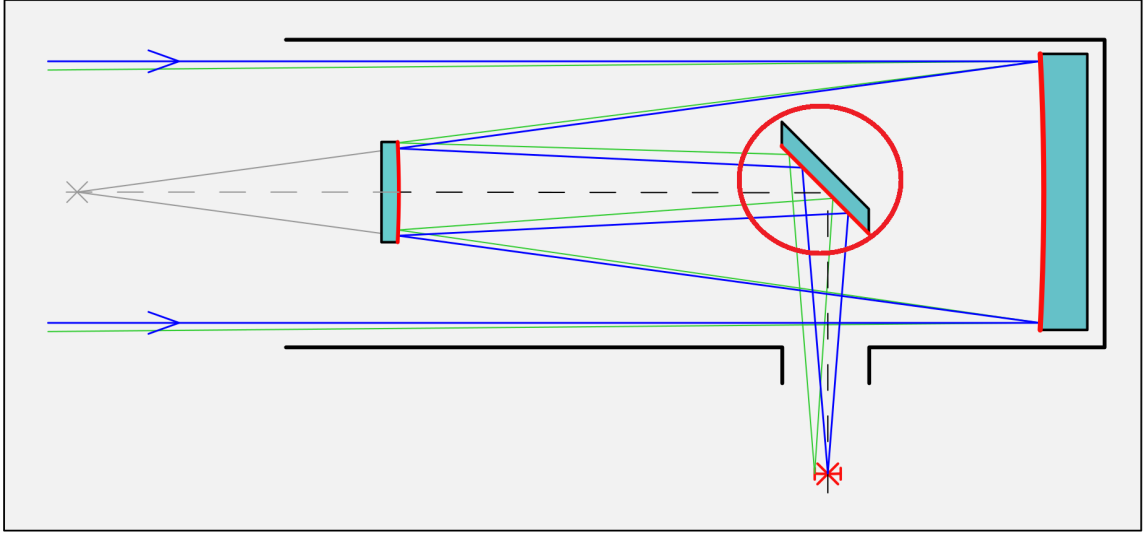
Figure 5.1: Illustration of a Nasmyth telescope setup. I have highlighted the tertiary mirror (red circle) where the significant fraction of the instrumental polarisation is produced. Image created by Wikipedia user Jailbird under a Creative Commons license.

telescope with a Nasmyth configuration comprises of three primary mirrors to focus the light onto the instrument and detector (see Figure 5.1 for example setup). Nasmyth mounted instruments exhibit a high level of instrumental polarisation (Tinbergen, 2007) which is dependent on the pointing direction of the telescope (the parallactic angle more precisely). This is included in the detected fluxes received by the CCD and has to be removed to obtain the correct source, polarimetric measurements.

I present a method and model below that, using a number of standard unpolarised star observations, can effectively remove the instrumental polarisation signal from NTT data.
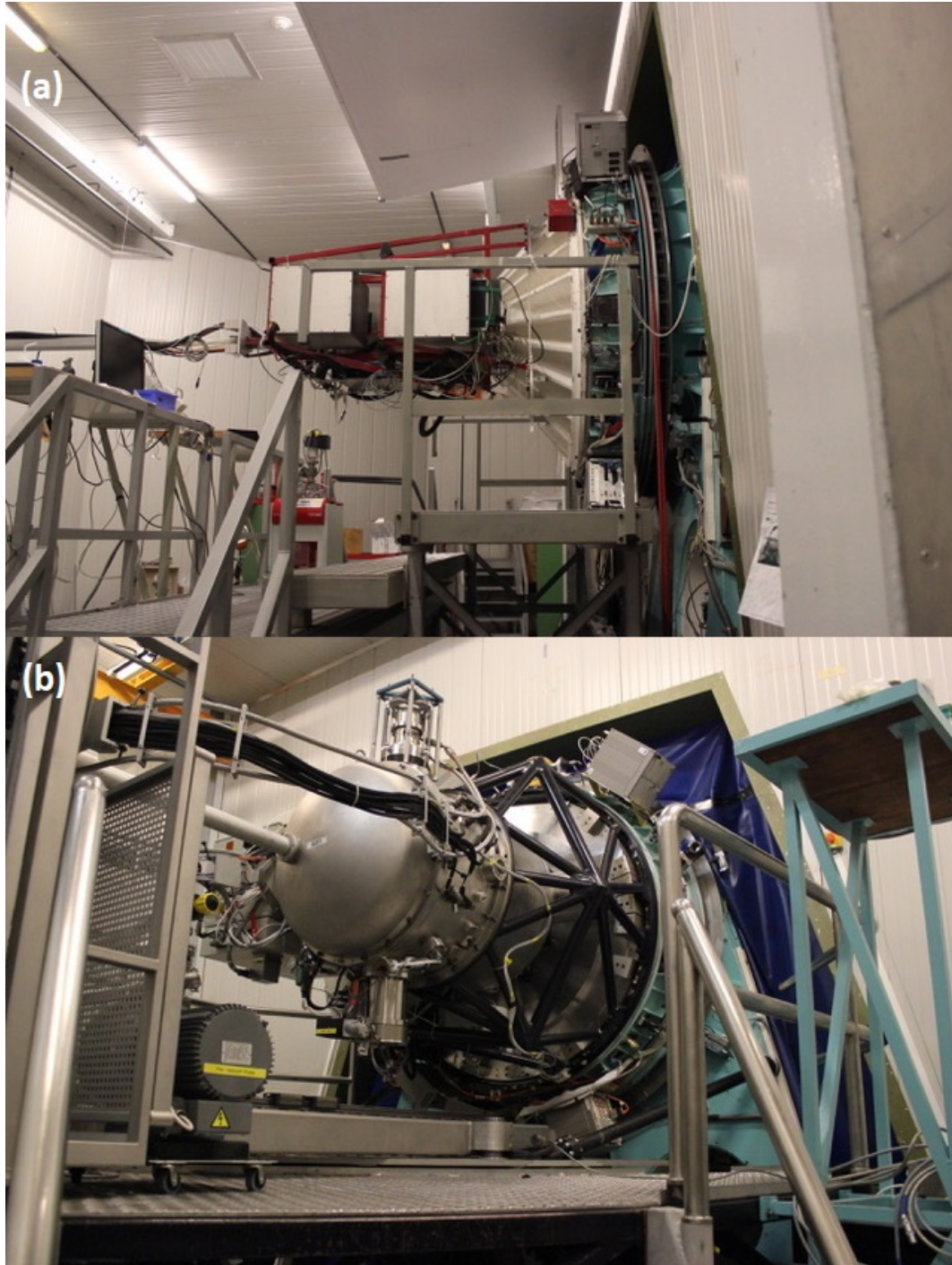
Figure 5.2: Photos of EFOSC2 (a) and SOFI (b) fixed onto their respective Nasmyth mounts, on either side of the NTT.

5.2 Observations

The observations taken to produce the calibration method for both EFOSC2 and SofI used an identical instrumental setup to that described in Section 4.5. This includes the prescription for the o and e beams, where for SofI observations, this beams are switched in comparison to EFOSC2. The calibration method required a number of observations of standard stars. The majority of the observations were unpolarised stars. These stars chosen had been confirmed to exhibit zero polarisation (i.e. $q = 0$ and $u = 0$) from recent investigations; all but one were observed by Fossati et al. (2007), and WD 1344+106 was observed by Żejmo et al. (2017). To ensure that the observational errors were low, and the execution times were quick, the standard stars were bright white dwarf (WD) stars, where $15 \lesssim V \lesssim 11$ mag. Observations were taken at various times of the observing nights, covering a large range of parallactic angles to ensure fitted models were robust.

Several polarised standard stars were observed as a second check to the calibration model results. The number of suitable polarised standard stars, such as within the above V-band range and available during the time of the SPLOT observing runs, was fairly limited. The polarised standard star q and u values for the B, V, and R filters were obtained from Fossati et al. (2007). The Z-band polarisation values for BD-12 5133 were estimated using the formula for the Serkowski parameters (Serkowski et al., 1975) defined as

$$P_\lambda = P_{\lambda_{\max}} e^{-\mathrm{K}\ln^2\left(\frac{\lambda_{\max}}{\lambda}\right)} \tag{5.1}$$

where $P_{\lambda_{\max}} = 4.37(\pm0.01)\%$, $\lambda_{\max} = 505(\pm3.5)$ nm and $\mathrm{K} = 1.20(\pm0.04)$ from observations given in Cikota et al. (2017). Some evidence suggests that the polarised standard star Vela 1 95 may exhibit some polarimetric variability, but this is thought to be small (Fossati et al., 2007).

I think it is important to highlight that the polarised standard stars are not an integral part of this calibration. However, the observations can be used to check if the calibration method can recreate the q, u, and θ_P values from the literature. The properties of both the polarised and unpolarised standard stars are displayed in Table 5.1.

Table 5.1: Standard stars observed during the three SPLOT runs. All polarised and unpolarised standards were observed in B, V, and R filters during the first run. All unpolarised standard stars and BD$-$12 5133 were observed in Z-band during the second run. The polarised standard stars with B, R, and V filter q and u and associated uncertainty values were taken from Fossati et al. (2007). The Z-band values for BD$-$12 5133 were derived using observations from Cikota et al. (2017). The unpolarised standard stars are assumed to have $q = 0$ and $u = 0$ at all wavelengths.

Object	q ($\times 100\%$)	u ($\times 100\%$)	Mag (V)	Exp. time (s)
BD$-$12 5133	$B : 1.87(\pm 0.04)$	$-3.95(\pm 0.05)$	10.4	1
	$V : 1.75(\pm 0.04)$	$-4.00(\pm 0.04)$		
	$R : 1.63(\pm 0.02)$	$-3.68(\pm 0.02)$		
	$Z : 1.00(\pm 0.02)$	$-2.75(\pm 0.06)$		
Hilt 652	$B : 5.70 \pm 0.01$	-0.11 ± 0.03	10.8	1, 2
	$V : 6.24 \pm 0.03$	-0.18 ± 0.04		
	$R : 6.07 \pm 0.02$	-0.18 ± 0.04		
Vela 1 95	$B : 7.12 \pm 0.05$	-1.66 ± 0.03	12.1	2
	$V : 7.91 \pm 0.05$	-2.38 ± 0.06		
	$R : 7.56 \pm 0.06$	-2.32 ± 0.03		
WD 1344+106	0	0	55.1	20
WD 1615$-$154	0	0	13.4	4
WD 1620$-$391	0	0	11.0	2
WD 2039$-$202	0	0	12.4	2
WD 2359$-$434	0	0	13.0	3

To obtain the measured q and u values for the standard stars I followed the same analysis described in Section 4.5.

5.2.1 First observing run: 2016 June 19, 20 and 22

Below I present all standard star observations taken during the first SPLOT observing run using EFOSC2. See Tables 5.2 and 5.3 for the properties of the unpolarised and polarised stars and properties.

Table 5.2: Observations of all unpolarised standard stars for the first observing run. Errors quoted are 1σ. The mid point of the observation is taken from the beginning of the third half-wave plate angle.

Object	Filter	Obs. date (mid, MJD)	Parallactic angle (mid; degrees)	q ($\times100\%$)	u ($\times100\%$)
WD 1344+106	V	57558.9832	-160.01	$-2.40(\pm0.17)$	$2.66(\pm0.13)$
	B	57558.9859	-161.19	$-2.68(\pm0.26)$	$2.10(\pm0.20)$
	R	57558.9886	-162.39	$-1.75(\pm0.14)$	$3.39(\pm0.11)$
WD 1615−154	V	57560.0979	-146.41	$-3.07(\pm0.15)$	$0.96(\pm0.12)$
	B	57560.0999	-148.16	$-2.95(\pm0.16)$	$0.59(\pm0.12)$
	R	57560.1019	-149.99	$-3.29(\pm0.15)$	$1.94(\pm0.12)$
	V	57560.1614	142.14	$3.08(\pm0.16)$	$1.19(\pm0.13)$
	B	57560.1634	140.68	$2.40(\pm0.16)$	$1.22(\pm0.13)$
	R	57560.1653	139.30	$3.82(\pm0.16)$	$0.39(\pm0.13)$
	V	57561.9884	-115.78	$-2.22(\pm0.13)$	$-2.17(\pm0.10)$
	B	57561.9905	-115.88	$-1.66(\pm0.15)$	$-2.29(\pm0.12)$
	R	57561.9925	-115.99	$-3.00(\pm0.13)$	$-2.23(\pm0.11)$
	V	57562.1725	131.98	$3.56(\pm0.34)$	$-0.46(\pm0.29)$
	B	57562.1745	131.01	$3.05(\pm0.27)$	$0.59(\pm0.16)$
	R	57562.1766	130.08	$4.16(\pm0.33)$	$-0.44(\pm0.27)$
WD 1620−391	V	57559.0593	-73.86	$1.91(\pm0.07)$	$-2.60(\pm0.05)$

Table 5.2: continued . . .

Object	Filter	Obs. date	Parallactic angle	q	u
		(mid, MJD)	(mid; degrees)	($\times 100\%$)	($\times 100\%$)
	B	57559.0612	-73.09	$2.04(\pm 0.07)$	$-2.08(\pm 0.06)$
	R	57559.0631	-72.31	$2.07(\pm 0.07)$	$-3.07(\pm 0.05)$
	V	57559.1679	49.13	$-3.28(\pm 0.07)$	$-0.72(\pm 0.05)$
	B	57559.1698	50.86	$-2.60(\pm 0.07)$	$-1.32(\pm 0.05)$
	R	57559.1716	52.47	$-3.74(\pm 0.07$	$-0.79(\pm 0.05)$
	V	57560.0292	-83.04	$1.05(\pm 0.10)$	$-3.07(\pm 0.07)$
	B	57560.0310	-82.51	$1.36(\pm 0.10)$	$-2.77(\pm 0.08)$
	R	57560.0328	-81.98	$0.72(\pm 0.09)$	$-3.60(\pm 0.07)$
WD 2039$-$202	V	57559.2199	-113.55	$-2.34(\pm 0.13)$	$-2.48(\pm 0.10)$
	B	57559.2218	-113.74	$-1.55(\pm 0.15)$	$-2.45(\pm 0.11)$
	R	57559.2237	-113.93	$-2.86(\pm 0.13)$	$-2.36(\pm 0.10)$
	V	57560.2688	-127.13	$-3.13(\pm 0.13)$	$-1.17(\pm 0.10)$
	B	57560.2707	-128.24	$-2.63(\pm 0.15)$	$-1.38(\pm 0.11)$
	R	57560.2726	-129.42	$-3.81(\pm 0.13)$	$-0.52(\pm 0.10)$
	V	57560.4149	112.67	$2.35(\pm 0.14)$	$-2.38(\pm 0.11)$
	B	57560.4168	112.56	$2.66(\pm 0.16)$	$-1.60(\pm 0.13)$
	R	57560.4187	112.46	$2.24(\pm 0.15)$	$-3.05(\pm 0.11)$
WD 2359$-$434	V	57559.3374	-80.87	$1.25(\pm 0.15)$	$-3.07(\pm 0.12)$
	B	57559.3393	-80.27	$1.44(\pm 0.20)$	$-2.62(\pm 0.15)$
	R	57559.3413	-79.66	$1.07(\pm 0.13)$	$-3.46(\pm 0.10)$
	V	57559.4309	-25.40	$2.44(\pm 0.14)$	$2.28(\pm 0.11)$
	B	57559.4329	-23.19	$1.14(\pm 0.19)$	$2.47(\pm 0.14)$
	R	57559.4348	-20.90	$2.88(\pm 0.12)$	$2.65(\pm 0.09)$
	V	57562.2912	-91.09	$-0.91(\pm 0.98)$	$-4.07(\pm 0.53)$
	B	57562.2931	-90.62	$-0.81(\pm 0.97)$	$-2.70(\pm 0.91)$
	R	57562.2950	-90.15	$0.17(\pm 0.46)$	$-3.54(\pm 0.36)$

Table 5.2: continued . . .

Object	Filter	Obs. date (mid, MJD)	Parallactic angle (mid; degrees)	q ($\times 100\%$)	u ($\times 100\%$)
	V	57562.3048	-87.68	$0.36(\pm 0.28)$	$-3.20(\pm 0.25)$
	B	57562.3068	-87.18	$1.08(\pm 0.47)$	$-2.39(\pm 0.34)$
	R	57562.3087	-86.67	$0.09(\pm 0.27)$	$-3.90(\pm 0.18)$
	V	57562.4243	-23.60	$2.35(\pm 0.21)$	$2.56(\pm 0.16)$
	B	57562.4262	-21.35	$1.31(\pm 0.25)$	$3.10(\pm 0.21)$
	R	57562.4282	-19.05	$2.44(\pm 0.17)$	$2.87(\pm 0.13)$

Table 5.3: Observations of all polarised standard stars for the first observing run. Errors quoted are 1σ. The mid point of the observation is taken from the beginning of the third half-wave plate angle.

Object	Filter	Obs. date (mid, MJD)	Parallactic angle (mid; degrees)	q ($\times 100\%$)	u ($\times 100\%$)
BD$-$12 5133	V	57562.2671	139.50	7.00($\pm$0.10)	2.86($\pm$0.07)
	V	57562.2688	138.54	7.06($\pm$0.10)	2.89($\pm$0.09)
	B	57562.2707	137.59	6.23($\pm$0.19)	3.80($\pm$0.14)
	B	57562.2724	136.71	6.31($\pm$0.34)	3.52($\pm$0.28)
	R	57562.2743	135.82	7.54($\pm$0.17)	1.19($\pm$0.14)
	R	57562.2760	135.01	7.66($\pm$0.13)	1.25($\pm$0.07)
Hilt 652	V	57562.2486	97.52	0.31($\pm$0.13)	3.67($\pm$0.09)
	V	57562.2504	97.64	0.27($\pm$0.07)	3.75($\pm$0.06)
	B	57562.2522	97.77	$-$0.56($\pm$0.21)	3.67($\pm$0.17)
	B	57562.2540	97.89	$-$0.62($\pm$0.14)	3.44($\pm$0.11)
	R	57562.2559	98.03	0.92($\pm$0.09)	2.87($\pm$0.07)
	R	57562.2577	98.16	0.89($\pm$0.05)	2.78($\pm$0.04)
Vela 1 95	V	57558.9728	84.17	1.45($\pm$0.12)	4.65($\pm$0.09)
	B	57558.9747	84.71	0.19($\pm$0.36)	4.17($\pm$0.27)
	R	57558.9765	85.24	1.64($\pm$0.06)	3.47($\pm$0.05)
	V	57559.9767	86.07	1.39($\pm$0.12)	4.68($\pm$0.09)
	B	57559.9785	86.59	0.40($\pm$0.33)	4.85($\pm$0.26)
	R	57559.9804	87.10	1.76($\pm$0.06)	3.39($\pm$0.05)
	V	57561.9775	87.80	1.55($\pm$0.12)	4.55($\pm$0.09)
	B	57561.9793	88.32	0.81($\pm$0.37)	5.35($\pm$0.29)
	R	57561.9812	88.82	2.09($\pm$0.06)	3.33($\pm$0.05)

5.2.2 Second observing run: 2017 August 7-9

Below I present all standard star observations taken during the second SPLOT observing run using SofI. See Table 5.4 and 5.5 for the properties of the unpolarised and polarised stars and properties.

Table 5.4: Observations of unpolarised standard stars from the second observing run, taken in the Z-band filter. Errors quoted are 1σ. The mid point of the observation is taken from the beginning of the third half-wave plate angle.

Object	Obs. Date (mid, MJD)	Parallactic Angle (mid, degrees)	q ($\times 100\%$)	u ($\times 100\%$)
WD 0310-688	57973.2626	-80.1	$-4.36(\pm 0.20)$	$-1.90(\pm 0.15)$
	57973.3567	-43.3	$0.05(\pm 0.21)$	$-4.63(\pm 0.16)$
	57973.4007	-23.3	$2.55(\pm 0.19)$	$-3.34(\pm 0.15)$
	57974.3143	-59.8	$-2.16(\pm 0.17)$	$-4.28(\pm 0.13)$
	57974.4247	-10.2	$4.13(\pm 0.17)$	$-1.69(\pm 0.13)$
WD 1344+106	57972.9930	139.5	$0.51(\pm 0.36)$	$-4.22(\pm 0.29)$
	57973.9927	138.9	$0.79(\pm 0.29)$	$-4.14(\pm 0.22)$
WD 1615-154	57973.0455	133.0	$0.11(\pm 0.27)$	$-4.47(\pm 0.21)$
WD 1620-391	57973.1131	85.9	$-4.50(\pm 0.15)$	$0.56(\pm 0.12)$
	57974.1577	96.4	$-4.18(\pm 0.15)$	$-1.08(\pm 0.11)$
	57975.0302	50.0	$-0.33(\pm 0.24)$	$4.03(\pm 0.19)$
WD 2359-434	57973.1813	-87.3	$-4.14(\pm 0.19)$	$-0.62(\pm 0.15)$
	57973.3807	60.1	$-1.73(\pm 0.19)$	$3.71(\pm 0.14)$
	57974.2676	-50.6	$-1.14(\pm 0.26)$	$-4.37(\pm 0.20)$

Table 5.5: Observations of the polarised standard star BD$-$12 5133 standard stars from the second observing run, taken in the Z-band filter. Errors quoted are 1σ. The mid point of the observation is taken from the beginning of the third half-wave plate angle.

Object	Obs. Date (mid, MJD)	Parallactic Angle (mid, degrees)	q ($\times 100\%$)	u ($\times 100\%$)
BD$-$12 5133	57974.1671	128.11	$0.35(\pm 0.20)$	$-2.91(\pm 0.15)$
	57975.0179	-129.06	$0.15(\pm 0.29)$	$1.07(\pm 0.23)$

5.3 Calibration Method

5.3.1 Analytical model

The first approach to characterising the instrumental polarisation of the NTT arose from previous work by Heidt & Nilsson (2011). Their investigation concluded that the instrumental polarisation could be well modelled by fitting unpolarised standard star observations with a simple, analytical function; in this case it was a cosine curve. I used the following relations

$$
\begin{aligned}
q &= A\cos(2\theta_{pa} - \theta_0) \\
u &= A\cos(2\theta_{pa} - (\theta_0 + 90))
\end{aligned}
$$
(5.2)

where A is the amplitude of the cosine wave (and instrumental polarisation), θ_{pa} is the parallactic angle, and θ_0 is an angular offset, to fit the data. The data were fit together and, for a given wavelength, it is expected that the amplitude of q and u should be equal and the phase difference between q and u data to be $90\,\mathrm{deg}$. At first, I fit the above relations separately to test that the amplitudes and offsets were correct. I then fit them simultaneously.

It is clear from the observations that both q and u are continuous, random discrete variables that are normally distributed. For n observations, they both follow a normal likelihood function of the form

$$
p(x|\theta) = \prod_{i=1}^{n}(2\pi\sigma^2)^{-\frac{1}{2}}e^{-\frac{(x_i-\mu)^2}{2\sigma^2}}
$$
(5.3)

where μ is the mean and σ^2 is the variance. To find the best-fit model, you can maximise the likelihood function or minimise the log-likelihood function. The combined log-likelihood for q and u can be written as

$$\ln[p(x|\theta)] = -\frac{1}{2}\left[\sum_{i=1}^{n}\frac{(q_i - qm_i)^2}{\sigma_{q_i}^2} + \frac{(u_i - um_i)^2}{\sigma_{u_i}^2} + \ln(4\pi^2\sigma_{q_i}^2\sigma_{u_i}^2)\right] \qquad (5.4)$$

where qm_i and um_i are the model estimates of q and u at the same θ_{pa} as the observations q_i and u_i.

This method was only used for the EFOSC2 data during the first observing run. The analytical method was not used for the SofI data. See Section 5.4 for results.

5.3.2   Mueller matrix method

A more thorough method was attempted to fully calibrate the instrumental polarisation. The analytical model could not correctly perform cross-talk calibration (see Section 5.4) and requires a large number of unpolarised star observations to constrain the cosine curve. This would reduce the amount of time used for target sources during an observing run.

A physical model, based on the telescopic configuration with all of the optical elements that the beam of light passes through, can be used (Tinbergen, 2007), and has been used for other Nasmyth mounted polarimeters (Giro et al., 2003; Joos et al., 2008; Covino et al., 2014). This method uses a chain of Mueller matrices which directly modify the Stokes vector which describes the properties of the observed light. The Mueller matrices describe the key components of the NTT setup, including the tertiary mirror (M3) highlighted in Figure 5.1, the most significant contributor to the instrumental polarisation. The mirror contribution is significant for two reasons. Firstly, it is coated in aluminium with a complex refractive index, described by the following relation

$$n_c = n - ik \qquad (5.5)$$

where n is the refractive index and k is the coefficient of extinction. Secondly, the M3 mirror reflects the incoming light from the secondary mirror (M2) at an angle of $45\,\mathrm{deg}$. These two

effects strongly polarise the incoming light. I calculated n and k for the B, V, R, and Z filters using the data supplied in Rakic et al. (1998). I used these wavelength-dependent values of the complex refractive indices in conjunction with the method described in (Stenflo, 1994) to derive the physical properties, and the matrices, of the M3 mirror. Aluminium slowly oxidises when exposed to air. This will, over time, affect the refractive index of the mirror. The refractive index of the mirror may also change if the mirror is disturbed; with a new coating or washed (van Harten et al., 2009). This taken into account by fitting for parameter f, a multiplication factor for the refractive index or the M3 mirror.

Figure 5.3 illustrates the configuration of the NTT and the path of the incoming light through the telescope and towards the instrument and detector. The model for the NTT comprises of five Mueller matrices, each representing a step of the calibration process. The matrix chain described below follows a very similar setup to the method described in Giro et al. (2003) for the TNG. The ordering of the matrices in Figure 5.3 works backwards from the detector. This arises as the matrix chain takes the measured Stokes vector at the detector and modifies the Stokes vector to recreate the incoming, undisturbed source signal.

The total matrix chain for the NTT comprises of the following five matrices

$$
\begin{aligned}
[M_{\text{NTT}}] = {} & [T(\phi_{\text{offset}})] \times [T(-\theta_{\text{pa}})] \times [M_{M3}(45 \deg; \lambda)] \\
& \times [T(-\theta_{\text{pa}})] \times [M_{M3}(0 \deg)]
\end{aligned}
\tag{5.6}
$$

where M_{NTT} represents the total NTT matrix chain. The matrices each perform a specific function:

(i) A rotation matrix is required to transform back from the detector coordinate frame to the M3 reference through an angle ϕ_{offset}: $[T(\phi_{\text{offset}})]$.

(ii) A second rotation matrix is required to transform from the derotator focal plane into the M3 focal plane: $[T(-\theta_{\text{pa}})]$.

(iii The third matrix represents the M3 mirror physical properties including the wavelength-dependent complex refractive index and the reflecting angle at $45 \deg$ from the mount: $[M_{M3}(45 \deg; \lambda)]$.
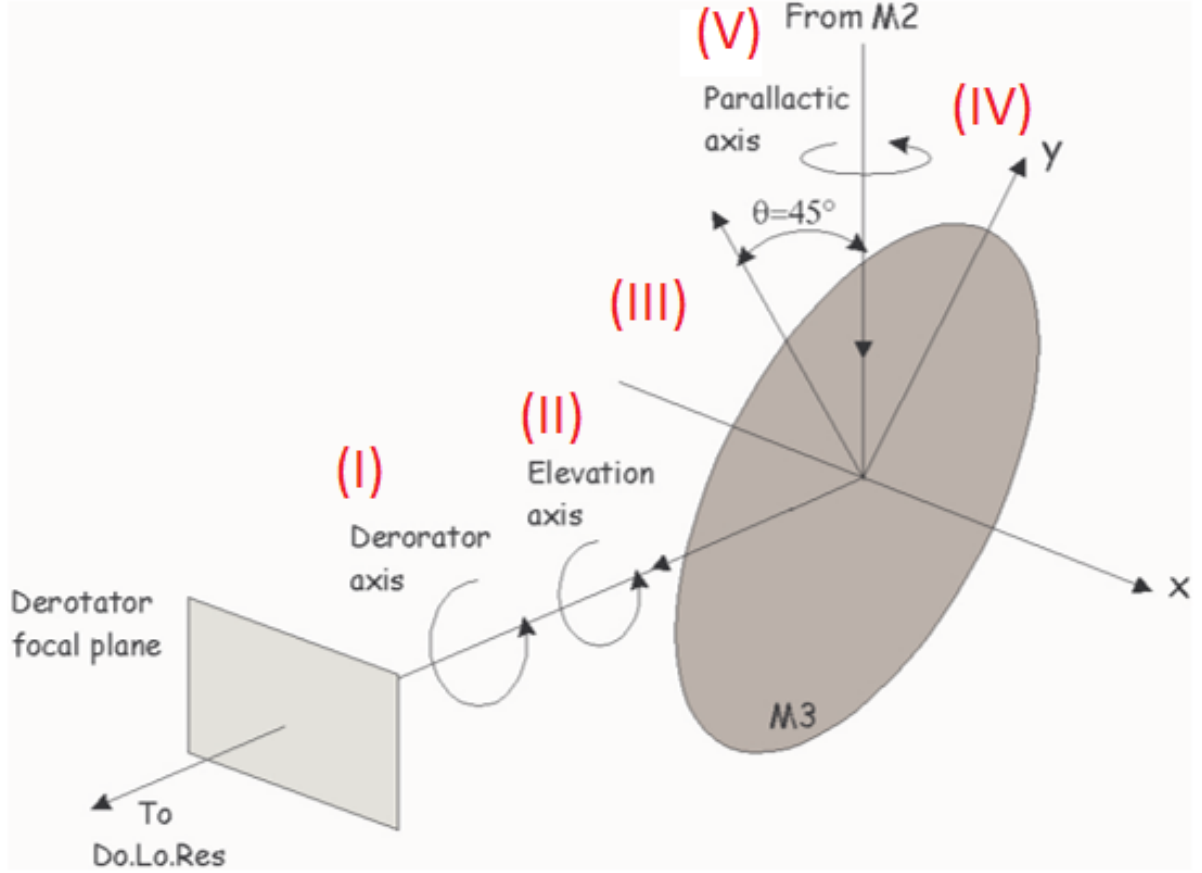
Figure 5.3: Telescope configuration of the TNG, which is very similar to the NTT, adapted from Giro et al. (2003). I have highlighted the five physical steps where the Mueller matrices describe the setup (red).

(iv) The fourth matrix is a third rotation matrix required to convert from the mirror coordinate reference frame to the sky coordinates reference frame, which is dependent on θ_{pa}: $[T(-\theta_{\mathrm{pa}})]$

(v) The final matrix represents the M2 mirror (equivalent in properties to a $0\,\mathrm{deg}$ reflection of the M3 mirror) where the incoming light originates. The numerical result of this matrix is to inverse the sign of u: $[M_{M3}(0\,\mathrm{deg})]$.

The numerical composition of each stage is described by the following matrices

$$
[T(\phi_{\text{offset}})] = \begin{bmatrix} 1 & 0 & 0 & 0 \\ 0 & \cos(2\phi_{\text{offset}}) & \sin(2\phi_{\text{offset}}) & 0 \\ 0 & -\sin(2\phi_{\text{offset}}) & \cos(2\phi_{\text{offset}}) & 0 \\ 0 & 0 & 0 & 1 \end{bmatrix} \tag{5.7}
$$

where ϕ_{offset} represents the offset angle between the mirror reference frame and the detector frame,

$$
[T(-\theta_{pa})] = \begin{bmatrix} 1 & 0 & 0 & 0 \\ 0 & \cos(2\theta_{\text{pa}}) & -\sin(2\theta_{\text{pa}}) & 0 \\ 0 & \sin(2\theta_{\text{pa}}) & \cos(2\theta_{\text{pa}}) & 0 \\ 0 & 0 & 0 & 1 \end{bmatrix} \tag{5.8}
$$

where θ_{pa} is taken from the start of the third half-wave plate observation,

$$
[M_{M3}(45\,\text{deg}; B)] = \begin{bmatrix} 0.9726 & 0.0274 & 0 & 0 \\ 0.0274 & 0.9726 & 0 & 0 \\ 0 & 0 & -0.9399 & -0.2484 \\ 0 & 0 & 0.2484 & -0.9399 \end{bmatrix},
$$

$$
[M_{M3}(45\,\text{deg}; V)] = \begin{bmatrix} 0.9699 & 0.0301 & 0 & 0 \\ 0.0301 & 0.9699 & 0 & 0 \\ 0 & 0 & -0.9487 & -0.1993 \\ 0 & 0 & 0.1993 & -0.9487 \end{bmatrix},
$$

$$
[M_{M3}(45\,\text{deg}; R)] = \begin{bmatrix} 0.9666 & 0.0334 & 0 & 0 \\ 0.0334 & 0.9666 & 0 & 0 \\ 0 & 0 & -0.9510 & -0.1700 \\ 0 & 0 & 0.1700 & -0.9510 \end{bmatrix}, \tag{5.9}
$$

$$
[M_{M3}(45\,\text{deg}; Z)] = \begin{bmatrix} 0.9607 & 0.0392 & 0 & 0 \\ 0.0392 & 0.9607 & 0 & 0 \\ 0 & 0 & -0.9458 & -0.1536 \\ 0 & 0 & 0.1536 & -0.9458 \end{bmatrix},
$$

where the physical mirror properties are wavelength dependent and

$$[M_{M3}(0\deg)] = \begin{bmatrix} 1 & 0 & 0 & 0 \\ 0 & 1 & 0 & 0 \\ 0 & 0 & -1 & 0 \\ 0 & 0 & 0 & -1 \end{bmatrix} \tag{5.10}$$

where this matrix is equivalent to the M3 mirror with a 0 deg reflection angle (the M2 mirror).

With the complete matrix chain, the measured Stokes vector from the detector can be written as

$$[S'] = [M_{\mathrm{NTT}}][S] \tag{5.11}$$

where $[S]$ is the Stokes vector representing the intrinsic polarisation properties of the source. I then rearranged this model for $[S]$ to get

$$[S] = [M_{\mathrm{NTT}}]^{-1}[S'] \tag{5.12}$$

where $[M_{\mathrm{NTT}}]$ is the inverse of the NTT matrix. The matrix model only has two fitting parameters, f and ϕ_{offset}. I also found the best-fit for this model using equation 5.4. The results of the matrix model are discussed in Section 5.4.

5.4 Results and discussion

5.4.1 Analytical model

Table 5.6 contains the analytical model results for the EFOSC2 data in the B, V, and R filters from observing run one.

The results from the individual fitting of q and u were fairly consistent in amplitude and angular offset. Nasmyth mounted polarimeters, such as PAOLO on the Telescopio Nazionale Galileo (TNG) have exhibited wavelength-dependent amplitude and phase differences in the instrumental polarisation curves (Covino et al., 2014). This is also seen in the results from

Table 5.6: Analytical best-fit parameter for the cosine model fit to the unpolarised standard star data for EFOSC2 B, V, and R filters. Errors quoted are 1σ.

Filter	Stokes Parameter	A	θ_0
B	q	$2.86(\pm0.05)$	$104.3(\pm1.2)$
	u	$3.07(\pm0.04)$	$103.5(\pm0.7)$
	q, u	$2.97(\pm0.28)$	$103.8(\pm0.5)$
V	q	$3.27(\pm0.06)$	$94.3(\pm1.3)$
	u	$3.32(\pm0.04)$	$94.5(\pm0.6)$
	q, u	$3.30(\pm0.24)$	$94.4(\pm0.5)$
r	q	$3.80(\pm0.05)$	$85.9(\pm0.7)$
	u	$3.73(\pm0.04)$	$87.4(\pm0.6)$
	q, u	$3.75(\pm0.21)$	$86.9(\pm0.4)$

the analytical model for EFOSC2. This was confirmed when I fit the q and u simultaneously. To test the effectiveness of this model, I corrected the polarised standard star measurements by subtracting the model values of q and u, at the observed θ_{pa}. The magnitude of P for the polarised standard stars was fairly well modelled using the cosine relation. However, the correct values of q and u, and therefore the angle of polarisation, θ_P, derived from this method did not align with the known values from the literature. This arises as the effect of cross-talk, correlations between q and u, are significant for polarised sources (Tinbergen, 2007). A crude analytical model was not sufficient to fully characterise the instrumental polarisation. In light of this, the analytical method was not used for the calibration of SofI.

5.4.2 Mueller matrix model

The matrix model fits the data very well and can remove the instrumental polarisation to a precision of $P \sim 0.1\%$ for EFOSC2 in the B, V, and R filters (see Figure 5.4) and $P \sim 0.2\%$ for the SofI Z-band data (see Figure 5.5). More importantly, the matrix model correctly recreated the polarised standard star q and u values from the literature, and can derive the correct

angle of polarisation, θ_P. I also see the same wavelength-dependent phase and amplitude of the instrumental polarisation that was exhibited in the analytical model fitting.

To get a better understanding of the distributions of the physical matrix model parameters, I used the PYTHON package EMCEE (Foreman-Mackey et al., 2013)[29]. This package utilises an implementation of Markov chain Monte Carlo (MCMC) to estimate the posterior distribution of the data. An MCMC uses 'walkers' to explore the posterior probability distribution allowing me to sample the shape of the posterior probability distribution and the marginalised distributions of both model parameters. The MCMC fit both model parameters simultaneously over the entire θ_{pa} range.

Using Bayes theorem, I can estimate the posterior distribution from the following relation

$$p(\theta|x) \propto p(x|\theta)p(\theta) \tag{5.13}$$

where $p(\theta)$ represents the prior function, $p(x|\theta)$ the likelihood function defined in equation 5.3, and x the data. In the case of my model, I defined the following prior

$$p(\theta) = \begin{cases} 1, & \text{if } 0 < f < 3 \text{ and} -180 < \phi_{\mathrm{offset}} < 180\,\mathrm{deg} \\ 0, & \text{otherwise} \end{cases} \tag{5.14}$$

where for physical values of f and ϕ_{offset} the prior is flat, and for unphysical values it is zero. Equation 5.13 can be equivalently written as the following

$$\ln[p(\theta|x)] \propto \ln[p(x|\theta)] + \ln[p(\theta)] \tag{5.15}$$

where the maximum-likelihood becomes the log-likelihood, which I defined in Equation 5.4, and $\ln[p(\theta|x)]$ represents the logarithm of the posterior probability function. I can define the log-prior as

$$\ln[p(\theta)] = \begin{cases} 0, & \text{if } 0 < f < 3 \text{ and} -180 < \phi_{\mathrm{offset}} < 180\,\mathrm{deg} \\ -\infty, & \text{otherwise} \end{cases} . \tag{5.16}$$

These walkers were uniformly spread out over the valid parameter space. The MCMC operates by using the initial set of model parameters, $\ln[p(\theta|x)]$ is calculated and stored. Then a

---

[29]http://dfm.io/emcee/current/
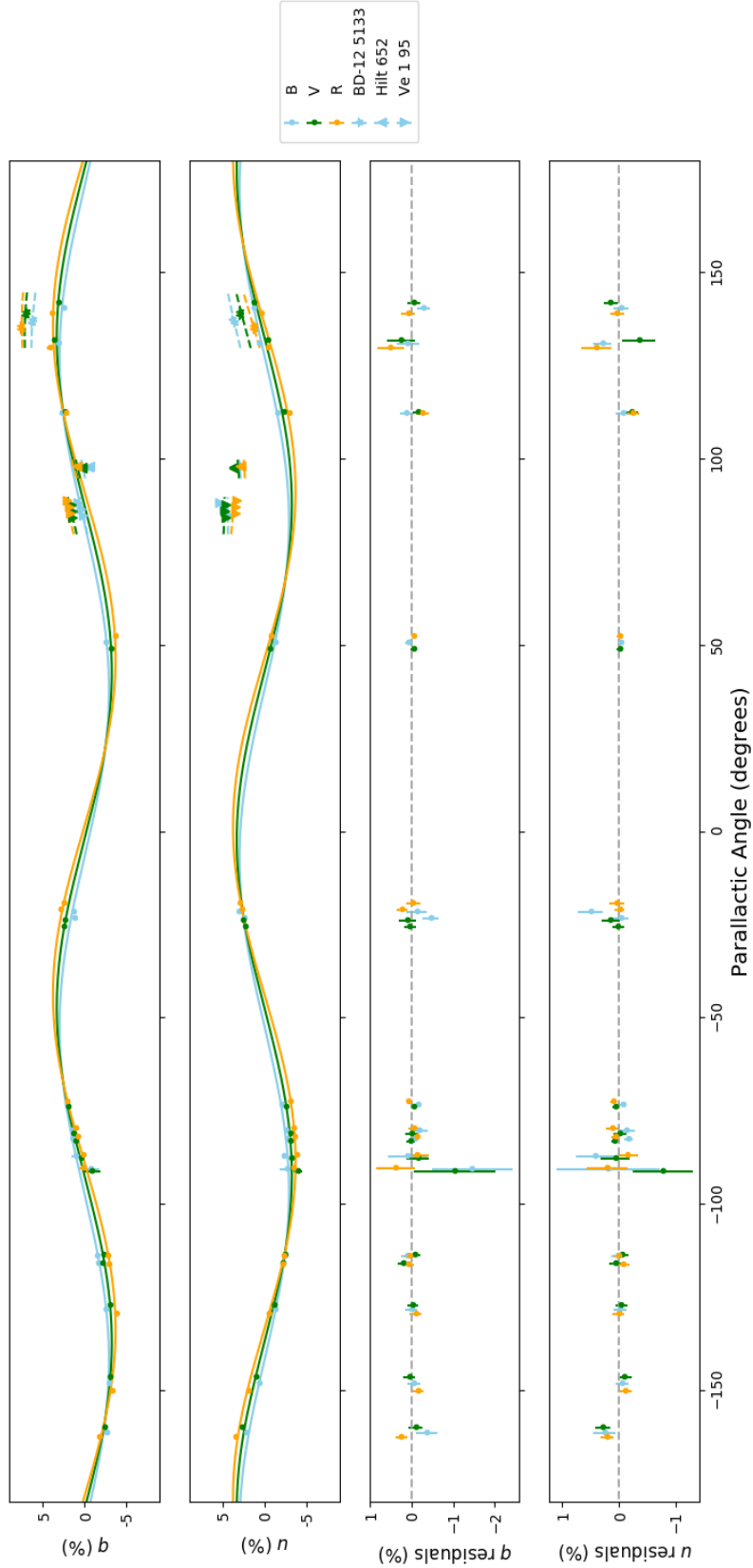
Figure 5.4: The best-fit Mueller matrix derived q (top panel) and u (second panel) models (solid lines) as a function of θ_{pa} in the EFOSC2 V, B, and R filters, overplotted with the unpolarised (circles) and polarised (triangles, stars) standard stars. The dashed lines show the model fits for the polarised standard stars. Also plotted are the model residuals for q (third panel) and u (bottom panel).
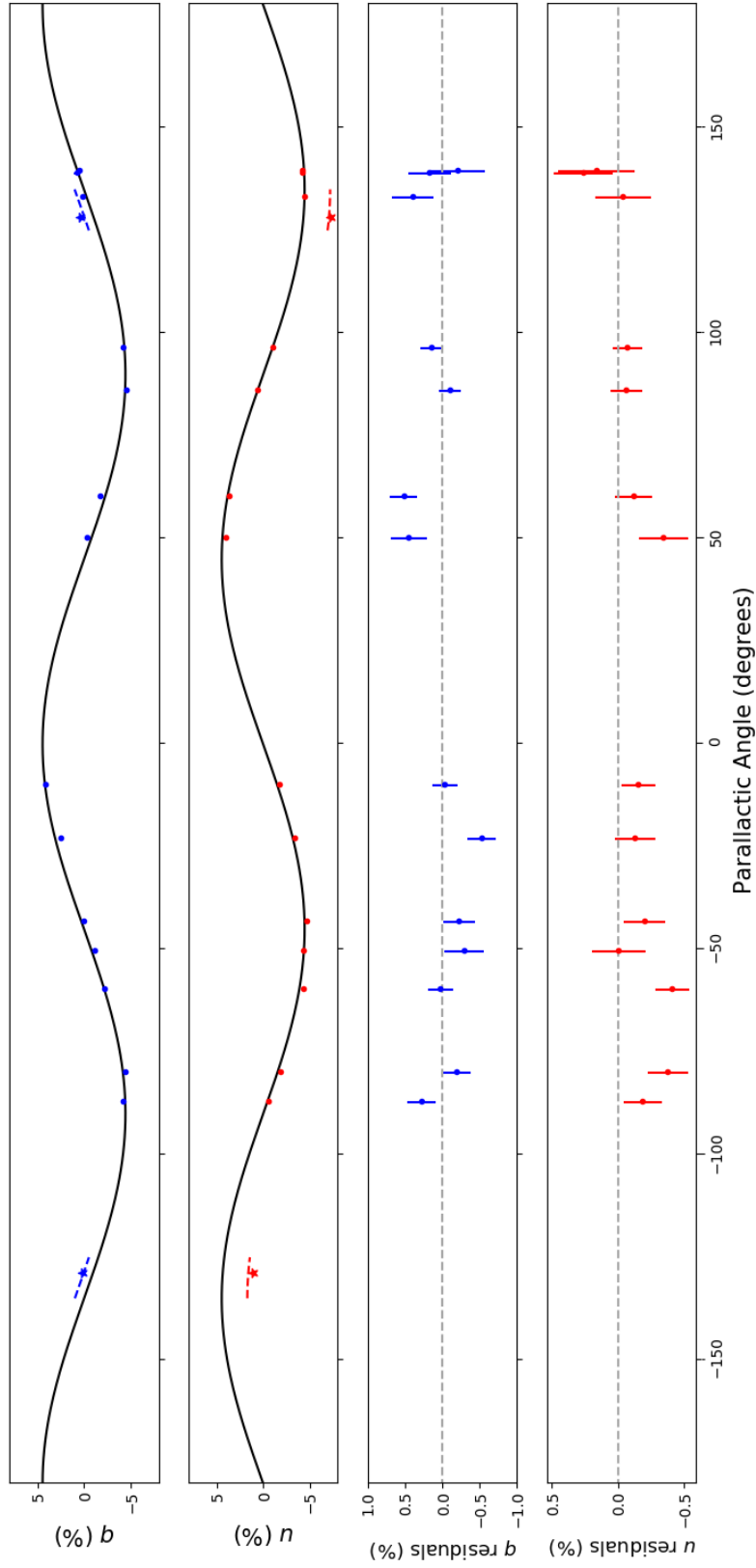
Figure 5.5: The best-fit Mueller matrix derived q (top panel) and u (second panel) models (solid lines) as a function of θ_{pa} for the SofI Z-band. The dashed lines show the model fits for BD$-$12 5133. Also plotted are the model residuals for q (third panel) and u (bottom panel).

Table 5.7: ϕ_{offset} and f estimated values from the MCMC analysis for the EFOSC2 B, R and V, and SofI Z filters. Errors quoted are 1σ. The SofI o and e beam prescription is the opposite to EFOSC2. The physical effect of this is to change the detector angle offset by $-90\,\text{deg}$. The V, B, and R filter measurements were taken in June 2016 and the Z-band measurements in 2017.

Filter	ϕ_{offset}	f
B	-51.9 ± 0.3	0.95 ± 0.01
V	-47.2 ± 0.3	0.94 ± 0.01
R	$-43.5\,^{+0.2}_{-0.3}$	0.92 ± 0.01
Z	-0.17 ± 0.3	0.92 ± 0.01

new set of model parameters are tested, and $\ln[p(\theta|x)]$ is calculated again. This is compared to the old value and if it is smaller (i.e. $p(\theta|x)$ is greater), then the walkers acquire the new values and repeat. If the number is greater, the walker may, or may not, accept the new parameters dependent on the difference between the two $\ln[p(\theta|x)]$ values. The MCMC had 20 walkers and 2500 steps and a 'burn-in' period of 250 steps.

Table 5.7 displays the model parameters for the EFOSC2 B, V, and R filters from the first observing run and SofI Z-band from the second observing run. The model parameters are well constrained and follow relatively normal distributions in all four filters (see Figure 5.6).
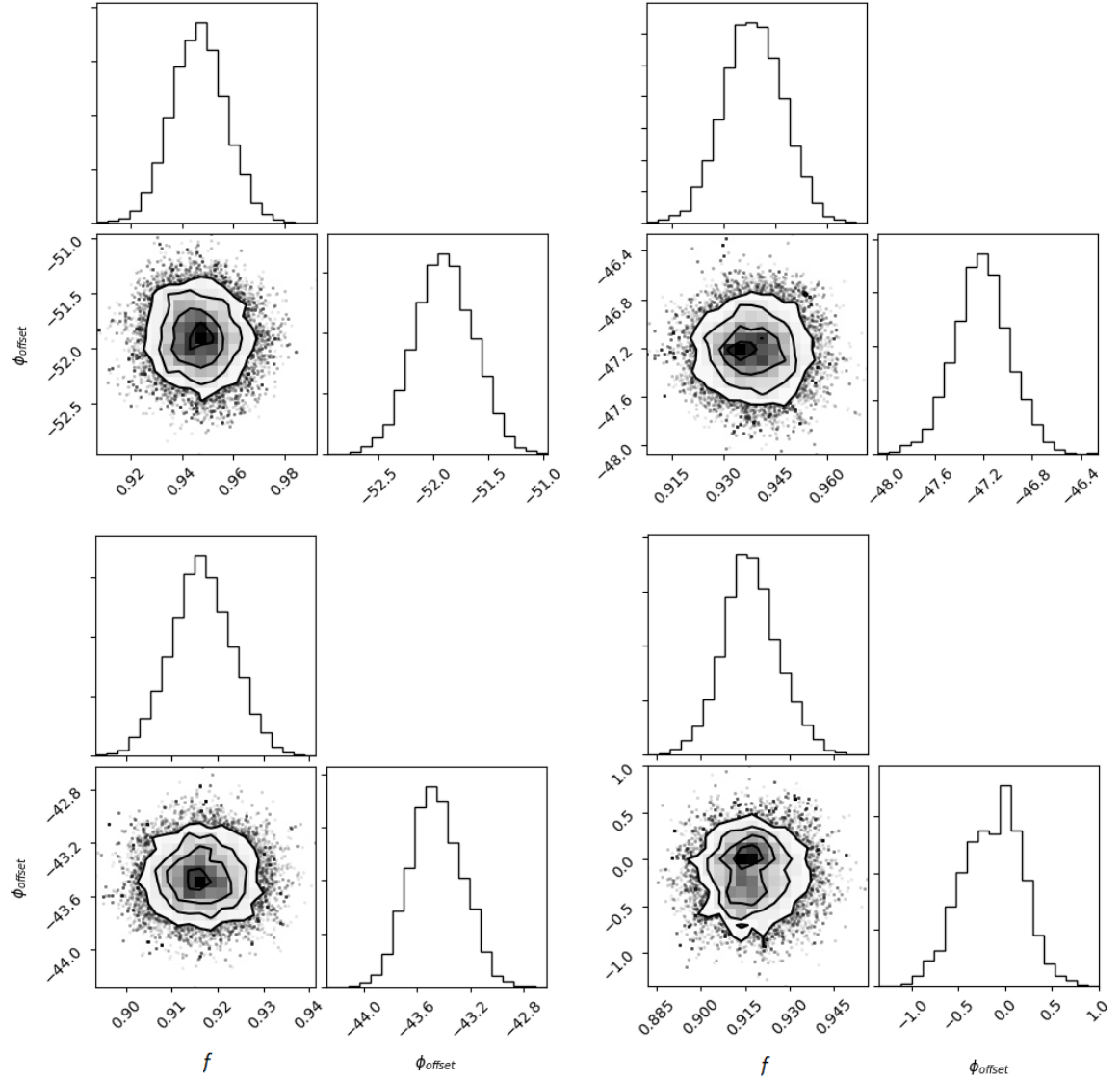
Figure 5.6: Projections of the normalised probability distributions for ϕ_{offset} and f from the MCMC analysis for the EFOSC2 B (top left), R (top right) and V (bottom left), and SofI Z (bottom right) filters.

5.5 Conclusions

I have produced a calibration pipeline of EFOSC2 and SofI linear imaging polarimetry in the B, V, R, and Z filters. The calibration uses a physically motivated, Mueller matrix model and can remove the instrumental polarisation to within $P \sim 0.1\%$ for EFOSC2 observations and $P \sim 0.2\%$ for SofI observations. This level of precision allowed me to sufficiently calibrate the SPLOT data.

Despite the fact that EFOSC2 and SofI are both mounted on similar Nasmyth platforms, and the light they receive comes from the same M3 mirror, the polarimetric setup for both instruments is quite different (as described in Section 4.5.1). It is quite remarkable that the same basic calibration method for both instruments could successfully removed the instrumental polarisation signal.

Additional filters can be easily added to the pipeline, simply by observing a number of standard stars in the desired filter and inputting the wavelength of the filter into the body of the code. The method can also be modified to work with other current or future Nasmyth mounted polarimeters.

6

Main conclusions and future work

6.1 Key thesis conclusions

The work I have presented in this thesis has covered a broad range of astrophysical transients, utilising a number of analytical techniques covering multiple wavelengths.

Chapter 2 discussed the focused investigation into the multiwavelength afterglow analysis of GRB 140713A. The GRB was well observed at X-ray and radio wavelengths but had no optical emission. Through modelling of the afterglow data, with the assistance of hydrodynamical jet simulations, I produced an estimate of the expected optical flux and explored the distributions of the physical parameters of the GRB afterglow. I determined that the source of the

optical darkness was likely due to high extinction from line-of-sight dust. Full modelling of GRB afterglows has long been essential in understanding the underlying physical properties of GRBs. This investigation adds a thorough analysis of a well sampled, optically dark GRB to a very limited sample of dark GRBs. Optically dark, dust obscured GRBs and their environments provide a unique way to both test extreme physical environments and potentially, dust-obscured star formation. Continuing to investigate this sub-set of GRBs will help to uncover the physics of these dusty environments.

I expanded the scope of my research from one source to the *INTEGRAL* IBAS GRB sample in Chapter 3. I presented a search of the *INTEGRAL* WEAK alerts for new GRBs utilising *Swift* multiwavelength follow-up. The investigation uncovered that real astrophysical events produced sub-threshold triggers (from the 15 alerts followed up, six sources had been identified, including five GRBs). I then compared the IBAS and *Swift* GRB samples to test if *INTEGRAL* could detect a fainter GRB population. I determined that both satellites observe the same underlying GRB distribution. Probing the faintest sources is always challenging and drives forward our continuous need for more sensitive instrumentation. This investigation highlighted that real transients exist in satellite sub-threshold populations. Future observations should not exclude large sets of triggers, or they risk missing out on some (potentially) very interesting sources.

My work concluded in Chapters 4 and 5 with the SPLOT survey, a pilot survey observing a whole host of astrophysical transient classes. I employed a separate observing technique, optical linear polarimetry, to determine if single-epoch polarimetry alone has the potential to quickly add scientific value to real-time transient alert streams and highlight sources of potential interest for further follow-up. In addition to the survey, I produced a full calibration pipeline for the EFOSC2 and SOFI instruments. The SPLOT survey revealed the value of polarimetry in enabling observers to pick out potential sources of interest. Polarimetry will provide an additional and invaluable tool for helping filter out new transients in the new epoch of large transient survey systems. The calibration pipeline for EFOSC2 and SofI can easily be modified to work with other current or future Nasmyth mounted polarimeters. The survey has paved the way for future larger, and possibly more sophisticated polarimetric surveys.

6.2 The future of transient astronomy

6.2.1 SPLOT II: the return of SPLOT

I embarked on a third SPLOT observing run in August 2018 utilising the EFOSC2 instrument for a second time. To expand the parameter space coverage of SPLOT, I observed a significant fraction of the ~ 30 target sources within $24 - 48$ hrs post-alert. The elapsed times between the distribution of the alert and SPLOT follow-up is, on average, greatly reduced from the first two SPLOT runs, so I can test the efficacy of SPLOT for very prompt follow-up analysis. Additionally, I observed a number of standard stars in the U and i filters. These observations will not only increase the wavelength coverage for the calibration pipeline but can investigate the variation of the instrumental polarisation at a given wavelength over time.

I have started analysing the target sources and calibration standard stars, and plan to submit a follow-up paper to SPLOT addressing the above questions (Higgins et al., in prep)

6.2.2 Multi-messenger astronomy

The immense success of the astrophysics community in observing the GW 170817 event utilising both GW and multiwavelength electromagnetic follow-up (Abbott et al., 2017a,b), has confirmed the progenitor of SGRBs, and opened up a new era of multi-messenger astronomy. Table 6.1 displays the range and detections rates of the previous two aLIGO observing runs. It also displays the expected values of future observing runs from aLIGO (including LIGO India), Advanced Virgo (aVirgo; Acernese et al. 2015) in Italy, and the Kamioka Gravitational Wave Detector (KAGRA; Aso et al. 2013) in Japan, set to come online in late 2019. It is clear that the upgrades to aLIGO and the addition of aVirgo and KAGRA will greatly improve source localisation making electromagnetic follow-up up of counterparts much more effective. The next decade of observations will shine the light on the physics of compact binary mergers and test our models on the most extreme events in the universe.

Table 6.1: Summary of the aLIGO observing runs past and future taken from Abbott et al. (2018). The 2018-2019 (O3) run is due to start in April 2019. The detection rates and ranges for binary neutron star (BNS) mergers in O3 and future runs are only estimations.

Epoch		$2015 - 2016$	$2016 - 2017$	$2018 - 2019$	$2020+$	$2024+$
Planned run duration		4 months	9 months	12 months	(per year)	(per year)
Expected burst range (Mpc)	LIGO	$40 - 60$	$60 - 75$	$75 - 90$	105	105
	Virgo	–	$20 - 40$	$40 - 50$	$40 - 70$	80
	KAGRA	–	–	–	–	100
Expected BNS range (Mpc)	LIGO	$40 - 80$	$80 - 120$	$120 - 170$	190	190
	Virgo	–	$20 - 65$	$65 - 85$	$65 - 115$	125
	KAGRA	–	–	–	–	140
Achieved BNS range (Mpc)	LIGO	$60 - 80$	$60 - 100$	–	–	–
	Virgo	–	$25 - 30$	–	–	–
	KAGRA	–	–	–	–	–
Estimated BNS detections		$0.05 - 1$	$0.2 - 4.5$	$1 - 50$	$4 - 80$	$11 - 180$
Actual BNS detections		0	1	–	–	–
BNS localisation (90% containment)	% within 5 deg^2	<1	$1 - 5$	$1 - 4$	$3 - 7$	$23 - 30$
	% within 20 deg^2	<1	$7 - 14$	$12 - 21$	$14 - 22$	$65 - 73$
	Median (deg^2)	$460 - 530$	$230 - 320$	$120 - 180$	$110 - 180$	$9 - 12$

6.2.3 Future transient missions

The rate of transients detected at optical wavelengths is also set to greatly increase over the next few years as the LSST survey is scheduled to begin in 2022[30] (Ivezic et al., 2008). Current estimates suggest that LSST will produce ~ 10 TB worth of data, detecting $>> 100$ new transients every night. In addition to an increase in optical surveys, high energy observatories such as the *SVOM* GRB mission (Götz & SVOM Collaboration, 2012), scheduled to launch in 2021, the X-ray satellite *Athena* (Barcons et al., 2015), scheduled for launch in 2028/2034, and the multiwavelength Transient High Energy Sky and Early Universe Surveyor (*THESEUS*; Amati et al. 2018) which, if selected in 2021, is scheduled for launch in 2032. With the huge advances in the numbers of transients being discovered, it will ever more important for photometry, polarimetry and spectroscopy campaigns to work in conjunction to rapidly follow-up and classify the properties of astrophysical transients.

Overall, my research has highlighted the benefit of utilising numerous observational techniques, over a broad range of wavelengths. In conjunction with physical models, the current and future observatories performing multiwavelength observations will be essential in understanding the complex physical nature of high energy transients and our observable universe.

---

[30]https://www.lsst.org/

A

GRB 140713A data tables

Below are the data tables for the multi-wavelength data used during my investigation into the cause of optical darkness in GRB 140713A.

Table A.1: AMI and WSRT observations of GRB 140713A where ΔT is the midpoint of each observation in days after the GRB trigger time. Non-detections are given as 3σ upper-limits.

Epoch	ΔT (days)	Integration time (hours)	Observatory	Frequency (GHz)	Flux (μJy)
Jul 13.784 - 13.867	0.05	2.0	AMI	15.7	< 270
Jul 14.791 - 14.958	1.09	4.0	AMI	15.7	< 180
Jul 16.884 - 17.050	3.18	4.0	AMI	15.7	$600(\pm 90)$
Jul 17.858 - 18.024	4.16	4.0	AMI	15.7	< 270
Jul 18.793 - 18.959	5.09	4.0	AMI	15.7	$780(\pm 90)$
Jul 19.687 - 20.185	6.15	12.0	WSRT	4.8	< 96
Jul 19.936 - 20.102	6.24	4.0	AMI	15.7	$840(\pm 70)$
Jul 20.943 - 21.109	7.24	4.0	AMI	15.7	$820(\pm 90)$
Jul 22.921 - 23.087	9.22	4.0	AMI	15.7	$1370(\pm 80)$
Jul 24.673 - 25.172	11.16	12.0	WSRT	4.8	$189(\pm 34)$
Jul 24.860 - 25.027	11.16	4.0	AMI	15.7	$1310(\pm 100)$
Jul 26.894 - 27.061	13.18	4.0	AMI	15.7	$1650(\pm 100)$
Jul 28.784 - 28.950	15.08	4.0	AMI	15.7	$870(\pm 70)$
Jul 30.657 - 31.155	17.11	12.0	WSRT	4.8	$205(\pm 28)$
Jul 30.807 - 30.973	17.11	4.0	AMI	15.7	$690(\pm 70)$
Aug 1.859 - 2.025	19.16	4.0	AMI	15.7	$890(\pm 70)$
Aug 3.860 - 4.026	21.16	4.0	AMI	15.7	$1050(\pm 70)$
Aug 5.815 - 5.981	23.12	4.0	AMI	15.7	$700(\pm 70)$
Aug 6.838 - 7.136	24.11	12.0	WSRT	4.8	$137(\pm 31)$
Aug 6.868 - 7.034	24.17	4.0	AMI	15.7	$790(\pm 60)$
Aug 7.635 - 8.133	25.10	12.0	GMRT	1.4	< 225
Aug 12.792 - 12.917	30.07	3.0	AMI	15.7	$710(\pm 70)$
Aug 14.871 - 14.995	32.15	3.0	AMI	15.7	$530(\pm 70)$
Aug 16.870 - 18.947	34.13	2.0	AMI	15.7	$400(\pm 60)$
Aug 18.605 - 19.103	36.07	12.0	WSRT	4.8	$189(\pm 32)$

Table A.1: continued ...

Epoch	ΔT (days)	Integration time (hours)	Observatory	Frequency (GHz)	Flux (μJy)
Aug 18.781 - 18.947	36.08	4.0	AMI	15.7	490($\pm$70)
Aug 20.786 - 20.869	38.05	2.0	AMI	15.7	< 180
Aug 23.726 - 28.014	41.03	4.0	AMI	15.7	350($\pm$50)
Aug 27.848 - 28.014	45.15	4.0	AMI	15.7	290($\pm$40)
Aug 29.823 - 29.989	47.12	4.0	AMI	15.7	270($\pm$50)
Aug 31.757 - 31.832	49.01	1.8	AMI	15.7	< 210
Sep 1.795 - 1.962	50.09	4.0	AMI	15.7	320($\pm$80)
Sep 2.596 - 3.062	51.05	12.0	WSRT	4.8	182($\pm$36)
Sep 2.683 - 2.928	51.02	5.9	AMI	15.7	180($\pm$40)
Sep 5.754 - 5.919	54.05	4.0	AMI	15.7	< 120
Sep 7.778 - 7.942	56.08	3.9	AMI	15.7	< 210
Sep 10.798 - 10.965	59.10	4.0	AMI	15.7	210($\pm$50)
Sep 14.716 - 14.882	63.02	4.0	AMI	15.7	< 150
Sep 17.543 - 18.021	66.00	12.0	WSRT	4.8	192($\pm$38)
Sep 17.658 - 17.899	66.00	5.8	AMI	15.7	< 90
Sep 23.766 - 23.932	72.07	4.0	AMI	15.7	< 120
Oct 2.482 - 2.980	80.95	12.0	WSRT	4.8	127($\pm$32)
Oct 2.590 - 2.833	80.93	5.8	AMI	15.7	< 150

Table A.2: X-ray data from *Swift*/XRT. Only data > 2000 s post-trigger were included in the modelling.

Time	Time upper	Time lower	Flux	Flux error
(s)	error (s)	error (s)	(μJy)	(μJy)
126.577	49.938	45.340	13.3	3.0
221.082	35.668	44.567	13.7	3.1
315.920	51.152	59.171	9.6	2.2
417.141	60.253	50.070	9.6	2.2
540.588	37.098	63.194	10.2	2.3
588.352	6.886	10.665	56.3	11.5
608.030	9.773	12.792	48.9	10.8
628.362	6.993	10.558	75.8	15.2
643.313	4.579	7.958	128	2.4
654.380	6.048	6.489	98.9	20.7
666.616	6.349	6.188	141	24.7
678.783	6.719	5.818	148	25.6
692.567	7.979	7.065	118	20.8
707.141	5.941	6.596	128	23.7
716.421	6.273	3.757	105	19.4
731.324	6.831	8.213	151	25.6
744.410	8.789	6.255	81.0	16.9
760.409	7.834	7.210	64.6	14.1
775.933	7.354	7.690	70.6	15.9
791.428	6.903	8.141	55.7	12.2
810.973	9.923	12.641	63.6	13.9
828.977	6.964	8.080	70.8	15.9
849.942	13.579	14.001	40.3	9.1
873.894	14.700	10.373	39.7	8.9
906.701	16.996	18.107	38.1	8.57
943.777	25.052	20.080	16.5	3.75

Table A.2: continued ...

Time	Time upper	Time lower	Flux	Flux error
(s)	error (s)	error (s)	(μJy)	(μJy)
1003.097	18.385	34.269	32.5	7.11
1038.581	20.511	17.098	18.0	4.05
1098.650	30.647	39.558	11.6	2.62
1182.440	37.121	53.143	10.6	2.32
1277.912	36.927	58.352	9.94	2.25
1385.849	49.341	71.010	12.1	2.66
1495.118	70.453	59.927	6.63	1.50
1644.579	68.923	79.009	6.41	1.24
5578.892	135.028	160.834	1.08	0.22
6699.213	170.206	188.341	0.53	0.14
6983.162	101.886	113.743	1.01	0.25
7284.625	259.255	199.576	0.66	0.14
12770.550	4737.306	1458.373	0.29	0.06
28337.081	7272.053	5607.037	0.15	0.04
49359.637	4278.079	8515.627	0.09	0.02
62601.911	2559.839	5215.479	0.11	0.02
69967.059	957.411	1028.371	0.2	0.04
142474.582	14306.700	-15209.788	0.06	0.02
162233.010	297.869	-296.361	0.08	0.06

B

INTEGRAL IBAS GRB properties

Below I have tabulated the prompt gamma-ray and X-ray data for the entire IBAS GRB sample. The data were used in Chapter 3.

Table B.1: Prompt Gamma-ray and X-ray properties of the IBAS GRB sample. Only GRBs with measured T$_{90}$ values were included. Some GRBs within the sample were not detectd by *Swift*/XRT or were very poorly sampled. I could not estimate an X-ray flux at 11 hours for these cases. Fluence values for GRB 150831, GRB 151120A, GRB 160221A, GRB 160629A are taken from the GCN Circulars (Mereghetti et al., 2015a,b, 2016; Gotz et al., 2016).

Name	Fluence [20 − 200 keV] (10^{-7} erg cm^{-2})	X-ray Flux at 11 hours [0.3 − 10 keV] (10^{-12} erg cm^{-2} s^{-1})	T$_{90}$ (s)
GRB 030227*	$6.10^{+3.50}_{-5.90}$	-	15
GRB 030320*	$54.2^{+13.3}_{-11.7}$	-	48
GRB 030501*	$17.2^{+1.60}_{-3.10}$	-	25
GRB 030529#	0.52	-	16
GRB 031203*	$10.6^{+2.70}_{-3.00}$	-	19
GRB 040106*	$95.0^{+23.0}_{-30.0}$	-	47
GRB 040223*	$27.2^{+0.80}_{-1.90}$	-	258
GRB 040323*	$20.6^{+2.30}_{-2.90}$	-	14
GRB 040403*	$4.00^{+1.60}_{-3.70}$	-	15
GRB 040422*	$4.90^{+1.00}_{-3.60}$	-	10
GRB 040624#	4.81	-	27
GRB 040730*	$6.30^{+4.40}_{-3.30}$	-	42
GRB 040812#	1.40	-	8
GRB 040827*	$11.1^{+2.80}_{-4.00}$	-	32
GRB 040903#	0.96	-	7
GRB 041015#	5.12	-	30
GRB 041218*	$58.2^{+3.50}_{-3.70}$	-	38
GRB 041219A*	$867^{+0.50}_{-129}$	-	239
GRB 050129#	4.10	-	30
GRB 050223	$10.8^{+2.70}_{-2.10}$	0.19	30
GRB 050502A*	$13.9^{+1.10}_{-4.00}$	-	> 11

Table B.1: continued . . .

Name	Fluence	X-ray Flux at 11 hours	T_{90}
	$[20 - 200\,\mathrm{keV}]$	$[0.3 - 10\,\mathrm{keV}]$	(s)
	$(10^{-7}\,\mathrm{erg\,cm^{-2}})$	$(10^{-12}\,\mathrm{erg\,cm^{-2}\,s^{-1}})$	
GRB 050504*	$10.0^{+4.10}_{-4.50}$	-	44
GRB 050520*	$16.6^{+4.90}_{-5.00}$	0.20	52
GRB 050522#	0.69	-	11
GRB 050525A*	$154^{+5.70}_{-8.40}$	1.5	9
GRB 050626*	$6.30^{+0.40}_{-1.00}$	-	52
GRB 050714A	$5.58^{+2.75}_{-1.84}$	-	34
GRB 050918*	$30.2^{+10.5}_{-9.0}$	-	280
GRB 050922A#	0.59	-	10
GRB 051105B*	$2.80^{+1.50}_{-2.00}$	-	14
GRB 051211B*	$16.1^{+4.60}_{-3.30}$	0.92	47
GRB 060114*	$16.0^{+4.60}_{-3.30}$	-	80
GRB 060130#	2.25	-	19
GRB 060204A*	$4.80^{+2.40}_{-3.30}$	-	52
GRB 060428C*	$18.6^{+2.20}_{-3.90}$	-	10
GRB 060901*	$62.2^{+3.50}_{-5.90}$	1.2	16
GRB 060930#	2.63	-	9
GRB 060912B*	$12.0^{+5.80}_{-5.10}$	-	140
GRB 061025*	$10.1^{+1.30}_{-4.80}$	0.14	11
GRB 061122*	$155^{+3.40}_{-5.30}$	2.2	12
GRB 070309	$4.93^{+3.12}_{-1.98}$	-	22
GRB 070311*	$23.6^{+1.70}_{-5.30}$	1.22	32
GRB 070615	2.01	-	15
GRB 070707	$3.58^{+4.04}_{-1.94}$	-	0.7
GRB 070925*	$36.1^{+1.70}_{-3.40}$	-	19
GRB 071003	$94.6^{+4.22}_{-2.96}$	3.5	38

Table B.1: continued ...

Name	Fluence [20 − 200 keV] (10⁻⁷ erg cm⁻²)	X-ray Flux at 11 hours [0.3 − 10 keV] (10⁻¹² erg cm⁻² s⁻¹)	T₉₀ (s)
GRB 071109*	$3.60^{+4.00}_{-3.50}$	-	30
GRB 080120	$13.2^{+17.0}_{-7.67}$	0.13	15
GRB 080603A	$12.3^{+1.70}_{-5.90}$	1.5	150
GRB 080613A*	$12.3^{+1.70}_{-5.90}$	-	30
GRB 080723B*	$396^{+6.70}_{-6.70}$	12.6	95
GRB 080922*	$17.3^{+6.90}_{-6.50}$	-	60
GRB 081003B*	$26.2^{+2.00}_{-24.5}$	-	20
GRB 081016*	$22.0^{+1.40}_{-4.50}$	-	30
GRB 081204*	$5.10^{+5.10}_{-4.80}$	-	12
GRB 090107B*	$12.4^{+1.30}_{-4.60}$	0.73	15
GRB 090625B*	$12.4^{+1.20}_{-2.00}$	0.38	8
GRB 090702	$1.93^{+1.44}_{-0.81}$	-	6
GRB 090704*	$54.0^{+4.90}_{-8.00}$	-	70
GRB 090814B*	$15.1^{+2.30}_{-2.40}$	1.4	42
GRB 090817*	$18.7^{+10.9}_{-9.80}$	2.4	30
GRB 091111	$20.0^{+5.90}_{-0.82}$	-	100
GRB 091202	$7.03^{+3.02}_{-2.35}$	-	25
GRB 091230	$17.9^{+20.5}_{-9.57}$	-	70
GRB 100103A*	$52.5^{+2.10}_{-4.00}$	2.1	30
GRB 100518A*	$5.20^{+4.40}_{-3.80}$	0.87	25
GRB 100713A	$5.65^{+2.65}_{-1.80}$	0.20	20
GRB 100909A	$21.5^{+7.00}_{-4.70}$	0.26	60
GRB 101112A*	$21.1^{+4.40}_{-7.40}$	0.50	6
GRB 110206A	$17.2^{+11.6}_{-6.10}$	2.0	15
GRB 110708A*	$24.8^{+1.90}_{-4.60}$	-	50

Table B.1: continued . . .

Name	Fluence [20 − 200 keV] (10^{-7} erg cm^{-2})	X-ray Flux at 11 hours [0.3 − 10 keV] (10^{-12} erg cm^{-2} s^{-1})	T$_{90}$ (s)
GRB 110903A[*]	$148^{+11.9}_{-17.5}$	3.8	430
GRB 120202A	$8.00^{+2.10}_{-7.70}$	-	70
GRB 120419A	$3.88^{+6.18}_{-2.49}$	-	15
GRB 120711A	$440^{+50.0}_{-5.00}$	40	135
GRB 121102A	$24.1^{+12.4}_{-8.10}$	0.56	25
GRB 121212A	1.50	0.46	10
GRB 130513A	$17.0^{+10.3}_{-6.50}$	-	50
GRB 130514B	$10.2^{+14.4}_{-6.20}$	1.6	10
GRB 130903A	$17.1^{+8.10}_{-5.40}$	-	70
GRB 131122A	$24.8^{+12.3}_{-8.20}$	-	80
GRB 140206A	$16.0^{+3.00}_{-3.00}$	9.2	> 60
GRB 140320B	$12.7^{+11.8}_{-5.94}$	0.55	100
GRB 140320C	3.52	-	30
GRB 140815A	$5.00^{+5.10}_{-2.59}$	-	8
GRB 141004A	$6.92^{+6.88}_{-3.40}$	0.09	4
GRB 150219A	$57.1^{+14.9}_{-11.2}$	0.62	60
GRB 150305A	$12.1^{+14.2}_{-6.45}$	-	100
GRB 150831A	≈ 3	0.33	2
GRB 151120A	≈ 20	0.66	50
GRB 160221A	≈ 5	-	10
GRB 160629A	≈ 60	-	100

[*] Fluence values taken from Bošnjak et al. (2014).

[#] Fluence values taken from Vianello et al. (2009).

C

SPLOT individual source information

Below I outline the polarisation and photometry results for each individual source. I have added information on source classification from additional follow-up. Additionally, if any historic observations were made for a source, I have detailed this information and compared it to the SPLOT data. Where available, I have collated any photometry and polarisation data from independent observations such as data from the Steward Observatory spectropolarimetric monitoring project (Smith et al., 2009), the *Gaia* transient alert system (Wyrzykowski & Hodgkin, 2012; Hodgkin et al., 2013) and the ASAS-SN Sky Patrol (Shappee et al., 2014; Kochanek et al., 2017). To attempt to quantify the Galactic dust contribution to the measured polarisation, I used the following relation

$$P_{\text{Gal,dust}} \leq 9 \times E(B - V)\% \tag{C.1}$$

where $E(B-V)$ is the Galactic colour excess (Serkowski et al., 1975). $E(B-V)$ was calculated using the method described in Schlafly & Finkbeiner (2011). For sources with independent *Gaia* light curve data only, I have displayed the figures together at the end of this section (see Figure C.5). For the few sources with independent data from other sources, I have produced independent figures, which are displayed within the individual source sections.

3C 454.3: This well observed Blazar has historically entered into periods of increased activity (Hunstead, 1972; Pauliny-Toth et al., 1987; Raiteri et al., 2007) and is one of the most luminous gamma-ray sources in the sky (see Ackermann et al. 2010 and Britto et al. 2016 for record *Fermi* observations). The source entered a recent outburst period on 2016 June 11 which was detected by a number of observatories (Jorstad, 2016; Lucarelli et al., 2016; Ojha, 2016). The source was observed twice as part of the SPLOT survey, on 2016 June 20 and 22. I found that the source exhibited significant levels of linear polarisation, $P = 11.70(\pm0.05)\%$ in V-band on June 20 and $P = 16.43(\pm0.14)\%$, $P = 17.56(\pm0.14)\%$ and $P = 13.29(\pm0.34)\%$ on June 22 in the V, B, and R bands. Over the two nights, the V-band angle of polarisation varied from $\theta = 54.7(\pm0.12)$ deg $\theta = 18.43(\pm0.24)$ deg. I calculated from $E(B-V) = 0.09$ that $P_{\mathrm{Gal,dust}} \leq 0.81\%$. Figure C.1 illustrated that the SPLOT observations were taken as 3C 454.3 entered a period of high activity. The significant variation of the V-band polarisation measurements in a short time period are consistent with previous measurements (Smith et al., 2009; Sasada et al., 2012)).

ASASSN-16fp: The source, also known as AT2016coi, Gaia16arp, PS16cvj and SN2016coi, was discovered on 2016 May 27 in the galaxy UGC 11868 (Holoien et al., 2016). Initially, this source was spectroscopically classified as a type Ic, broad line SN (Elias-Rosa et al., 2016). However, analysis highlighted Helium I absorption lines in the early-time spectrum. Yamanaka et al. (2017) proposed that ASASSN-16fp was a type Ib, broad line SN. The SPLOT observation was taken $\sim$ three weeks post-alert. I measured a polarisation of $P < 0.08\%$, $P = 0.34(\pm0.05)\%$ and $P < 0.10\%$ in the V, B, and R bands. See Figure C.5 for photometry information. I estimated from $E(B-V) = 0.07$ that $P_{\mathrm{Gal,dust}} \lesssim 0.6\%$. This
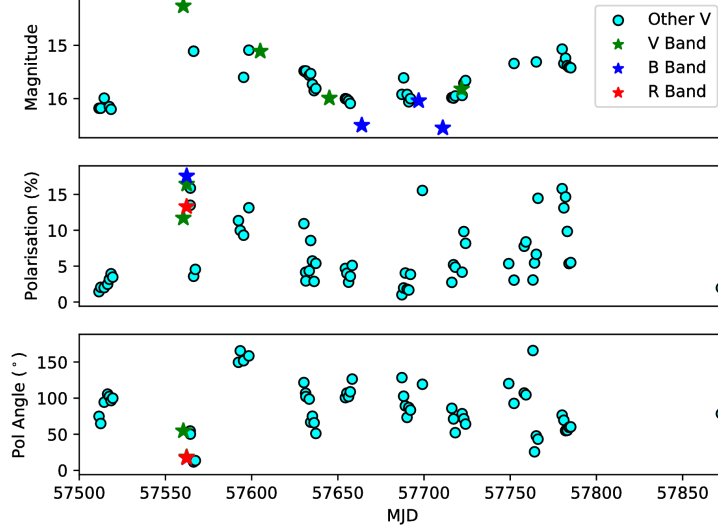
Figure C.1: Illustration of the brightness and polarisation time evolution of 3C 454.3. 'Other V' data taken from the Steward Observatory spectropolarimetric monitoring project.

result is consistent with an intrinsically unpolarised source.

ASASSN-16fq: This source, also known as AT2016cok and SN2016cok, was discovered in the galaxy M66, on 2016 May 28 (Bock et al., 2016). Spectroscopic follow-up classified ASASSN-16fq as a type IIP SN (Zhang et al., 2016b). The SPLOT observations were taken $\sim$ three weeks post-alert. I measured a polarisation of $P = 1.44(\pm 0.18)\%, P = 2.24(\pm 0.46)\%$ and $P = 1.05(\pm 0.12)\%$ in the V, B, and R bands. I calculated from $E(B - V) = 0.03$ that $P_{\text{Gal,dust}} \leq 0.27\%$.

ASASSN-16fs: This source, also known as AT2016cpy and SN2016cpy, was discovered in the galaxy UGC09523 on 2016 June 4 (Masi et al., 2016). Spectroscopic follow-up classified ASASSN-16fs as a type Ia SN (Pan et al., 2016). The SPLOT observations were taken $\sim$ two weeks post-alert. I measured a polarisation of $P = 0.53(\pm 0.10)\%$ in V-band. I calculated from $E(B - V) = 0.03$ that $P_{\text{Gal,dust}} \leq 0.27\%$. This result is consistent with the expected intrinsic levels of polarisation from type Ia SN.

ASASSN-16ft: This source, also known as AT2016cqj and SN2016cqj, was discovered in the galaxy CGCG 382-005, on 2016 June 5 (Brimacombe et al., 2016a). Spectroscopic follow-up observations classified ASASSN-16ft as a type II SN (Hosseinzadeh et al., 2016). The SPLOT observations were taken $\sim$ two weeks post-alert. I measured a polarisation of $P = 1.21(\pm0.28)\%$ in V-band. I calculated from $E(B-V) = 0.03$ that $P_{\text{Gal,dust}} \leq 0.27\%$.

ASASSN-16fv: This source, also known as AT2016cgz and SN2016cgz, was discovered in the galaxy IC4705 on 2016 June 7 (Brimacombe et al., 2016c). Spectroscopic follow-up observations classified ASASSN-16fv as a type Ia SN (Prieto et al., 2016). The SPLOT observations were taken $\sim$ 13 days post-alert. I measured polarisations of $P = 0.35(\pm0.08)\%$, $P < 0.22\%$ and $P = 0.58(\pm0.09)\%$ in the V, B, and R bands. I calculated from $E(B-V) = 0.09$ that $P_{\text{Gal,dust}} \leq 0.81\%$. This result is consistent with the expected intrinsic levels of polarisation from type Ia SN.

ASASSN-16fx: This source, also known as AT2016csd, Gaia16avj and SN2016csd, was discovered in galaxy GALEXASC J020044.56-461644.0 on 2016 June 8 (Brown et al., 2016a). Spectroscopic follow-up observations classified ASASSN-16fx as a type Ia SN (Morrell & Shappee, 2016). The SPLOT observations were taken $\sim$ 12 days post-alert. I measured a polarisation of $P \leq 0.56\%$ in V-band. For photometry information see Figure C.5.

ASASSN-16ga: This source was detected on 2016 June 9 (Shappee et al., 2014). The short-time variability in brightness suggested that the source is a CV candidate. The SPLOT observations were taken $\sim$ 11 days post-alert. I measured a polarisation of $P \leq 3.35\%$ in V-band.

ASASSN-16gg: This source was detected on 2016 June 17 (Shappee et al., 2014). Its behaviour was similar to ASASSN-16ga, suggesting this source was also a CV candidate. The SPLOT observations were taken $\sim$ two and three nights post-alert. I measured polarisations of $P \leq 8.55\%$, $P \leq 18.04\%$ and $P \leq 9.50\%$ in the V, B, and R bands on the first observing

night, and $P < 10.77\%$, $P < 15.98\%$ and $P < 12.60\%$ in the V, B, and R bands on the second observing night.

ASASSN-17gs: This source, also known as AT2017egv, was detected on 2017 May 25 (Stanek, 2017). The position of the source was coincident with a new gamma-ray source, Fermi J1544-0649, initially detected on 2017 May 15 (Ciprini et al., 2017). Multi-wavelength radio observations classified ASASSN-17gs as a BL Lac object(Bruni et al., 2018). The SPLOT observations were taken ~ 10 weeks post-alert. I measured a polarisation of $P = 9.03(\pm0.52)\%$ in Z-band. I calculated from $E(B - V) = 0.14$ that $P_{\text{Gal,dust}} \leq 1.26\%$. The result is consistent with previously observed high levels of polarisation in BL Lac objects from non-thermal emission (Smith et al., 2007). Photometry information is displayed in Figure C.5.

ASASSN-17km: This source was detected on 2017 August 5 (Shappee et al., 2014). The short-time variability in brightness suggested that this source was a CV candidate. The SPLOT observations were taken $\sim$ three days post-alert, with two exposures several hours apart. I measured polarisations of $P \leq 0.51\%$ and $P \leq 1.39\%$ in Z-band. Photometry information is displayed in Figure C.5.

AT2016bvg: This source, also known as CTRS 160505-150133 and PS16bux, was discovered on 2016 April 16 (Chambers et al., 2016a). The SPLOT observations were taken > two months post-alert. I measured polarisations of $P < 3.91\%$ and $P = 1.73(\pm0.28)\%$ in V-band on June 19 and 20.

AT2016cvk: This source, also known as ASASSN-16jt and SN2016cvk, was discovered on 2016 June 12 (Brimacombe et al., 2016b). AT2016cvk and ASASSN-16jt were detected separately, several days apart. Follow-up observations found that the two detections were spatial coincident and classified the source as a type IIn SN(Brown et al., 2016b). The SPLOT observations were taken $\sim$ one week post-alert. I measured a polarisation of $P \leq 1.90\%$

in V-band. Brown et al. (2016b) highlight that the source resembles the unusual transient SN2009ip, a SN which had shown prior violent outbursts. The polarisation measurement is consistent with is consistent with those obtained for SN 2009ip (Mauerhan et al., 2014).

ATLAS16bcm: This source, also known as AT2016csr and SN2016crs, was discovered in galaxy SDSS J151431.52+064123.9 on 2016 June 3 (Tonry et al., 2016a). Spectroscopic follow-up observations classified ATLAS16bcm as a type Ia SN (Hangard & Manulis, 2016). The SPLOT observations were taken ~ 12 days post-alert. I measured a polarisation of $P < 0.91\%$ in V band.

ATLAS16bdg: This source, also known as AT2016cvn and SN2016cvn, was discovered in galaxy NGC 4708 on 2016 June 5 (Tonry et al., 2016b). Spectroscopic follow-up observations classified ATLAS16bdg as a type Ia SN (Mundell et al., 2016). The SPLOT observations were taken $\sim$ two weeks post-alert. I measured polarisations of $P = 2.12(\pm 0.22)\%$, $P = 3.55(\pm 0.59)\%$ and $P = 0.97(\pm 0.19)\%$ in the V, B, and R bands. I calculated from $E(B - V) = 0.04$ that $P_{\mathrm{Gal,dust}} \leq 0.36\%$.

ATLAS17jfk: This source, also known as AT2017fvz and kait-17bm, was discovered in galaxy NGC 6822, on 2017 August 2 (Hestenes & Filippenko, 2017). SPectroscopic follow-up observations classified ATLAS17jfk as an extragalactic Novae (Williams & Darnley, 2017). The SPLOT observations were taken $\sim$ six days post-alert. I measured a polarisation of $P = 2.30(\pm 0.57)\%$ in Z band. I calculated from $E(B - V) \sim 0.20$ that $P_{\mathrm{Gal,dust}} \leq 1.80\%$.

CTA 102: This source was first discovered at radio wavelengths in 1960 (Harris & Roberts, 1960) and has since been extensively observed. Optical observations in the 1960s classified CTA 102 as a Quasar (Sandage & Wyndham, 1965). CTA 102 was observed during both the first and second observing runs. The SPLOT observations for the first run were taken $\sim$ 11 days after an alert of increased optical activity (Larionov & Kopatskaya, 2016). I mea-
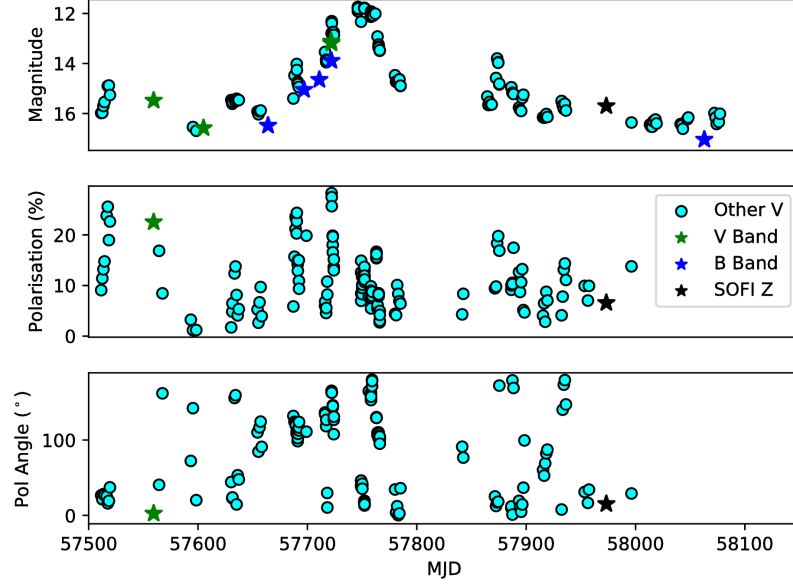
Figure C.2: Illustration of the brightness and polarisation time evolution of 3C 454.3. 'Other V' data taken from the Steward Observatory spectropolarimetric monitoring project.

sured a polarisation of $P = 22.53(\pm0.14)\%$ in V-band. The SPLOT observations for the second run were taken $\sim$ one month after an alert of increased gamma-ray activity (Bulgarelli et al., 2017). I measured a polarisation of $P = 6.58(\pm0.45)\%$ in Z-band. I calculated from $E(B-V) = 0.06$ that $P_{\mathrm{Gal,dust}} \leq 0.54\%$. Figure C.2 illustrated the short-time brightness and polarisation variability of CTA 102 and when the SPLOT observations occurred.

Gaia16aau: This source, also known as AT2016dbu and OGLE-SMC 710.08.1, was detected on 2016 January 25 (Delgado et al., 2016a). Spectroscopic follow-up observations classified Gaia16aau as a RCB star within the SMC (Tisserand et al., 2016). The SPLOT observations were taken $\sim$ five months post-alert. I measured a polarisation of $P = 0.22(\pm0.05)\%$ in V-band. Figure C.5 highlights the interesting time evolution of the brightness of Gaia16aau.

Gaia16agw: The source, also known as AT2016dth, was detected on 2016 February 29 (Delgado et al., 2016b). The source was spacially coincident with a previous detection from ASASSN (ASASSN15mw; Shappee et al. 2014). It therefore was classified as a Blazar can-

174

didate. The SPLOT observations were taken ~ 16 weeks post-*Gaia* alert. I measured a polarisation of $P \leq 0.36\%$ in V-band. Figure C.5 highlights the significant variability of the source, suggesting that Gaia16agw is a Blazar candidate.

Gaia16alw: Gaia16alw, also known as AT2016dxp, was detected on 2016 April 19 (Delgado et al., 2016b). The SPLOT observations were taken $\sim$ two months post-alert. I measured a polarisation of $P = 5.48(\pm 1.20)\%$ in V-band. For photometry information see Figure C.5.

Gaia16aoa: Gaia16aoa, also known as AT2016eab, was detected on 2016 May 9 (Delgado et al., 2016b). The SPLOT observations were taken $\sim$ six weeks post-alert, coinciding with an increase in activity. I measured a polarisation of $P = 1.59(\pm 0.38)\%$ in V-band. For photometry information see Figure C.5.

Gaia16aob: Gaia16aob (also known as AT2016eaa) was detected on 2016 May 10, where the AGN candidate, 2MASX J11431053-2946384, entered a period of high activity (Delgado et al., 2016b). The SPLOT observations were taken $\sim$ six weeks post-alert. I measured a polarisation of $P = 0.37(\pm 0.12)\%$ in V-band. I calculated form $E(B - V) = 0.06$ that $P_{\mathrm{Gal,dust}} \leq 0.54\%$. The polarisation measurement is therefore consistent with an intrinsically unpolarised source. For photometry information see Figure C.5.

Gaia16aok: This source, also known as AT2016eap, was detected on 2016 May 12 (Delgado et al., 2016b). The alert arose due to increased activity of radio source NVSS J115815-314702. The SPLOT observations were taken $\sim$ five weeks post-alert. I measured a polarisation of $P = 11.51(\pm 0.07)\%$ in V-band. For photometry information see Figure C.5.

Gaia16aol: This source, also known as AT2016eaq and PS16cni, was detected in the galaxy IC 690, on 2016 May 12 (Delgado et al., 2016b). The SPLOT observations were taken $\sim$ five

weeks post-alert. I measured a polarisation of $P \leq 4.08\%$ in V-band. The time evolution of the brightness of Gaia16aol in Figure C.5 suggests that the source may be a SN candidate.

Gaia16aoo: This source, also known as ASASSN-16dm, AT2016blb, PS16bop and SN2016blb, was discovered in the galaxy 2MASX J11372059-0454450, on 2016 March 30 (Kiyota et al., 2016). Spectroscopic follow-up observations classified Gaoa16aoo as a type IIP SNe (Falco et al., 2016). The SPLOT observations were taken $\sim$ five weeks post-alert. I measured a polarisation of $P \leq 2.21\%$ in V-band. For photometry information see Figure C.5.

Gaia16aqe: This source, also known as AT2017fqg, was detected on 2016 May 22 (Delgado et al., 2016b). It was tentatively classified as a type Ia SNe. The SPLOT observations were taken $\sim$ four weeks post-alert. I measured a polarisation of $P \leq 2.07\%$ in V-band. The source was suspected to be a Type Ia SN candidate. For photometry information see Figure C.5.

Gaia17blw: This source, also known as AT2017eni and SN2017eni, was discovered on 2017 June 5 (Delgado et al., 2017a). Spectroscopic follow-up observations classified Gaia17blw as a type IIn SN via (Strader et al., 2017). The SPLOT observations were taken $\sim$ two months post-alert. I measured a polarisation of $P \leq 1.65\%$ in Z-band. For photometry information see Figure C.5.

Gaia17bro: This source, also known as AT2017fck and SN2017fck, was discovered on 2017 July 2 (Delgado et al., 2017b).Spectroscopic follow-up observations classified Gaia17bro as a type IIn SN(Strader et al., 2017). The SPLOT observations were taken $\sim$ five weeks post-alert. I measured a polarisation of $P \leq 1.99\%$ in Z-band. For photometry information see Figure C.5.

Gaia17bvo: This source, also known as AT2017fqg, was detected on 2017 July 23 (Delgado et al., 2017c). The alert arose from increased activity from a known variable source residing in the Galactic plane, possible a YSO. The SPLOT observations were taken ~ 17 days post-alert. I measured a polarisation of $P = 8.37(\pm0.25)\%$ in Z-band. For photometry information see Figure C.5.

Gaia17bwu: This source, also known as AT2017fum, was detected on 2017 July 27 (Delgado et al., 2017d). The alert arose from increased activity from a previously known red star that exhibited strong emission lines. The SPLOT observations were taken ~ 12 days post-alert. I measured a polarisation of $P = 1.16(\pm0.30)\%$ in Z-band. For photometry information see Figure C.5.

Gaia17bxl: This source, also known as AT2017fve, was detected nearby to the galaxy GALEXASC J012208.86-484752.8, on 2017 July 29 (Delgado et al., 2017e). The SPLOT observations were taken $\sim$ nine days post-alert. I measured a polarisation of $P \leq 10.45\%$ in Z-band. The source was probably a SN. For photometry information see Figure C.5.

Gaia17byh: This source, also known as AT2017fwm and SN2017fwm, was discovered on 2017 July 31 (Delgado et al., 2017f). Spectroscopic follow-up observations classified Gaia17byh as a type Ic SN (Lyman et al., 2017). The SPLOT observations were taken $\sim$ one week post-alert. I measured a polarisation of $P \leq 2.22\%$ in Z- band. For photometry information see Figure C.5.

Gaia17byk: This source, also known as AT2017fwt, was detected on 2017 August 1 (Delgado et al., 2017f). The alert arose from increased activity of a known source in the Galactic plane. The SPLOT observations were taken $\sim$ eight days post-alert. I measured a polarisation of $P = 5.99(\pm0.49)\%$ in Z-band. For photometry information see Figure C.5.

Gaia17bzc: This source, also known as AT2017fxl, was detected on 2017 August 3 (Delgado et al., 2017g). The alert arose from increased activity of a red source in the Galactic centre. The SPLOT observations were taken $\sim$ six days post-alert. I measured a polarisation of $P = 6.86(\pm 0.64)\%$ in Z-band. For photometry information see Figure C.5.

GX 304-1: This source, also known as 4U 1258-61, is a well known HMXB. Initially observed as an X-ray source with a period of $272\,\mathrm{s}$ (Huckle et al., 1977; McClintock et al., 1977), later observations at optical wavelengths identified a spatially coincident counterpart (Mason et al., 1978). This counterpart was determined to be a Be star. GX 304-1 periodically enters phases on increased X-ray activity (Manousakis et al., 2008; Jenke et al., 2012). A recent alert of increased activity was distributed on 2016 May 17 (Nakajima et al., 2016). The SPLOT observations were taken $\sim$ five weeks post-alert. I measured polarisations of $P = 6.80(\pm 0.16)\%$, $P = 6.17(\pm 0.45)\%$ and $P = 6.80(\pm 0.08)\%$ in the V, B and R bands. Historic detections of polarisation from GX 304-1 have suggested that the signal arises due to scattering of light from Galactic dust(Mason et al., 1978).

MASTER OT J023819.81-521134.1: This source was detected in the galaxy PGC 009998 on 2017 August 7 (Balanutsa et al., 2017). The detection was thought to have arose from high AGN activity within the galaxy (Stanek et al., 2017). The SPLOT observations were taken $\sim$ eight hours post-alert. I measured a polarisation of $P = 0.66(\pm 0.20)\%$ in V-band. I calculated from $E(B - V) = 0.03$ that $P_{\mathrm{Gal,dust}} \leq 0.27\%$.

MASTER OT J220727-053121.8: This source, also known as AT2016ecw, Gaia16arv and SN2016ecw, was discovered on 2016 June 16 (Shurpakov et al., 2016). Spectroscopic follow-up observations classified MASTER OT J220727-053121.8 as a type Ia SN (Blagorodnova et al., 2016). The SPLOT observations were taken $\sim$ three days post-alert. I measured a polarisation of $P = 1.06(\pm 0.34)\%$ in V-band. I calculated from $E(B - V) = 0.06$ that $P_{\mathrm{Gal,dust}} \leq 0.54\%$. This result is consistent with the expected intrinsic levels of polarisation from type Ia SN.

OGLE16aaa: This source was detected on 2016 January 2 (Wyrzykowski et al., 2016). Three months of extensive follow-up observations highlighted shallow increases and decreases of the temporal and spectral properties. The presence of broad He II and Hα emission lines suggested that this source was a TDE (Wyrzykowski et al., 2017). The SPLOT observations were taken $\sim$ five months post detection. I measured a polarisation of $P = 1.81(\pm0.42)\%$ in V-band. This level of polarisation is significantly lower than previously observed relativistic TDEs (Wiersema et al., 2012a). I calculated from $E(B-V) \sim 0.02$ that $P_{\mathrm{Gal,dust}} \lesssim 0.18\%$. I conducted image analysis on the host nucleus from observations pre-TDE and SPLOT. Using an aperture of one arcsec, I determined that the source brightness was comparable in both images. I concluded that at the time of the SPLOT observation, no TDE contamination of the host light was seen.

P13 NGC 7793: This source was first discovered as an ULX source in the galaxy NGC 7793 (Fabbiano et al., 1992). Later investigations suggested that P13 NGC 7793 is an X-ray binary containing a stellar mass black hole ($\sim 15 M_\odot$) and a donor star (spectral type B9Ia), with a period of ~ 64 days (Motch et al., 2014). Recent observations have shown that the X-ray emission pulsates with a period of ~ 0.42 s (Fürst et al., 2016; Israel et al., 2017). This pulsation suggests that the compact object is a neutron star. An alert arose from increased activity of P13 NGC 7793 on 2016 May 20 (Soria et al., 2016). The SPLOT observations were taken $\sim$ one month post-alert. I measured a polarisation of $P < 6.54\%$ in V-band. This is possibly the first measurement of optical polarimetry of a ULX. The measured optical brightness of the emission is dominated by the companion star. Emission from the compact object, perhaps in the form of a jet, may produce polarised emission. A more constraining limit on the polarisation would have made this more clear.

PG 1553+113: This source, also known as HESS J1555+111, is an extensively studied BL Lac object, first discovered in the Palomar-Green survey (Green et al., 1986). Previous observations have shown that the source periodically enters states of increased activity (Aharonian et al., 2006; Abdo et al., 2010; Aleksić et al., 2015). A recent increase in activity from PG

Figure C.3: Illustration of the polarisation time evolution of PG 1553+113. 'Other V' data taken from the Steward Observatory spectropolarimetric monitoring project.

1553+113 produced an alert on 2016 April 27 (Kapanadze, 2016). The SPLOT observations were taken $\sim$ seven weeks post-alert. I measured polarisations of $P = 5.15(\pm0.09)\%$, $P = 5.26(\pm0.13)\%$ and $P = 4.78(\pm0.07)\%$ in V, B, and R bands, with corresponding angles of polarisation of $\theta = 31.50(\pm0.49)$ deg, $\theta = 31.55(\pm0.73)$ deg and $\theta = 30.62(\pm0.43)$ deg. I calculated from $E(B-V) = 0.04$ that $P_{\text{Gal,dust}} \leq 0.36\%$. The SPLOT polarisation measurements are higher than previously observed levels and the angle of polarisation has significantly shifted (Andruchow et al., 2011). Figure C.3 highlights some of this variation.

PKS 1510-089: This source is a well known Blazar that often outbursts producing very high energy photons (Wu et al., 2005; D'Ammando et al., 2011). Historically, PKS 1510-089 shows significant polarisation variation over timescales $\sim$ few days (Marscher et al., 2010). The source was observed three times during the first run, on 2016 June 19, 20 and 22. Increased multi-wavelength activity triggered an alert recent alerts (De Naurois, 2016; Mirzoyan, 2016; Carrasco et al., 2016). I measured polarisations of $P = 8.76(\pm0.16)\%$, $P = 3.14(\pm0.16)\%$ and $P = 1.94(\pm0.35)\%$ in V-band, with corresponding angles of polarisation
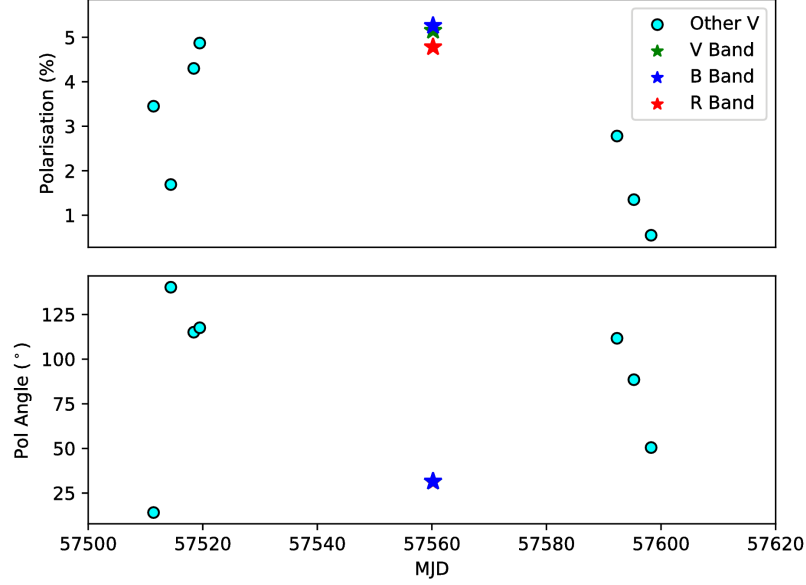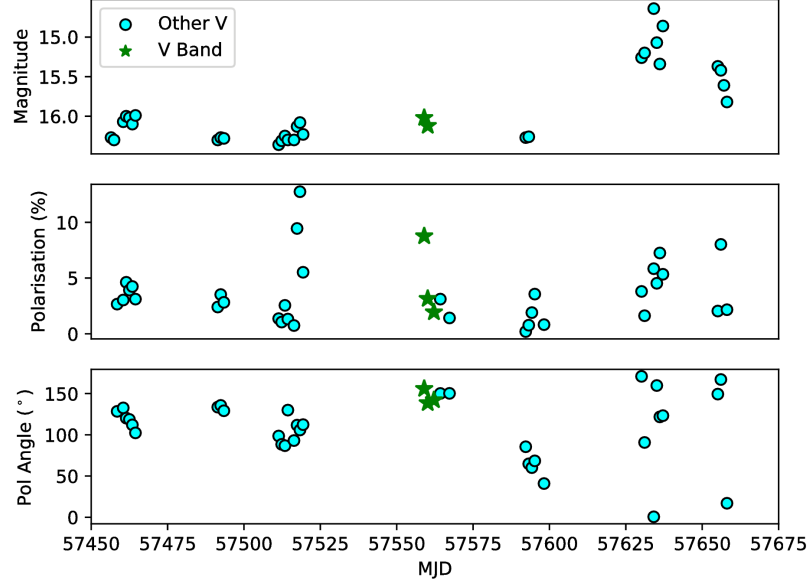
Figure C.4: Illustration of the polarisation and brightness time evolution of PKS 1510-089. 'Other V' data taken from the Steward Observatory spectropolarimetric monitoring project.

of $\theta = 155.77(\pm 0.54)\,\mathrm{deg}$, $\theta = 138.55(\pm 1.49)\,\mathrm{deg}$ and $\theta = 142.03(\pm 5.08)\,\mathrm{deg}$. I calculated from $E(B-V) = 0.09$ that $P_{\mathrm{Gal,dust}} \leq 0.81\%$. The SPLOT measurements are in agreement with previously seen variability and are illustrated in Figure C.4.

PKS 2023-07: This source is also a previously, well studied Blazar. PKS 2023-07 often enters periods of increased activity including high energy photon emission (Vercellone & AGILE Team, 2008; Gasparrini, 2009). A recent alert on 2016 April 13 arose from an increase in high energy emission from PKS 2023-07 (Verrecchia et al., 2016). The SPLOT observations were taken $\sim$ nine weeks post-alert. I measured a polarisation of $P = 7.36(\pm 0.35)\%$ in V-band. I calculated from $E(B-V) = 0.03$ that $P_{\mathrm{Gal,dust}} \leq 0.27\%$.

PS16cnz: This source, also known as AT2016cnm, was discovered on 2016 May 23 (Chambers et al., 2016b). The SPLOT observations were taken $\sim$ four weeks post-alert. I measured a polarisation of $P < 0.60\%$ in V-band.

PS16crs: This source, also known as AT2016cor and SN2016cor, was discovered in the galaxy SDSS J154431.47+161814.9 on 2016 May 25. Spectroscopic follow-up observations classified PS16crs as a type Ia SN (Zhang et al., 2016b).The SPLOT observations were taken $\sim$ three weeks post-alert. I measured a polarisation of $P \leq 3.72\%$ in V-band.

PS16ctq: This source, also known as AT2016cut, was discovered on 2016 June 11 (Chambers et al., 2016c).The SPLOT observations were taken $\sim$ nine days post alert. I measured a polarisation of $P \leq 0.50\%$ in V-band.

PS16cvc: This source, also known as AT2016cxb, MASTER OT J211223+144645.1 and SN2016cxb, was discovered on 2016 June 19 (Chambers et al., 2016b). Spectroscopic follow-up observations classified PS16cvc as a type Ia SN (Tomasella et al., 2016). The SPLOT observations were taken $\sim$ 24 and 96 hours post-alert. I measured polarisations of $P < 0.71\%$ and $P < 0.74\%$ in V-band.

SXP 15.3: This source, also known as RX J0052.1$-$7319 and MASTER OT J211223+144645, is a well studied Pulsar/XRB, comprised of a compact object and a Be donor star. SXP 15.3 is located in the SMC and exhibits a period of 15.3 s (Lamb et al., 1999; Covino et al., 2001). SXP 15.3 has historically entered periods of increased emission (Galache et al., 2008; Rajoelimanana et al., 2011). A recent alert arose from increased activity on 2017 July 25 (Kennea et al., 2017). The SPLOT observations were taken $\sim$ 12 days post-alert. I measured a polarisation of $P < 1.45\%$ in Z-band.

XTE J1709-267: This source, also known as RX J1709.5-2639 is a low-mass XRB, first detected by *ROSAT* (Voges et al., 1999). The compact object is thought to be a neutron star. XTE J1709-267 has been extensively observed at multiple wavelengths (Jonker et al., 2004). A recent alert arose from increased activity on 2016 May 31 (Nakahira et al., 2016). The SPLOT observations were taken $\sim$ three weeks post-alert. I measured a polarisation

of $P < 2.00\%$ in V-band. Polarisation at infrared wavelengths has been observed in low-mass XRBs, probably arising from jet emission. There have been a few detections at optical wavelengths too (Russell, 2018). The above limit suggests that the emission at the time of the SPLOT observation from XTE J1709-267 is not produced from a jet.
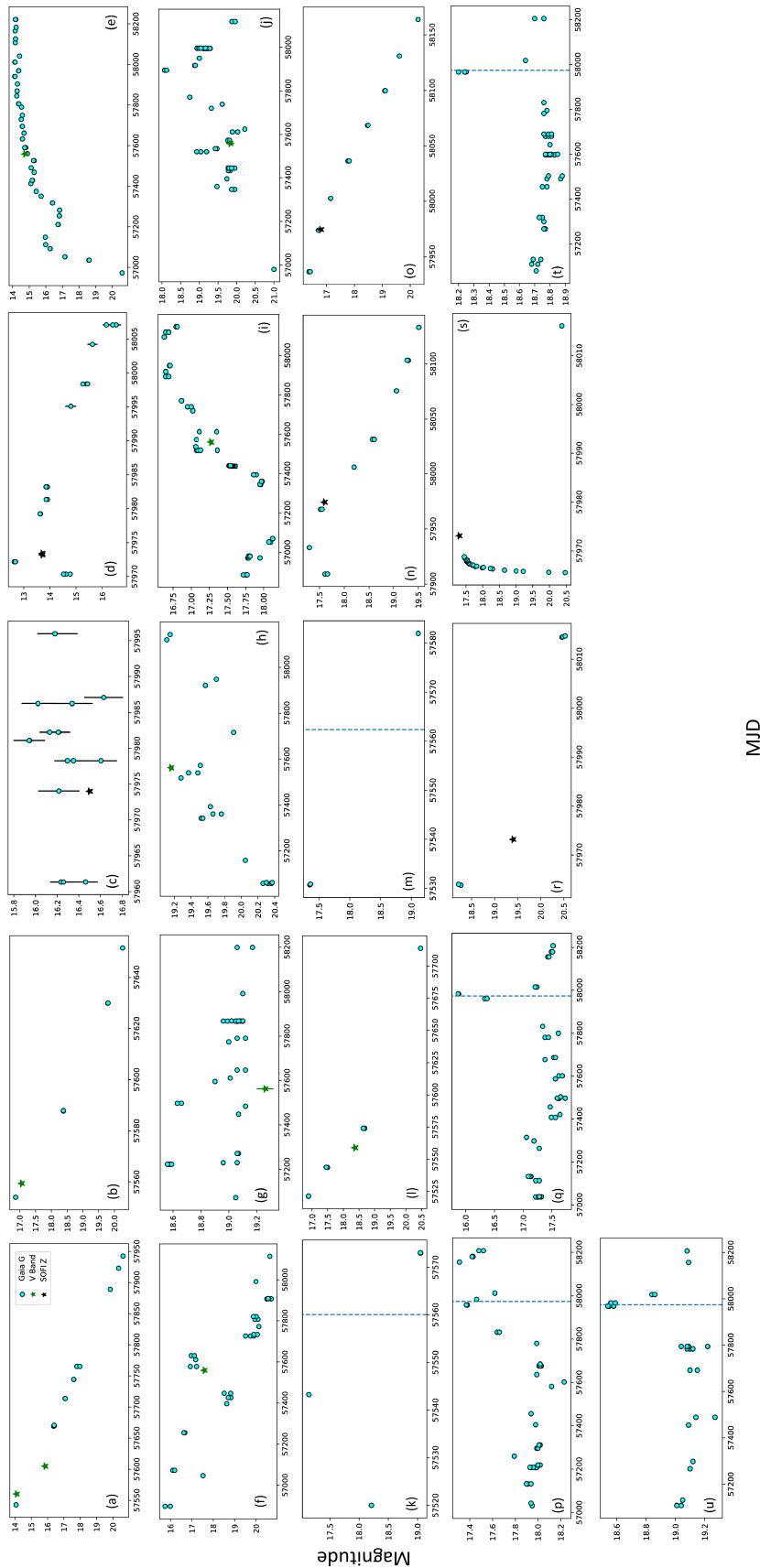
Figure C.5: Illustration of the time evolution of source brightness. Sources shown here are ASASSN-16fp (a), ASASSN-16fx (b), ASASSN-17gs (c), ASASSN-17km (d), Gaia16aau (e), Gaia16agw (f), Gaia16alw (g), Gaia16aoa (h), Gaia16aob (i), Gaia16aok (j), Gaia16aol (k), Gaia16aoo (l), Gaia16aqe (m), Gaia17blw (n), Gaia17bro (o), Gaia17bvo (p), Gaia17bwu (q), Gaia17bxl (r), Gaia17byh (s), Gaia17byk (t) and Gaia17bzc (u). The V (green) and Z (black) measurements were taken from the SPLOT survey. *Gaia G*-band data taken from the *Gaia* transient alert system. For SPLOT source images where I could not estimate a magnitude, I have highlighted the time of observation with a blue dotted line.

Bibliography

Abbott, B. P., Abbott, R., Abbott, T. D., et al. 2016, Physical Review Letters, 116, 061102

Abbott, B. P., Abbott, R., Abbott, T. D., et al. 2017a, ApJL, 848, L13

Abbott, B. P., Abbott, R., Abbott, T. D., et al. 2017b, ApJL, 848, L12

Abbott, B. P., Abbott, R., Abbott, T. D., et al. 2018, Living Reviews in Relativity, 21, 3

Abdo, A. A., Ackermann, M., Arimoto, M., et al. 2009, Science, 323, 1688

Abdo, A. A., Ackermann, M., Ajello, M., et al. 2010, ApJ, 708, 1310

Acernese, F., Agathos, M., Agatsuma, K., et al. 2015, Classical and Quantum Gravity, 32, 024001

Ackermann, M., Ajello, M., Baldini, L., et al. 2010, ApJ, 721, 1383

Aharonian, F., Akhperjanian, A. G., Bazer-Bachi, A. R., et al. 2006, A&A, 448, L19

Aleksić, J., Ansoldi, S., Antonelli, L. A., et al. 2015, MNRAS, 450, 4399

Amati, L., O'Brien, P., Götz, D., et al. 2018, Advances in Space Research, 62, 191

Anderson, G. E., Fender, R. P., Staley, T. D., & van der Horst, A. J. 2014, GRB Coordinates Network, 16603

Anderson, G. E., Staley, T. D., van der Horst, A. J., et al. 2018, MNRAS, 473, 1512

Andruchow, I., Combi, J. A., Muñoz-Arjonilla, A. J., et al. 2011, A&A, 531, A38

Arnaud, K. 1996, ASP Conf. Ser, 101

Aso, Y., Michimura, Y., Somiya, K., et al. 2013, Phys. Rev. D, 88, 043007

Balanutsa, P., Lipunov, V., Buckley, D., et al. 2017, The Astronomer's Telegram, 10625

Band, D., Matteson, J., Ford, L., et al. 1993, ApJ, 413, 281

Barbary, K., Boone, K., McCully, C., et al. 2016, kbarbary/sep: v1.0.0, doi:10.5281/zenodo.159035

Barcons, X., Nandra, K., Barret, D., et al. 2015, in Journal of Physics Conference Series, Vol. 610, Journal of Physics Conference Series, 012008

Barthelmy, S. D., Cline, T. L., Butterworth, P., et al. 2000, in American Institute of Physics Conference Series, Vol. 526, Gamma-ray Bursts, 5th Huntsville Symposium, ed. R. M. Kippen, R. S. Mallozzi, & G. J. Fishman, 731–735

Barthelmy, S. D., Cline, T. L., Gehrels, N., et al. 1994, in American Institute of Physics Conference Series, Vol. 307, Gamma-Ray Bursts, ed. G. J. Fishman, 643

Barthelmy, S. D., Barbier, L. M., Cummings, J. R., et al. 2005, Space Science Rev., 120, 143

Beardmore, A. P., Evans, P. A., Goad, M. R., & Osborne, J. P. 2014, GRB Coordinates Network, 16585

Belczynski, K., Perna, R., Bulik, T., et al. 2006, ApJ, 648, 1110

Berger, E. 2010, ApJ, 722, 1946

Berger, E. 2014, ARA&A, 52, 43

Bertin, E., & Arnouts, S. 1996, A&AS, 117, 393

Bethe, H. A. 1990, Reviews of Modern Physics, 62, 801

Blagorodnova, N., Neill, D., & Walters, R. 2016, The Astronomer's Telegram, 9230

Blain, A. W., & Natarajan, P. 2000, MNRAS, 312, L35

Blandford, R. D., & McKee, C. F. 1976, Physics of Fluids, 19, 1130

Blandford, R. D., & Payne, D. G. 1982, MNRAS, 199, 883

Blandford, R. D., & Znajek, R. L. 1977, MNRAS, 179, 433

Bloom, J. S., Frail, D. A., & Kulkarni, S. R. 2003, ApJ, 594, 674

Bloom, J. S., Kulkarni, S. R., & Djorgovski, S. G. 2002, AJ, 123, 1111

Bloom, J. S., Prochaska, J. X., Pooley, D., et al. 2006, ApJ, 638, 354

Bloom, J. S., Giannios, D., Metzger, B. D., et al. 2011, Science, 333, 203

Bock, G., Dong, S., Kochanek, C. S., et al. 2016, The Astronomer's Telegram, 9091

Boella, G., Butler, R. C., Perola, G. C., et al. 1997, A&AS, 122, 299

Bošnjak, Ž., Götz, D., Bouchet, L., Schanne, S., & Cordier, B. 2014, A&A, 561, A25

Bradley, L., Sipocz, B., Robitaille, T., et al. 2019, astropy/photutils: v0.6, doi:10.5281/zenodo.2533376

Bray, J. C., & Eldridge, J. J. 2016, MNRAS, 461, 3747

Breeveld, A. A., Curran, P. A., Hoversten, E. A., et al. 2010, MNRAS, 406, 1687

Brightman, M., & Nandra, K. 2011, MNRAS, 413, 1206

Brimacombe, J., Brown, J. S., Stanek, K. Z., et al. 2016a, The Astronomer's Telegram, 9117

Brimacombe, J., Brown, J. S., Stanek, K. Z., et al. 2016b, The Astronomer's Telegram, 9117

Brimacombe, J., Nicholls, B., Brown, J. S., et al. 2016c, The Astronomer's Telegram, 9123

Britto, R. J., Bottacini, E., Lott, B., Razzaque, S., & Buson, S. 2016, ApJ, 830, 162

Brown, G. C., Levan, A. J., Stanway, E. R., et al. 2015, MNRAS, 452, 4297

Brown, J. S., Stanek, K. Z., Holoien, T. W.-S., et al. 2016a, The Astronomer's Telegram, 9127

Brown, J. S., Prieto, J. L., Shappee, B. J., et al. 2016b, The Astronomer's Telegram, 9445

Bruni, G., Panessa, F., Ghisellini, G., et al. 2018, ApJL, 854, L23

Bulgarelli, A., Parmiggiani, N., Lucarelli, F., et al. 2017, The Astronomer's Telegram, 10560

Burrows, D. N., Romano, P., Falcone, A., et al. 2005a, Science, 309, 1833

Burrows, D. N., Hill, J. E., Nousek, J. A., et al. 2005b, Space Science Rev., 120, 165

Burrows, D. N., Kennea, J. A., Ghisellini, G., et al. 2011, Nature, 476, 421

Buzzoni, B., Delabre, B., Dekker, H., et al. 1984, The Messenger, 38, 9

Campana, S., Lodato, G., D'Avanzo, P., et al. 2011, Nature, 480, 69

Cano, Z., Malesani, D., & Nielsen, M. 2014, GRB Coordinates Network, 16587

Cardelli, J. A., Clayton, G. C., & Mathis, J. S. 1989, ApJ, 345, 245

Carrasco, L., Porras, A., Recillas, E., Chavushyan, V., & Leon-Tavares, J. 2016, The Astronomer's Telegram, 9160

Castro-Tirado, A. J., Jeong, S., Gorosabel, J., & Reverte, D. 2014, GRB Coordinates Network, 16602

Castro-Tirado, A. J., Bremer, M., McBreen, S., et al. 2007, A&A, 475, 101

Cavallo, G., & Rees, M. J. 1978, MNRAS, 183, 359

Cenko, S. B., Krimm, H. A., Horesh, A., et al. 2012, ApJ, 753, 77

Chambers, K. C., Huber, M. E., Flewelling, H., et al. 2016a, Transient Name Server Discovery Report, 310

Chambers, K. C., Huber, M. E., Flewelling, H., et al. 2016b, Transient Name Server Discovery Report, 373

Chambers, K. C., Huber, M. E., Flewelling, H., et al. 2016c, Transient Name Server Discovery Report, 418

Chambers, K. C., Magnier, E. A., Metcalfe, N., et al. 2016d, ArXiv e-prints, arXiv:1612.05560

Chandra, P., & Nayana, A. J. 2014, GRB Coordinates Network, 16641

Chandrasekhar, S. 1960, Radiative transfer

Chapman, R., Tanvir, N. R., Priddey, R. S., & Levan, A. J. 2007, MNRAS, 382, L21

Church, R. P., Levan, A. J., Davies, M. B., & Tanvir, N. 2011, MNRAS, 413, 2004

Cikota, A., Patat, F., Cikota, S., & Faran, T. 2017, MNRAS, 464, 4146

Ciprini, S., Cheung, C. C., Kocevski, D., et al. 2017, The Astronomer's Telegram, 10482

Cline, T. L., Barthelmy, S., Butterworth, P., et al. 1999, A&AS, 138, 557

Colgate, S. A. 1968, Canadian Journal of Physics, 46, S476

Connaughton, V. 2011, GRB Coordinates Network, 11569

Contini, T., Garilli, B., Le Fèvre, O., et al. 2012, A&A, 539, A91

Costa, E., Frontera, F., Heise, J., et al. 1997, Nature, 387, 783

Courvoisier, T. J.-L., Walter, R., Beckmann, V., et al. 2003, A&A, 411, L53

Covino, S., & Gotz, D. 2016, Astronomical and Astrophysical Transactions, 29, 205

Covino, S., Negueruela, I., Campana, S., et al. 2001, A&A, 374, 1009

Covino, S., Molinari, E., Bruno, P., et al. 2014, Astronomische Nachrichten, 335, 117

Covino, S., Wiersema, K., Fan, Y. Z., et al. 2017, Nature Astronomy, 1, 791

Cucchiara, A., Levan, A. J., Fox, D. B., et al. 2011, ApJ, 736, 7

Curran, P. A., Evans, P. A., de Pasquale, M., Page, M. J., & van der Horst, A. J. 2010, ApJL, 716, L135

Cutri, R. M. 2014, VizieR Online Data Catalog, 2328

Dai, X., Halpern, J. P., Morgan, N. D., et al. 2007, ApJ, 658, 509

Daigne, F., & Mochkovitch, R. 2007, A&A, 465, 1

D'Ammando, F., Raiteri, C. M., Villata, M., et al. 2011, A&A, 529, A145

D'Avanzo, P., Malesani, D., Covino, S., et al. 2009, A&A, 498, 711

De Naurois, M. 2016, The Astronomer's Telegram, 9102

Delgado, A., Harrison, D., Hodgkin, S., et al. 2016a, Transient Name Server Discovery Report, 480

Delgado, A., Harrison, D., Hodgkin, S., et al. 2016b, Transient Name Server Discovery Report, 481

Delgado, A., Harrison, D., Hodgkin, S., et al. 2017a, Transient Name Server Discovery Report, 632

Delgado, A., Harrison, D., Hodgkin, S., et al. 2017b, Transient Name Server Discovery Report, 730

Delgado, A., Harrison, D., Hodgkin, S., et al. 2017c, Transient Name Server Discovery Report, 800

Delgado, A., Harrison, D., Hodgkin, S., et al. 2017d, Transient Name Server Discovery Report, 818

Delgado, A., Harrison, D., Hodgkin, S., et al. 2017e, Transient Name Server Discovery Report, 826

Delgado, A., Harrison, D., Hodgkin, S., et al. 2017f, Transient Name Server Discovery Report, 842

Delgado, A., Harrison, D., Hodgkin, S., et al. 2017g, Transient Name Server Discovery Report, 846

Dermer, C. D. 2004, ApJ, 614, 284

Djorgovski, S. G., Frail, D. A., Kulkarni, S. R., et al. 2001, ApJ, 562, 654

Dyks, J., Zhang, B., & Fan, Y. Z. 2005, arXiv Astrophysics e-prints, astro-ph/0511699

Eichler, D., & Granot, J. 2006, ApJL, 641, L5

Eichler, D., Livio, M., Piran, T., & Schramm, D. N. 1989, Nature, 340, 126

Eichler, D., & Waxman, E. 2005, ApJ, 627, 861

Eldridge, J. J., & Stanway, E. R. 2016, MNRAS, 462, 3302

Elias-Rosa, N., Mattila, S., Lundqvist, P., et al. 2016, The Astronomer's Telegram, 9090

Elliott, J., Krühler, T., Greiner, J., et al. 2013, A&A, 556, A23

ESO. 2016a, EFOSC2 User Manual issue 4.1; LSO-MAN-ESO-361000-0004 (European Southern Observatory)

ESO. 2016b, SofI User Manual issue 2.4; LSO-MAN-ESO-401000-0004 (European Southern Observatory)

Evans, P. A., Beardmore, A. P., Page, K. L., et al. 2007, A&A, 469, 379

Evans, P. A., Beardmore, A. P., Page, K. L., et al. 2009, MNRAS, 397, 1177

Fabbiano, G., Kim, D.-W., & Trinchieri, G. 1992, ApJS, 80, 531

Falco, E., Challis, P., Kirshner, R., et al. 2016, The Astronomer's Telegram, 8896

Fenimore, E. E., Palmer, D., Galassi, M., et al. 2003, in American Institute of Physics Conference Series, Vol. 662, Gamma-Ray Burst and Afterglow Astronomy 2001: A Workshop Celebrating the First Year of the HETE Mission, ed. G. R. Ricker & R. K. Vanderspek, 491–493

Fishman, G. J., & Meegan, C. A. 1995, ARA&A, 33, 415

Fishman, G. J., Meegan, C. A., Parnell, T. A., et al. 1985, International Cosmic Ray Conference, 3

Foley, S., McGlynn, S., Hanlon, L., McBreen, S., & McBreen, B. 2008, A&A, 484, 143

Foreman-Mackey, D., Hogg, D. W., Lang, D., & Goodman, J. 2013, PASP, 125, 306

Fossati, L., Bagnulo, S., Mason, E., & Landi Degl'Innocenti, E. 2007, in Astronomical Society of the Pacific Conference Series, Vol. 364, The Future of Photometric, Spectrophotometric and Polarimetric Standardization, ed. C. Sterken, 503

Fox, D. B., Frail, D. A., Price, P. A., et al. 2005, Nature, 437, 845

Frail, D. A., Kulkarni, S. R., Nicastro, L., Feroci, M., & Taylor, G. B. 1997, Nature, 389, 261

Frail, D. A., Waxman, E., & Kulkarni, S. R. 2000, ApJ, 537, 191

Frail, D. A., Kulkarni, S. R., Sari, R., et al. 2001, ApJL, 562, L55

Frei, Z., & Gunn, J. E. 1994, AJ, 108, 1476

Fürst, F., Walton, D. J., Harrison, F. A., et al. 2016, ApJL, 831, L14

Fynbo, J. P. U., Jakobsson, P., Prochaska, J. X., et al. 2009, ApJS, 185, 526

Gaia Collaboration, Prusti, T., de Bruijne, J. H. J., et al. 2016, A&A, 595, A1

Galache, J. L., Corbet, R. H. D., Coe, M. J., et al. 2008, ApJS, 177, 189

Galama, T. J., Vreeswijk, P. M., van Paradijs, J., et al. 1998, Nature, 395, 670

Gasparrini, D. 2009, The Astronomer's Telegram, 2175

Gehrels, N., Chipman, E., & Kniffen, D. A. 1993, A&AS, 97, 5

Gehrels, N., Chincarini, G., Giommi, P., et al. 2004, ApJ, 611, 1005

Gehrels, N., Barthelmy, S. D., Burrows, D. N., et al. 2008, ApJ, 689, 1161

Gendre, B., Stratta, G., Atteia, J. L., et al. 2013, ApJ, 766, 30

Giro, E., Bonoli, C., Leone, F., et al. 2003, in Proc. SPIE, Vol. 4843, Polarimetry in Astronomy, ed. S. Fineschi, 456–464

Goad, M. R., Tyler, L. G., Beardmore, A. P., et al. 2007, A&A, 476, 1401

Goodman, J. 1986, ApJL, 308, L47

Gordon, K. D., Clayton, G. C., Misselt, K. A., Landolt, A. U., & Wolff, M. J. 2003, ApJ, 594, 279

Gorenstein, P. 1975, ApJ, 198, 95

Gotz, D., Mereghetti, S., Bozzo, E., et al. 2016, GRB Coordinates Network, 19621

Götz, D., & SVOM Collaboration. 2012, Memorie della Societa Astronomica Italiana Supplementi, 21, 162

Granot, J., & Sari, R. 2002, ApJ, 568, 820

Green, R. F., Schmidt, M., & Liebert, J. 1986, ApJS, 61, 305

Greiner, J., Clemens, C., Krühler, T., et al. 2009, A&A, 498, 89

Groot, P. J., Galama, T. J., van Paradijs, J., et al. 1998, ApJL, 493, L27

Gruber, D., Krühler, T., Foley, S., Nardini, M., & Burlon, D. 2011, in American Institute of Physics Conference Series, Vol. 1358, American Institute of Physics Conference Series, ed. J. E. McEnery, J. L. Racusin, & N. Gehrels, 29–32

Grupe, D., Nousek, J. A., Veres, P., Zhang, B.-B., & Gehrels, N. 2013, ApJS, 209, 20

Güver, T., & Özel, F. 2009, MNRAS, 400, 2050

Hangard, L., & Manulis, I. 2016, Transient Name Server Classification Report, 434

Harris, D. E., & Roberts, J. A. 1960, PASP, 72, 237

Harrison, F. A., Bloom, J. S., Frail, D. A., et al. 1999, ApJL, 523, L121

Hartmann, D., Epstein, R. I., & Woosley, S. E. 1990, ApJ, 348, 625

Heidt, J., & Nilsson, K. 2011, A&A, 529, A162

Hestenes, J. C., & Filippenko, W. Z. A. A. V. 2017, Transient Name Server Discovery Report, 831

Higgins, A. B., Starling, R. L. C., Götz, D., et al. 2017, MNRAS, 470, 314

Higgins, A. B., van der Horst, A. J., Starling, R. L. C., et al. 2019a, MNRAS, 484, 5245

Higgins, A. B., Wiersema, K., Covino, S., et al. 2019b, MNRAS, 482, 5023

Hillebrandt, W., & Niemeyer, J. C. 2000, ARA&A, 38, 191

Hjorth, J., & Bloom, J. S. 2012, The Gamma-Ray Burst - Supernova Connection, 169–190

Hjorth, J., Sollerman, J., Møller, P., et al. 2003, Nature, 423, 847

Hjorth, J., Watson, D., Fynbo, J. P. U., et al. 2005, Nature, 437, 859

Hodgkin, S. T., Wyrzykowski, L., Blagorodnova, N., & Koposov, S. 2013, Philosophical Transactions of the Royal Society of London Series A, 371, 20120239

Holoien, T. W.-S., Stanek, K. Z., Brown, J. S., et al. 2016, The Astronomer's Telegram, 9086

Hosseinzadeh, G., Howell, D. A., Arcavi, I., Mccully, C., & Valenti, S. 2016, Transient Name Server Classification Report, 411

Hoyle, F., & Fowler, W. A. 1963, MNRAS, 125, 169

Hubbell, J. 2006, Radiation Physics and Chemistry, 75, 614 , pair Production

Huckle, H. E., Mason, K. O., White, N. E., et al. 1977, MNRAS, 180, 21P

Hunstead, R. W. 1972, Astrophys. Lett., 12

Israel, G. L., Papitto, A., Esposito, P., et al. 2017, MNRAS, 466, L48

Ivezic, Z., Axelrod, T., Brandt, W. N., et al. 2008, Serbian Astronomical Journal, 176, 1

Jakobsson, P., Hjorth, J., Fynbo, J. P. U., et al. 2004, ApJL, 617, L21

Jakobsson, P., Frail, D. A., Fox, D. B., et al. 2005, ApJ, 629, 45

Janesick, J. R. 2001, Scientific charge-coupled devices

Jenke, P., Finger, M. H., Wilson-Hodge, C. A., & Connaughton, V. 2012, The Astronomer's Telegram, 4547

Jones, E., Oliphant, T., Peterson, P., et al. 2001, SciPy: Open source scientific tools for Python, [Online; accessed ¡today¿]

Jonker, P. G., Galloway, D. K., McClintock, J. E., et al. 2004, MNRAS, 354, 666

Joos, F., Buenzli, E., Schmid, H. M., & Thalmann, C. 2008, in Proc. SPIE, Vol. 7016, Observatory Operations: Strategies, Processes, and Systems II, 70161I

Jorstad, S. 2016, The Astronomer's Telegram, 9150

Kapanadze, B. 2016, The Astronomer's Telegram, 8998

Katz, J. I. 1994, ApJ, 422, 248

Kawabata, K. S., Akitaya, H., Yamanaka, M., et al. 2014, ApJL, 795, L4

Keller, S. C., Schmidt, B. P., Bessell, M. S., et al. 2007, PASA, 24, 1

Kennea, J. A., Evans, P. A., Coe, M. J., & Udalski, A. 2017, The Astronomer's Telegram, 10600

Kirkpatrick, S., Gelatt, C. D., & Vecchi, M. P. 1983, Science, 220, 671

Kiyota, S., Masi, G., Brown, J. S., et al. 2016, The Astronomer's Telegram, 8882

Klebesadel, R. W., Strong, I. B., & Olson, R. A. 1973, ApJL, 182, L85

Kochanek, C. S., Shappee, B. J., Stanek, K. Z., et al. 2017, PASP, 129, 104502

Komossa, S. 2015, Journal of High Energy Astrophysics, 7, 148

Kormendy, J., & Ho, L. C. 2013, Annual Review of Astronomy and Astrophysics, 51, 511

Kouveliotou, C., Meegan, C. A., Fishman, G. J., et al. 1993, ApJL, 413, L101

Kraft, R. P., Burrows, D. N., & Nousek, J. A. 1991, ApJ, 374, 344

Krühler, T., Fynbo, J. P. U., Geier, S., et al. 2012, A&A, 546, A8

Kulkarni, S. R. 2016, in American Astronomical Society Meeting Abstracts, Vol. 227, American Astronomical Society Meeting Abstracts, 314.01

Kumar, P., & Panaitescu, A. 2000, ApJL, 541, L51

Kumar, P., & Zhang, B. 2015, Phys. Rep., 561, 1

Lacy, J. H., Townes, C. H., & Hollenbach, D. J. 1982, ApJ, 262, 120

Laher, R. R., Gorjian, V., Rebull, L. M., et al. 2012, PASP, 124, 737

Lamb, D. Q. 1995, PASP, 107, 1152

Lamb, R. C., Prince, T. A., Macomb, D. J., & Finger, M. H. 1999, IAU Circ., 7081

Larionov, V. M., & Kopatskaya, E. N. 2016, The Astronomer's Telegram, 9130

Le Floc'h, E., Duc, P.-A., Mirabel, I. F., et al. 2003, A&A, 400, 499

Levan, A. J., Tanvir, N. R., Starling, R. L. C., et al. 2014, ApJ, 781, 13

Liang, E., Zhang, B., Virgili, F., & Dai, Z. G. 2007, ApJ, 662, 1111

LIGO Scientific Collaboration, Aasi, J., Abbott, B. P., et al. 2015, Classical and Quantum Gravity, 32, 074001

Lindegren, L., Hernandez, J., Bombrun, A., et al. 2018, ArXiv e-prints, arXiv:1804.09366

Lipunov, V. M., Krylov, A. V., Kornilov, V. G., et al. 2004, Astronomische Nachrichten, 325, 580

Lithwick, Y., & Sari, R. 2001, ApJ, 555, 540

Lucarelli, F., Pittori, C., Verrecchia, F., et al. 2016, The Astronomer's Telegram, 9157

Lund, N., Budtz-Jørgensen, C., Westergaard, N. J., et al. 2003, A&A, 411, L231

Lyman, J., Homan, D., Magee, M., et al. 2017, The Astronomer's Telegram, 10650

Lynden-Bell, D. 1969, Nature, 223, 690

MacFadyen, A. I., & Woosley, S. E. 1999, ApJ, 524, 262

Magalhaẽs, A. M., de Oliveira, C. M., Carciofi, A., et al. 2012, in American Institute of Physics Conference Series, Vol. 1429, American Institute of Physics Conference Series, ed. J. L. Hoffman, J. Bjorkman, & B. Whitney, 244–247

Mangano, V., Barthelmy, S. D., Chester, M. M., et al. 2014, GRB Coordinates Network, 16581

Manousakis, A., Beckmann, V., Bianchin, V., et al. 2008, The Astronomer's Telegram, 1613

Margutti, R., Zaninoni, E., Bernardini, M. G., et al. 2013, MNRAS, 428, 729

Marscher, A. P., Jorstad, S. G., Larionov, V. M., et al. 2010, The Astrophysical Journal Letters, 710, L126

Mas-Hesse, J. M., Giménez, A., Culhane, J. L., et al. 2003, A&A, 411, L261

Masi, G., Fernandez, J. M., Holoien, T. W.-S., et al. 2016, The Astronomer's Telegram, 9114

Mason, K. O., Murdin, P. G., Parkes, G. E., & Visvanathan, N. 1978, MNRAS, 184, 45P

Mauerhan, J., Williams, G. G., Smith, N., et al. 2014, MNRAS, 442, 1166

Maund, J. R., Wheeler, J. C., Baade, D., et al. 2009, ApJ, 705, 1139

McClintock, J. E., Nugent, J. J., Li, F. K., & Rappaport, S. A. 1977, ApJL, 216, L15

Meegan, C., Lichti, G., Bhat, P. N., et al. 2009, ApJ, 702, 791

Meegan, C. A., Fishman, G. J., Wilson, R. B., et al. 1992, Nature, 355, 143

Mereghetti, S., Götz, D., Borkowski, J., Walter, R., & Pedersen, H. 2003, A&A, 411, L291

Mereghetti, S., Gotz, D., Ferrigno, C., et al. 2015a, GRB Coordinates Network, 18210

Mereghetti, S., Gotz, D., Ferrigno, C., et al. 2016, GRB Coordinates Network, 19046

Mereghetti, S., Gotz, D., Ferrigno, C., et al. 2015b, GRB Coordinates Network, 18623

Mészáros, P. 2006, Reports on Progress in Physics, 69, 2259

Mészáros, P., & Rees, M. J. 1993, ApJ, 405, 278

Metzger, M. R., Djorgovski, S. G., Kulkarni, S. R., et al. 1997, Nature, 387, 878

Mingo, B., Watson, M. G., Rosen, S. R., et al. 2016, MNRAS, 462, 2631

Mirzoyan, R. 2016, The Astronomer's Telegram, 9105

Moorwood, A., Cuby, J.-G., & Lidman, C. 1998, The Messenger, 91, 9

Morrell, N., & Shappee, B. J. 2016, The Astronomer's Telegram, 9170

Motch, C., Pakull, M. W., Soria, R., Grisé, F., & Pietrzyński, G. 2014, Nature, 514, 198

Mundell, C. G., Smith, R. J., & Childress, M. J. 2016, The Astronomer's Telegram, 9165

Nakahira, S., Matsuoka, T. M. M., Negoro, H., et al. 2016, The Astronomer's Telegram, 9108

Nakajima, M., Tanaka, K., Mihara, T., et al. 2016, The Astronomer's Telegram, 9064

Nandra, K., & Pounds, K. A. 1994, MNRAS, 268, 405

Narayan, R., Paczynski, B., & Piran, T. 1992, ApJL, 395, L83

Nelder, J. A., & Mead, R. 1965, The Computer Journal, 7, 308

Norris, J. P. 2002, ApJ, 579, 386

Norris, J. P., Bonnell, J. T., Kazanas, D., et al. 2005, ApJ, 627, 324

Norris, J. P., Nemiroff, R. J., Bonnell, J. T., et al. 1996, ApJ, 459, 393

Nousek, J. A., Kouveliotou, C., Grupe, D., et al. 2006, ApJ, 642, 389

O'Brien, P. T., Willingale, R., Osborne, J., et al. 2006, ApJ, 647, 1213

Ochsenbein, F., Bauer, P., & Marcout, J. 2000, A&AS, 143, 23

Ojha, R. 2016, The Astronomer's Telegram, 9190

Oke, J. B., Cohen, J. G., Carr, M., et al. 1995, PASP, 107, 375

Paczynski, B. 1986, ApJL, 308, L43

Paczynski, B. 1990, ApJ, 363, 218

Pan, Y.-C., Foley, R. J., Jha, S. W., Rest, A., & Scolnic, D. 2016, The Astronomer's Telegram,
    9129

Panaitescu, A., & Kumar, P. 2002, ApJ, 571, 779

Pasham, D. R., Cenko, S. B., Levan, A. J., et al. 2015, ApJ, 805, 68

Patat, F., & Romaniello, M. 2006, PASP, 118, 146

Pauliny-Toth, I. I. K., Porcas, R. W., Zensus, J. A., et al. 1987, Nature, 328, 778

Perley, D. A., Cenko, S. B., Bloom, J. S., et al. 2009, AJ, 138, 1690

Perley, D. A., Levan, A. J., Tanvir, N. R., et al. 2013, ApJ, 778, 128

Perley, D. A., Krühler, T., Schulze, S., et al. 2016, ApJ, 817, 7

Pescalli, A., Ghirlanda, G., Salvaterra, R., et al. 2016, A&A, 587, A40

Piran, T. 1999, Phys. Rep., 314, 575

Piran, T. 2002, Science, 295, 986

Piran, T. 2003, Nature, 422, 268

Piro, L., Frail, D. A., Gorosabel, J., et al. 2002, ApJ, 577, 680

Planck Collaboration, Ade, P. A. R., Aghanim, N., et al. 2016, A&A, 594, A13

Plaszczynski, S., Montier, L., Levrier, F., & Tristram, M. 2014, MNRAS, 439, 4048

Predehl, P., & Schmitt, J. H. M. M. 1995, A&A, 293, 889

Prieto, J. L., Morrell, N., Rudie, G., & Shappee, B. J. 2016, The Astronomer's Telegram, 9142

Qin, Y., Liang, E.-W., Liang, Y.-F., et al. 2013, ApJ, 763, 15

Quashnock, J. M., & Lamb, D. Q. 1993, MNRAS, 265, L45

Racusin, J. L., Liang, E. W., Burrows, D. N., et al. 2009, ApJ, 698, 43

Raiteri, C. M., Villata, M., Larionov, V. M., et al. 2007, A&A, 473, 819

Rajoelimanana, A. F., Charles, P. A., & Udalski, A. 2011, MNRAS, 413, 1600

Rakic, A. D., Djurisic, A. B., Elazar, J. M., & Majewski, M. L. 1998, ApOpt, 37, 5271

Ramirez-Ruiz, E., Trentham, N., & Blain, A. W. 2002, MNRAS, 329, 465

Rau, A., Kulkarni, S. R., Law, N. M., et al. 2009, PASP, 121, 1334

Rees, M. J. 1988, Nature, 333, 523

Rees, M. J., & Mészáros, P. 1992, MNRAS, 258, 41P

Rees, M. J., & Meszaros, P. 1994, ApJL, 430, L93

Rees, M. J., & Mészáros, P. 1998, ApJL, 496, L1

Reilly, E., Maund, J. R., Baade, D., et al. 2017, ArXiv e-prints, arXiv:1701.08885

Rice, S. O. 1944, Bell Systems Tech. J., Volume 23, p. 282-332, 23, 282

Rol, E., Wijers, R. A. M. J., Kouveliotou, C., Kaper, L., & Kaneko, Y. 2005, ApJ, 624, 868

Rol, E., van der Horst, A., Wiersema, K., et al. 2007, ApJ, 669, 1098

Roming, P. W. A., Kennedy, T. E., Mason, K. O., et al. 2005, Space Science Rev., 120, 95

Ruderman, M. 1975, Annals of the New York Academy of Sciences, 262, 164

Russell, D. 2018, Galaxies, 6, 3

Russell, D. M., & Fender, R. P. 2008, MNRAS, 387, 713

Ryan, G., van Eerten, H., MacFadyen, A., & Zhang, B.-B. 2015, ApJ, 799, 3

Rybicki, G. B., & Lightman, A. P. 1979, Radiative processes in astrophysics

Saha, A., Wang, Z., Matheson, T., et al. 2016, in Proc. SPIE, Vol. 9910, Observatory Operations: Strategies, Processes, and Systems VI, 99100F

Sajina, A., Partridge, B., Evans, T., et al. 2011, ApJ, 732, 45

Salpeter, E. E. 1964, ApJ, 140, 796

Salvaterra, R., Della Valle, M., Campana, S., et al. 2009, Nature, 461, 1258

Sandage, A., & Wyndham, J. D. 1965, ApJ, 141, 328

Sari, R., & Piran, T. 1995, ApJL, 455, L143

Sari, R., Piran, T., & Halpern, J. P. 1999, ApJL, 519, L17

Sari, R., Piran, T., & Narayan, R. 1998, ApJ, 497, L17

Sasada, M., Uemura, M., Fukazawa, Y., et al. 2012, PASJ, 64, 58

Savaglio, S., Glazebrook, K., & Le Borgne, D. 2009, ApJ, 691, 182

Savaglio, S., Rau, A., Greiner, J., et al. 2012, MNRAS, 420, 627

Sazonov, S. Y., Lutovinov, A. A., & Sunyaev, R. A. 2004, Nature, 430, 646

Schady, P. 2017, Royal Society Open Science, 4, 170304

Schady, P., Dwelly, T., Page, M. J., et al. 2012, A&A, 537, A15

Schady, P., Krühler, T., Greiner, J., et al. 2015, A&A, 579, A126

Schlafly, E. F., & Finkbeiner, D. P. 2011, ApJ, 737, 103

Schmidt, W. K. H. 1978, Nature, 271, 525

Serkowski, K. 1958, Acta Astronomica, 8, 135

Serkowski, K., Mathewson, D. S., & Ford, V. L. 1975, ApJ, 196, 261

Shapiro, P. R., & Sutherland, P. G. 1982, ApJ, 263, 902

Shappee, B., Prieto, J., Stanek, K. Z., et al. 2014, in American Astronomical Society Meeting Abstracts, Vol. 223, American Astronomical Society Meeting Abstracts #223, 236.03

Shemi, A., & Piran, T. 1990, ApJL, 365, L55

Shurpakov, S., Vladimirov, V., Lipunov, V., et al. 2016, The Astronomer's Telegram, 9161

Simmons, J. F. L., & Stewart, B. G. 1985, A&A, 142, 100

Smartt, S. J., Valenti, S., Fraser, M., et al. 2015, A&A, 579, A40

Smith, P. S., Montiel, E., Rightley, S., et al. 2009, ArXiv e-prints, arXiv:0912.3621

Smith, P. S., Williams, G. G., Schmidt, G. D., Diamond-Stanic, A. M., & Means, D. L. 2007, ApJ, 663, 118

Soderberg, A. M., Kulkarni, S. R., Berger, E., et al. 2004, Nature, 430, 648

Soderberg, A. M., Berger, E., Kasliwal, M., et al. 2006, ApJ, 650, 261

Soria, R., Motch, C., Pakull, M., & Grise', F. 2016, The Astronomer's Telegram, 9068

Staley, T. D., & Fender, R. 2016, arXiv:astro-ph/1606.03735, arXiv:1606.03735

Staley, T. D., Titterington, D. J., Fender, R. P., et al. 2013, MNRAS, 428, 3114

Stamatikos, M., Barthelmy, S. D., Baumgartner, W. H., et al. 2014, GRB Coordinates Network, 16584

Stanek, K. Z. 2017, Transient Name Server Discovery Report, 589

Stanek, K. Z., Shappee, B. J., Kochanek, C. S., et al. 2017, The Astronomer's Telegram, 10627

Starling, R. 2015, GRB Coordinates Network, 17551

Starling, R. L. C., Rol, E., van der Horst, A. J., et al. 2009, MNRAS, 400, 90

Stenflo, J. O. 1994, Instrumentation for Solar Polarimetry (Dordrecht: Springer Netherlands), 312–350

Stevance, H. F., Maund, J. R., Baade, D., et al. 2017, MNRAS, 469, 1897

Strader, J., Chomiuk, L., Tremou, E., et al. 2017, The Astronomer's Telegram, 10616

Tan, G. H. 1991, in Astronomical Society of the Pacific Conference Series, Vol. 19, IAU Colloq. 131: Radio Interferometry. Theory, Techniques, and Applications, ed. T. J. Cornwell & R. A. Perley, 42–46

Tanvir, N. R., Fox, D. B., Levan, A. J., et al. 2009, Nature, 461, 1254

Tanvir, N. R., Rol, E., Levan, A. J., et al. 2010, ApJ, 725, 625

Thöne, C. C., de Ugarte Postigo, A., Fryer, C. L., et al. 2011, Nature, 480, 72

Tinbergen, J. 2007, PASP, 119, 1371

Tisserand, P., Wyrzykowski, L., Clayton, G., Welch, D., & Udalski, A. 2016, The Astronomer's Telegram, 8681

Tomasella, L., Pastorello, A., Benetti, S., et al. 2016, The Astronomer's Telegram, 9182

Tonry, J., Denneau, L., Stalder, B., et al. 2016a, The Astronomer's Telegram, 9131

Tonry, J., Denneau, L., Stalder, B., et al. 2016b, The Astronomer's Telegram, 9151

Tozzi, P., Gilli, R., Mainieri, V., et al. 2006, A&A, 451, 457

Trippe, S. 2014, Journal of Korean Astronomical Society, 47, 15

Turatto, M. 2003, Classification of Supernovae, ed. K. Weiler, 21–36

Ubertini, P., Lebrun, F., Di Cocco, G., et al. 2003, A&A, 411, L131

van der Horst, A. J., Kouveliotou, C., Gehrels, N., et al. 2009, ApJ, 699, 1087

van der Horst, A. J., Levan, A. J., Pooley, G. G., et al. 2015, MNRAS, 446, 4116

van Eerten, H. 2018, International Journal of Modern Physics D, 27, 1842002

van Eerten, H., van der Horst, A., & MacFadyen, A. 2012, ApJ, 749, 44

van Harten, G., Snik, F., & Keller, C. U. 2009, PASP, 121, 377

van Paradijs, J., Groot, P. J., Galama, T., et al. 1997, Nature, 386, 686

Vedrenne, G., Roques, J.-P., Schönfelder, V., et al. 2003, A&A, 411, L63

Vercellone, S., & AGILE Team. 2008, in AAS/High Energy Astrophysics Division, Vol. 10, AAS/High Energy Astrophysics Division #10, 20.03

Verner, D. A., Ferland, G. J., Korista, K. T., & Yakovlev, D. G. 1996, ApJ, 465, 487

Verrecchia, F., Tavani, M., Lucarelli, F., et al. 2016, The Astronomer's Telegram, 8960

Vianello, G., Götz, D., & Mereghetti, S. 2009, A&A, 495, 1005

Voges, W., Aschenbach, B., Boller, T., et al. 1999, A&A, 349, 389

von Kienlin, A., Beckmann, V., Rau, A., et al. 2003, A&A, 411, L299

Wang, L., & Wheeler, J. C. 2008, ARA&A, 46, 433

Wang, L., Wheeler, J. C., & Höflich, P. 1997, The Astrophysical Journal Letters, 476, L27

Wang, L., Wheeler, J. C., Li, Z., & Clocchiatti, A. 1996, ApJ, 467, 435

Wardle, J. F. C., & Kronberg, P. P. 1974, ApJ, 194, 249

Wiersema, K., Higgins, A. B., Covino, S., & Starling, R. L. C. 2018, PASA, 35, e012

Wiersema, K., Curran, P. A., Krühler, T., et al. 2012a, MNRAS, 426, 2

Wiersema, K., van der Horst, A. J., Levan, A. J., et al. 2012b, MNRAS, 421, 1942

Wiersema, K., Covino, S., Toma, K., et al. 2014, Nature, 509, 201

Williams, S. C., & Darnley, M. J. 2017, The Astronomer's Telegram, 10630

Willingale, R., Starling, R. L. C., Beardmore, A. P., Tanvir, N. R., & O'Brien, P. T. 2013, MNRAS, 431, 394

Willingale, R., O'Brien, P. T., Osborne, J. P., et al. 2007, ApJ, 662, 1093

Wilms, J., Allen, A., & McCray, R. 2000, ApJ, 542, 914

Winkler, C., Courvoisier, T. J.-L., Di Cocco, G., et al. 2003, A&A, 411, L1

Woosley, S. E. 1993, ApJ, 405, 273

Woosley, S. E., & Heger, A. 2006, ApJ, 637, 914

Woosley, S. E., & Weaver, T. A. 1986, ARA&A, 24, 205

Wright, E. L. 2006, PASP, 118, 1711

Wu, J., Zhou, X., Peng, B., et al. 2005, MNRAS, 361, 155

Wyrzykowski, Ł., & Hodgkin, S. 2012, in IAU Symposium, Vol. 285, New Horizons in Time Domain Astronomy, ed. E. Griffin, R. Hanisch, & R. Seaman, 425–428

Wyrzykowski, Ł., Kostrzewa-Rutkowska, Z., Kozłowski, S., et al. 2014, Acta Astronomica, 64, 197

Wyrzykowski, L., Kostrzewa-Rutkowska, Z., Udalski, A., et al. 2016, The Astronomer's Telegram, 8577

Wyrzykowski, Ł., Zieliński, M., Kostrzewa-Rutkowska, Z., et al. 2017, MNRAS, 465, L114

Yamanaka, M., Nakaoka, T., Tanaka, M., et al. 2017, ApJ, 837, 1

Zaroubi, S., Jelić, V., de Bruyn, A. G., et al. 2015, MNRAS, 454, L46

Zauderer, B. A., Berger, E., Margutti, R., et al. 2013, ApJ, 767, 161

Żejmo, M., Słowikowska, A., Krzeszowski, K., Reig, P., & Blinov, D. 2017, MNRAS, 464, 1294

Zel'dovich, Y. B. 1964, Soviet Physics Doklady, 9, 195

Zhang, B. 2007, Advances in Space Research, 40, 1186

Zhang, B., Fan, Y. Z., Dyks, J., et al. 2006, ApJ, 642, 354

Zhang, B., Kobayashi, S., & Mészáros, P. 2003, ApJ, 595, 950

Zhang, B., & Mészáros, P. 2004, International Journal of Modern Physics A, 19, 2385

Zhang, B.-B. 2014, GRB Coordinates Network, 16590

Zhang, B.-B., Uhm, Z. L., Connaughton, V., Briggs, M. S., & Zhang, B. 2016a, ApJ, 816, 72

Zhang, J., Zhang, T., Li, W., & Wang, X. 2016b, The Astronomer's Telegram, 9103

Zwart, J. T. L., Barker, R. W., Biddulph, P., et al. 2008, MNRAS, 391, 1545